REFERENCE ONLY

UNIVERSITY OF LONDON THESIS

Degree PhD Year 2005 Name of Author BENSON, T. N.

IN SITU PARTICLE SIZE INSTRUMENTATION FOR IMPROVED PARAMETERISATION AND VALIDATION OF ESTUARINE SEDIMENT TRANSPORT MODELS

Thomas D. Benson
Coastal and Estuarine Research Unit
Department of Geography

Supervisor:
Dr Jon R. French

Submitted in fulfilment of the requirements for the Degree of Doctor of Philosophy at the University of London as part of a Postgraduate Training Partnership between University College London and Sira Technology Centre

June 2004

ProQuest LLC
789 East Eisenhower Parkway
P.O. Box 1346
Ann Arbor, MI 48106-1346

Abstract

In estuaries containing cohesive sediment, flocculation and break-up of the suspended particles during the tidal cycle has implications for the monitoring and modelling of sediment transport. Monitoring of suspended sediment concentration using *in situ* optical or acoustic instruments is problematic since the amount of light or sound scattered from the suspended sediment is proportional to both the suspended concentration and the size of the particles. Numerical sediment transport models are heavily reliant upon such concentration data. Particle size variation also directly affects model parameterisation by influencing the settling velocity.

A critical review of current particle sizing techniques shows that *in situ* imaging offers the best option in terms of cost, accuracy and versatility. This thesis presents a new, low cost video-based instrument for measuring the *in situ* particle size distribution. The system uses two CCTV cameras to view a total size range of 4 to 3000 μm. Illumination is provided by miniature microsecond flash units. These allow blur-free images of particles to be obtained in current speeds of up to 1.4 ms^{-1}, which are saved to hard disk at a frame rate of up to 10 s^{-1}. The instrument package is designed for small-boat operation and deployment in profile mode. Calculation of size and shape parameters is accomplished in software using automated image-processing algorithms. An efficient and accurate edge coincidence technique is developed to detect in focus particles.

Instrument performance is evaluated through a case study of the Blyth estuary (Suffolk, UK). Particle size data from a small reach of the estuary are presented for both a spring and neap tide. The process of flocculation is clearly shown, and a semi-empirical model of particle size variation is derived based on turbulent intensity and suspended sediment concentration. The modelled sizes are used to derive settling velocity data for a 2DH model of sediment transport using a simplified model of floc density. Model output is improved in comparison to using a fixed value of settling velocity. Two distinct particle size subpopulations are observed which affect both the settling velocity and the calibration of ADCP backscatter data for sediment concentration between flood and ebb. In addition, rapid resuspension of bed material at the beginning of the flood tide is successfully simulated using a two-layer bed model. It is concluded that the new instrument is a valuable aid to monitoring and modelling of sediment transport.

Contents

LIST OF FIGURES 6
LIST OF TABLES 14

1. INTRODUCTION 15
1.1 The importance of estuaries 15
1.2 Numerical modelling of estuarine hydraulics and sediment transport 17
1.2.1 Overview 17
1.2.2 Parameterisation of bed friction 25
1.2.3 Sediment dispersion coefficients 27
1.2.4 Sediment influx at the flow boundaries 29
1.2.5 Sediment properties 30
1.3 Problems associated with monitoring and modelling of cohesive sediment transport 36
1.3.1 Flocculation 36
1.3.2 Consolidation and bed layering 44
1.3.3 Fluid mud formation 47
1.4 Instrumentation for sediment concentration measurement 49
1.4.1 Optical scattering instruments 49
1.4.2 The acoustic Doppler current profiler 53
1.4.3 The effect of particle size on transmissometer and ADCP calibration 56
1.5 Aims and Objectives 67

2. RESEARCH APPROACH 69
2.1 Overview 69
2.2 Case study description: The Blyth estuary 71
2.2.1 Physical setting 71
2.2.2 Geomorphology 71
2.2.3 Reclamations 72
2.3 Previous investigations 74
2.3.1 Conceptual model 74
2.3.2 Emergent issues 76
2.4 Field measurements 77
2.5 Modelling 82
2.5.1 Choice of modelling software 82
2.5.2 Hydrodynamic equations 83
2.5.3 Sediment transport equations 84
2.5.4 Model dimensionality 85

3. SUSPENDED PARTICLE SIZING TECHNIQUES 86
3.1 Coulter Counters 86
3.2 Field Settling Tubes 89
3.3 Laser Diffractometers 94
3.4 Time-of-Transition laser systems 98
3.5 Multiple wavelength acoustic systems 101
3.6 Model-dependent inversion techniques 105
3.7 Imaging Systems 107
3.7.1 Photographic systems 107

3.7.2 Videotape systems 112
3.7.3 Digital imaging systems 114
3.7.4 Sizing and settling velocity video systems 117
3.7.5 Holographic imaging systems 122
3.8 Summary 127
3.8.1 Review of instrument features 127
3.8.2 Requirements for a low cost estuarine instrument 127

4. INSIPID: INSTRUMENT DESIGN 131
4.1 Overview 131
4.2 Hardware components 134
4.2.1 Camera 134
4.2.2 Lens system and calibration 137
4.2.3 Light Source 141
4.2.4 Waterproof housing 144
4.2.5 Computer and framegrabber 145
4.2.6 Data communication and power supply 148
4.2.7 Additional instrumentation 149
4.3 Software components 150
4.3.1 Data acquisition software 150
4.3.2 Noise filtering 152
4.3.3 Image segmentation 156
4.3.4 Particle sizing 173
4.3.5 Particle shape analysis 175
4.4 Laboratory assessment and validation 179
4.4.1 Test method 179
4.4.2 Test results 182

5. MONITORING AND MODELLING OF PARTICLE SIZE AND SEDIMENT TRANSPORT: BLYTH ESTUARY CASE STUDY 189
5.1 Overview 189
5.2 Field Observations 189
5.2.1 ADCP time-series 192
5.2.2 InSiPID profiles 196
5.3 Particle size modelling 202
5.3.1 Controls on flocculation 202
5.3.2 Conversion to a volume weighted median diameter 207
5.3.3 Floc density 208
5.3.4 Particle sub-populations 213
5.3.5 Flocculation model 224
5.4 Sediment transport model 230
5.4.1 Hydrodynamic model 230
5.4.2 Bed layer module 236
5.4.3 Settling velocity module 238
5.5 Sediment transport simulations 241
5.5.1 Model 1 – Basic parameterisation 243
5.5.2 Model 2 – Subtidal zonation of critical shear stress for erosion 248
5.5.3 Model 3 – Freshly deposited bed layer 253
5.5.4 Model 4 – Variable settling velocity 254
5.6 Effects of particle size on ADCP backscatter calibration for SSC 260

6. DISCUSSION 265
6.1 Evaluation of the InSiPID system 265
6.2 Evaluation of improvements to sediment transport model parameterisation 267
6.2.1 Overview 267
6.2.2 Reassessing the use of floc size to derive settling velocity 268
6.2.3 Bed layer modelling: reducing the problem 277
6.2.4 A conceptual model of sediment transport in the Blyth estuary 280
6.2.5 The feasibility of using the sediment transport model output to provide a switch between ADCP calibrations 287
6.3 Future work 290
6.3.1 Possible improvements to the InSiPID design 290
6.3.2 Possible improvements to the sediment transport model 292

7. CONCLUSIONS 301
7.1 Immediate findings 301
7.2 Further work 305

ACKNOWLEDGEMENTS 306
REFERENCES 307
APPENDIX 327

List of figures

Figure 1.1 – Overview of the stages involved in the implementation of a numerical estuarine sediment transport model 21
Figure 1.2 – Conceptual diagram of sediment transport model parameterisation – For explanation of terms, see text. 24
Figure 1.3 –Rouse model of sediment concentration with depth 35
Figure 1.4 - (a) Idealised tidal flow diagram (neglecting any flood-ebb asymmetry). (b) Schematic of flocculation during a tidal cycle in the upper part of the water column. 40
Figure 1.5 – Theoretical model of floc size variability with turbulent shear and suspended sediment concentration (Dyer, 1989) 42
Figure 1.6 - Idealised implementation of a layered bed to simulate consolidation 46
Figure 1.7 – Deviations from the theoretical Rouse profile caused by the properties of cohesive sediments. 48
Figure 1.8 - The physical principle of the transmissometer 52
Figure 1.9 - Schematic of a transmissometer calibration curve. 52
Figure 1.10 – Photo of RD Instruments Workhorse broadband ADCP on customised mount (with Partech IR40 transmissometer and pump sampler intake tube on a 1m pole) prior to field deployment. 53
Figure 1.11 - Determining 3D velocity components with the ADCP (RD Instruments manual) 55
Figure 1.12 - Diagram of ADCP principle of operation. 55
Figure 1.13- A typical transmissometer calibration curve (re-drawn from Wells & Kim, 1991). 56
Figure 1.14 - Diffraction of a light beam by a small particle. 59
Figure 1.15 - Variation of scattering efficiency factor with particle size. 59
Figure 1.16 - (a) Calibration curves for different sized glass bead solutions, (b) Slopes of the calibration curves plotted against inverse particle diameter (from Wiberg *et al*, 1994). 61
Figure 1.17 - Various estimates for the change in calibration with inverse particle size (from Wiberg *et al*, 1994) 61
Figure 1.18 - Theoretical graph of transmissometer calibration variation versus inverse particle size. 62
Figure 1.19 - Measurements of SSC using ADCP backscatter data across the River Mersey (from Wither *et al* 1998). 63
Figure 2.1 – Research approach organisation diagram 70
Figure 2.2 – The Blyth estuary: (A) Location within the UK; (B) Detailed map showing the data collection site near Reydon (dashed box). 73
Figure 2.3 – The three geomorphological compartments defined by French *et al* (2004). 1 = upper estuary (low energy environment), 2 = mid-estuary (predominantly mudflats with moderate tidal current speeds and wind induced wave stresses), 3 = lower estuary (constrained environment with strong tidal flow). 75
Figure 2.4 – The field data collection site near Reydon showing instrument locations. 79
Figure 2.5 – The ADCP bottom rig (with transmissometer and water sample hose) 80
Figure 2.6 – Deploying the ADCP bottom rig at Reydon 80
Figure 2.7 – Weather station located at the northern end of the Bulcamp tidal flats 81

Figure 3.1 - (a) Schematic of the Coulter Counter (redrawn from Barth, 1984), (b) Difference between size distribution measurements by Coulter Counter and the In Situ Benthos Plankton Camera (from Milligan, 1996). 88
Figure 3.2 – Field settling tubes. (a) The Owen Tube (Owen, 1971); (b) The QUISSET settling tube (redrawn from Jones & Jago, 1996); (c) The FIPIWITU (i) lowering and sampling position, (ii) raising position (Cornelisse, 1996). 92
Figure 3.3 - Optical field settling tubes. (a) ROST (Zaneveld *et al*, 1982); (b) Backscatter settling tube designed by Kineke *et al* (1989); (c) In situ settling box, Cambridge University, with detail of custom-made backscatter sensor (redrawn from Murray *et al*, 1996)..... 93
Figure 3.4 – (a) The Malvern laser diffractometer (http://www.malvern.co.uk). (b) Schematic diagram of laser diffraction apparatus (from Swithenbank *et al*, 1977). (c) Detail of specialised annular detector used in laser diffractometers. 96
Figure 3.5 – Field deployable laser diffractometers. (a) The adapted Malvern particle sizer used by Bale & Morris (1987): (i) Fourier Transform lens, (ii) detector, (iii) He/Ne laser, (iv) light guide, (v) sample volume. (b) LISST-ST with automated settling column (from Sequoia Scientific Inc.; http://www.sequoiasci.com). 97
Figure 3.6 – Time-of-transition particle sizers: (a) Transmission type (Tsai, 1996), (b) Reflectance type (Law *et al*, 1997), (c) Adapted Par-tec 100 for *in situ* measurements (Law *et al*, 1997). 100
Figure 3.7 – The Aquatec multiple frequency Acoustic Backscatter System, with detail of the sensor head, showing the three transducers (Smerdon *et al*, 1998)..... 101
Figure 3.8 – Variation of the backscatter form function (f) with ka (k = wavenumber, a = particle radius) calculated using Equation 3.3. 104
Figure 3.9 – Rouse profiles calculated from Equation 1.16 with a variety of settling velocities: **a** = 1, **b** = 3, **c** = 5, **d** = 10 mm s^{-1}. The reference concentration (C_a) and shear velocity (u_*) are set to be constant at 100 mgl^{-1} and 0.01 ms^{-1} respectively.... 106
Figure 3.10 – (a) The Benthos Plankton Camera (Milligan, 1996), and (b) its internal workings. 108
Figure 3.11 - ISAAC (Knowles & Wells, 1996). 109
Figure 3.12 – Multiple camera systems (a) The camera system designed at the Netherlands Institute of Sea Research (Eisma *et al*, 1990). (b) The Floc Camera Assembly (i) detail of the three cameras and flash unit, (ii) full deployment rig, with stilling tanks (Heffler *et al*, 1991). 111
Figure 3.13- Video camera system from Thomsen *et al*, 1996. 113
Figure 3.14 – In situ digital imaging systems: (a) Endoscope video system (Maldiney & Mouchel, 1995). (b) VMSS configuration – adapted from Pfeiffer (1996). 115
Figure 3.15 – The Video Plankton Recorder (adapted from Davis *et al*, 1992)..... 116
Figure 3.16 – (a) Video In Situ (VIS), (b) results from VIS (Van Leussen & Cornelisse, 1993). 119
Figure 3.17 – (a) In Situ Size and Settling Velocity system (INSSEV) (Fennessy *et al*, 1994), (b) Results from INSSEV (Fennessy & Dyer, 1996). 120
Figure 3.18 – (a) Automated settling velocity sediment trap (Sternberg *et al*, 1996), (b) Results from this system (•) compared with INSSEV results (+)..... 121
Figure 3.19 – In-line hologrammetry (a) Recording, (b) Playback, showing the virtual and real images. As shown, a camera may be passed through the 3D image to record 2D slice images for particle sizing (redrawn from Foster & Watson, 1997) 124

Figure 3.20 – Submersible holocamera systems: (a) The system developed by Carder et al (1982), with a detail to highlight the use of flow dampers, (b) The towable system developed by Katz *et al* (1999). 126
Figure 4.1 - In Situ Particle Imaging Device (30cm rule for scale)..... 132
Figure 4.2 - Cut away diagram of INSIPID housing showing main electronic components. 133
Figure 4.3 - The Sony XC-55 Progressive scan CCD camera..... 136
Figure 4.4 - The lens magnification systems: (a) high magnification - 9:1; (b) low magnification - 1:2.5. 139
Figure 4.5 - High power system calibration: (a) image of 50μm graticule line; (b) binary threshold image; (c) pixel greyscale profile..... 140
Figure 4.6 - Low power system calibration: (a) image of a 1 mm graticule marking with the low power camera; (b) binary close up of the circle..... 140
Figure 4.7 - The EG&G miniature microsecond xenon flash unit..... 142
Figure 4.8 - (a) The RSL-2100-1 flash bulb (units in inchs); (b) Beam Profile. 143
Figure 4.9 - Typical beam spectrum characteristics of the miniature flash (Manufacturers' data). 143
Figure 4.10 - The Matrox 4Sight II standalone imaging system (Matrox Imaging Ltd.; http://www.matrox.co.uk). 147
Figure 4.11 – Customised housing for computer components 147
Figure 4.12 – Close up of underwater junction box for splitting cables..... 148
Figure 4.13 – Additional instrumentation: (a) Quasar Electronics parallel port ADC; (b) Druck pressure sensor; (c) Partech IR40 transmissometer..... 149
Figure 4.14 – User console window for data acquisition..... 151
Figure 4.15 – 100x100 pixel sub-sample of a low-resolution image (a) before filtering; and (b) after applying Wiener filter, showing a reduction in the image 'graininess'. Although this appears minimal to the naked eye, it greatly reduces the detection of false particle edges in the segmentation stage..... 155
Figure 4.16 – The edge detection operators: (a) schematic diagram of the implementation of a 3x3 Sobel operator used for the low power images; (b) normalised greyscale image of the 21x21 Gaussian edge detection operator (standard deviation = 2) used for the high power images: (i) horizontal edges, (ii) vertical edges..... 161
Figure 4.17 - Binary thresholding of a low-resolution image using various thresholding techniques – (a) Subset of original image, with arrows indicating some out of focus particles; (b) histogram/cluster-based method of Otsu (1979), T=172; (c) iterative edge coincidence method of Toriu *et al* (1990), T=153; (d) dark-side edge pixel intensity method with removal of out of focus particles (presented here)..... 162
Figure 4.18 - Iterative edge measure method of Toriu *et al* (1990) for finding the threshold according to edge coincidence, applied to the low-resolution image shown in Figure 4.17a, with the edge threshold set at 0.07, resulting in T_{max}=153.. 163
Figure 4.19 - Greyscale pixel intensity histograms for: (a) entire image, showing lack of double peak; (b) edges obtained using normal edge thinning (edge threshold = 0.07); (c) edges obtained using dark-side edge thinning (edge threshold = 0.07). 164
Figure 4.20 - Raw images: (a) low-resolution system; (b) high-resolution system..... 165
Figure 4.21 - Reference images: (a) low-resolution system; (b) high-resolution system..... 166
Figure 4.22 - Raw minus reference images, rescaled from 0 to 255: (a) low-resolution system; (b) high-resolution system. 167

Figure 4.23 - High frequency filtered images: (a) low-resolution system; (b) high-resolution system 168
Figure 4.24 - Edge detection images: (a) low-resolution image, using a 3x3 Sobel dark-side edge detector, with an edge gradient threshold of 0.07; (b) high-resolution image, using a 21x21 Gaussian edge detector, with an edge gradient threshold of 0.35. 169
Figure 4.25 - Histogram of edge pixel intensities, showing the located maxima within the predefined range of 50 to 200 grey levels: (a) low-resolution image, with size maxima; (b) high-resolution image with eleven maxima. 170
Figure 4.26 - Perimeters of the binary images for each threshold (shown here as a single image): (a) low-resolution system; (b) high-resolution system. 171
Figure 4.27 - Final image, produced by the logical combination of each binary threshold image. Out of focus particles are removed at each threshold according to the edge coincidence (R_e) between the edge image and the binary perimeter image: (a) low-resolution image (R_e= 0.3); (b) high-resolution image (R_e = 0.15)... 172
Figure 4.28 – Schematic diagram of particle counting and sizing process: (a) Binary image showing white particles; (b) labelling of individual particles, ignoring any particles with pixels touching the perimeter of the image (grey) 174
Figure 4.29 - Determining step length from step size for a section of a particle boundary 177
Figure 4.30 – Fractal dimension calculation for the low-resolution binary image shown in Figure 4.27 (F_D=1.77). 178
Figure 4.31 – Test set-up, showing the sample volume between the high power camera and strobe housing. 180
Figure 4.32 – Manual sizing using calibrated microscope images (see scale): (a) Polymer microspheres; (b) Lycopodium spores (subsection of a whole image) 181
Figure 4.33 – Low-magnification images of the polymer microspheres: (a) greyscale image (after noise removal); (b) Binary image using InSiPID software with region filling to account for transparent spheres. 185
Figure 4.34 – High-magnification images of a lycopodium spore: (a) greyscale image (after noise removal); (b) Binary image using InSiPID software. 186
Figure 4.35 – Low-resolution system particle size distribution results using neutrally buoyant microspheres (histogram bin size = 10), showing manual counts and results obtained from the InSiPID instrument 187
Figure 4.36– High-resolution system particle size distribution results using Lycopodium spores (histogram bin size = 2), showing manual counts and results obtained from the InSiPID instrument. 188
Figure 5.1 – Predicted tides for Southwold harbour between September 25th and October 22nd showing ADCP deployment periods (hatched regions) and the InSiPID data collection periods (bold line) 190
Figure 5.2 – The Blyth estuary (A) and aerial photo of the field data collection site near Reydon showing instrument locations (B). 191
Figure 5.3 - Upward looking ADCP velocity magnitude profiles at Reydon field site for neap tide (A) and spring tide (B) deployments (note the difference in velocity scale and the deployment duration between the two plots). The water surface is also plotted from the ADCP's integral pressure sensor. 194
Figure 5.4 - ADCP backscatter coefficient at Reydon, corrected for beam spreading and attenuation, for the neap (A) and spring (B) tide deployments (note that the colour bar scaling is the same for each plot). 195
Figure 5.5 - Deploying the In Situ Particle Imaging Device at Reydon 197

Figure 5.6 - Neap tide depth profile time series data showing the water level (A), suspended sediment concentration from water samples (B), low magnification D_{50} (C) and high magnification D_{50} (D). Note that depths are normalised. 198
Figure 5.7 - Spring tide depth profile time series data showing the water level (A), suspended sediment concentration from water samples (B), low magnification D_{50} (C) and high magnification D_{50} (D). Note that depths are normalised. 199
Figure 5.8 – Neap tide depth averaged data set for Reydon showing tide gauge water level (A), ADCP depth mean current speed from power law (B), ADCP bin 2 beam average backscatter (C), suspended sediment concentration from water samples (D), low magnification D_{50} (E) and high power D_{50} (F). In D to F, dots represent individual samples and the trend line represents the assumed depth average. 200
Figure 5.9 – Spring tide depth averaged data set for Reydon showing tide gauge water level (A), ADCP depth mean current speed from power law (B), ADCP bin 2 beam average backscatter (C), suspended sediment concentration from water samples (D), low magnification D_{50} (E) and high power D_{50} (F). Note the distinct peaks in particle size in (E) at slack water. 201
Figure 5.10 – Depth mean D_{50} vs suspended sediment concentration for the entire data from the low (A) and high (B) magnification systems. Circles mark the neap tide data and squares mark the spring tide. Flood spring tide data are represented by unfilled markers. The regression lines are fitted through the neap tide data in both graphs. 205
Figure 5.11 - Depth mean D_{50} vs turbulence parameter (G) for the entire data from the low (A) and high (B) magnification systems. Circles mark the neap tide data and squares mark the spring tide. Flood tide spring data are represented by unfilled markers. The two log regression lines in graph A are fitted through the spring tide flood (dashed curve) and ebb (solid curve). The quadratic polynomial in graph B is fitted through the spring ebb data (solid squares) 206
Figure 5.12 – Graph of floc diameter versus effective density, composed of data from a variety of authors: A = Manning & Dyer (1999); B = Al Ani *et al* (1991); C = Alldredge & Gotschalk (1988); D = Fennessy *et al* (1994); E = Gibbs (1985); F = McCave (1975); G = McCave (1984); H = Kranck *et al* (1993); I = Syvitski *et al* (1995); J = Sternberg *et al* (1999); K = linear regression through all data, forced through a fixed origin of 5 μm at an effective density of 1318 kgm^{-3} (see text for explanation). 210
Figure 5.13 – Neap tide D_{50} calculated from a number (A), volume weighted (B) and quasi-mass weighted (C) particle size distribution from the combined camera data. The solid line represents the average for each vertical InSiPID profile (assumed to be equivalent to the depth average particle size). 211
Figure 5.14 – Spring tide D_{50} calculated from a number (A), volume weighted (B) and quasi-mass weighted (C) particle size distribution from the combined camera data. 212
Figure 5.15 - Quasi-mass weighted, depth-averaged particle size distribution for each InSiPID profile (neap tide). Each graph is normalised to a common maximum mass. 215
Figure 5.16 - Quasi-mass weighted, depth averaged particle size distribution for each InSiPID profile (spring tide). Each graph is normalised to a common maximum mass. 216

Figure 5.17 – Percentage of total suspended sediment mass distribution present as macro-flocs (d>125 μm) for the neap (A) and spring (B) tides. Note the low percentage of macro-flocs at the start of the neap tide due to settling, and the very low percentage (<10%) during the spring flood tide, possibly due to the advection of two different particle sub-populations. Also note the larger percentage of macro-flocs during the spring ebb tide 217
Figure 5.18 – Neap tide representative images of filter papers from the mid flood (A) and ebb (B) water samples. Note the presence of large organic material (seen as darker fragments) 220
Figure 5.19 – Spring tide representative images of water sample filter papers taken during mid flood (A) and towards the end of the ebb (B). Note the darker colouration as compared to the neaps (indicating higher sediment concentrations) and lower proportion of organic material in the flood sample. 221
Figure 5.20 – Neap tide particle characteristics other than size: (A) total concentration, (B) total area (solid line) and D_{50} (dashed line) of organic particles on filter paper, (C) mass (solid line) and percentage (dashed line) loss on ignition, (D) fractal dimension from low (solid line) and high (dashed line) magnification cameras 222
Figure 5.21 – Spring tide particle characteristics other than size: (A) total concentration, (B) total area (solid line) and D_{50} (dashed line) of organic particles on filter paper, (C) mass (solid line) and percentage (dashed line) loss on ignition, (D) fractal dimension from low (solid line) and high (dashed line) magnification cameras 223
Figure 5.22 – Calibration of ψ by testing the modelled particle size against observations at a range of values using the linear regression R^2 values. 227
Figure 5.23 – Linear regression curves of particle size calibration coefficient (ζ) versus D_{50}. (A) Entire neap data and spring ebb and spring flood plotted separately. (B) Combined spring and neap tide calibrations, with late flood data plotted separately from rest of data, indicating the advection of different sub-populations of sediment during the flood and ebb. 228
Figure 5.24 – Particle size model (using the estuarine sourced sediment calibration), showing: (A) 2D surface plot of calibrated D_{50} with suspended sediment concentration and turbulence parameter. (B) Modelled particle D_{50} versus turbulence parameter at a range of suspended concentrations. Observed particle size data are also plotted with symbols representing different concentrations (■=10-20; ♦ = 20-40; ✱=40-80; ● = 80-160 mgl^{-1}). Mid to late flood tide data (after resuspension at the beginning of flood) are represented by unfilled markers (which are overestimated by the model using this calibration, particularly at higher values of G). Note the shift in the floc size peak towards higher turbulence with decreasing suspended concentration. The dashed line indicates the calibration point $G_p = 15\ s^{-1}$, which marks a peak in flocculation at $C_p = 40\ mgl^{-1}$ 229
Figure 5.25 - Finite element mesh for the Blyth estuary model 232
Figure 5.26 - Bathymetry for the Blyth estuary model 233
Figure 5.27 -Spatially varied Manning friction coefficients 234
Figure 5.28 – Modelled (solid line) and observed (dotted line) hydrodynamic data at Reydon: (A) neap levels, (B) neap depth averaged current speeds (low pass filtered), (C) spring levels and (D) spring depth averaged current speeds (low pass filtered). 235
Figure 5.29 - Bed module erosion carried out in two passes for each time step to simulate bed armouring 237

Figure 5.30 – Modelled settling velocity versus particle size using Stokes' Law, showing constant density model (dashed line) and adjusted density curves (solid lines). The dotted curve defines the maximum settling velocity before initiation of turbulent flow (Re = 1) around the settling particles for each size. Fine-tuning of the settling velocity curve can be performed during the sediment transport model calibration phase by adjusting the maximum settling velocity (and hence the slope of the graph) as shown. The two adjusted density curves are for the empirically derived density model (1.1 mms^{-1}) and the maximum settling velocity for applicability of Stokes' Law (3.3 mms^{-1}) both determined from the largest value of D_{50} measured in the Blyth estuary (300 μm). 240
Figure 5.31 - Sediment transport model computation steps. Note the inclusion of a sub-loop for calculating the maximum erosion layer and total concentrations. 242
Figure 5.32 – Basic model sedimentary zones defined for the SUBIEF-2D bed model. 246
Figure 5.33 – Settling periods for high (green) and low (red) slack water, calculated from the modelled shear velocities at Reydon assuming u_{*cd} = 0.01 ms^{-1} for the neap (A) and spring (B) tide simulations. Note that the same scale is used for both graphs to highlight the differences between the spring and neap tide settling periods. 247
Figure 5.34 - Additional zonation of u_{*ce} in the subtidal zone (models 2 to 4). 251
Figure 5.35 - Mean shear velocity for the spring tide hydrodynamic data 252
Figure 5.36 – Modelled and observed (bold line) particle size for neap (A) and spring (B) tides. Each graph shows the calibration using one (dashed line) and two (solid line) sediment types. The equivalent settling velocity is marked on the second y-axis. Note the improvement in the modelled particle size for the spring flood tide when using two sediment types. The neap tide is not significantly improved in this way, possibly due to the greater mixing of the marine and estuarine water masses and higher proportions of organic material. 257
Figure 5.37 – Neap tide modelled (solid line) and observed (dashed line) suspended sediment concentration. Showing basic parameterisation (A) followed by sequential addition of spatially varied u_{*ce} (B), a resuspension bed layer (C), and a variable settling velocity model (D). The modelled water level at Reydon is plotted at the top. 258
Figure 5.38 – Spring tide modelled (solid line) and observed (dashed line) suspended sediment concentration. Showing basic parameterisation (A) followed by sequential addition of spatially varied u_{*ce} (B), a resuspension bed layer (C), and a variable settling velocity model (D). The modelled water level at Reydon is plotted at the top. 259
Figure 5.39 – (A) Single ADCP calibration for suspended sediment concentration using beam average backscatter for bin 2. (B) Modelled (solid line) and ADCP derived suspended concentrations (dashed line) for neap (i) and spring (ii) tides. Water bottle sample data are also plotted (•). 261
Figure 5.40 - (A) Separate flood and ebb ADCP calibration for suspended sediment concentration using beam average backscatter for bin 2. (B) Modelled (solid line) and ADCP derived suspended concentrations (dashed line) for neap (i) and spring (ii) tides. Water bottle sample data are also plotted (•). 264

Figure 6.1 – Schematic diagram of the three calibration stages of the settling velocity model, showing (A) particle size model calibration, (B) preliminary calibration of the floc density power law relationship (using past data) and (C) application of the two models to provide settling velocity data to the sediment transport model, with iterative calibration of the particle density model if required. Note that the solid boxes represent observations, and the dashed boxes are data derived from model output. 274
Figure 6.2 – Parameterisation of u_{*ce} for the neap (dashed line) and spring (solid line) tide simulations in the subtidal channel zones. (Zone numbering starts furthest from the estuary mouth as follows: 3 = upper channel, 4 = New cut to Tinkers Bend, 5 = Tinkers Bend to Wolsey Creek, 6 = Reydon section, 7 = Blackshore Quay, 8 = Harbour mouth). Note the shift in poorly consolidated sediment from zone 4 during the spring tide to zone 6 during the neap tide. 279
Figure 6.3 – Conceptual model of **flood** tide sediment transport observed at Reydon for (A) neap tide and (B) spring tide. In this model, the x-axis represents time from low water to high water. Note the conversion of marine sourced sediment to estuarine sourced sediment on deposition at slack high water. 282
Figure 6.4 – Conceptual model of **ebb** tide sediment transport observed at Reydon for (A) neap tide and (B) spring tide. In this model, the x-axis represents time from high water to low water. 283
Figure 6.5 – Modelled level and suspended concentrations at Reydon (model 4) for the estuarine sourced (solid line) and marine sourced (dashed line) sediment types for the neap (A) and spring (B) tides. Note the different timing of resuspension of the top bed layer (indicated by the solid arrows) in relation to the advection of the marine sediment past the point of measurement. Also observe that the second layer is resuspended at approximately the mid flood in both simulations (dashed arrow), hence there is a visible separation between the two resuspension events during the spring tide, whereas they are merged during the neap tide. 284
Figure 6.6 – (A) Separate estuarine and marine sourced sediment ADCP calibration for suspended sediment concentration using beam average backscatter for bin 2. (B) Modelled (solid line) and ADCP derived suspended concentrations (dashed line) for neap (i) and spring (ii) tides. Water bottle sample data are also plotted (•). 288
Figure 6.7 – Shear velocity induced at the bed by wind induced waves, calculated using Equation 5.11 (f_w = 0.003). Wave heights are limited to half the water depth. 295
Figure 6.8 – (A) Suspended sediment concentration versus particle size calibration coefficient (ζ) with a power law regression fitted to data below the critical shear velocity, u_{*cd} = 0.01 ms^{-1} represented by filled markers (B) Suspended sediment concentration versus D_{50} for data below u_{*cd} = 0.01 ms^{-1}, with a power law regression line fitted through the data. The unfilled markers in graph B define mid to late flood tide data, indicating the requirement for two separate calibrations. 300

List of tables

Table 1.1 – Commercial and ecological importance of British estuaries (Soulsby *et al*, 1997) 16

Table 3.1 – Inherent capabilities (●) and possible capabilities with adaptation (○) of the various estuarine particle size measurement techniques. 130

Table 4.1 - Calculation of the equivalent diameter of a sphere for the particles in Figure 4.28b. 175

Table 4.2 – Statistical comparison between manually counted and automated InSiPID size distributions. 183

Table 5.1 – Bed parameterisation for the basic model run (for both springs and neaps) 243

Table 5.2 – Bed parameterisation for subtidal channel zonation model (shaded boxes indicate changes made between the neaps and springs simulations). 248

Table 5.3 – Critical shear velocity for erosion by zone for the resuspension bed layer. 253

1. Introduction

1.1 The importance of estuaries

Estuaries around the world provide an important resource in terms of transport, industry, commerce, settlement, fishing, habitat, agriculture and recreation (e.g. UK, Soulsby *et al*, 1997; Brazil, Wells & Daborne, 1997; South Africa, Slinger & Breen, 1995; Ecuador, Arriaga *et al*, 1999; South-east Australia, Roy *et al*, 2001; China, Shi *et al*, 2001; The Netherlands, de Jonge, 2000; Bangladesh, Alam & Thomson, 2001; USA, Wenner & Geist, 2001). Often the various roles of an estuary, such as flood defence, navigation, nature conservation and water quality are in direct conflict with one another (Soulsby *et al*, 1997; Edwards *et al*, 1997). Research programmes initiated to help address these issues include the National Estuaries Research Reserves (NERR) program in the United States (Wenner & Geist, 2001); the Consortium for Estuarine Research and Management (CERM) in South Africa (Slinger & Breen, 1995); and the Estuaries Research Programme (ERP) in the United Kingdom (EMPHASYS Consortium, 2000a).

The United Kingdom offers prime examples of estuaries that have been affected by the increasing pressures being placed upon them. In 1997, it was estimated that 11.5 million people were living within one kilometre of an estuary within Great Britain. As a consequence of this large-scale historical development of naturally low-lying land, there are roughly 2,150 km of tidal defences, costing in the order of £48m per annum to maintain (Soulsby *et al*, 1997). In 1993, it was estimated that 30 million tonnes of sediment were dredged from UK ports, often with little understanding of the consequences for fluvial and tidal dynamics and the intertidal ecosystem. With an increase in the size of container ships, further maintenance dredging is likely to be necessary. In addition, the predicted increase in sea level rise as a result of global warming will put further pressures upon the estuarine environment and its defences (Titus *et al*, 1991; Pethick, 2001).

Table 1.1 lists the estimated annual revenue or expenditure, where these are known, and the percentage of estuary based usage for a variety of activities or interests in Great Britain (adapted from Soulsby *et al*, 1997). This table highlights the continuing importance of UK estuaries, and provides a strong argument for further research into

both the short-term and long-term effects caused by the various activities associated with them.

The UK Estuaries Research Programme (ERP) has placed considerable emphasis on various forms of numerical modelling as a basis for understanding and managing the complexity of estuarine responses to human activities and environmental change (French *et al*, 2002). This approach has been driven by the economic benefits of research into flood defence and dredging, particularly in the industrial and agricultural areas of Southeast England where the problem of sea-level rise is intensified due to land subsidence (Sheldon, 1968; Beardall *et al*, 1991).

Direct		Intangible or unquantified	
Activity	Annual cost/value (£m)	Activity or interest	% estuary based
Sea defence	48	Human population	21
Navigation dredging	75	Imports/exports (by value)	69
Aggregate winning	57	Power generation	57
Water treatment	650	Oil refineries	81
Commercial fishing	130	Recreation	
		marinas	41
		sailing clubs	24
		leisure fishing	30
		visitors	20-30
		Bird population[(i)]	40
		Conservation areas[(ii)]	80

Notes (i) % of Northwest European over-wintering population
(ii) % of estuaries containing some form of designated site

Table 1.1 – Commercial and ecological importance of British estuaries (Soulsby *et al*, 1997)

1.2 Numerical modelling of estuarine hydraulics and sediment transport

1.2.1 Overview

Three broad approaches to the modelling of estuarine processes and morphodynamic behaviour are identified by EMPHASYS (2000a): *Top-Down*, *Bottom-Up* and *Hybrid* models. The *Top-Down* approach is based on large-scale, description and conceptualisation of the whole estuary morphology and its long-term evolutionary behaviour. In this approach, estuaries are usually classified into groupings, or regimes, based on self-similar aspects. Bases for such groupings include channel geomorphology (Pritchard, 1952; Fairbridge, 1980), salinity structure (Pritchard, 1952; Cameron & Pritchard, 1963), tidal range/volume (Davies, 1964; O'Brien, 1969; Hayes, 1975), or the relative dominance of tide, river and waves (Dalrymple *et al*, 1992). Although useful for indicative prediction of long-term behaviour, this approach suffers from several limitations. First, due to the long time-scales involved, model predictions cannot usually be fully verified against existing data. Results from this type of model must therefore be assessed with caution (Soulsby *et al*, 1997). Second, due to the poor spatial and temporal resolution of such models, it is not possible to model much of the non-linear real-world complexity, such as the immediate effects of building a breakwater (Dennis *et al*, 2000; French & Clifford, 2000). Third, many of the conceptual foundations remain insufficiently tested (French *et al*, 2002)

The *Bottom-Up* approach provides a means with which to look at short-term variability within estuaries, with the added capability of modelling small-scale processes. By using physically based numerical models of the more fundamental estuarine processes, non-linear effects such as wave stress or anthropogenic modifications can be modelled with a higher degree of confidence (Kirkby *et al*, 1992; French & Clifford, 2000), thus incorporating any site-specific variability. The downside of this approach is that numerical diffusion introduces cumulative errors into such models, thus only making them suitable for short-term predictions of the order of a few tidal cycles (de Vriend *et al*, 1993; Dennis *et al*, 2000).

Both the top-down and bottom-up approaches to modelling are of value for understanding the complexities of estuarine system behaviour. However, a more holistic approach to tackling the problem has been advocated by the Estuaries Research Programme (EMPHASYS Consortium, 2000a). By applying a more intensive, bottom-up, approach to modelling, impacts to individual estuaries may be assessed, thus providing a more secure foundation for generalisation in the top-down models. The main impetus of investigation is now, therefore, to combine geomorphological models with numerical models to form what is known as *Hybrid* models (Soulsby *et al*, 1997; Dennis *et al*, 2000; EMPHASYS Consortium, 2000a). Hybrid models are still in their infancy, however, and there is still considerable scope for enhancement and application of existing bottom-up models (French *et al*, 2002).

From the preceding overview, it is clear that physically based numerical models remain the main tool for understanding and predicting estuarine sediment dynamics at short time-scales. Figure 1.1 shows the five main stages typically involved in the implementation such a model, summarised as:

- Conceptualisation
- Parameterisation
- Computation
- Visualisation
- Calibration and validation

The first stage of any model is to gain a conceptual idea of the estuarine system. This is usually carried out by collecting extensive data sets from charts and preliminary investigations of the field site. During this stage, the estuary boundaries are usually defined, thus reducing the size and complexity of the problem to a manageable domain. This involves the truncation of river inflow channels (usually close to the limit of tidal intrusion) and the location of the tidal boundary at (or near) the estuary mouth. The lateral solid boundaries must also be defined, usually by the maximum high water mark. In this stage, there is often some degree of approximation depending upon the intended model resolution, required accuracy and computer resources. It is preferential to have finer resolution in the locality of the region of interest, whereas other regions may be more approximated.

The conceptualised boundaries are subsequently used in the second, parameterisation stage of the modelling process. Intensive time-series data sets are required for the model parameterisation, as well as in the final calibration and validation stage. The conceptual model provides the rationale for making appropriate choices for the type and location of measurement and to inform the selection of model parameters. For example, the river and seaward boundaries may need to be parameterised with discharge and elevation time series data respectively, thus requiring the deployment of a pressure sensor at the mouth and a flow meter at the river input. For calibration and validation of the model output, measurements are generally required from discrete locations within the domain. For the hydrodynamic model validation, such data include tidal levels and current speeds. For calibrating and validating the sediment transport model, sediment concentration data are required from either water samples or instrumentation such as transmissometers or acoustic devices.

At this stage, it is important to ensure that, first, the relevant variables are being measured for the parameterisation and validation of the model, second, the data represent the spatial and temporal variability within the real system and, third, the data provided by the instrumentation are accurate. The first two requirements should be satisfied by the preceding conceptual model. The last requirement relates not only to the calibration of the instrumentation but also to the need for *in situ* measurements. Laboratory based flume studies are useful aids for understanding hydrological processes. However, estuaries show a large diversity in form and function and, individually, they exhibit extensive temporal and spatial variability. This means that it is usually necessary to use *in situ* field instrumentation.

The conceptual boundaries are also used in the parameterisation stage as the basis for generating the model mesh. This is usually produced using commercially available software, such as MATISSE (part of the TELEMAC software; Janin *et al*, 1997) and SMS (SMS User Manual, 2003), or freeware, such as Triangle (Shewchuk, 1996). Model stability and performance relies strongly upon having a well-conditioned mesh, especially in terms of resolution (i.e. element size) and accurate bathymetry. Bathymetric data are usually obtained from charts supported by further echo soundings of the local region to add detail and account for any recent changes in bed elevation. These data are then interpolated onto the mesh to provide the model geometry. It is

important to keep the mesh resolution to the minimum required to sustain reasonable model accuracy since the computation time increases with larger mesh sizes, often with little improvement in accuracy.

The mesh and relevant boundary condition data are then passed to the main computational stage of the estuarine model (Stage 3 in Figure 1.1). Changes made in the parameterisation of the model may necessitate changes to the model software. Consequently, commercially available software usually allows access to some (e.g. TELEMAC) or all (e.g. RMA2) of the source code.

The calculated results are then visualised in the fourth stage of the modelling process. Because of the large data sets that are often produced, software tools are generally needed to help visualise and post-process the data to make it more understandable.

The final stage of the modelling process is the calibration and validation of the model output against the *in situ* measurements. As can be seen in Figure 1.1, the production of a working model is an iterative process, often requiring numerous model runs for a satisfactory calibration. Model run-time is thus an important issue.

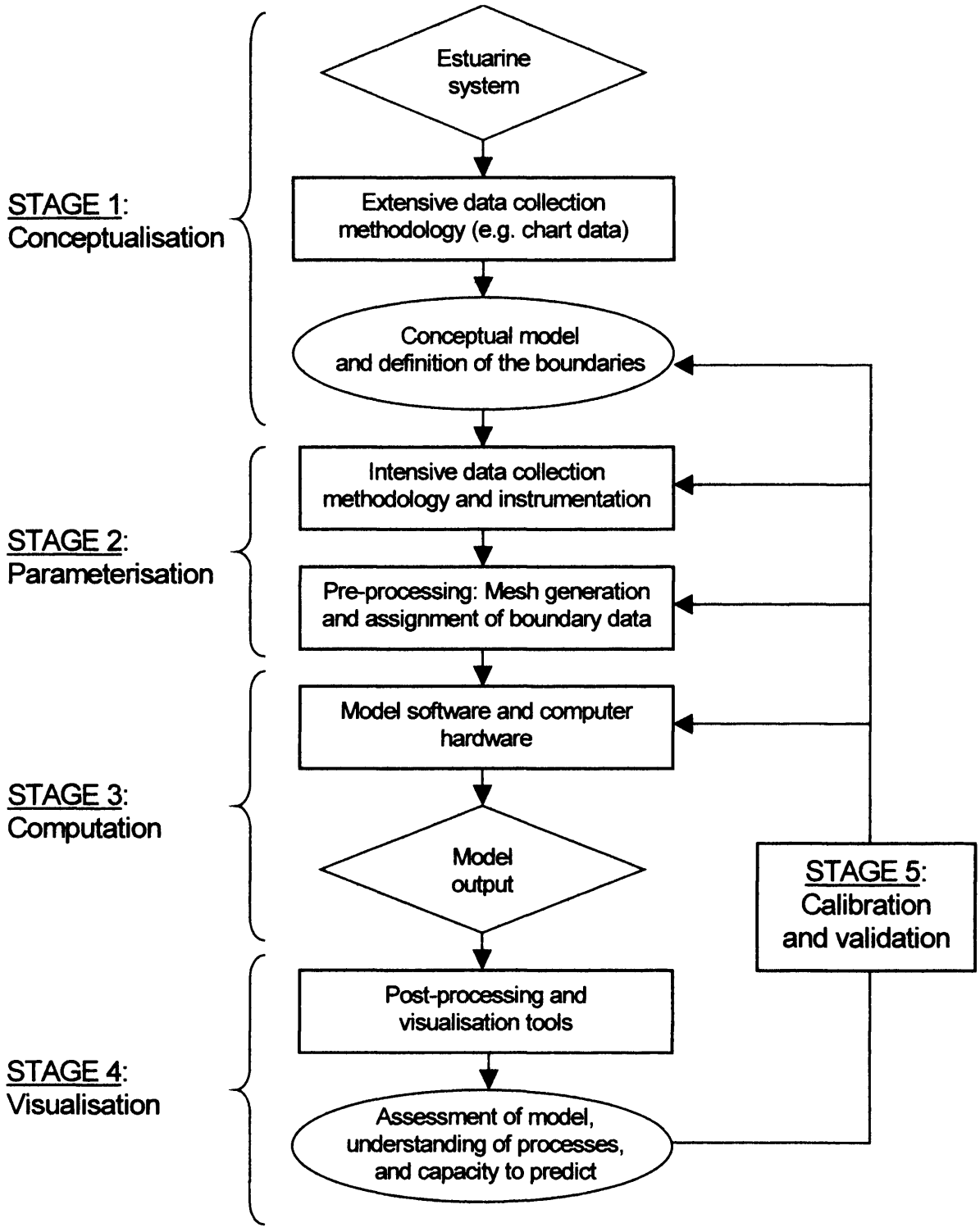

Figure 1.1 – Overview of the stages involved in the implementation of a numerical estuarine sediment transport model

In the past, the implementation of bottom-up, estuarine, sediment transport models was limited primarily by computer processing costs and capabilities. Scaled physical models were often a cheaper and more accessible option (Hughes, 1993) and are still occasionally used for model validation (Ferrier & Anderson, 1997; Moulin & Ben Slama, 1998) or to simulate very complex situations, such as scouring around structures (Jia *et al*, 2000). Rapid improvements in computer technology over the last two decades has allowed for a growth in the complexity, duration and size of mathematical estuarine simulations. This has been paralleled with improvements to the model software, such as:

- the development of more efficient and accurate schemes and solvers (Brooks & Hughes, 1982; Hervouet, 1986).
- a shift from finite-difference (Falconer & Chen, 1996) to finite-element (Hervouet & Haren, 1996) based model structures, which can be used to simulate complex bathymetry more realistically.
- a move from one-dimensional (Odd & Owen, 1972; De Vries *et al*, 1989; Dyer & Evans, 1989; Ross & Mehta, 1989; Smith & Kirby, 1989) to two-dimensional (O'Connor, 1971; Ariathurai & Krone, 1976; Mulder & Udink, 1991; Moulin & Ben Slama, 1998) or fully three-dimensional (O'Connor & Nicholson, 1988; Cancino & Neves, 1994; Lin & Falconer, 1996; Le Normant, 1998) models.
- the refinement of formulae for accurately describing the processes (e.g. settling velocity, Dyer & Manning, 1999; consolidation, Le Normant, 2000).

In conjunction with these improvements, research fronts are currently active in the following two key areas:

(1) an increase in the volume of data produced in the model output files has led to the need for improved pre-processing, post-processing and visualisation tools as an aid to understanding complex data sets (French & Clifford, 2000).

(2) the increasing sophistication of the models necessitates the acquisition of more accurate and higher resolution data for the parameterisation, calibration and validation stages. Hence, there is a requirement for more advanced instrumentation systems and data collection methods (Van Rijn *et al*, 1990; Richards *et al*, 1997).

The challenge of acquiring data in support of model parameterisation is illustrated in Figure 1.2. Several aspects of this schematisation are worthy of note.

First, it is evident that the sediment transport model sits on top of a hydrodynamic model. The latter provides the flow velocity (u, v) and depth (h) variables that are used for calculating the bed shear stress and advection terms in the model. The sediment transport model relies heavily upon the accuracy of these underlying hydrodynamic calculations. Hence, a large proportion of time and resources needs to be concentrated on this stage of the modelling process before continuing to the sediment transport stage. A detailed account of the issues involved with producing a working hydrodynamic estuarine model is beyond the scope of this project (fuller treatments are given by Hervouet & van Haren (1996) and French (2001)).

Second, in this schematic model, the bed morphology is allowed to adjust due to sediment transport and it is therefore described as having a *mobile bed* rather than a *fixed bed*. In the case of a mobile bed, if it is supposed that all the parameters in Figure 1.2 (other than channel geometry) are constant over time, the geometry of the system will eventually reach equilibrium where the net sediment transport will equate to zero. If any changes in the boundary conditions are imposed, such as sea level rise, dredging, or realignment of constraining flood defences (Dennis *et al*, 2000, French & Clifford, 2000), the system will become unstable resulting in sediment transport and a change in the geometry (Pethick, 1996). Therefore, sediment transport can be seen to be a mediating process that acts to restore equilibrium in the system. In reality, each parameter listed in Figure 1.2 has a large scope for adjustment, both naturally and artificially. This means that a wide range of variability in channel geometry is seen from one estuary to another. Fixed bed models simulate the transport of suspended sediment without allowing changes to the geometry and are thus only suitable for simulating short-term sediment transport where changes in bed elevation are likely to be small. However, it has already been mentioned that *bottom-up* style numerical models are also only suited to short-term simulations. It has also been found that changes to the bed elevation of less than 10% generally have little effect of the hydrodynamics (Moulin & Ben Slama, 1998). Therefore, it is usually sufficient to use a fixed bed in numerical sediment transport models, whereas longer-term *top-down* or *hybrid* methods require a mobile bed.

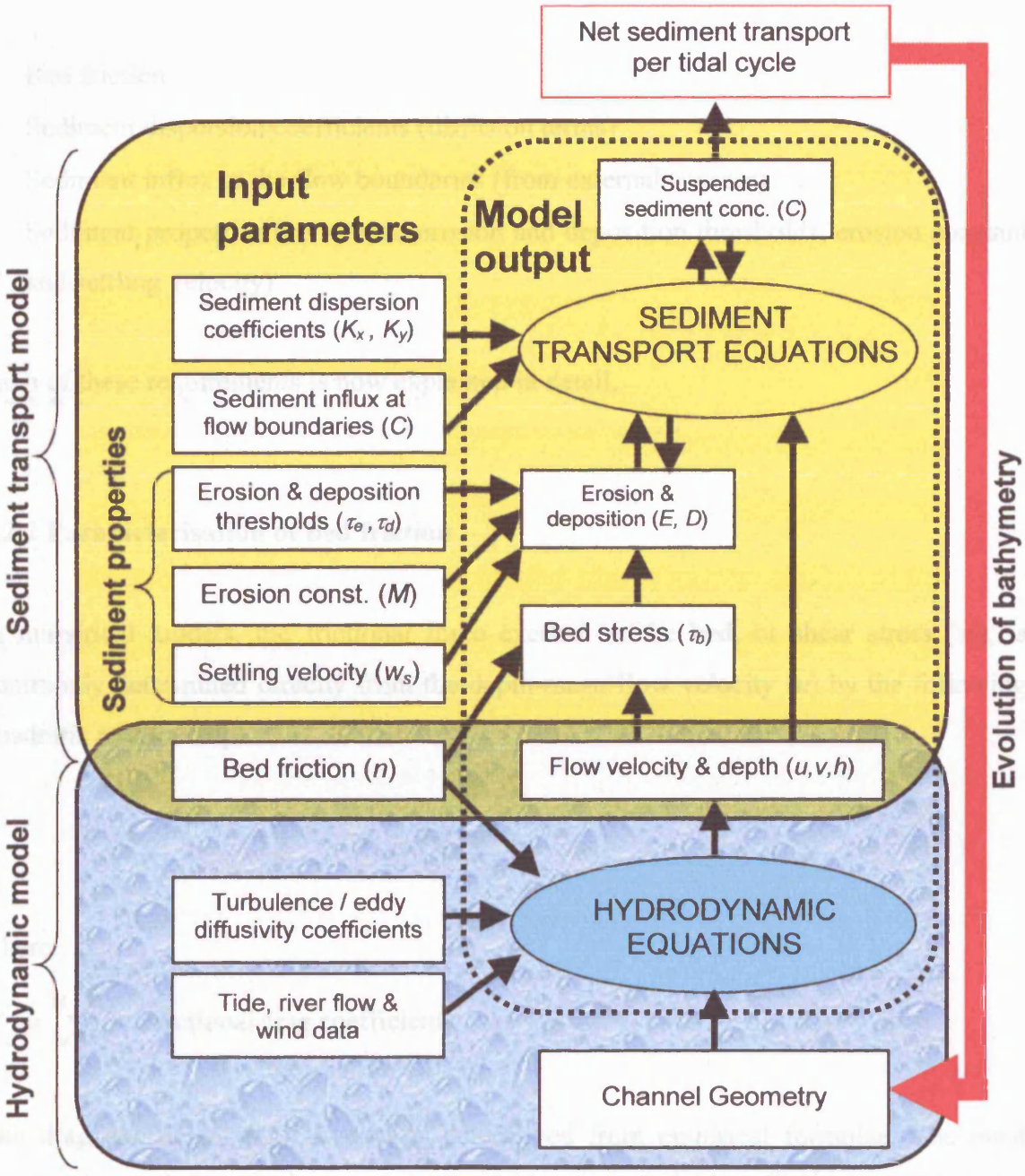

Figure 1.2 – Conceptual diagram of sediment transport model parameterisation – For explanation of terms, see text.

Third, if the focus of attention is centred on the sediment transport model, it can be seen that the four main data requirements for estuaries (apart from the hydrodynamic data) relate to:

- Bed friction
- Sediment dispersion coefficients (diffusion terms)
- Sediment influx at the flow boundaries (from external sources)
- Sediment properties (i.e. critical erosion and deposition thresholds, erosion constant and settling velocity)

Each of these requirements is now explained in detail.

1.2.2 Parameterisation of bed friction

In numerical models, the frictional force exerted on the bed, or shear stress (τ_b), is commonly determined directly from the depth-mean flow velocity (u) by the following quadratic relationship:

$$\tau_b = \rho C_D u^2 \tag{1.1}$$

where:

$C_D = {}^{u_*}/_{u}$ = Frictional drag coefficient

The drag coefficient (C_D) is usually determined from empirical formulae. The most commonly used formulations are those of Manning, Strickler, Chézy and Nikuradse (Chadwick & Morfett, 1998; Janin *et al*, 1992). Each method relates the apparent roughness, or friction, of the bed to a range of empirical values. The Chézy formulation is given as:

$$C_D = \frac{\sqrt{g}}{C_z} \tag{1.2}$$

where :

C_z = Chezy coefficient ($m^{1/2}s^{-1}$)

g = force of gravity ($9.81\ ms^{-2}$)

C_z can be determined empirically using the Manning or Strickler formulation defined as:

$$C_z = K_s R_H^{1/6} \tag{1.3}$$

where :

K_s = Strickler coefficient = n^{-1}

n = Manning coefficient

R_H = Hydraulic radius (equivalent to water depth, h) (m)

In Equation 1.3, the Manning friction coefficient is simply the inverse of the Strickler coefficient. In addition, Nikuradse's formulation states that C_z may be related to a roughness parameter (k_s) as:

$$C_z = 7.63 \ln\left(11\frac{h}{k_s}\right) \tag{1.4}$$

Where k_s may be taken to be the grain size (on a flat bed) or related to the roughness length (on a rough bed) by k_s=$30z_0$.

There are numerous sources of published data giving friction factors for different bed types (e.g. Chow, 1959; Arcement & Schneider, 1989), which can be used to provide initial values for a model. These are then iteratively adjusted during the hydrodynamic model calibration phase. The same friction factors may then be transferred to the sediment transport model for calculation of the bed shear stress.

Bed friction is a particularly important model parameter in estuaries since it independently affects the modelling of both the hydrodynamics and the sediment transport. In the hydrodynamic modelling stage, bed friction is a dominant parameter controlling the overall accuracy of the simulation (Hervouet & van Haren, 1996). A

detailed discussion of its implementation is not given here, and the reader is referred to Bates *et al* (1996), Hervouet & van Haren (1996) and French & Clifford (2000). It is important to note, however, that in an estuarine context there are usually several distinct 'sub-environments' such as mud flats, saltmarsh and subtidal channels, each with its own unique type of vegetation, sediment and morphology, and hence friction factor. This means that a single value for bed friction over the entire model domain is not usually satisfactory and spatially varied values are more appropriate. Indeed, a recent intercomparison of 1D, 2D and 3D bottom-up models (Wright & Norton, 2000) indicated that a 1D model with spatially varied friction provides similar accuracy to the 2D and 3D models that use a single friction value for the whole domain.

1.2.3 Sediment dispersion coefficients

Although turbulent dispersion is already taken into account in the hydrodynamic model, parameterisation of suspended sediment dispersion is necessary because suspended particles tend to diffuse at a slower rate than the water itself (Rouse, 1937). Depending on the model used, sediment dispersion may be defined in one of two ways. First, by multiplying the calculated hydrodynamic turbulence by a Prandtl number, which is merely a value expressing the proportionality between dispersion of sediment versus the dispersion of momentum (Rouse, 1937; Guan *et al*, 1998; Rose & Thorne, 2001). Second, by a complete recalculation of the turbulence from the flow field (Falconer & Lin, 1997). The most commonly used turbulence models, in order of increasing complexity, are: (1) *constant eddy viscosity*, which specifies a single dispersion coefficient for the entire domain, or uses a simple algebraic expression to calculate the coefficient as a function of depth and shear velocity (Equation 1.5) with a proportionality constant in the range 0.06-0.25 (Fischer, 1973; Rastogi & Rodi, 1978; Wood & Liang, 1990; Jenkins, 1993); (2) *Elder's model*, which is similar to the constant eddy viscosity model, but calculates the anisotropic eddy viscosity (Equation 1.6a,b) according to depth and shear velocity in the longitudinal and transverse direction of the flow using two dimensionless coefficients (Elder, 1959; Wilson *et al*, 2002); (3) a *mixing-length model* (Equation 1.7), which calculates turbulent eddy viscosity as a function of a characteristic length-scale (Golstein, 1938), and (4) the *k-ε model* (Equation 1.8), which describes the turbulent eddy viscosity as a function of turbulent

kinetic energy (k) and the rate of dissipation (ε) using a standard set of predefined constants for channel flow (Hervouet & van Haren, 1996; Wilson *et al*, 2002).

Constant eddy viscosity: $$v_T = \Theta u_* h \tag{1.5}$$

Elder's model: $$v_{T,x} = \Theta_x u_* h \tag{1.6a,b}$$

$$v_{T,y} = \Theta_y u_* h$$

Mixing-length model: $$v_T = l_m^2 \left| \frac{\partial u}{\partial y} \right| \tag{1.7}$$

k-ε model: $$v_T = c_\mu \frac{k^2}{\varepsilon} \tag{1.8}$$

where:

v_T = turbulent eddy viscosity
Θ = non-dimensional constant (e.g. 0.15; Fischer, 1973)
$\Theta_{x,y}$ = anisotropic non-dimensional constants, longitudinally and transversely to the flow (e.g. $\Theta_x = 6.0$, $\Theta_y = 0.6$; for the flow field proportionality (Wilson *et al*, 2002)
u_* = shear velocity (ms^{-1})
h = water depth (m)
du/dy = change in current velocity with distance from rigid wall (or bed)
l_m = length-scale, often assumed to be distance from wall times von Karman constant, $\kappa = 0.41$ in estuaries (Dyer, 1997)
k = turbulent kinetic energy
ε = dissipation rate
c_μ = predefined constant

When using models (1) or (2) with a fully 3D model (or width-integrated 2D model) in order to calculate the vertical diffusion coefficient (in the absence of stratification) it is common to assume a linear shear stress distribution and a logarithmic velocity distribution, giving (Lin & Falconer, 1996; Rose & Thorne, 2001):

$$K_z = \beta \kappa u_* z \left(1 - \frac{z}{h}\right) \tag{1.9}$$

where:

K_z = vertical diffusion coefficient

κ = von Karman constant

β = Prandtl number (proportionality constant for sediment dispersion)

A fixed value for eddy viscosity is not suitable for use in the context of estuaries due to large variations in bed type and water depth, which result in significant spatial and temporal changes in turbulence. Comparisons of the constant viscosity, Elder and k-epsilon turbulence models have been made by Wilson *et al* (2002) on a simulated floodplain flow. Although all models performed well in deep water, the Elder and k-epsilon models significantly out-performed a constant eddy viscosity model in the case of slow, shallow flows. Differences between the Elder and k-epsilon models were very small. The k-epsilon model requires a smaller mesh size, a shorter time step (Janin *et al*, 1997) and hence greater computation times. Thus, the Elder or mixing length models are generally used more frequently.

1.2.4 Sediment influx at the flow boundaries

Estuaries are open systems found at the interface between the adjoining river catchment and the ocean. Suspended sediment thus has the opportunity to enter the system via both the head and the mouth of the estuary from land or marine sources (Dyer, 1997).

In an ideal situation, sediment flux time-series data should be collected at each flow boundary to parameterise the sediment input into the model. These data can then also be used to validate the model output and net fluxes (Liu *et al*, 2002).

If only sparse or archived data are available, another option is to model the variation of suspended sediment at a particular boundary as a function of flow rate. This is particularly suitable for the river input boundaries. For instance, Le Normant (2000) describe the input of riverine sediment into the Gironde estuary as a function of freshwater discharge (Q_f) using the simple empirical formula:

$$C = 40\log(Q_f) - 80 \tag{1.10}$$

where, C = suspended sediment concentration (mgl^{-1})

Often, empirical formulae are inappropriate or cannot be calibrated due to a lack of observations. In such cases, the quantities of suspended sediment entering the fluid boundaries can be approximated by a constant value (Moulin & Slama, 1998; Cancino & Neves, 1999b; Le Normant, 2000; Liu *et al*, 2002; Lumborg & Windelin, 2003; Tattershall, 2003). This assumption is most appropriate in the case of marine input where the seaward boundary of the model is far enough downstream of the estuary to avoid unwanted edge effects within the domain of interest (Cancino & Neves, 1999b). Therefore, the provision of sediment boundary conditions is often grossly simplified and is usually heavily reliant on assumptions.

1.2.5 Sediment properties

From Figure 1.2 it can be seen that the properties of the sediment are typically parameterised using the following variables:

- Critical erosion and deposition thresholds (τ_e, τ_d)
- Erosion rate constant (M)
- Settling velocity (w_s)

In most sediment transport models, the exchange of sediment between the bed and the water column is parameterised by the empirical formulae of Partheniades (1965) and Krone (1962) for erosion and deposition respectively (Cancino & Neves, 1999a,b; Ariathurai & Krone, 1976; Mulder & Udink, 1991; Li *et al*, 1994; O'Connor & Nicholson, 1988; Falconer & Chen, 1996; Wijngaarden, 1999; Guan *et al*, 1998; Le Normant, 1998; van der Ham & Winterwerp, 2001; Ciffroy *et al*, 2000; Moulin & Ben Slama, 1998; Clarke & Elliott, 1998; Kusuda & Futawatari, 1992). These are of the form:

$$Q_E = M\left(\frac{\tau_b}{\tau_e} - 1\right) \qquad \text{when } \tau_b > \tau_e \qquad (1.11)$$

$$Q_D = -Cw_s\left(1 - \frac{\tau_b}{\tau_d}\right) \qquad \text{when } \tau_b < \tau_d \qquad (1.12)$$

where:

Q_E, Q_D = flux of sediment by erosion and deposition (kg m^{-2} s^{-1})

τ_b = bed shear stress (N m^{-2})

τ_e, τ_d = critical shear stress for erosion & deposition (N m^{-2})

M = erosion rate constant (kg m^{-2} s^{-1})

w_s = particle settling velocity (m s^{-1})

C = suspended sediment concentration (kg m^{-3})

In place of the shear stress, some models are parameterised using the shear velocity, $u_* = \sqrt{\tau_b/\rho}$, where ρ is the water density (usually taken to be 1020 kg m^{-3} in estuaries). Equations 1.11 and 1.12 show that the amount of erosion and deposition is dependent upon the balance between the stress exerted on the bed (τ_b) and the properties of the sediment. In the simplest sediment transport models (Rouse, 1937), it is assumed that the sediment consists of a single particle size, which is suspended (eroded) when the shear stress exceeds the threshold for erosion (τ_e). The rate at which it is eroded is defined by the erosion rate constant (M). The sediment then remains in suspension, thus being carried (advected) by the flow, until the shear stress falls below the threshold for deposition (τ_d). The sediment then settles from suspension at a rate defined by the settling velocity (w_s).

Values for the sediment properties (τ_e, τ_d, M, and w_s) vary according to the size and mineralogy of the individual particles. Commonly, the two forms of suspended matter in estuaries and coastal regions are inorganic (clastic) material, derived from the land and/or the reworking of bed deposits, and organic (biological) material such as diatoms, phytoplankton, macro-flora and biological deposits such as peat. The majority of the suspended and bottom sediment in most UK estuaries is usually inorganic. For example,

McCave (1984), found a general ratio of 20% organic to 80% inorganic in several estuaries in the UK. Inorganic sediment is usually categorised according to its bulk properties as being either *cohesive* (i.e. mud) or *non-cohesive* (i.e. sands and gravels). The Coastal Engineering Manual of the U.S. Army Corps of Engineers (1998) defines cohesive sediments as consisting of primarily clay minerals, with a diameter of less than 0.0039 mm, whereas non-cohesive sediments are generally composed of quartz sand grains with a diameter range of 0.0625-2.00 mm. The component of sediment between these two size classes is classified as silt and has varying degrees of cohesiveness.

In coastal environments dominated by fine non-cohesive sediments, such as sandy beaches, the bulk sediment property parameters (τ_e, τ_d, M, and w_s) can be determined relatively easily and accurately by using empirical formulae combined with laboratory studies using sediment from the field site. For example, for non-cohesive sediment, there is a strong relationship between particle size and the critical shear stress for erosion, as exemplified in Shield's diagram (Raudkivi, 1990; Le Roux, 1998). Falconer & Chen (1996) describe the use of this method for parameterisation of a sediment transport model of the Humber estuary, which contains 80% non-cohesive sediment (Lin & Falconer, 1996).

Another example is the relationship between particle size and settling velocity (w_s), which for fine sand particles (<0.1mm) can be described with reasonable accuracy using Stokes' Law (Stokes, 1851; Droppo *et al*, 1997). This predicts the settling velocity of a spherical particle to be proportional to the square of its diameter such that:

$$w_s = \frac{1}{18}\frac{d^2(\rho_f - \rho_w)g}{\eta} \qquad (1.13)$$

where :

w_s = settling velocity (m s^{-1})

d = particle diameter (m)

ρ_f = particle density (kg m^{-3})

ρ_w = water density (kg m^{-3})

η = dynamic water viscosity (kinematic viscosity $\times \rho_w$)

g = force of gravity (9.81 m s^{-2})

This is often simplified further by presuming that the density and viscosity of the water remains constant to give:

$$w_s = KD^N \tag{1.14}$$

where:

K = constant relating to the sediment density

N = exponent (= 2 for solid spheres)

Therefore, simple size measurements can be made of sand taken from the field site and the settling velocity calculated accordingly. However, Stokes' Law should be used with caution since it becomes inapplicable for grains larger than approximately 0.1 mm and for non-spherical grains, which spin and oscillate as they settle. In both cases, the flow around the particles becomes turbulent, which increases the drag, thus reducing the settling velocity (Komar & Reimers, 1978).

Non-cohesive sediments can also be modelled in a relatively simple manner. By assuming a fixed settling velocity, it is possible to use a simplified transport model because the sediment concentration profile tends to follow a fixed pattern. For example, if the water column is homogenously mixed and the flow is in steady state, the shape of the velocity profile can be modelled using Prandtl's *logarithmic law of the wall* equation (Soulsby & Dyer, 1981; Lueck & Lu, 1997), given as:

$$u = \frac{u_*}{\kappa} \ln\left(\frac{z}{z_0}\right) \tag{1.15}$$

where :

u = velocity at a height z ($m\ s^{-1}$)

u_* = bed shear velocity ($m\ s^{-1}$)

z_0 = bed roughness length scale (m)

κ = von Karman constant (0.4)

The resultant form of the mean velocity profile is logarithmic (Figure 1.3), which has a direct effect on the sediment concentration profile. This can be visualised using the *sediment diffusion equation* proposed by Rouse (1937), which is derived from Equation 1.15, as:

$$\frac{c(z)}{c_a} = \left(\frac{(h-z)a}{(h-a)z} \right)^{\frac{w_s}{\beta \kappa u_*}} \tag{1.16}$$

where:

$c(z)$ = SSC at height z above the bed (kg m^{-3})

c_a = reference SSC at height a above the bed (kg m^{-3})

β = proportionality constant (Prantl number) between turbulent transport for sediment and momentum.

κ = von Karman constant (assumed to be 0.4)

w_s = mean particle settling velocity (ms^{-1})

In Equation 1.16, the reference concentration (c_a) may be related to the critical shear stress for erosion (Dyer, 1980; Schauer, 1987; Rose & Thorne, 2001) or Shield's skin-friction parameter (Green & Black, 1999) by an empirical formula. Figure 1.3 also shows the resultant instantaneous sediment flux calculated from the product of the sediment concentration and velocity profiles. The simple form of these depth profiles means that 2D, depth-integrated, models are a viable option when dealing with non-cohesive sediments in well-mixed estuaries (Lin & Falconer, 1996).

In reality, variations in sediment grain size and composition, both spatially and temporally, lead to complications when using such simplistic models. For instance, a slight variation in either τ_e or w_s will have a pronounced effect on the predicted suspended concentrations. Parameterisation of the physical properties of both the bottom deposits and suspended sediment is, therefore, crucial if fluxes are to be modelled accurately (Burt *et al*, 1997). These problems become particularly apparent in the case of cohesive sediments, which will now be described in detail.

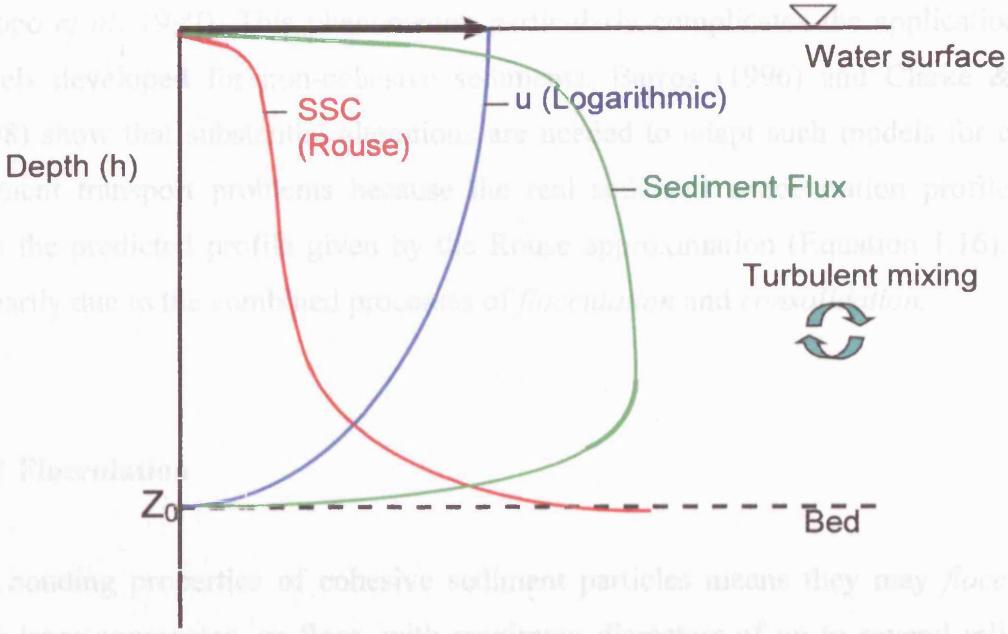

Figure 1.3 –Rouse model of sediment concentration with depth

1.3 Problems associated with monitoring and modelling of cohesive sediment transport

Cohesive estuarine sediments consist primarily of clay minerals such as illite, montmorillonite and kaolinite. These primary particles are of the order of a few microns in diameter and tend to adhere to one another due to electrostatic forces between the ions on their surface (Edzwald *et al*, 1975; Krone, 1978; McCave, 1984; Eisma, 1991; Droppo *et al*, 1997). This phenomenon particularly complicates the application of 2D models developed for non-cohesive sediments. Barros (1996) and Clarke & Elliott (1998) show that substantial alterations are needed to adapt such models for cohesive sediment transport problems because the real sediment concentration profiles differ from the predicted profile given by the Rouse approximation (Equation 1.16). This is primarily due to the combined processes of *flocculation* and *consolidation.*

1.3.1 Flocculation

The bonding properties of cohesive sediment particles means they may *flocculate* to form large aggregates, or flocs, with maximum diameters of up to several millimetres (Eisma, 1991; Chen *et al*, 1994; Syvitski *et al*, 1995). From Equation 1.13, it can be seen that the diameter of the particles has a strong influence on the settling velocity. However, the problem is made more complex by the structural characteristics of the flocs. An important property of estuarine flocs is that they are fractal in shape, which affects their overall density (Li & Ganczarczyk, 1989; Meakin, 1991; Chen & Eisma, 1995). Kranenburg (1994) uses fractal theory to show that the diameter of the flocs (d_f) are related to the diameter of the primary particles (d_p), i.e. the clay minerals, as follows:

$$N \sim \left[\frac{d_f}{d_p}\right]^{n_f} \tag{1.17}$$

where:

N = the number of primary particles in the fractal aggregate

n_f = fractal dimension

Using this approach, the effective density (ρ_e) of the mud flocs is related to the fractal dimension by the following formula (Kranenburg, 1994):

$$\rho_e = \rho_f - \rho_w = (\rho_s - \rho_w)\left[\frac{d_p}{d_f}\right]^{3-n_f} \tag{1.18}$$

where:

ρ_f = floc dry density (kgm^{-3})
ρ_w = water density (kgm^{-3})
ρ_s = density of the primary particles (kgm^{-3})

Substituting Equation 1.18 into Stokes' Law (Equation 1.13), the settling velocity of the particles is obtained from the following relationship (Winterwerp, 1998):

$$w_s = \frac{\alpha}{18\beta}\frac{(\rho_s - \rho_w)g}{\eta} d_p^{3-n_f} d_f^{n_f-1} \tag{1.19}$$

where:

α, β = particle shape parameters (=1 for spherical particles)
n_f = fractal dimension of flocs
d_p = diameter of the primary particles (μm)
d_f = diameter of the flocs (μm)

Typical values of n_f for suspended flocs in estuaries and coastal regions lie the range of $1.7<n_f<2.2$, with an average of n_f = 2 (Kranenburg, 1994; Winterwerp, 1998, 2002). Using this value in Equation 1.19, it can be seen that the settling velocity becomes linearly proportional to particle diameter, i.e. $w_s \propto d^1$ and, hence, the floc effective density ($\rho_e = \rho_s - \rho_w$) is inversely proportional floc diameter, i.e. $\rho_e \propto d^{-1}$. This shows that fractal aggregates are very porous, and therefore have a low density in comparison to the individual clay minerals: this results in a relatively low mass concentration in exchange for a high volume concentration (Teisson, 1997). As the flocs become larger, the porosity increases, thus reducing the effective density and, hence, settling velocity of the particles. Paradoxically, an opposite effect occurs if the porosity of the particles becomes large enough to allow the flow of water *through* the floc structure. In this case, the flocs may settle *faster* than solid spheres of the same size and density (Gregory,

1997). This means that the relationship between particle size and settling velocity is not as simple as that described by Stokes' Law.

The degree to which suspended particles flocculate depends primarily on (Manning & Dyer, 1999; Winterwerp, 2002):

- the strength of the interparticle bonds
- the collision rate of the particles

As particles move from a freshwater environment into more saline water, attraction between the particles is induced due to changes in the ions on the surface of the clay minerals. It has been suggested that particle aggregation becomes noticeable above a salinity threshold of approximately 0.1 to 1‰ (Guan *et al*, 1998; Cancino & Neves, 1999b). Above this threshold, it appears that the rate of flocculation increases linearly to between 2.5 to 4‰, after which the rate becomes constant (Edzwald *et al*, 1975; Wollast, 1986; Barros, 1996). Therefore, in most well mixed estuarine situations, the rate of flocculation due to salinity effects will be almost constant both spatially and temporally. In stratified estuaries, however, particularly during periods of heavy rainfall, flocculation may be impeded towards the head of the estuary and within any other regions of freshwater run-off.

Flocculation occurs more rapidly if particle collisions are more frequent. The particle collision rate is affected by several variables including Brownian motion, differential settling (whereby particles collisions become more frequent during settling due to different settling velocities), suspended sediment concentration, and water turbulence (Manning & Dyer, 1999; Winterwerp, 2002). In deep, low energy environments (such as the deep ocean), Brownian motion (i.e. micro-scale particle motion) and differential settling are both considered important factors in causing collisions between particles to form flocs (McCave, 1984). However, in energetic, shallow water environments such as estuaries and coastal regions, these processes become negligible in comparison to the effects of suspended concentration and turbulence (O'Melia, 1980; McCave, 1984; Stolzenbach & Elimelich, 1994; Winterwerp, 2002). The effect of turbulence is two-fold. At low turbulence, an increase in turbulence will increase particle collision rate. Above a certain turbulence threshold, the particles are broken up with any further

increase (Manning & Dyer, 1999). Therefore, in most estuarine situations, flocculation is more likely to occur where there is: (1) high particle concentration, which increases the probability of collision between particles; and (2) low to moderate turbulent shear, allowing weak flocs to remain intact (Owen, 1971; Thorn, 1981; Eisma, 1991; Wolanski *et al*, 1995).

Figure 1.4 provides a theoretical overview of how the average size of flocs might be expected to change throughout a tidal cycle as a result of interplay of these factors. This schematic is based on observations made by Eisma & Li (1993) in the Dollard estuary (Dutch Wadden Sea). In principle, particles are able to form large flocs in the absence of turbulent shear during slack water (point E in Figure 1.4). Consequently, particles rapidly sink to the bed during slack water, resulting in a concentration minimum near the surface just after high or low water (A). The settled particles form a low-density layer on the bed, which is then rapidly resuspended on the following tide (B). Paradoxically, flocculation may also occur during maximum tidal current flow (C to D). This was highlighted by Eisma (1991) who observed similar size flocs during mid-tidal flow as compared to slack water using an *in situ* camera system in the Zaire estuary. However, this estuary is exceptionally deep (>100 m), and in most macrotidal estuaries, the surface waters are more turbulent. In another paper on estuaries in Western Europe, Eisma *et al* (1991) noted the fact that large flocs tended to be present in the bottom 10 to 15% of the water column. This was attributed to: (1) the larger flocs settling more rapidly, and (2) an increased likelihood of collision between particles due to the higher SSC. It was also postulated that the higher suspended concentrations reduced the turbulence nearer to the bed, thus preventing flocs from being broken-up.

In addition to the physical controls described above, biological factors may influence the floc size and strength (Paterson, 1994, 1997; Tolhurst *et al*, 2002). In particular, it is known that diatoms secrete extracellular polymeric substance (EPS), which primarily consists of polysaccharides (Holland *et al,* 1974). This aids the flocculation process in two ways: (1) By increasing molecular attractive forces between clay particles, thus promoting flocculation (Eisma *et al,* 1991; Decho, 1990), and (2) by forming polymer strands between sediment particles, thus increasing the strength of the inter-particle bonds (Chenu, 1993; Paterson, 1995; Défarge, 1997). Quantification of biological mediation of flocculation is still in its infancy and is not within the scope of this project.

(a)

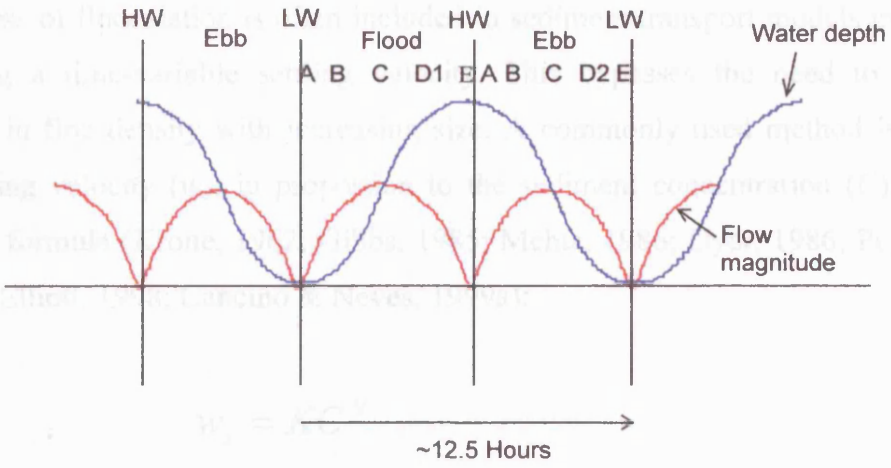

(b)

	**(A)** ***End of slack HW/LW:*** • Low particle concentration • Particles have settled rapidly during slack water
	**(B)** ***~30 minutes after slack HW/LW:*** • Moderate current velocity • Rapid resuspension of particles from bed due to low density of recently settled surface sediment
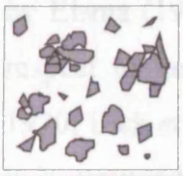	**(C)** ***Mid Flood/Ebb:*** • Maximum current velocities • High particle concentration • Turbulence prevents floc formation near bed, but high density flocs may form in rest of water column due to high collision rates and lower turbulence
 	**(D)** ***~1 hr after mid flood/ebb*** ***(1) Flood (in a deep/stratified estuary)*** • Increasing water depth • particles, which are not near the bed, continue to form large flocs (>1mm) ***(2) Ebb (and flood in a well mixed/turbulent estuary):*** • Decreasing water depth • Highly turbulent flow throughout the water column • Flocs are broken up
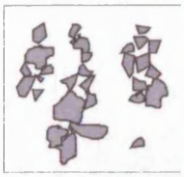	**(E)** ***Start of high/low slack water*** • No current shear • Initially high particle concentration • Differential settling forms large flocs and 'stringers' (up to 5 mm) • larger flocs may form at high water slack due to lower turbulence in previous stage (D1) or higher concentrations on ebb may reverse this trend

Figure 1.4 - (a) Idealised tidal flow diagram (neglecting any flood-ebb asymmetry). (b) Schematic of flocculation during a tidal cycle in the upper part of the water column.

The process of flocculation is often included in sediment transport models indirectly by calculating a time-variable settling velocity. This bypasses the need to model the reduction in floc density with increasing size. A commonly used method is to simply vary settling velocity (w_s) in proportion to the sediment concentration (C), using the following formula (Krone, 1962; Gibbs, 1985; Mehta, 1986; Dyer, 1986; Pejrup, 1988; Clarke & Elliott, 1998; Cancino & Neves, 1999a):

$$w_s = KC^N \tag{1.20}$$

where:

K = constant depending on mineralogy of mud
e.g. 1.5×10^{-3} (van der Ham & Winterwerp, 2001)

N = constant depending on size, shape and porosity of particles (in the range 0.5 - 2)

This method benefits from only needing two parameters for calibration. However, the two parameters can vary greatly from one estuary to another (Whitehouse *et al*, 2000) and the formulation does not include the effect of turbulence on floc formation as noted by Eisma (1991). A more realistic approach is to model the flocculation process with respect to turbulence and suspended sediment concentration (Argaman & Kaufman, 1970; Lick *et al*, 1993; Dyer & Manning, 1999; Winterwerp, 2002). At low turbulence, it is assumed that flocculation is enhanced due to increased collision rates, whilst at higher levels of turbulence, the resultant shear causes floc break-up. Dyer (1989) provides a theoretical diagram of this process, shown in Figure 1.5.

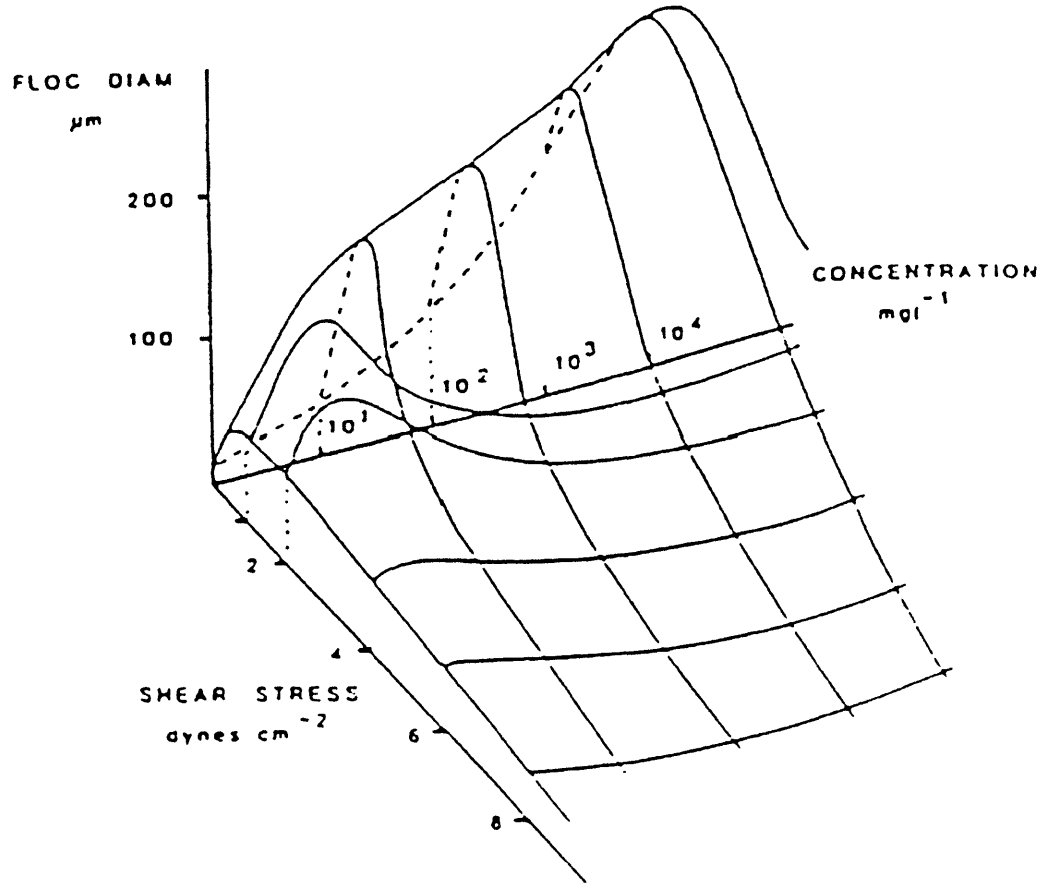

Figure 1.5 – Theoretical model of floc size variability with turbulent shear and suspended sediment concentration (Dyer, 1989)

The effect of turbulence is commonly represented by the dissipation parameter (G), given as:

$$G = \left(\frac{\varepsilon}{\upsilon}\right)^{1/2} = u_* \left(\frac{u}{\upsilon} h\right)^{1/2} \tag{1.21}$$

where:

ε = turbulent kinetic enargy dissipation rate
υ = kinematic viscosity of water
h = water depth

Van Leussen (1994) uses the dissipation parameter to extend Equation 1.20 to include the effects of turbulence in the following semi-empirical relationship:

$$w_s = KC^N \frac{1 + aG}{1 + bG^2} \tag{1.22}$$

where:

a, b = empirically derived constants determining the effect of floc break - up due to turbulence on settling velocity

This formulation has successfully been used to model the settling velocity in the Weser estuary (Peltier *et al*, 1996; Violeau *et al,* 2002).

Dyer & Manning (1999) adopt a more empirical approach by relating settling velocities, determined from video analysis of settling flocs, with turbulent dissipation (G) and sediment concentration (C) using multiple linear regression. This method has been applied with some success using *in situ* settling velocity measurements from the Tamar estuary (Manning & Dyer, 2002) to give the following formula:

$$w_s = -0.243 + 0.000567C + 0.981G - 0.0934G^2 \tag{1.23}$$

The empirical nature of this equation means it is only suitable if there are a large number of *in situ* measurements of settling velocity. It is therefore very site specific and cannot be applied to numerical models in general (Spearman & Roberts, 2002).

Another model is proposed by Winterwerp (1998) based on the assumption that flocculated mud can be represented by its fractal structure (Kranenburg, 1994). This method differs from those previously described because the particle size is first calculated. The full model is complex and includes a flocculation time variable, which accounts for the time required for the particle size to obtain equilibrium. However, by assuming that a stable equilibrium is obtained, the full equation can be simplified to:

$$D_e = D_p + \frac{K_A C}{K_B \sqrt{G}} \tag{1.24}$$

where:

D_e = floc diameter at stable equilibrium (m)

D_p = diameter of the primary particles (m)

K_A, K_B = empirical constants governing the relative importance of the mechanisms of floc break - up and aggregation

The settling velocity is then determined using the modified version of Stokes' Law (Equation 1.13) to account for density changes with floc size due to their fractal formation.

Each of the described methods of modelling flocculation and its effect on settling velocity relies upon *in situ* measurements of floc size, fractal dimension and/or settling velocity.

1.3.2 Consolidation and bed layering

A secondary effect of the fractal nature of flocs is that they may undergo post-depositional consolidation. For non-cohesive sediment, there is a direct relationship between particle size and the critical shear stress for erosion (Kench & McLean, 1996; Le Roux, 1998). However, cohesive sediments do not follow this simple rule. When fractal flocs are initially deposited on the bed, they have a relatively low density. This means that, as the current velocity begins to increase after slack water, there is usually a rapid resuspension of particles and any weak flocs are broken up by the turbulence (point B in Figure 1.4). However, if current velocities are low enough to prevent re-erosion on the following tide (for instance during neap tides), the flocs begin to undergo compaction, or consolidation, due to the weight of newly deposited overlying sediment (Guan *et al*, 1998). Consequently, there is an increase in the particle density in relation to the age of the sediment so that the deeper, older deposits are more consolidated and resistant to erosion. Consolidation results in the hardening of the bed, which in turn results in a higher erosion threshold (τ_e) in Equation 1.11. Consolidated sediments also

tend to be eroded as large chunks before being broken up in the water column, thus affecting the erosion rate, M (Le Normant, 2000). In addition, the stability of intertidal cohesive sediments may be influenced by biological parameters such as diatom surface films, which increase the stability, and bioturbation due to meso- and macro-fauna, which acts to decrease the stability (Paterson, 1997).

Consequently, within a given estuary, there is usually a large spatial and temporal variation in the τ_e and M. Laboratory flume studies using sediment cores from the field site have been shown to produce inaccurate results, unless extreme care is taken when transporting the samples, and it is therefore preferable to obtain *in situ* measurements (Tolhurst *et al*, 2000). Several *in situ* instruments have been designed for this purpose, which can be categorised into: (1) imitating current flow over a section of mud using a straight or circular *in situ* flume (Young, 1976; Amos *et al*, 1992; Maa *et al*, 1993; Black & Cramp, 1995; Gust & Müller, 1997; Houwing & van Rijn, 1998); (2) generating turbulent motion of the water column above the sediment surface by a propeller (Schünemann & Kühl, 1991) or an oscillating horizontal grid (Tsai & Lick, 1986); (3) generating a vertical jet of water directed towards the bed (Paterson, 1989); (4) drawing water upwards through an inverted funnel (Williamson & Ockenden, 1996). Comparison studies have shown that there is considerable variation between instruments (Tolhurst *et al*, 2000) and very few researchers have access to such instrumentation. Therefore, τ_e and M are often estimated using large-scale observations of changes in sediment concentration (e.g. Clarke & Elliott, 1998).

Consolidation generally occurs over time-scales greater than the spring-neap tidal cycle and is especially relevant for models of long-term cohesive sediment transport. Short-term studies are largely unaffected by this process and it may be possible to ignore consolidation altogether for simulations running for only a few tidal cycles (Cancino & Neves, 1999a). However, the inclusion in the model of a layered bed is undoubtedly important since this will take into account any past consolidation.

A layered bed model simulates consolidation of the bed at each element in the numerical model by a pile of two or more sediment layers of increasing concentration with depth, as shown in Figure 1.6 (Teisson & Fritsch, 1988). Each layer is characterised by a maximum residence duration (after which the mud is moved to the

lower layer), a critical shear stress for erosion, and an erosion rate. Only when one layer is completely eroded is the next layer evaluated.

Numerically, this may be formulated according to Le Normant (2000). In this formulation, the quantity of mud that remains in layer L after time $T(L)$ goes into the more consolidated layer $(L+1)$. The thickness of the latter then increases according to:

$$H(L+1) = H(L+1) + H(L)\frac{C(L)}{C(L+1)} \tag{1.25}$$

and

$$H(L) = 0$$

Consequently, the bottom level decreases due to the removal of the remainder of the top layer.

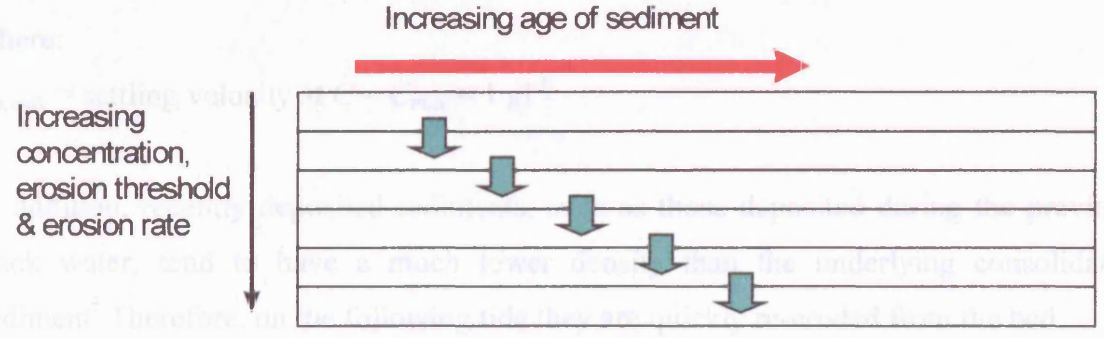

Figure 1.6 - Idealised implementation of a layered bed to simulate consolidation

1.3.3 Fluid mud formation

In very turbid estuaries (SSC>1 gl^{-1}), the processes of flocculation and consolidation described above combine to create marked differences in the theoretical Rouse profile derived for non-cohesive sediments. In particular, estuaries are often observed to have a steep concentration gradient, or *lutocline* towards the bottom of the water column (Ross & Mehta, 1989). This phenomenon arises fundamentally because of the fractal nature of the flocs, which causes there to be a higher volume concentration than there would be for more compact aggregates. Consequently, at high enough concentrations (about 2 to 5 gl^{-1}), the particles start to interact with one another, thus inhibiting their settling in a process known as *hindered settling* (Owen, 1971; Pejrup, 1988; Puls & Kühl, 1996). Cancino & Neves (1999a) and Van der Ham & Winterwerp (2001) present numerical implementations of this process. In these studies, normal settling (Equation 1.20) is limited to a threshold concentration, above which a separate equation for the hindered settling range is applied, given as:

$$w_s = w_{s,\max}(1 - KC)^N \qquad \text{for } C>1 \text{ gl}^{-1} \tag{1.26}$$

where:

$w_{s,max}$ = settling velocity at $C = C_{max} = 1$ gl^{-1}

In addition, recently deposited sediments, such as those deposited during the previous slack water, tend to have a much lower density than the underlying consolidated sediment. Therefore, on the following tide they are quickly re-eroded from the bed.

A relatively straightforward chain of events can lead to the formation of a dense *fluid mud* layer (Figure 1.7). First, at slack water, flocculation leads to an increase in settling velocity. Particles, nearer the bed then experience hindered settling due to the high volume concentration, thus initiating the formation of a sharp concentration gradient. At the start of the following tide, the rapid resuspension of the low density, unconsolidated particles therefore add to the lower layer. Second, it has been suggested that the presence of particles in the water affects the overall density of the water in a similar way to salinity (Darbyshire & West, 1993; Lindsay *et al*, 1996; Guan *et al*, 1998). The presence of a lutocline thus produces a buoyancy effect, resulting in a two-layer flow

regime with minimal mixing between the two layers. This has the effect of allowing the surface water to be relatively unaffected by the bottom friction as it *slips* over the turbulent lower layer. Therefore, if fluid mud is present in an estuary, this buoyancy effect should be included in the calculation of the vertical dispersion coefficient (K_z) in Equation 1.9. This suggests that highly turbid estuaries require the use of a three-dimensional, layered model, or a width-integrated (rather than depth-integrated) 2D model (Guan *et al*, 1998).

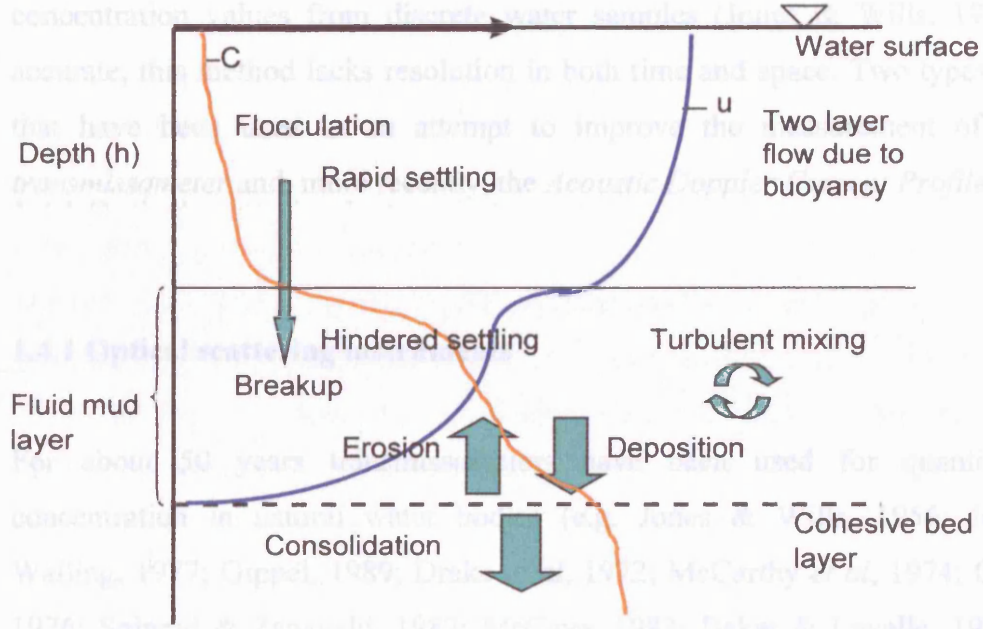

Figure 1.7 – Deviations from the theoretical Rouse profile caused by the properties of cohesive sediments.

1.4 Instrumentation for sediment concentration measurement

Temporal variation in the size of cohesive sediment particles also has implications for the calibration of instrumentation used to measure suspended concentration (SSC). The need for higher temporal and spatial resolution SSC measurements for the calibration and validation of sediment transport models has been the main driving force behind improvements in *in situ* instrumentation.

The ability for an estuary to carry suspended load varies both on a spatial scale, from the high energy tidally dominated regions near the mouth, to the sheltered regions further upstream, and also on a temporal scale due to current velocity variation induced by the tides, waves and river flow. In the past, it was only possible to obtain point concentration values from discrete water samples (Jones & Wills, 1956). Although accurate, this method lacks resolution in both time and space. Two types of instrument that have been used in an attempt to improve the measurement of SSC are the *transmissometer* and, more recently, the *Acoustic Doppler Current Profiler* (ADCP).

1.4.1 Optical scattering instruments

For about 50 years transmissometers have been used for quantifying particle concentration in natural water bodies (e.g. Jones & Wills, 1956; Jackson, 1964; Walling, 1977; Gippel, 1989; Drake *et al*, 1972; McCarthy *et al*, 1974; Callaway *et al*, 1976; Spinrad & Zaneveld, 1982; McCave, 1983; Baker & Lavelle, 1984; Finlayson, 1985; Sternberg *et al*, 1986; Moody *et al*, 1987; Wells & Kim, 1991; French *et al*, 1993; Wiberg *et al*, 1994; Wolanski *et al*, 1995; Clifford *et al*, 1995; Uncles & Stephens, 2000; French *et al*, 2000; and many others). They are now the standard instruments used for automated, near continuous, monitoring of particulate concentrations in the ocean, estuaries, rivers and lakes.

As shown in Figure 1.8, the transmissometer operates by shining a collimated beam of light through a sample volume of water. A portion of the light is scattered by the particles in the water, and the remainder of the beam intensity is measured at the other end by a photodetector. This is the most common form of the turbidity meter set-up

although there is a variety of other instruments that measure the light scattered at right angles (Nephelometers), or in the backward direction (Optical Backscatter Sensors) rather than the transmitted remainder of the beam (Bunt *et al*, 1999). Here the discussion is based purely on the in-line transmissometer geometry.

The ratio between the initial beam intensity (V_0) and the received intensity (V) follows an exponential relationship as defined by the Lambert-Beer Law, as given below:

$$V = V_0 e^{-cL} \tag{1.27}$$

where :
V_0 = detected voltage after passing through pure water (V)
V = detected voltage after passing through water containing particles (V)
L = pathlength (m)
c = beam attenuation coefficient (m^{-1})

The beam attenuation coefficient, c, in Equation 1.27 is primarily a measure of the amount of scattering caused by the particles, and is a useful parameter because it is independent of the beam pathlength (L). Theoretically, this means that results from different types of transmissometer should be comparable, although the electronic differences between systems usually disrupt this relationship (Walling, 1977; Finlayson, 1985).

Calibration of a transmissometer must be carried out in order to obtain the calibration coefficient, α, which expresses the proportionality between the measured beam attenuation coefficients into SSC values. Since the quantity of light scattered from the transmissometer beam is a function of the particle characteristics (such as size, shape and density), it is common practice to carry out the calibration by using numerous discrete water samples from the location of interest. The SSC is then determined by standard filtration methods (Walling, 1977; Gippel, 1989). The transmissometer output at the sampling times is then used to produce a graph of beam attenuation coefficient versus SSC (Figure 1.9). The following equation describes the relationship between transmissometer output and SSC.

$$M_T = \frac{1}{\alpha L} \log_e \left(\frac{V_0}{V} \right) \tag{1.28}$$

where:

M_T = suspended sediment mass concentration (kg m^{-3})

α = calibration slope

By substituting in c from Equation 1.27 this can be simplified to:

$$M_T = \frac{c}{\alpha} \tag{1.29}$$

Therefore:

$$c = M_T \alpha \quad (+\phi) \tag{1.30}$$

where:

ϕ = offset due to absorption by water.

In Equation 1.30, a small amount of the beam is attenuated as a result of absorption by the water, which causes an offset in the calibration (ϕ). In turbid estuaries, this value is generally small in comparison to the beam attenuation caused by scattering from the suspended particles. However, in regions of low SSC such as shelf seas, where scattering is minimal, the effects of absorption become relatively more important. Variability in ϕ between different locations highlights the importance of obtaining *in situ* transmissometer calibrations.

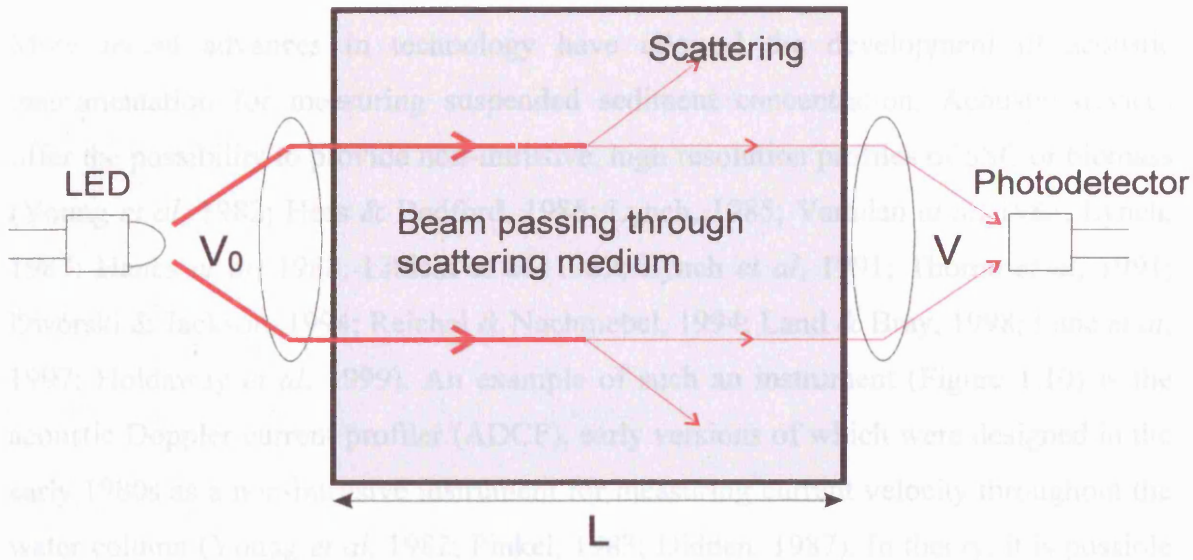

Figure 1.8 - The physical principle of the transmissometer.

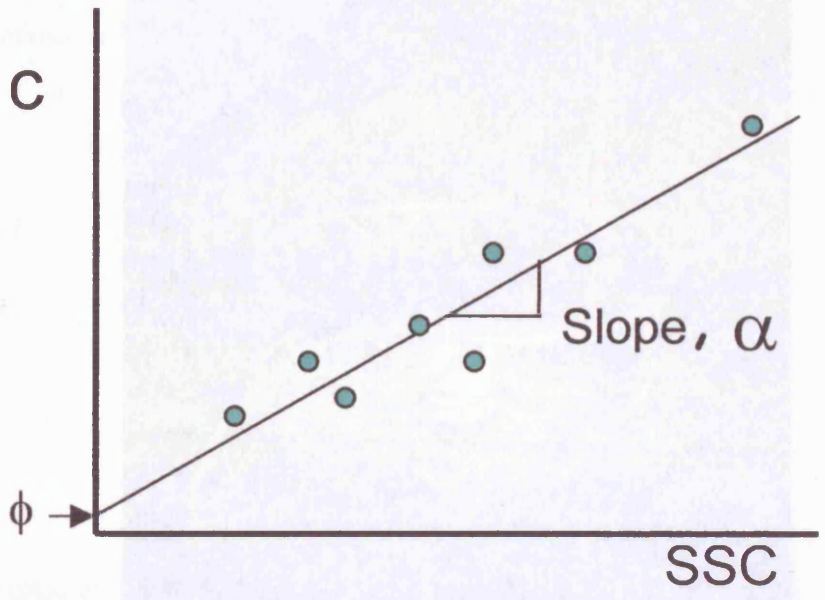

Figure 1.9 - Schematic of a transmissometer calibration curve.

1.4.2 The acoustic Doppler current profiler

More recent advances in technology have allowed the development of acoustic instrumentation for measuring suspended sediment concentration. Acoustic devices offer the possibility to provide non-intrusive, high resolution profiles of SSC or biomass (Young *et al*, 1982; Hess & Bedford, 1985; Lynch, 1985; Varadan *et al*, 1985; Lynch, 1987; Hanes *et al*, 1988; Libicki *et al*, 1989; Lynch *et al*, 1991; Thorne *et al*, 1991; Dworski & Jackson, 1994; Reichel & Nachtnebel, 1994; Land & Bray, 1998; Lane *et al*, 1997; Holdaway *et al*, 1999). An example of such an instrument (Figure 1.10) is the acoustic Doppler current profiler (ADCP), early versions of which were designed in the early 1980s as a non-intrusive instrument for measuring current velocity throughout the water column (Young *et al*, 1982; Pinkel, 1983; Didden, 1987). In theory, it is possible to use an ADCP to obtain instantaneous measurements of both current velocity and sediment concentration since the backscatter intensity is related to the number of particles in suspension. This has obvious advantages since, by combining the measurements of current velocity and SSC, an instantaneous approximation of sediment flux may be determined (Lane *et al*, 1997).

Figure 1.10 – Photo of RD Instruments Workhorse broadband ADCP on customised mount (with Partech IR40 transmissometer and pump sampler intake tube on a 1m pole) prior to field deployment.

Typically, ADCPs operate by transmitting an acoustic pulse of the order of a few milliseconds at a frequency of approximately 1 MHz. A small fraction of this pulse will then be scattered from any particles that are present in the water, and the backscattered portion of the signal is measured by the instrument transceiver. If the particles are moving towards or away from the transceiver, a change in the frequency will occur in the backscattered signal due to Doppler shift. As a result, the velocity of the particles, and hence the water flow velocity, can be calculated using the following equation:

$$f_d = 2f_s\left(\frac{v}{c}\right)\cos A \tag{1.31}$$

where :

f_d = Doppler shift frequency (s^{-1})

f_s = transmitted frequency (s^{-1})

v = relative velocity between source and scatterer ($m\ s^{-1}$)

c = speed of sound in water ($m\ s^{-1}$)

A = angle between the relative velocity vector and the line between the ADCP and scatterers (°)

In this equation, the Doppler shift is multiplied by two because the beam is both transmitted and received by the ADCP, therefore the frequency is shifted once when it reaches the scatterers, and once again when the reflected sound is received by the ADCP. By knowing the speed of sound in the water and range-gating the transceiver, instantaneous measurements of velocity can be made at various depths in the water column, thus giving the current profile. Commercial ADCP instruments usually have four transceivers mounted at 20 degrees to one another as shown in the photograph in Figure 1.10. The function of each beam is demonstrated in Figure 1.11. One pair of beams obtains one horizontal component and the vertical velocity component. The second pair of beams produces a second, perpendicular horizontal component as well as a second estimate of the vertical velocity component (RD Instruments, 1998). Figure 1.12 shows how the ADCP may be attached to the bottom of a moving boat, and still allows accurate measurements of current velocity to be obtained due to *bottom tracking,* whereby the velocity of the bed is subtracted from the measured current velocities.

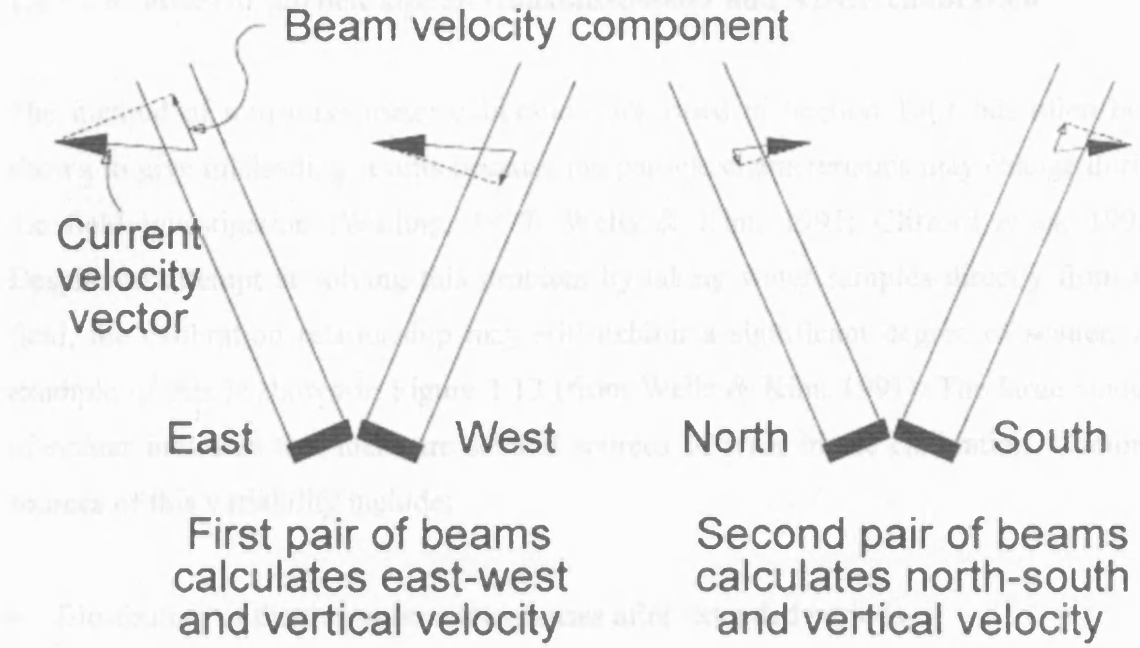

Figure 1.11 - Determining 3D velocity components with the ADCP (RD Instruments manual)

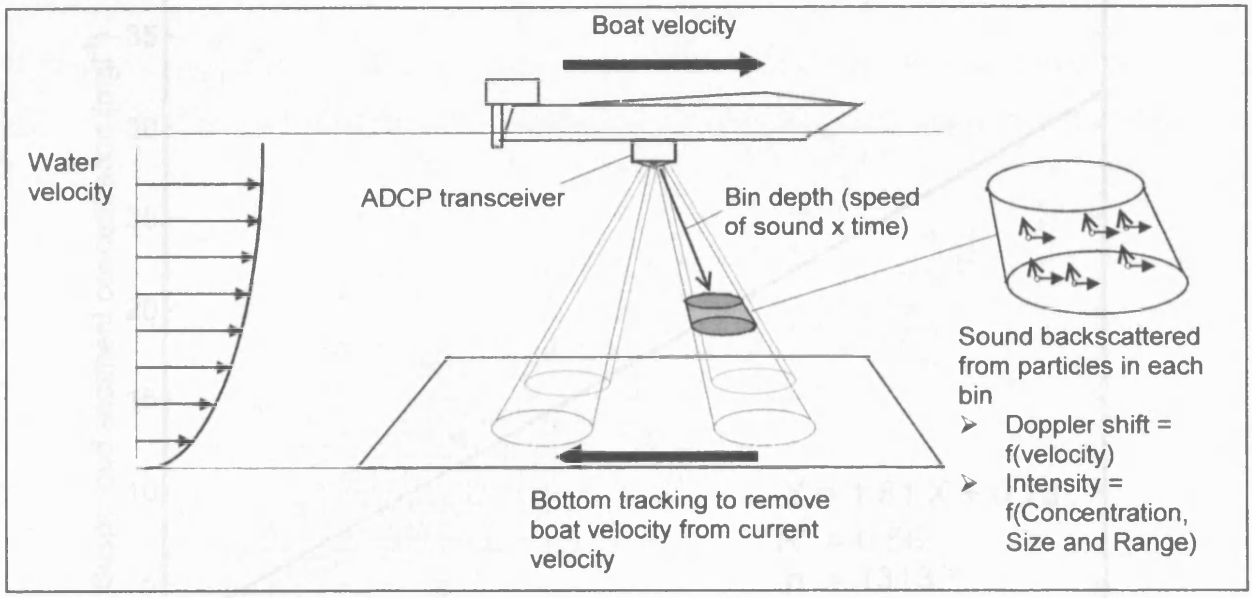

Figure 1.12 - Diagram of ADCP principle of operation.

1.4.3 The effect of particle size on transmissometer and ADCP calibration

The method of transmissometer calibration described in Section 1.4.1 has often been shown to give misleading results because the particle characteristics may change during the field investigation (Walling, 1977; Wells & Kim, 1991; Clifford *et al*, 1995). Despite an attempt at solving this problem by taking water samples directly from the field, the calibration relationship may still exhibit a significant degree of scatter. An example of this is shown in Figure 1.13 (from Wells & Kim, 1991). The large amount of scatter indicates that there are several sources of error in the calibration. Common sources of this variability include:

- Bio-fouling of the transmissometer lenses after extended periods
- Temperature affects, causing resistance changes in the electronics
- Changes in the particle characteristics

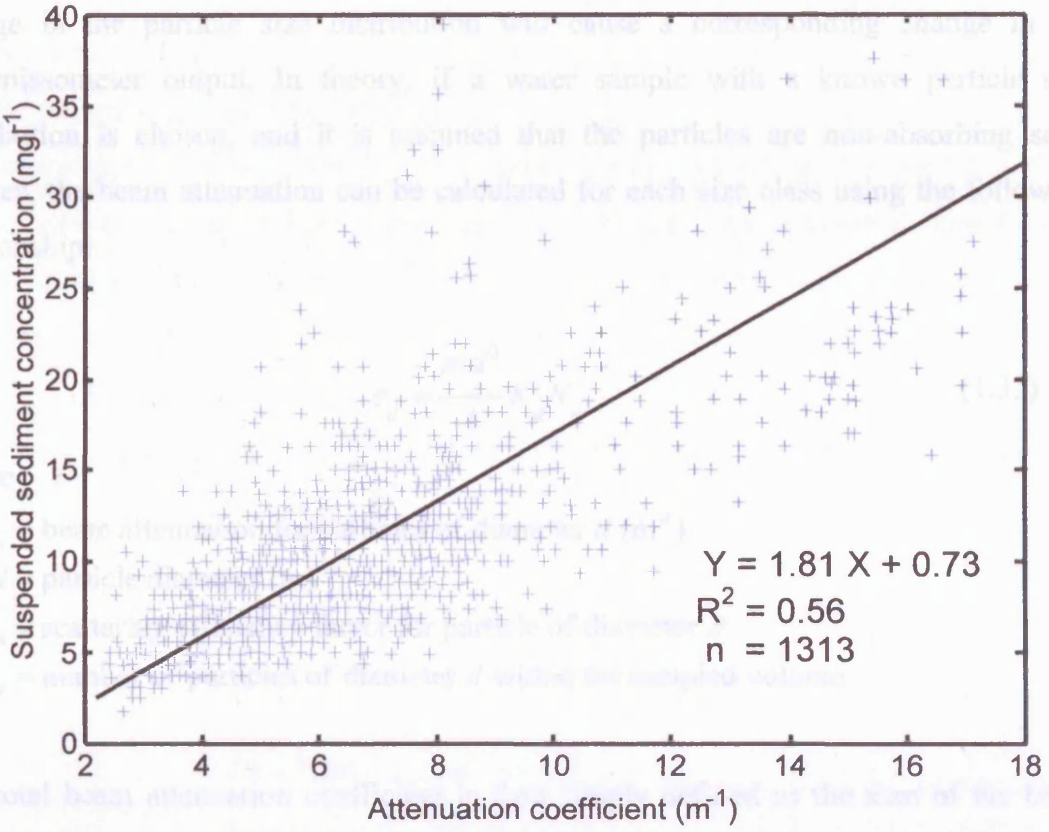

Figure 1.13- A typical transmissometer calibration curve (re-drawn from Wells & Kim, 1991).

Modern transmissometers usually contain electronics to compensate for temperature effects, and regular cleaning of the lenses will reduce the effects of bio-fouling. The remaining source of error, however, still poses a problem. In order to understand why this problem exists, it is necessary look closely at the physics of light scattering from small particles. The particle characteristic that causes most variation in beam attenuation is size. The reason for this is that most of the beam attenuation is caused by diffraction with minor contributions from absorption, reflection and refraction (Van Der Hulst, 1989). Figure 1.14 shows how the angle of diffraction is proportional to particle diameter (d) and the wavelength of light used (λ). The angle (θ) between the centre of the particle and the first minimum of the Airy Disc pattern may be approximated by $sin\theta \approx \lambda/d$, so the smaller the particle the greater the scattering angle. By placing a large lens in front of the detector, so that the Fourier Transform of the diffraction pattern is imaged, the image produced is the mean Airy Disc pattern for an entire ensemble of particles. As was seen in Figure 1.8, the transmissometer already works by this principle, but it only measures the intensity at the centre of the Airy pattern. Hence, a change in the particle size distribution will cause a corresponding change in the transmissometer output. In theory, if a water sample with a known particle size distribution is chosen, and it is assumed that the particles are non-absorbing solid spheres, the beam attenuation can be calculated for each size class using the following relationship:

$$c_d = \frac{\pi d^2}{4} K_d N_d \qquad (1.32)$$

where :

c_d = beam attenuation for particles of diameter d (m^{-1})
d = particle diameter (m)
K_d = scattering efficiency factor for particle of diameter d
N_d = number of particles of diameter d within the sampled volume

The total beam attenuation coefficient is then simply defined as the sum of the beam attenuation coefficients for all the different particle size classes. It is interesting to note that the first term of this equation is simply the cross-sectional area of the particle. Consequently, at a fixed SSC, the beam attenuation coefficient is proportional to the square of the particle diameter.

The second term (K_d) in Equation 1.32 is sometimes called the 'effective area coefficient' or the 'scattering area ratio' (Swift *et al*, 1972). According to Mie scattering theory (Van Der Hulst, 1989) for non-absorbing particles in the region of anomalous diffraction, (where: $(m - 1) << 1$ and $x = \pi d/\lambda >> 1$):

$$K_d = 2 - \frac{4}{\sigma}\sin\sigma + \frac{4}{\sigma^2}(1 - \cos\sigma) \qquad (1.33)$$

where :

m = refractive index

λ = wavelength of beam light in water (m)

$\sigma = 2x(m - 1) =$ phase index parameter

The variation in the value of K_d at different particle sizes can be seen clearly when plotted as a graph against inverse particle diameter as given in Figure 1.15. This graph was produced assuming $m = 1.20$ and $\lambda = 1$ μm. Hodkinson (1963) suggested that, when dealing with a natural sediment suspension, the oscillations seen in this graph are largely damped out. He also found that it was reasonable to assume that K_d could be approximated to 2 for particles with a phase index exceeding a value of 6. This corresponds to a particle size of about 5 microns (0.2 μm^{-1}) and appears to coincide with the point where the oscillations become excessively large either side of the value of 2. Therefore, as a first approximation, for particles above 5 microns, it may be assumed that $K_d = 2$. Taking the assumption that K_d does not vary with particle size, the calibration slope (α) can therefore be shown to be inversely proportional to the particle diameter, as explained below:

from Equation 1.29: $M_T = \frac{c}{\alpha}$

since: $M_T \propto d^3$ and $c \propto d^2$ (1.34)

therefore: $d^3 \propto \frac{d^2}{\alpha}$ (1.35)

hence: $\alpha \propto d^{-1}$ (1.36)

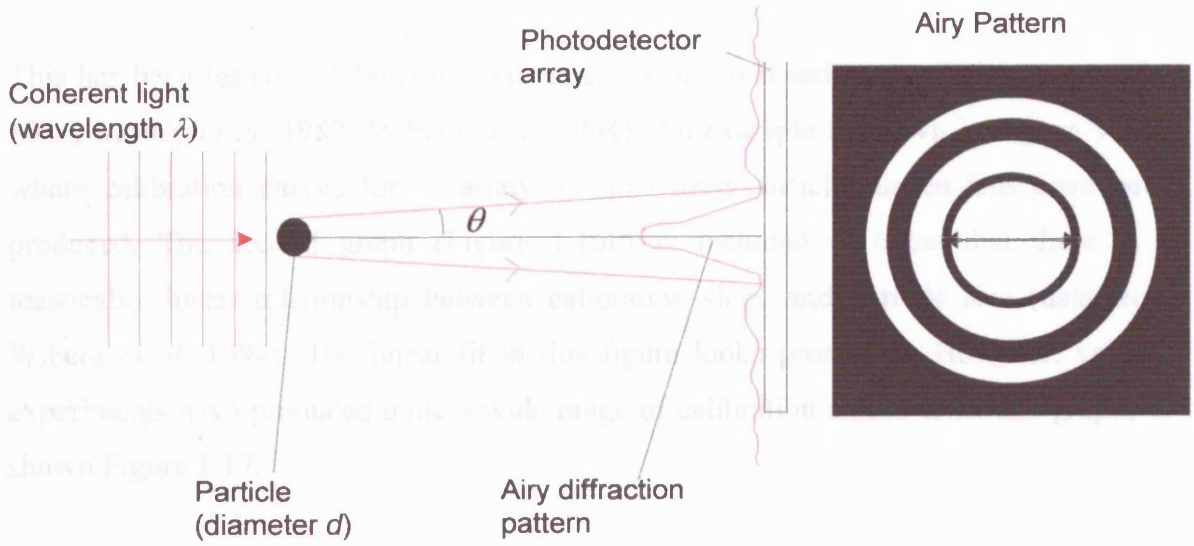

Figure 1.14 - Diffraction of a light beam by a small particle.

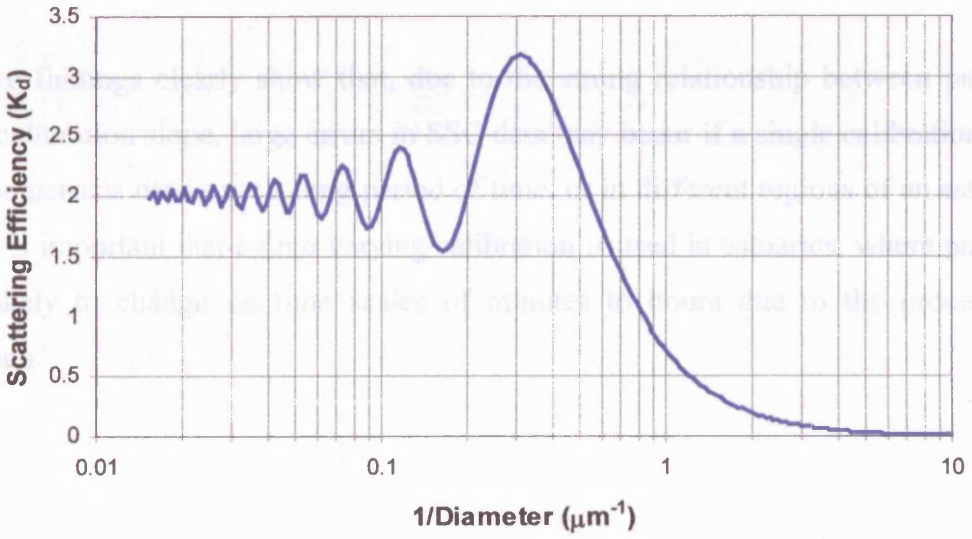

Figure 1.15 - Variation of scattering efficiency factor with particle size.

This has been tested in laboratory experiments using real sediments (Baker & Lavelle, 1984; Moody *et al*, 1987; Wiberg *et al*, 1994). An example is shown in Figure 1.16a, where calibration curves for a variety of monosized particle suspensions have been produced. The second graph (Figure 1.16b) is included to show that there is a reasonably linear relationship between calibration slope and particle size (data from Wiberg *et al*, 1994). The linear fit in this figure looks promising. However, various experiments have produced quite a wide range of calibration slopes to fit this graph, as shown Figure 1.17.

It is thought that the cause of this wide variation is due to differences in particle characteristics other than size, such as shape, refractive index, and density (Baker & Lavelle, 1984). If a completely theoretical graph is produced directly from Mie scattering theory for solid spheres (Figure 1.18) the slopes match well for the lower estimates given in Figure 1.17. In the calculations to produce this graph, it was assumed that λ = 1 μm and the particles were assumed to have a density of 2.65 gcm^{-3} and a refractive index of 1.20.

The above findings clearly show that, due to the strong relationship between particle size and calibration slope, large errors in SSC data may occur if a single calibration of a transmissometer is used over a long period of time, or in different regions of an estuary. Hence, it is important that a time-varying calibration is used in estuaries, where particle size is likely to change on time scales of minutes to hours due to the process of flocculation.

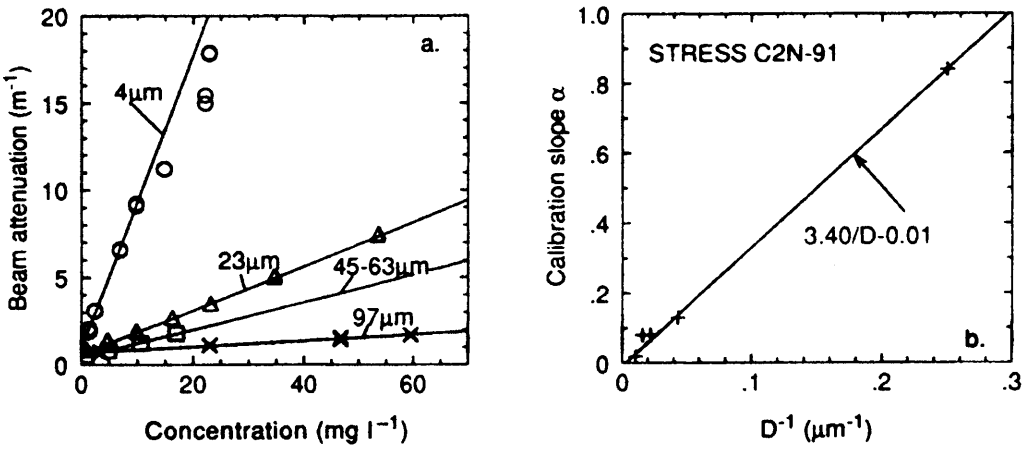

Figure 1.16 - (a) Calibration curves for different sized glass bead solutions, (b) Slopes of the calibration curves plotted against inverse particle diameter (from Wiberg *et al*, 1994).

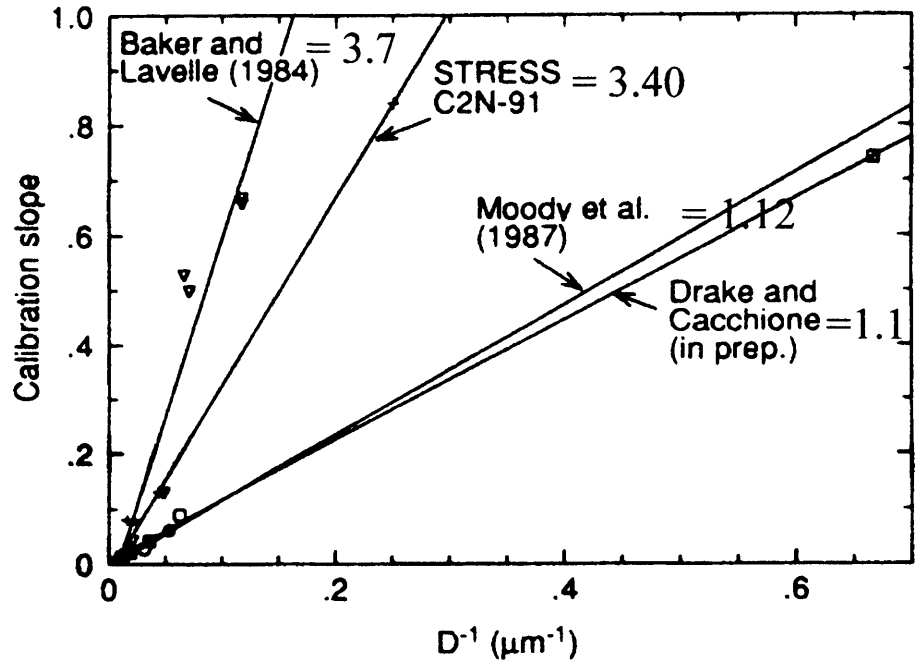

Figure 1.17 - Various estimates for the change in calibration with inverse particle size (from Wiberg *et al*, 1994)

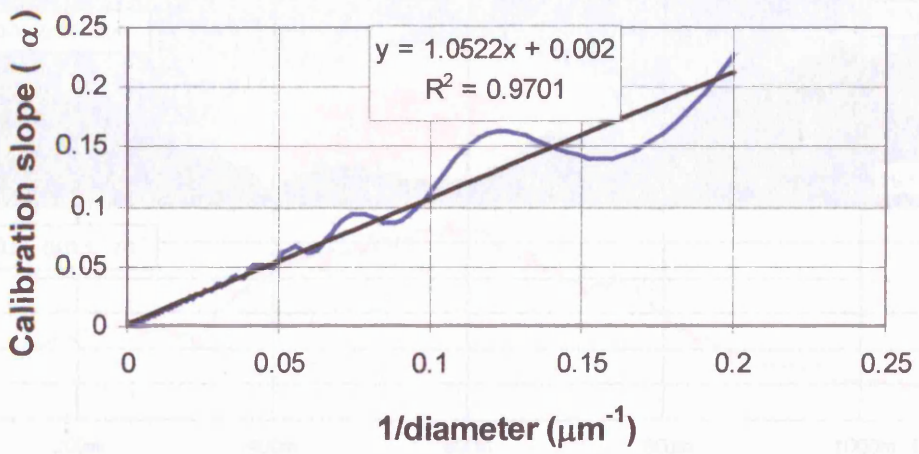

Figure 1.18 - Theoretical graph of transmissometer calibration variation versus inverse particle size.

A similar dependency on SSC and particle size distribution also exists for the backscatter intensity measured by an acoustic instrument (Holdaway *et al*, 1999). Therefore, for a suspension of sediment with a constant grain size it is possible to calibrate the ADCP for measuring SSC. For example, Wither *et al* (1998) carried out a study of the River Mersey, whereby an ADCP was calibrated empirically using water bottle samples, in a similar fashion to the typical transmissometer calibration exercise. Figure 1.19 shows a cross-section of the Mersey estuary taken during this experiment whereby acoustic backscatter strength data were recorded from the ADCP, which was attached to the bottom of a ship as it traversed the channel. During this study, it was found that particle size played an important role in the calibration of the ADCP. For most of the time during a tidal cycle, the mean particle diameter was of the order of 5 μm. However, at slack water the particles flocculated over a period of about 30 minutes to form aggregates with a diameter of up to 1500 μm, which were then broken up again after slack water. For this reason, a time varying calibration was carried out in order to prevent errors being introduced due to particle size variation. Wither *et al* (1998) state that, if a single calibration had been used, errors in excess of 600% would have occurred in the concentration values due to the particle size variation caused by flocculation. Clearly to carry out a time varying calibration, large numbers of water samples were required. This was both time consuming and laborious, and may not be feasible for long-term surveys, or if a small boat is being used.

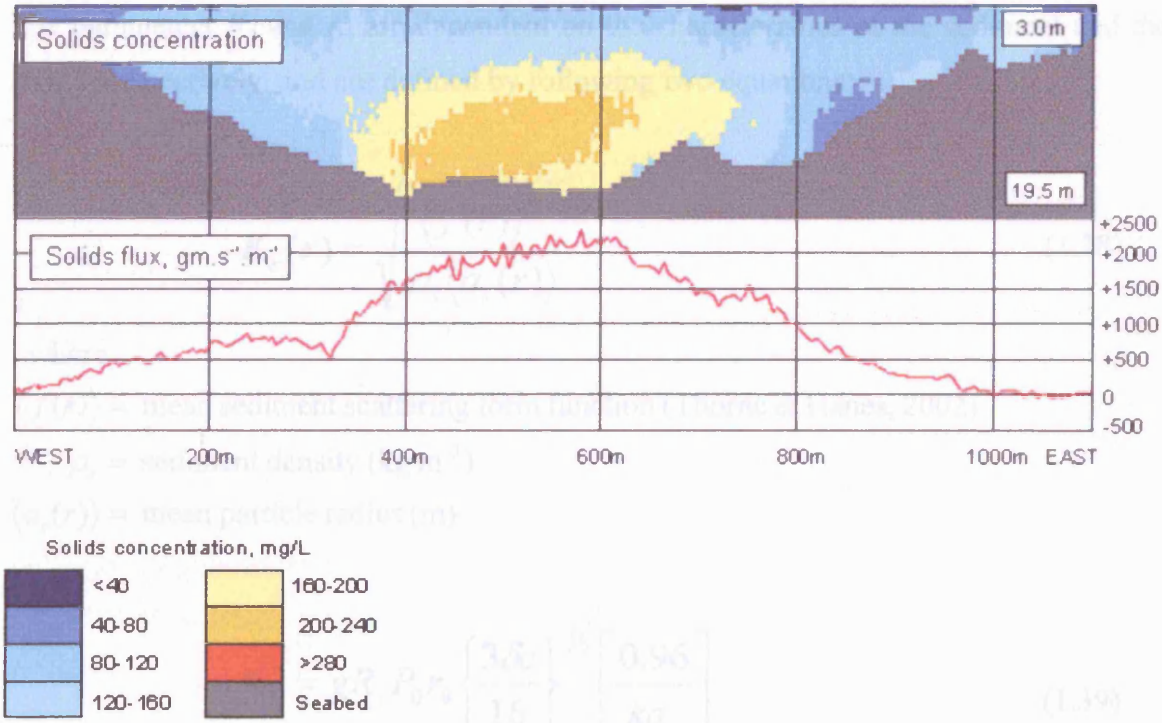

Figure 1.19 - Measurements of SSC using ADCP backscatter data across the River Mersey (from Wither *et al* 1998).

The theory of converting acoustic backscatter to sediment concentration is now well understood, although it is more complex than the calibration of the transmissometer. The following relationship can be defined for calculating the suspended mass concentration from the acoustic backscatter strength measured by the ADCP (Thorne *et al*, 1993):

$$M_A(r) = \left\{ \frac{V_{rms}}{K_s K_t} \right\}^2 r^2 e^{4r(\alpha_w + \alpha_s)} \qquad (1.37)$$

where :

$M_A(r)$ = suspended mass concentration at range r (kg m^{-3})

V_{rms} = recorded voltage from transceiver (V)

α_w = attenuation coefficient due to water absorption (m^{-1})

α_s = attenuation coefficient due to scatterers in suspension (m^{-1})

K_s = contains sediment information

K_t = ADCP system parameters

The parameters K_s and K_t are dependent on the characteristics of the sediment and the ADCP respectively, and are defined by following two equations:

$$K_s(r) = \sqrt{\frac{\langle f(r) \rangle^2}{\rho_s \langle a_s(r) \rangle}} \tag{1.38}$$

where :

$\langle f(r) \rangle$ = mean sediment scattering form function (Thorne & Hanes, 2002)

ρ_s = sediment density (kg m^{-3})

$\langle a_s(r) \rangle$ = mean particle radius (m)

$$K_t = gR_s P_0 r_0 \left\{ \frac{3\delta c}{16} \right\}^{1/2} \left[\frac{0.96}{ka_t} \right] \tag{1.39}$$

where :

g = system gain (dB)

R_s = receive sensitivity of transceiver (dB m)

P_0 = pressure at range r_0 (usually 1 m), i.e. no scattering region (kg m^{-2})

δ = pulse duration (s)

c = speed of sound in water (m s^{-1})

k = wave number of sound in water = $2\pi f / c$

a_t = transceiver radius (m)

In Equation 1.37, a proportion of the acoustic beam is attenuated both by the water and suspended sediment. Attenuation due to water (α_w) occurs by absorption, which is dependent on temperature, pressure and salinity and can be estimated using tables or empirical formulae (Fisher & Simmons, 1977; Kaye & Laby, 1986; Medwin & Clay, 1998). Attenuation of the beam due to the suspended sediment (α_s) is caused both by absorption and scattering. For particles (or flocs) larger than cohesive sediment primary particles (i.e. >5μm), the scattering component dominates (Richards *et al*, 1996). The sediment attenuation can be described by the following equation (Thorne & Hanes, 2002):

$$\alpha_s = \frac{1}{r}\int_0 \xi(r) M_A(r) \partial r \tag{1.40}$$

In Equation 1.40, ξ is known as the sediment attenuation constant, defined as:

$$\xi = \frac{3}{4\langle a_s \rangle \rho_s} \cdot \left(\frac{\langle a_s \rangle \cdot \langle a_s^2 \chi \rangle}{\langle a_s^3 \rangle} \right) \tag{1.41}$$

where :

χ = the normalised total scattering cross - section
determined from empirical formula (Thorne & Hanes, 2002)

The form function (f) in Equation 1.38 and the normalised total scattering cross-section (χ) in Equation 1.41 are both dependent upon the suspended particle size (and shape) and are derived from empirical formulae (Thorne & Hanes, 2002).

Equation 1.37 may be simplified by considering just one of the bins at a fixed distance from the transceiver and calibrating with filtered water samples in a similar fashion to the transmissometer. It is then possible to remove all the variables other than SSC (M_T) and backscattered intensity (V^2_{rms}), and introduce a calibration coefficient (β) to described the rest of the variables. A similar equation to that given previously for the transmissometer calibration (Equation 1.29) can then be formulated as:

$$M_{A(r)} = \frac{V^2_{rms(r)}}{\beta_{(r)}} \tag{1.42}$$

where :

M_A = suspended sediment concentration measured by ADCP (kg m^{-3})
V^2_{rms} = measured backscattered intensity (V)
β = Calibration coefficient
r = distance from transducer (m)

At a frequency of ~1 MHz (as used by most commercial ADCPs), and for particles finer than about 500 μm, the intensity of the backscattered signal is governed by the Rayleigh scattering model (Lynch *et al*, 1994). This states that at a constant SSC (M_T), the backscattered intensity (measured as voltage V^2_{rms}) is proportional to the volume squared of the particles (i.e. d^6) (Hay, 1983; Lynch *et al*, 1991). This is in contrast to the relationship described earlier between the transmissometer beam attenuation and particle cross-sectional area (d^2). Consequently:

since: $$M_A \propto d^3 \quad \text{and} \quad V^2_{rms} \propto d^6$$

therefore: $$d^3 \propto \frac{d^6}{\beta} \tag{1.43}$$

hence: $$\beta \propto d^3 \tag{1.44}$$

Equation 1.44 shows that, when obtaining SSC estimates from acoustic backscatter, the calibration is strongly affected by particle size and clearly, for accurate implementation of Equation 1.37, accurate particle size data are required. It should be noted, however, that for particles above 500 μm for a 1 MHz system, the backscatter is no longer within the Rayleigh regime. Instead of the cubed relationship, the intensity is now relatively unaffected by any further increase in particle size, i.e. $\beta \propto d^0$ (Lynch *et al*, 1994).

It is clear from the preceding discussion that, in estuaries, time-varying particle size distributions will produce marked differences in the calibration of both transmissometers and ADCPs. For a transmissometer, the values of SSC will tend to decrease proportionally to an increase in particle diameter, whereas an ADCP measuring the same particle population will show an apparent increase in concentration, proportional to the volume of the particles. Therefore, any comparison made between the two sets of readings needs to be able to take into consideration the particle size. For this reason, it is essential that ADCP measurements of SSC are calibrated correctly. To carry out a suitable calibration, the combined use of a transmissometer, water samples and an *in situ* particle-sizing instrument is vital. Values from each instrument could then

be used to corroborate readings from the other. The weaker dependence of the transmissometer calibration on particle size means that an initial calibration of the ADCP backscatter data may be obtained simply from cross-calibration with transmissometer beam attenuation data. Further improvements could then be made to the accuracy of the SSC values by including data from a particle-sizing instrument, which could be used to weight the outputs from each instrument according to the particle size distribution.

1.5 Aims and Objectives

The preceding review has drawn attention to a series of outstanding problems regarding the monitoring and modelling of cohesive sediment transport in estuaries. The following key observations are made:

(1) The settling velocity of the particles is directly related to the size distribution, which has important implications for the modelling of sediment transport.
(2) Particle size variation has implications for the monitoring of sediment transport because it affects the calibration of instrumentation commonly used for measuring SSC.
(3) Flocculation of cohesive sediments causes variations in particle size on time scales of less than one hour due to tidal flow variations, thus causing a time variation in observations (1) and (2).
(4) The fractal nature of cohesive flocs means that they gradually consolidate with time after they have settled, which alters the erosion rate, thus introducing a longer-term variable into a sediment transport model.

The fundamental parameter that links all these observations is the *in situ* particle size distribution. Because of the time varying nature of particle size, *in situ* measurements of the size distribution are a prerequisite for the accurate monitoring and modelling of estuarine suspended sediment dynamics. Existing techniques for particle sizing all suffer serious limitations, although some promising advances seem possible by using the latest imaging technologies.

Within this context, the present study has two primary aims:

(1) *Instrument design*: Design, fabrication and testing of an improved *in situ* imaging system for particle sizing in estuaries.
(2) *Sediment transport modelling*: Evaluation of the new instrument in respect of the parameterisation, calibration and validation of a sediment transport model of a UK estuary.

Specific objectives include:

(1) Critical evaluation of existing methods and instrumentation used for particle size measurement.
(2) Development of a new, compact, low-cost instrument, which is capable of making *in situ* measurements of particle size at a range of depths throughout the water column of an estuary, and from a small boat.
(3) Critical evaluation of the performance of the particle sizing system.
(4) Exploration of the effects of particle size on the performance of a numerical model of sediment transport.
(5) Evaluation of the potential of using *in situ* size measurements for the calibration of ADCP instrumentation to drive and/or validate the numerical model.

2. Research Approach

2.1 Overview

In accordance with the aims and objectives set out in the previous chapter, the research has been organised into four areas of study (Figure 2.1). In Chapter 3, a desk based review and critical appraisal of currently available particle sizing techniques is presented from which a design specification for a new system is derived. This is followed, in Chapter 4, by an account of the design, construction and calibration of the new *in situ* video particle-sizing system. Main facilities and funding for the construction of the particle-sizing instrument have been provided by Sira Ltd. (Kent, UK). Additional facilities have been provided by the Coastal & Estuarine Research Unit (UCL) for the laboratory calibration and field-testing phases. An assessment of the instrument performance is given in Chapter 5 in the form of a case study of an estuary in Southeast England. The particle size results are then further analysed in Chapter 6 with respect to improving both a sediment transport model of the case study estuary, and the calibration of acoustic backscatter data from an ADCP to yield unbiased sediment concentration measurements.

It has been decided to use a field-based case study of an individual estuary, rather than a more generalised approach, because it provides the framework for developing the system as well as providing a test case for a high-resolution numerical model of sediment transport. With respect to instrument development, the process of flocculation means that particle size data need to be collected *in situ*. Rather than attempt to simulate the flocculation process in a laboratory, it is simpler and more realistic to evaluate the camera system's ability to measure *in situ* particle size by using a fieldwork-based approach. Also, in terms of the development of a sediment transport model, the choice of a bottom-up approach (as defined in Section 1.2) leads to a requirement for intensive data sets in order to quantify the complex processes within the estuarine system. A case study of a single estuary is therefore preferable to a more generalised approach since it makes best use of limited time and resources.

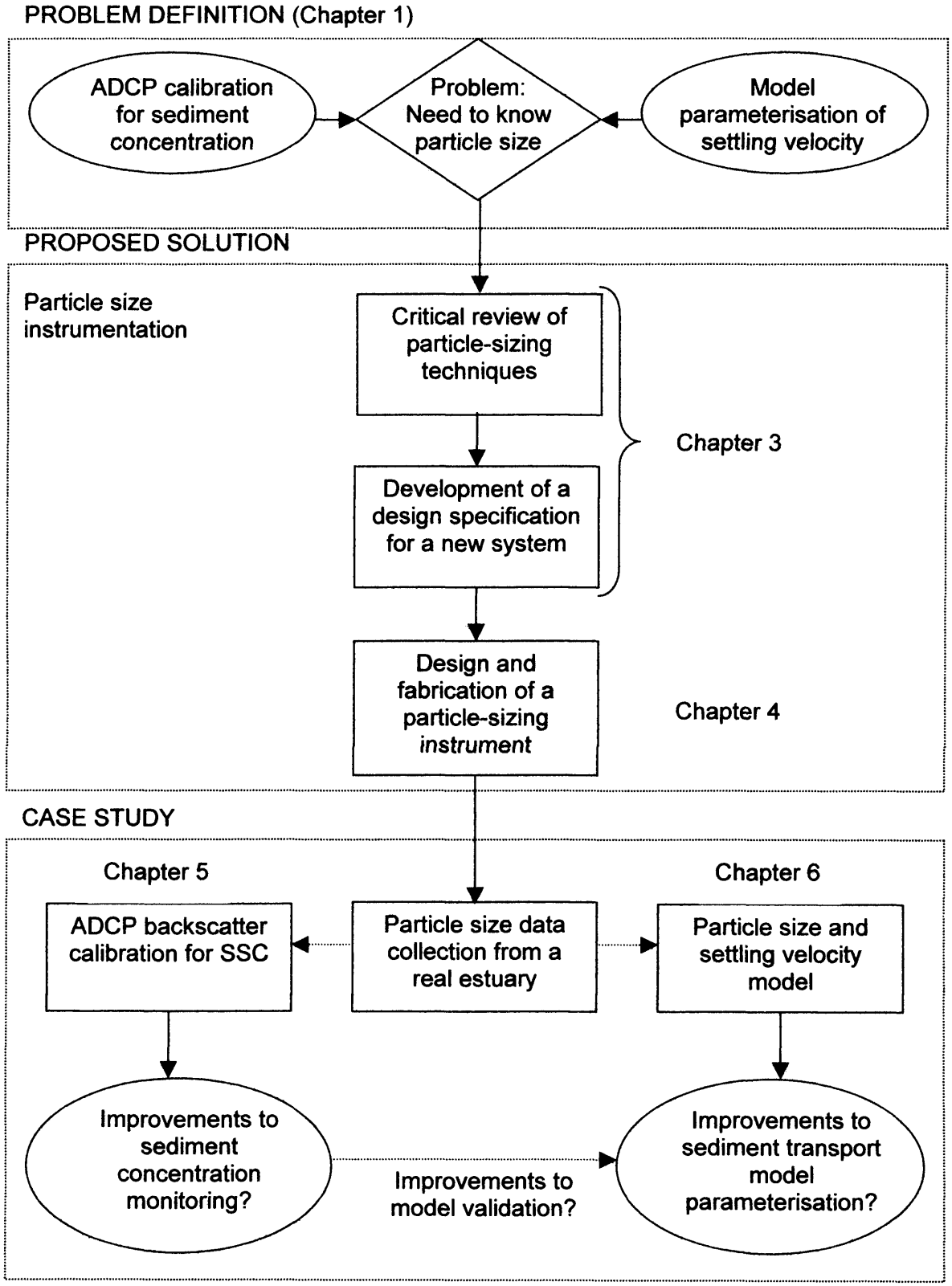

Figure 2.1 – Research approach organisation diagram

2.2 Case study description: The Blyth estuary

2.2.1 Physical setting

The Blyth is located in the rural area of northern Suffolk (Figure 2.2). It is the smallest estuary in the region with a tidal length of 10.7 km from the mouth at Southwold to the tidal limit near Blyford. The catchment is approximately 214 km^2 with a geology consisting of glacial tills (44%), Pliocene-Pleistocene shelly marine sands and clays (the Coralline and Red Crags; 42%) and alluvium (13%) (Beardall *et al*, 1991). At Southwold, mean spring and neap tidal ranges are 2.0 m and 1.2 m respectively. As a result, the tidal exchange at the mouth during a spring tide may exceed 200 m^3s^{-1}, with current speeds exceeding 2 ms^{-1} due to the constricted harbour entrance (French *et al*, 2004). In contrast, riverine input is low, with a mean monthly discharge of 0.32 m^3s^{-1} (National Water Archive, based on data from 1990-96). Peak river run-off rarely exceeds 5 m^3s^{-1}, and 90% of the flows are below 0.81 m^3s^{-1}. The relative dominance of the tide means that the estuary is generally well-mixed (French, 2001).

2.2.2 Geomorphology

The Blyth can be classified as a barrier-enclosed estuary (in the sense of Healy & Kirk, 1992). An abundance of shingle and sand along the coast between Lowestoft and Aldeburgh, combined with a predominant wave driven littoral sediment transport from north to south (Motyka & Brampton, 1993) acts to choke the estuary, and hence the narrow estuary mouth (~30 m wide) is maintained by breakwaters. Dune backed shingle and sand beaches flank the mouth, the wider of which stretches northwards towards the elevated headland on which Southwold is situated.

Past evidence for episodic sealing and migration of the mouth is suggested by analysis of both geomorphological and historical sources. Geomorphological evidence is given by Brew *et al* (1992) from a series of boreholes sunk in the reclaimed marshes of the outer estuary. These show that the underlying mid-Pleistocene Westleton Beds (pebbly and sandy gravels) are overlain with an alternating sequence of four sedimentary layers of peat and clay: a basal freshwater Lower Peat (6450-6750 ^{14}C years BP); an estuarine

Lower Clay (6750-4500 ^{14}C years BP); a freshwater/brackish Middle Peat (4500-4300 ^{14}C years BP); and an estuarine Upper Clay (4300 ^{14}C years BP to present). It is feasible that this transition between freshwater, brackish and estuarine conditions reflects episodic sealing of the Blyth by ancient barriers (French, 2001). Parker (1978) gives historical evidence that the mouth of the estuary was also sealed temporarily between 1500 and 700 BP. At this time, the mouth of the estuary was co-located several km to the south with the Dunwich River. In 1328 this was blocked by shingle during a storm, and a new entrance was artificially cut close to Southwold. The excavation of the present harbour occurred in 1630.

2.2.3 Reclamations

The Blyth, like all the other estuaries in Suffolk, has been extensively reclaimed (French, 2001). The present day morphology largely reflects human influence over the past three hundred years (Posford Duvivier, 1999). The original intertidal area of the Blyth was approximately 1300ha. In the 16th and 17th centuries, lucrative trade in agricultural produce prompted large-scale reclamation of the intertidal zone. By 1842 about 1100ha of the intertidal zone (including both saltmarsh and mudflats) had been converted into agricultural land, restricting the estuary to a thin channel extending from the mouth to Blyford Bridge. The reduction in the tidal prism caused siltation problems at Southwold Harbour making it necessary to dredge the channel to allow navigation for vessels carrying coal and grain (French, 2001). Between 1805 and 1818, it had to be dredged 13 times (Lawrence, 1990) and gales caused major blockages of the harbour entrance in 1827, 1838 and 1859. By the beginning of the 20th century, the combined effects of a diminished sea trade (due to expansion of the railways) and a depression in agriculture meant that some of the seawalls fell into disrepair resulting in 'breaches' at several locations due to tidal action. The Sandpit Covert marshes were abandoned in the 1920s, followed by the Angel marshes and a large portion of the Bulcamp marshes in the 1940s (Simper, 1994). To date, approximately 250ha have been returned to the intertidal zone (Posford Duvivier, 1999).

Figure 2.2 – The Blyth estuary: (A) Location within the UK; (B) Detailed map showing the data collection site near Reydon (dashed box).

2.3 Previous investigations

The current project is designed to fit into an ongoing research programme focused on the impacts of sea-level rise on the coast and estuaries of Southeast England. A number of research projects have already been carried out on the Blyth estuary over the past few years by several authorities and research organisations, including the Jackson Environment Institute (CE French *et al*, 2000), the Environment Agency funded Suffolk Estuarine Strategies programme (Posford Duvivier, 1999) and the UCL Coastal and Estuarine Research Unit (French, 2001; French *et al*, 2004).

A high-resolution hydrodynamic model has already been produced for the estuary. This provides the basis for the creation of a sediment transport model. The hydrodynamic model is described in a recent report funded by the Jackson Environment Institute (UCL) and the Environment Agency (French, 2001). It demonstrates the use of a high-resolution model (Telemac2d), within a conceptual framework provided by geomorphological and historical analyses, to investigate the sensitivity of the estuary process regime to sea level rise. The report also investigates possible outcomes of further realignments by adjusting the hydrodynamic model mesh to include areas of currently reclaimed land.

2.3.1 Conceptual model

The long history of anthropogenic alterations to the morphology of the Blyth estuary mean it does not conform to simple geomorphological models developed for naturally formed estuarine systems. As an aid to understanding the complexity of this system, French (2001) presents a conceptual model of the estuary based upon extensive field monitoring of hydrodynamics and sediment fluxes, coupled with intensive studies of intertidal processes, and the examination of historical data. French *et al* (2004) present a simplified scheme in which the estuary is divided into three geomorphological compartments each with its own set of dominating processes (Figure 2.3). The first compartment is the upper estuary (1). The narrow cross-section of this region, and the long distance from the sea, results in a low energy environment with little wind-wave or

tidal influence. The mean river inflow is approximately 0.3 m^2s^{-1} and so there is negligible sediment input from terrestrial sources and stratification is rare.

The second compartment (2) is the middle estuary consisting of large areas of tidal flats, formed by the re-inundation of previously reclaimed land. Some small patches of saltmarsh are also present. The large fetch of the tidal flats means that this region is often subjected to considerable wave action in the prevailing southwesterly winds. Tidal forces are also moderate in this region, due to the wetting and drying of the mudflats.

The third compartment (3) is the channelised region extending to the mouth of the estuary. This region is highly constrained due to the presence of seawalls resulting in strong tidal currents, which often exceed 2 ms^{-1} at the mouth. The narrow cross-section also means that wave action is minimal in this compartment.

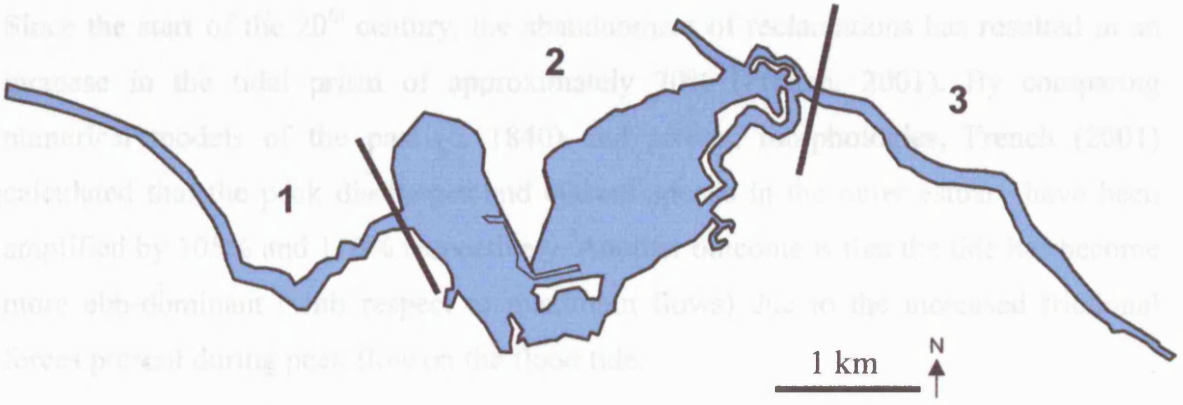

Figure 2.3 – The three geomorphological compartments defined by French *et al* (2004). 1 = upper estuary (low energy environment), 2 = mid-estuary (predominantly mudflats with moderate tidal current speeds and wind induced wave stresses), 3 = lower estuary (constrained environment with strong tidal flow).

Together, these three units provide a framework with which to derive a conceptual model of the estuarine form and function. In terms of the sediment transport processes, key elements of this model (French & Burningham, 2003) include:

- A morphology which is substantially inherited and bears the imprint of past dredging and reclamation, followed by abandonment of mid-estuary reclamations. The remaining flood defences and resistant muddy bottom sediments constrain the potential for morphodynamic adjustment. Accordingly, the morphology exerts a strong control on hydrodynamics.
- A strongly ebb-dominated tidal regime within the middle and outer estuary and weak flood dominance in the inner estuary.
- A delicate balance between sedimentation and sediment import under the influence of tidal currents, and re-suspension and sediment export under intermittent high wind-stress events.

2.3.2 Emergent issues

Since the start of the 20th century, the abandonment of reclamations has resulted in an increase in the tidal prism of approximately 70% (French, 2001). By comparing numerical models of the past (c. 1840) and present morphologies, French (2001) calculated that the peak discharges and current speeds in the outer estuary have been amplified by 105% and 110% respectively. Another outcome is that the tide has become more ebb-dominant (with respect to maximum flows) due to the increased frictional forces present during peak flow on the flood tide.

The increased erosional capacity of the tide towards the mouth (Unit 3) has been both beneficial and detrimental to the management of the estuary. For instance, there has been a reduction in the need for maintenance dredging of the harbour, which is currently used by leisure craft and local fishermen (recent improvements were made to the harbour in 1980 and 1991, highlighting its success as a local facility). However, the increased tidal forces in the outer estuary have led to erosion of the seawalls at several locations. The combination of a constrained channel and high discharge has led to the formation of a central (partly incised) thread of high intensity flow, which meanders at a shorter wavelength than the older fixed channel, resulting in several 'pressure-points'

along the channel margins (French, 2001). Consequently, steel pilings have been put in place at a number of locations, notably at Reydon Quay, where the saltmarsh fringe has been completely lost.

The development of a sediment transport model may help in the management of these issues by providing a quantitative understanding of the linkages between the hydrodynamics on the estuarine geomorphology.

2.4 Field measurements

The conceptual model of the Blyth estuary provides an understanding of the spatial distribution of hydrodynamic conditions that control the sediment dynamics. It can therefore be used as a basis for planning the field data collection methods and locations. In particular, the combination of a constrained outer estuary with a wind influenced middle estuary provides an excellent opportunity for measuring sediment transport fluxes with minimal field instrumentation. Sediment that is re-suspended and advected from the mudflats (Unit 2) is effectively funnelled into the main channel (Unit 3) where it is mixed due to the high levels of turbulence. Similarly, sediment entering the estuary must be carried through the same location. Therefore, a data collection point along the outer estuary should be indicative of sediment movement as a whole. With this in mind, the chosen location for deployment of suspended sediment concentration and particle size instrumentation was situated at Reydon (Figure 2.4). This location also benefits from being relatively secluded, yet easily accessible.

Field data were collected for both a spring and neap tide in the Blyth estuary with a variety of instrumentation. These data have been collected as part of an ongoing investigation into the tidal and sedimentary processes within the estuary between 2001 and 2003. Neap tide data were collected between 26th and 27th September 2001. During this field campaign, the rising tide of the first semidiurnal tidal cycle was monitored between low and high water. Data collection was then halted during the night until the ebb of the consecutive tidal cycle. Spring tide data were collected between 19th and 20th October 2001. In this case, a complete 12 hour tidal cycle was monitored in a single period.

In both of the field experiments, an RD Instruments Workhorse Sentinel 1200kHz Acoustic Doppler Current Profiler (ADCP) with integral pressure, tilt and compass sensors was placed in the middle of the main channel near Reydon (Figure 2.4). The water depth at this point is between 3 and 6 m during spring tides. *In situ* particle size profiles were recorded simultaneously with the ADCP measurements from a 4 m inflatable dinghy using the new imaging system described in this thesis (Chapter 4).

An automatic weather station was already installed close to the Reydon (Figure 2.7) as part of the Coastal & Estuarine Research Units ongoing field monitoring of the Blyth estuary. This consisted of sensors for measuring wind speed and direction at a 15 minute sample interval over a 1 minute averaging burst. Data have subsequently been recorded for the period between 18/6/2001 to 6/5/2002.

A tide gauge, consisting of an atmospherically corrected Druck pressure sensor (10 m range) connected to a Technolog self-contained datalogger, was installed within 100 m of the ADCP at the Reydon sluice gate (Figure 2.4). Depth data were recorded at 15 minute intervals and levelled to Ordnance Datum (OD) by reference to a known benchmark level on the sluice gate (CERU data archives). The ADCP pressure sensor data were also levelled in this way. For the parameterisation of the hydrodynamic model of the estuary, it was necessary to obtain a record of the tidal elevations at the mouth. However, the installation of a pressure sensor at this location was not feasible for two reasons. First, the harbour mouth is heavily used by fishing vessels, leisure craft and the local lifeboat, which poses a problem with respect to instrument loss or damage. Second, it is a popular tourist location and open to the public, which introduces security risks (a sensor was removed during a previous field deployment from this location). Therefore, for modelling requirements, it was decided to use predicted tidal levels.

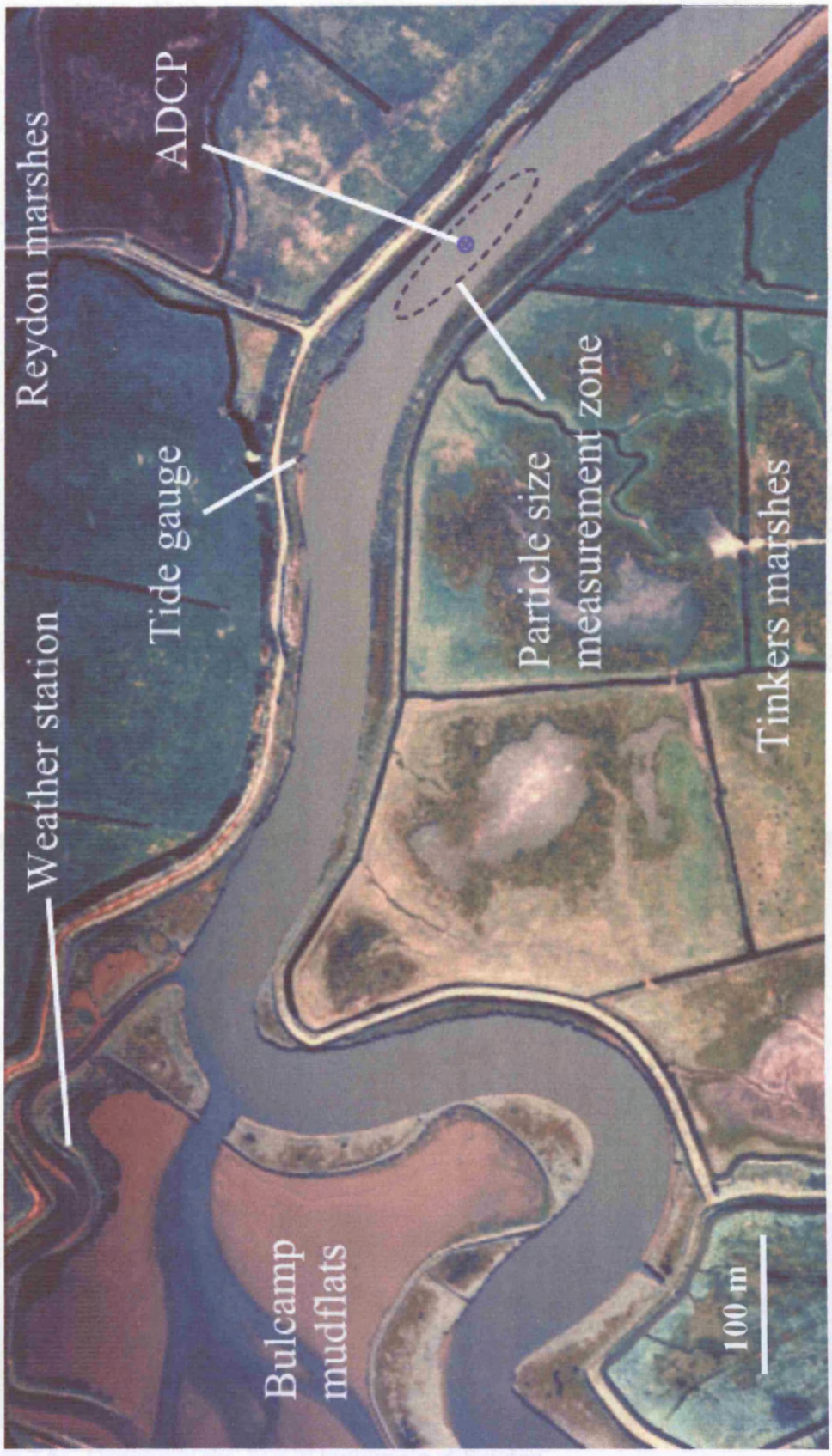

Figure 2.4 – The field data collection site near Reydon showing instrument locations.

Figure 2.5 – The ADCP bottom rig (with transmissometer and water sample hose)

Figure 2.6 – Deploying the ADCP bottom rig at Reydon.

Figure 2.7 – Weather station located at the northern end of the Bulcamp tidal flats

2.5 Modelling

2.5.1 Choice of modelling software

A depth-averaged hydrodynamic model of the Blyth estuary already exists (French, 2001), which provides the basis for the development of a sediment transport model. This model has been implemented using the TELEMAC-2D software, a full description of which is given by Hervouet & van Haren (1996). Although there are numerous other modelling systems available, the TELEMAC software was chosen for this project for three main reasons. First, it uses a *finite element* scheme based upon a non-uniform mesh that can be formed within irregular terrain features. This is preferable to a *finite difference* scheme, which consists of a uniform grid and is less suitable for modelling the morphology of complex estuaries (French & Clifford, 2000).

Second, TELEMAC-2D is relatively stable if there are large regions of wetting and drying. The user can select either of two options in the program to search for partially wet elements (Janin *et al*, 1997). The first option solves the equations everywhere in the domain, but applies corrections in the partially covered areas to prevent spurious values. This option is suited to river and tidal flows (Hervouet & van Haren, 1996) and is therefore used in this application. The second option, which is more suited to steep slope situations, applies a mask to the mesh, effectively removing any partially covered elements from the domain. The availability of this facility is essential for model stability. Other models, such as RMA2, provide similar options but have been found to be less stable in extreme cases such as the Blyth estuary, where the majority of the elements are intertidal (French & Clifford, 2000).

Third, a series of add-on modules are included in the software, which use the hydrodynamic results to compute variables such as sediment transport and water quality. This makes it suitable for this study. In addition, for programming of complex cases, the user is able to access most of the Fortran source code (other than the mathematical solvers), thus allowing development of customised algorithms to describe the processes.

2.5.2 Hydrodynamic equations

The TELEMAC-2D software code solves the non-conservative 2D Shallow Water, or *Saint-Venant*, equations. These equations (Equations 2.1 to 2.3) are derived by averaging the full 3D Reynold's averaged Navier-Stokes equations for turbulent flow over the water depth (Hervouet & van Haren, 1996), giving:

Continuity:

$$\frac{\partial h}{\partial t} + \vec{u}.\overrightarrow{\mathbf{grad}}(h) + h\,\mathrm{div}(u) = 0 \qquad (2.1)$$

Momentum:

$$\frac{\partial u}{\partial t} + \vec{u}.\overrightarrow{\mathbf{grad}}(u) = -g\frac{\partial Z}{\partial x} + F_x + \frac{1}{h}\mathrm{div}\left(h\nu_T\,\overrightarrow{\mathbf{grad}}\,u\right) \qquad (2.2)$$

$$\frac{\partial v}{\partial t} + \vec{u}.\overrightarrow{\mathbf{grad}}(v) = -g\frac{\partial Z}{\partial y} + F_y + \frac{1}{h}\mathrm{div}\left(h\nu_T\,\overrightarrow{\mathbf{grad}}\,v\right) \qquad (2.3)$$

where:

u, v = flow velocity components in x and y directions (m s^{-1})
h = water depth (m)
t = time (s)
Z = free surface elevation (m)
F_x, F_y = source terms to account for boundary friction
ν_T = eddy viscosity
g = force of gravity

For solving the advection terms of the hydrodynamic computations (i.e. those terms with the form $\vec{u}.\overrightarrow{\mathbf{grad}}\,(f)$, with f equal to h, u or v), a combination of numerical methods is used (Hervouet & van Haren, 1996). In terms of model stability, an important feature of TELEMAC-2D is that it uses an implicit method for solving these equations.

The F_x and F_y source terms in the momentum equations (Equations 2.2 and 2.3) represent the force induced by boundary friction in the x- and y-directions. As discussed in Section 1.2.2, friction can be parameterised using the Manning, Strickler, Chézy or Nikuradse coefficients. The most commonly used form in Britain and the United States is that of Manning (TELEMAC-2D Manual). In terms of the Manning friction coefficient (n), the frictional force components (F_x and F_y) are defined as:

x-direction:

$$F_x = -\frac{1}{\cos\theta}\frac{g}{h^{4/3}n^2}u\sqrt{u^2+v^2} \tag{2.4}$$

y-direction:

$$F_y = -\frac{1}{\cos\theta}\frac{g}{h^{4/3}n^2}v\sqrt{u^2+v^2} \tag{2.5}$$

where:

θ = bottom slope

n = Manning coefficent

2.5.3 Sediment transport equations

The sediment transport module for TELEMAC-2D is SUBIEF-2D (version 3.2). Velocity and depth information from the TELEMAC-2D hydrodynamic model is post-processed by SUBIEF-2D to calculate sediment erosion, flux and deposition, using the following equation:

$$\frac{\partial C}{\partial t} + \vec{u}.\overrightarrow{\mathbf{grad}}\,C = \mathrm{div}\left(\vec{K}.\overrightarrow{\mathbf{grad}}\,C\right) + \frac{Q_e - Q_d}{h} + S \tag{2.6}$$

where:

C = suspended concentration (kg m^{-3})

t = time (s)

$\vec{u}$ = velocity components in x and y direction (m s^{-1})

K = dispersion coefficients in x and y direction

Q_e, Q_d = flux of sediment for erosion and deposition (kg m^{-2} s^{-1})

h = water height (m)

S = sediment input from sources (e.g. boundary)

2.5.4 Model dimensionality

Although a 3D version of TELEMAC is available, tests have shown that the total duration for each computation is excessively long for such a large-scale, high-resolution problem (even when using modern processors). In addition, the absence of any vertical stratification in the Blyth estuary, combined with large areas of shallow intertidal mudflats, means that the problem can be modelled with a reasonable degree of confidence using a vertically averaged 2D model (Telemac-2D). This greatly reduces the processing time, as well as the size and complexity of the results files, thus reducing the time for development of the model. The spatial complexity of the Blyth estuary effectively precludes the use of a 1D model.

As described in Section 1.3, issues may arise when using a 2D model for the transport of cohesive sediment due to changes in the vertical distribution of sediment in the water column. The combined processes of flocculation and hindered settling lead to the formation of a layer of high sediment concentration near the bed, resulting in buoyancy effects on the flow and a reduction in turbulence. However, this only becomes important at very high concentrations of suspended sediment (>500mgl^{-1}). Concentrations in the main channel of the Blyth rarely exceed 200mgl^{-1} and are generally less than 100mgl^{-1} (CE French *et al*, 2000). No observations of fluid mud have been reported. Occasionally, however, concentrations on the mudflats may exceed 1gl^{-1} during storms (CERU data archives), but this is restricted to shallower regions where vertical structuring is likely to be minimal and less important in terms of mass transport.

3. Suspended Particle Sizing Techniques

There are numerous methods available for particle size analysis and a full account is beyond the scope of this study. Therefore, this discussion is limited to the following techniques, which have found application to the analysis of suspended sediments in estuarine and coastal waters:

- Coulter Counters
- Field settling tubes
- Laser diffractometers
- Time-of-transition laser systems
- Multi-frequency acoustic backscatter systems
- Model-dependent inversion techniques
- Imaging systems

3.1 Coulter Counters

Probably the first automated method of determining the size distribution of suspended particles in the laboratory was the Coulter Counter (Figure 3.1a), named after Wallace Coulter who discovered the principle in 1948. This instrument, which is still in widespread use, works by measuring changes in electrical impedance as particles of different volumes are sucked through a narrow gap between two electrodes (McCave & Jarvis, 1973; Griffiths *et al*, 1998).

This method has the advantage that it requires relatively small samples of test suspension. However, due to clogging of the narrow apertures it cannot cope with high concentrations, so naturally high sediment concentrations usually have to be diluted. De-aggregating compounds (e.g. Calgon) are often used to prevent flocculation of the particles, thus altering the natural size distribution. In addition, if a large particle size range is to be measured, the gap width needs to be adjusted since a particle size range ratio of only 30:1 can be obtained at each setting (Barth, 1984).

Apart from these issues, the main problem with this method of particle sizing is that it is an *in vitro* (i.e. laboratory based) instrument and therefore does not give a true measurement of the *in situ* size distribution. The fragile nature of estuarine flocs means that the particle size distribution is altered during by sampling, transportation, storage and measurement (Swift *et al*, 1972; Gibbs, 1982). This helps to answer why Sheldon (1968), in an early study of the Crouch estuary (Essex, UK) found it "difficult to explain" why, at slack water, particles appeared to settle out from the surface water more quickly than would be expected for their size during slack water. In this study, the particle size was measured in the laboratory using a Coulter Counter, which meant that any large flocs would have been broken up resulting in an underestimation of the particle settling velocity. Figure 3.1b shows the discrepancy between Coulter Counter size measurements, compared to a size distribution determined using an underwater camera system. There is an order of magnitude discrepancy between the two sets of results, presumably due to floc break-up. This highlights the importance of *in situ* measurements of particle size.

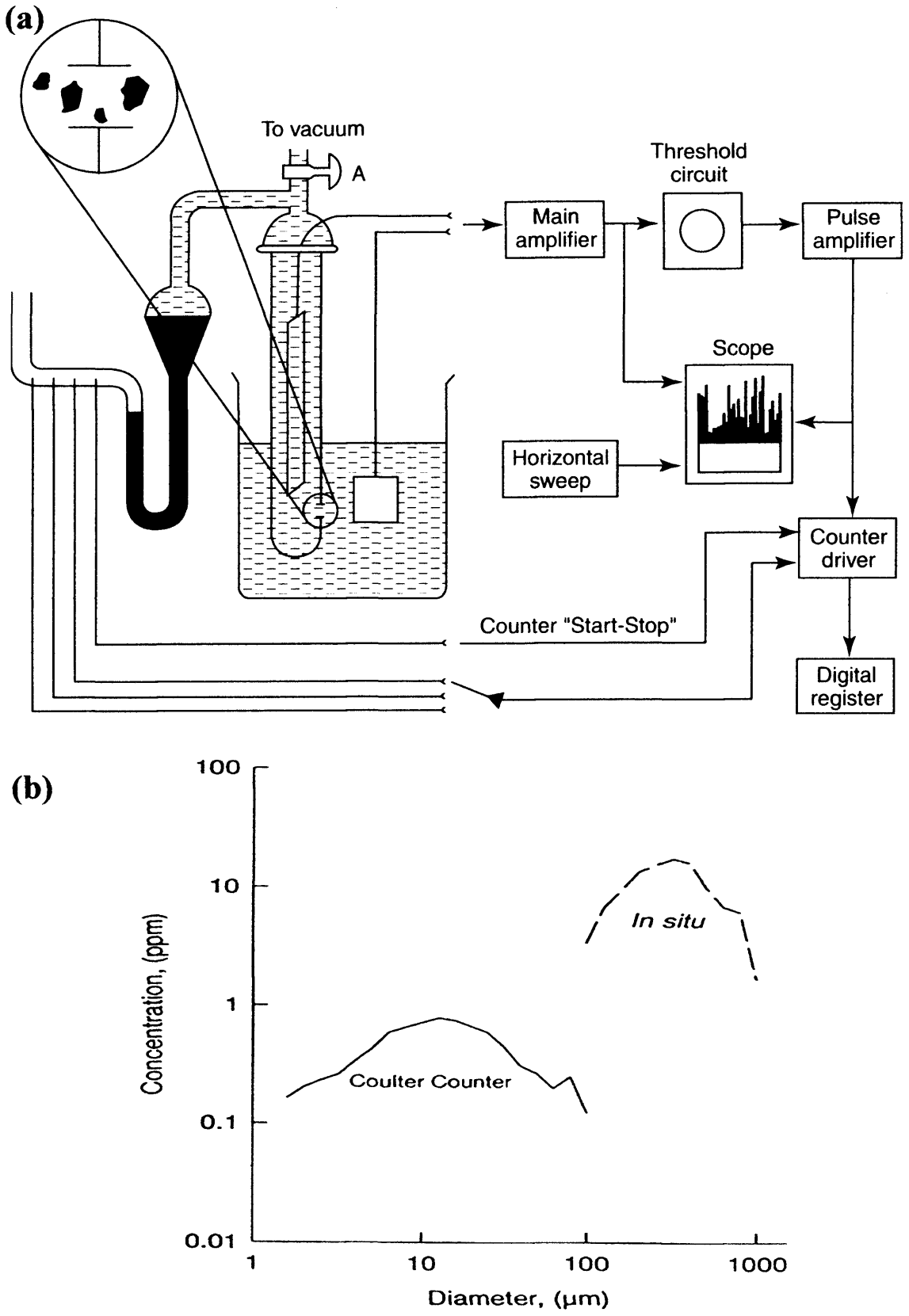

Figure 3.1 - (a) Schematic of the Coulter Counter (redrawn from Barth, 1984), (b) Difference between size distribution measurements by Coulter Counter and the In Situ Benthos Plankton Camera (from Milligan, 1996).

3.2 Field Settling Tubes

Another method of particle sizing relies on a direct implementation of Stokes' Law (given previously in Equation 1.13). Since particle diameter is directly proportional to the settling velocity of a particle in suspension (assuming spherical particles of equal density) the size distribution may be obtained by carrying out simple settling experiments. The *field settling tube* was originally called the Owen Tube after the inventor (Owen, 1971, 1976) who adapted the laboratory based *pipette* method (Jennings *et al*, 1922; Swift *et al*, 1972) for field deployment.

The Owen Tube (Figure 3.2a) consists of a 5 cm internal diameter Perspex tube with a length of 100 cm. To obtain a sample the tube is lowered horizontally into the estuary to the required depth. A water sample is then captured by mechanically shutting off both ends of the tube by means of a messenger weight, immediately after which the device is hauled back to the surface as rapidly as possible. After retrieval, settling of the captured suspended sediment is initiated by rotating the tube 90 degrees to make it vertical. After waiting for a few seconds for turbulence to diminish, a stopwatch is started. Water samples are then drawn from the bottom of the tube at measured time intervals after the start of settling. These samples are then filtered and the residue dried and weighed to give the mass concentration of sediment at various sample times. The size of the particles in each fraction can then be determined from the time taken to settle using Stokes' Law. Because of its simplicity, the Owen Tube has been used extensively in field research projects as a quasi *in situ* method for determining particle size distributions. It has several limitations, however:

- Some of the particles may have already settled in the time taken to haul the settling tube to the surface, therefore giving a size distribution which is artificially void of larger particles (Wolfstein, 1996).
- Turbulence introduced while sampling may induce floc break-up (Jones & Jago, 1996) thus reducing the settling velocity. Conversely, by artificially removing the flow conditions, the fine particles may rapidly form flocs which will sink more rapidly (Hawley, 1982). Both problems result in a false size distribution measurement.

- The time taken to wait for turbulence to diminish after rotating the tube to the vertical varies between users, and problems therefore occur when trying to compare results from different authors (Dyer *et al*, 1996).
- Temperature gradients introduced once the tube is at the surface may induce water circulation due to convection (Jones & Jago, 1996).
- Stokes' Law is only valid for solid spheres and therefore size determination is not accurate when applied to cohesive sediments, which tend to form fractal shaped flocs, which have been shown to have very different settling characteristics to solid spheres (Johnson *et al*, 1996).
- Observations have shown that large particles may drag smaller particles down behind them (*differential settling*), thus giving a greater apparent distribution in the larger size range (Puls *et al*, 1988, Bhagat, 1996).
- The optimum length and diameter of the tube is dependent upon the concentration of sediment in the water. Estuaries tend to have higher concentrations than the open ocean, and therefore require smaller tubes in order to prevent clogging (Jones & Jago, 1996). This also complicates the intercomparison of results from different studies.

Numerous variants of the original Owen Tube have subsequently been designed in an attempt to reduce some of the problems associated with its use (Zaneveld *et al*, 1982; Bartz *et al*, 1985; Van Rijn & Nienhuis, 1985; Pejrup, 1988; Kineke *et al*, 1989; Van Leussen & Cornelisse, 1993; Van Leussen, 1996; Fennessy *et al*, 1994; Jones & Jago, 1996; Murray *et al*, 1996; Puls & Kühl, 1996). As an example, Figure 3.2b shows a typical version called the QUISSET tube (Quasi-In Situ Settling Tube) developed by Jones & Jago (1996). In an attempt to prevent floc break-up this system uses a Perspex tube which slides over a piston in order to trap a portion of undisturbed water. A thermal jacket is also placed around the system when it reaches the water surface to prevent thermally induced circulation.

Figure 3.2c shows another version called the FIPIWITU (Field Pipette Withdrawal Tube) developed by Delft Hydraulics (Van Rijn & Nienhuis, 1985). Although this system looks very different to the Owen and QUISSET tubes, it does in fact perform the same task. The only major difference is that the other two tubes use *bottom withdrawal* which means the tap is located at the very base of the tube, while the FIPIWITU uses

pipette withdrawal which means the water samples are siphoned off at a fixed height above the base of the tube. The latter arrangement is thought to be less susceptible to clogging (Dyer *et al*, 1996; Puls & Kühl, 1996).

A more exotic version of a settling tube is the ROST instrument (Remote Optical Settling Tube) developed by Zaneveld *et al* (1982). This was designed in order to avoid having to haul the sample to the surface before settling measurements could be carried out, thereby reducing the problem of flocculation of the particles while lifting and preventing thermal circulation within the tube. As can be seen in Figure 3.3a, this system is basically a settling tube with a transmissometer situated near the base. The two ends of the tube can be closed remotely, thus allowing measurements to be taken of optical beam attenuation while the particles settle. The beam attenuation values are then converted into mass concentrations at timed intervals, allowing calculation of the particle size distribution. Similar systems have also been designed by Kineke *et al* (1989) and Cambridge University (Murray *et al*, 1996) shown in Figure 3.3b,c that use optical backscatter rather than attenuation to determine the instantaneous concentration.

Clearly, these optical settling tubes rely heavily upon theory to determine the particle size distribution. They depend upon both Stokes' Law for calculation of settling velocity rates and Mie's theory of light scattering by different sized particles to derive concentrations (Swithenbank *et al*, 1977; Van der Hulst, 1989). Both theories assume that the particles are spherical.

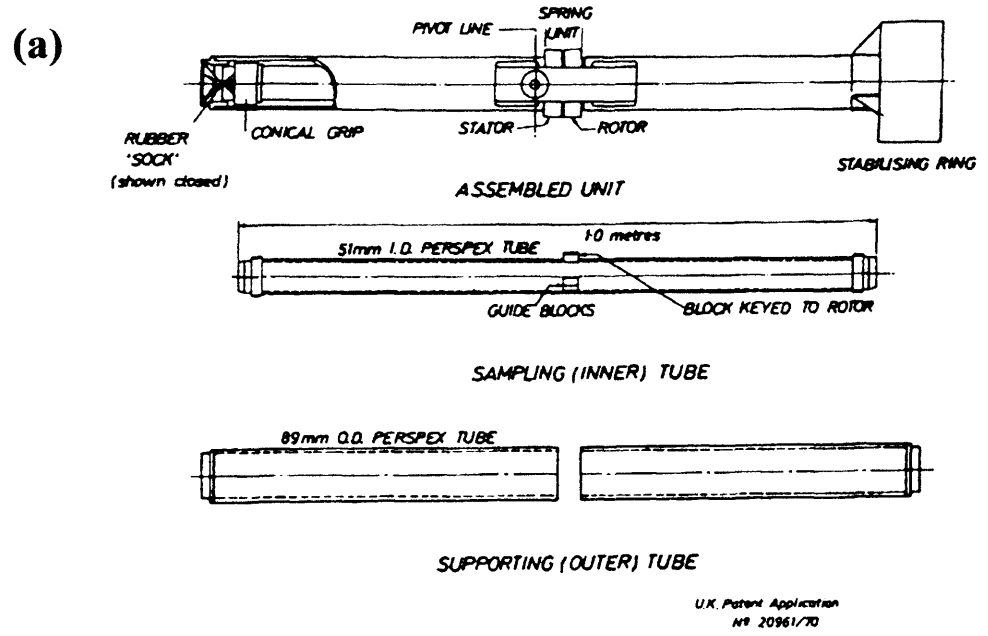

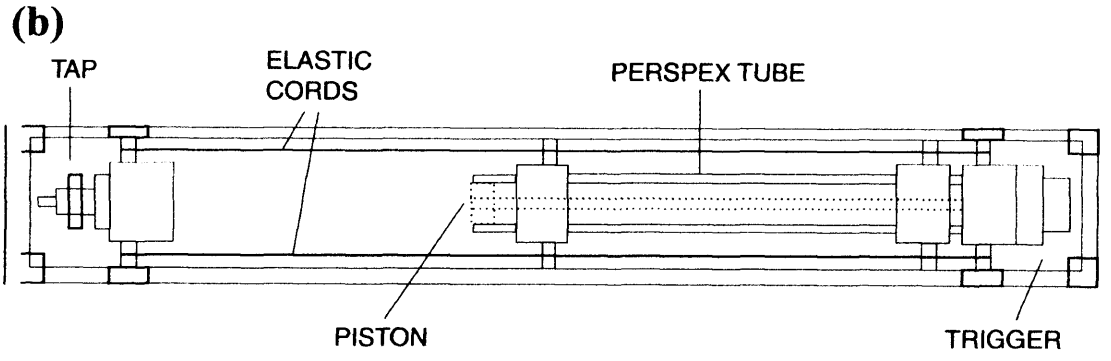

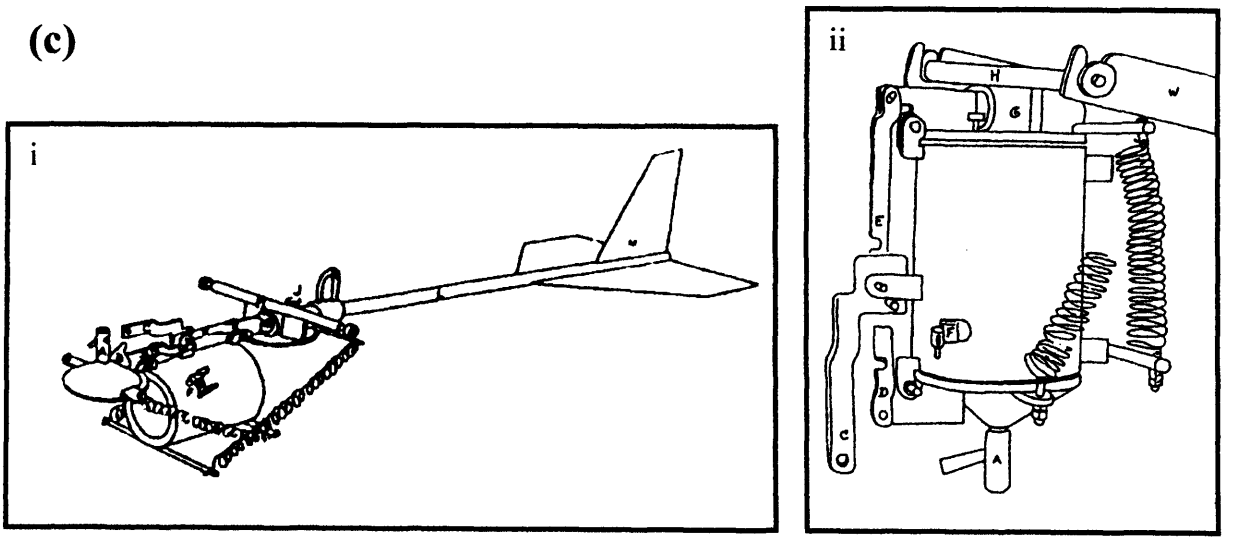

Figure 3.2 – Field settling tubes. (a) The Owen Tube (Owen, 1971); (b) The QUISSET settling tube (redrawn from Jones & Jago, 1996); (c) The FIPIWITU (i) lowering and sampling position, (ii) raising position (Cornelisse, 1996).

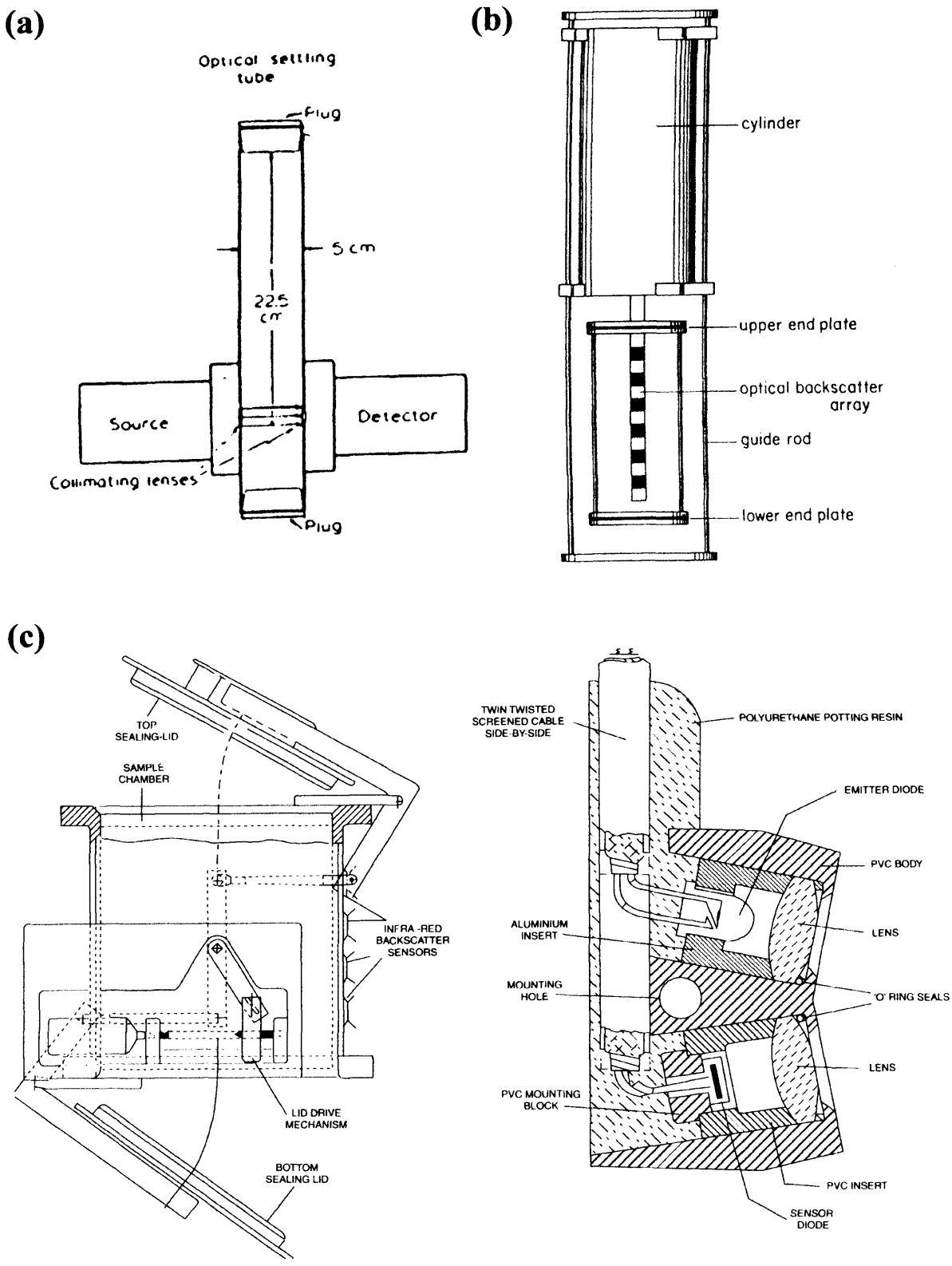

Figure 3.3 - Optical field settling tubes. (a) ROST (Zaneveld *et al*, 1982); (b) Backscatter settling tube designed by Kineke *et al* (1989); (c) In situ settling box, Cambridge University, with detail of custom-made backscatter sensor (redrawn from Murray *et al*, 1996).

3.3 Laser Diffractometers

Examples of the Laser Diffractometer are the Malvern Multisizer (Swithenbank *et al*, 1977), shown in Figure 3.4a, and the Coulter LS-100 (Loizeau *et al*, 1994; Beuselinck *et al*, 1998). These instruments have been available since the mid-1970s and they are now standard pieces of equipment in many sedimentological laboratories. In essence, a laser diffractometer is an advanced version of a transmissometer. Instead of an LED, a laser is used to produce a coherent, parallel beam of light (Figure 3.4b). The diffraction pattern is measured using a detector array with logarithmically spaced rings of light sensitive detectors (Figure 3.4c). This detector measures the angular intensity of the light scattered at small angles in the forward direction by the particles. From this pattern (known as the Airy Disc), the particle size can be estimated using Mie scattering theory (Swithenbank *et al*, 1977). At the centre of the detector the intensity of the unscattered laser beam is measured in the same way as a transmissometer, thus allowing calculation of sediment concentration from the beam attenuation.

As a laboratory instrument this method is advantageous because it produces an instant volume-based measurement of particle size. By using several differently powered Fourier Transform lenses it is possible to measure particle size over a range of 0.05μm to 1mm. Bale & Morris (1987) attempted to develop this instrument for *in situ* sizing in estuaries by encasing a modified Malvern particle sizer into a waterproof box (Figure 3.5a). Due to the large power consumption of the He/Ne laser, bulky size and the limited size range of any single lens, this instrument proved problematic. However, Agrawal & Pottsmith (1994) describe a commercially available *in situ* laser diffraction instrument that uses a low power diode laser. This is called the Laser In Situ Scattering and Transmissometry (LISST; Figure 3.5b). The latest version of this instrument (LISST-ST) even has the option of an additional *in situ* settling column for determining the particle settling velocity, although this can only be used when the instrument is mounted on a frame on the estuary bed to reduce ambient water motion (Agrawal & Pottsmith, 2000). Since its release, the LISST instrument has been used with varying degrees of success in a variety of applications for particle sizing and sediment concentration measurement (Agrawal & Pottsmith, 1994; Lynch *et al*, 1994; Agrawal & Pottsmith, 2000; Mikkelsen & Pejrup, 2000; Gartner *et al*, 2001; Fugate & Friedrichs, 2002; Mikkelsen, 2002)

In these experiments it was shown that *in situ* laser diffractometers offer the possibility of obtaining long term direct measurements of particle size and concentration, without the need for calibration. However, there are several problems with adapting the laser diffraction technique for use as a field instrument.

- He/Ne lasers are large and inefficient so a large power supply is needed. In the LISST instrument, a laser diode is used. This greatly reduces power consumption and the size of the instrument, but larger errors are introduced due to shorter coherence length and asphericity of the beam.
- Although the LISST instrument has a stated size measurement range of either 0.25 to 250 μm or 0.5 to 500 μm, it is known that estuarine particles may flocculate to sizes larger than 1000 μm (Eisma, 1991). Laboratory experiments also suggest that the accuracy of the instrument decreases towards the upper limit of the size range due to the logarithmically spaced rings of the detector (Gartner *et al*, 2001; Traykovski *et al*, 1999).
- Laser diffraction instruments are also affected by the concentration of the suspended material due to multiple scattering at higher particle numbers. The stated working limit for the LISST instrument is that 30% of the laser beam must be transmitted through the suspension. This is equivalent to concentrations of 150 or 500 mgl^{-1} for particle size ranges of 5 to 25 μm or 26 to 65 μm respectively (Traykovski *et al*, 1999).
- Cost is also a factor with this type of instrument due to the expensive optics and detector design. The LISST-ST shown in Figure 3.5b currently costs approximately £40K (Sequoia Scientific Inc., pers. comm.).
- Laser diffractometers are based on the theory of light scattering caused by spherical particles, whereas cohesive estuarine sediments generally form fractal shaped flocs (Agrawal & Pottsmith, 2000).

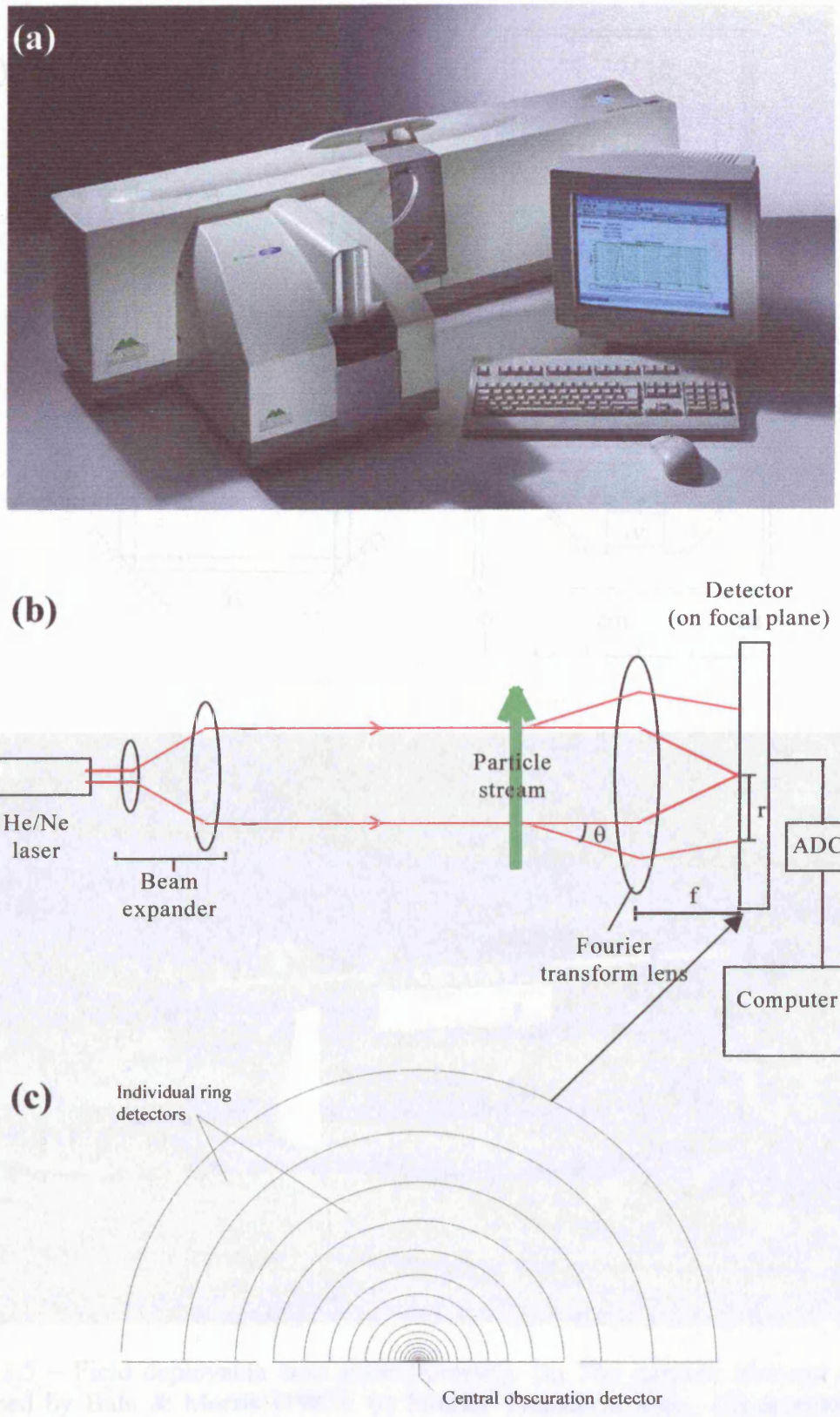

Figure 3.4 – (a) The Malvern laser diffractometer (http://www.malvern.co.uk). (b) Schematic diagram of laser diffraction apparatus (from Swithenbank *et al*, 1977). (c) Detail of specialised annular detector used in laser diffractometers.

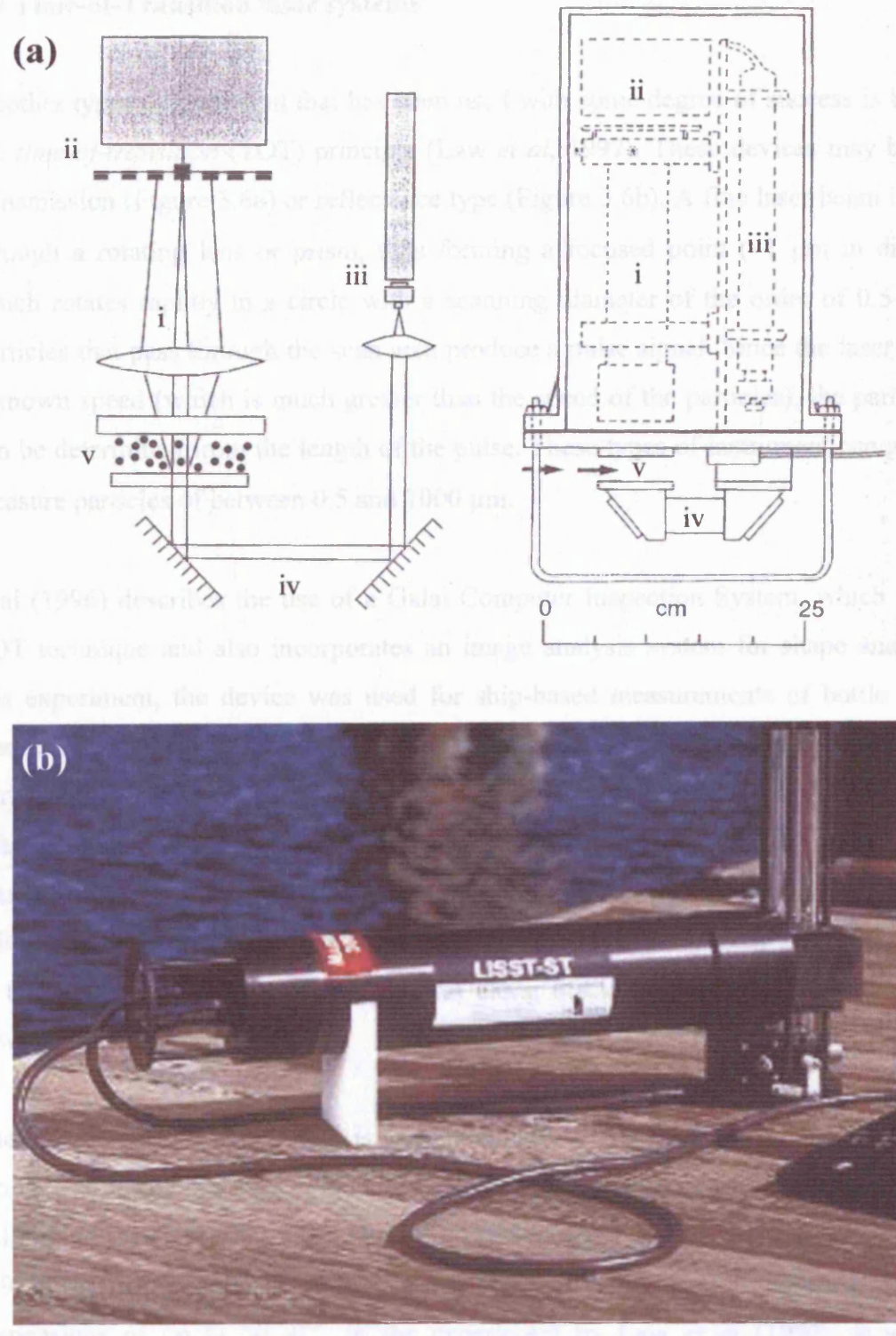

Figure 3.5 – Field deployable laser diffractometers. (a) The adapted Malvern particle sizer used by Bale & Morris (1987): (i) Fourier Transform lens, (ii) detector, (iii) He/Ne laser, (iv) light guide, (v) sample volume. (b) LISST-ST with automated settling column (from Sequoia Scientific Inc.; http://www.sequoiasci.com).

3.4 Time-of-Transition laser systems

Another type of instrument that has been used with some degree of success is based on the *time-of-transition* (TOT) principle (Law *et al*, 1997). These devices may be of the transmission (Figure 3.6a) or reflectance type (Figure 3.6b). A fine laser beam is passed through a rotating lens or prism, thus forming a focused point (~1 μm in diameter), which rotates rapidly in a circle with a scanning diameter of the order of 0.5-10 mm. Particles that pass through the scan area produce a pulse signal. Since the laser scans at a known speed (which is much greater than the speed of the particles), the particle size can be determined from the length of the pulse. These types of instrument can generally measure particles of between 0.5 and 1000 μm.

Tsai (1996) describes the use of a Galai Computer Inspection System, which uses the TOT technique and also incorporates an image analysis system for shape analysis. In this experiment, the device was used for ship-based measurements of bottle samples from the continental shelf sea off western Taiwan. Reproducibility was poor, which was attributed to the fact that this is a point measurement system, and the samples were very dilute. Tsai also concluded that the process of obtaining the water samples, and placing them inside cuvettes, disrupted the flocs. For these reasons, the Galai system is better suited to sizing of non-cohesive sediments, and has been successfully used, for example, in the analysis of sand particle dispersal along black sand beaches in New Zealand (Swales *et al*, 2001).

The Par-tec 100 (Lasentec Inc.) is a commercially available, laser reflectance, particle-sizing instrument that was originally designed for process control in the grinding and milling industries, but has been adapted for *in situ* underwater measurements (Law *et al*, 1997). The main advantage of this system is that it can be used in highly concentrated suspensions of up to 50 gl^{-1}. In the experiment by Law *et al* (1997), it was used successfully to measure the flocculation process in the Humber Estuary, and showed that particle size varied by two orders of magnitude over a tidal cycle. During laboratory testing of the device, it was observed that the smaller size ranges were overestimated, whereas the larger sizes were underestimated. A simple calibration was used to empirically fix this problem, but this suggests that data from this instrument suffer from statistical errors due to the small point measurement area. Large particles, which tend to

be less frequent, will thus be under-observed. As with the Galai system, this type of device is not suited to the measurement of low particle concentrations (<10 mg/l), owing to the long averaging times required.

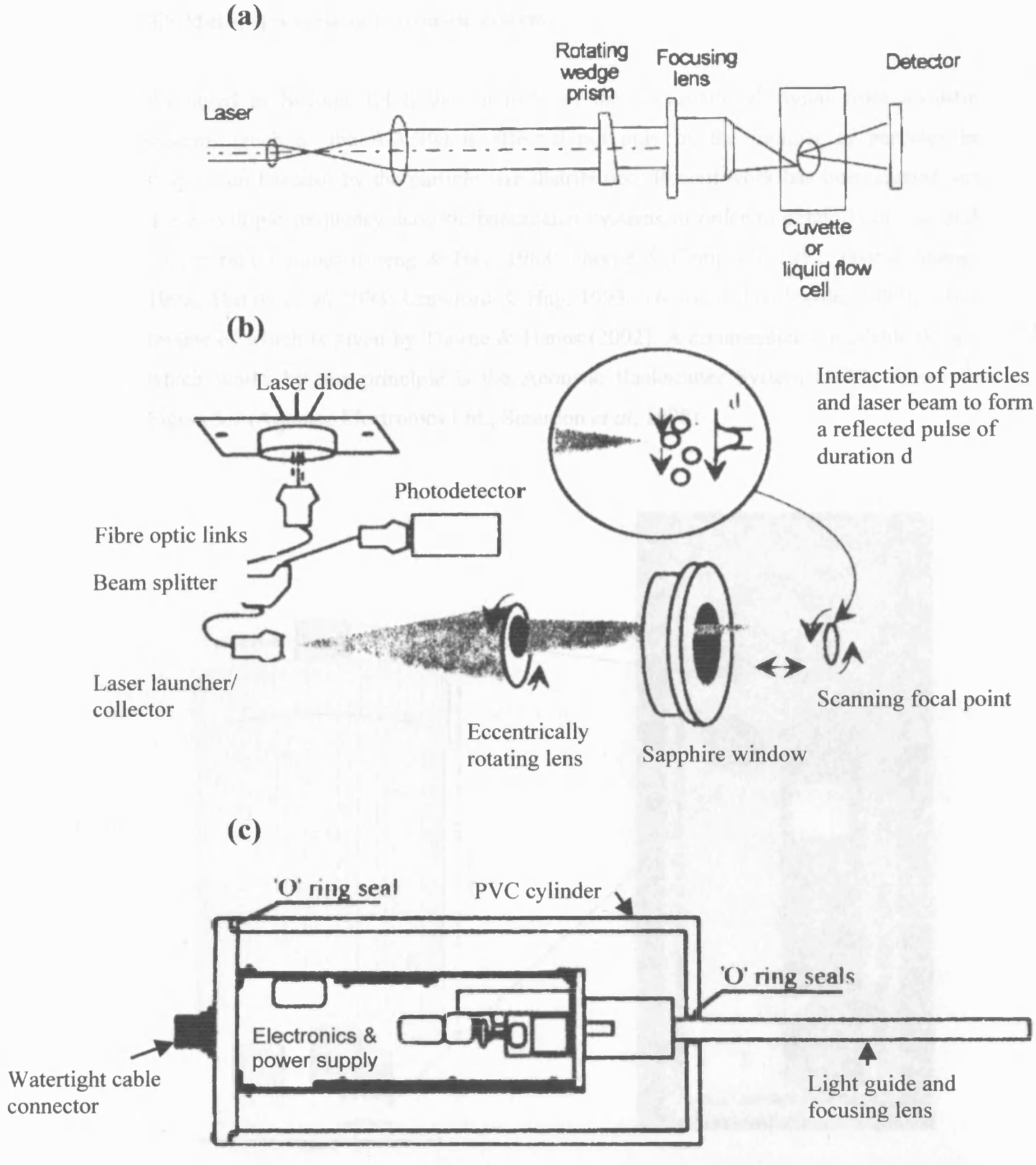

Figure 3.6 – Time-of-transition particle sizers: (a) Transmission type (Tsai, 1996), (b) Reflectance type (Law *et al*, 1997), (c) Adapted Par-tec 100 for *in situ* measurements (Law *et al*, 1997).

3.5 Multiple wavelength acoustic systems

As noted in Section 1.4.2, the intensity of the backscattered signal from acoustic systems (such as the ADCPs) is affected not only by the number of particles in suspension but also by the particle size distribution. Recent work has been carried out using multiple frequency acoustic backscatter systems in order to obtain both size and concentration values (Sheng & Hay, 1988; Thorne & Campbell, 1992; Hay & Sheng, 1992; Thorne *et al*, 1993; Crawford & Hay, 1993; Thorne & Hardcastle, 1997), a full review of which is given by Thorne & Hanes (2002). A commercially available device which works by this principle is the Acoustic Backscatter System (ABS) shown in Figure 3.7 (Aquatec Electronics Ltd.; Smerdon *et al*, 1998).

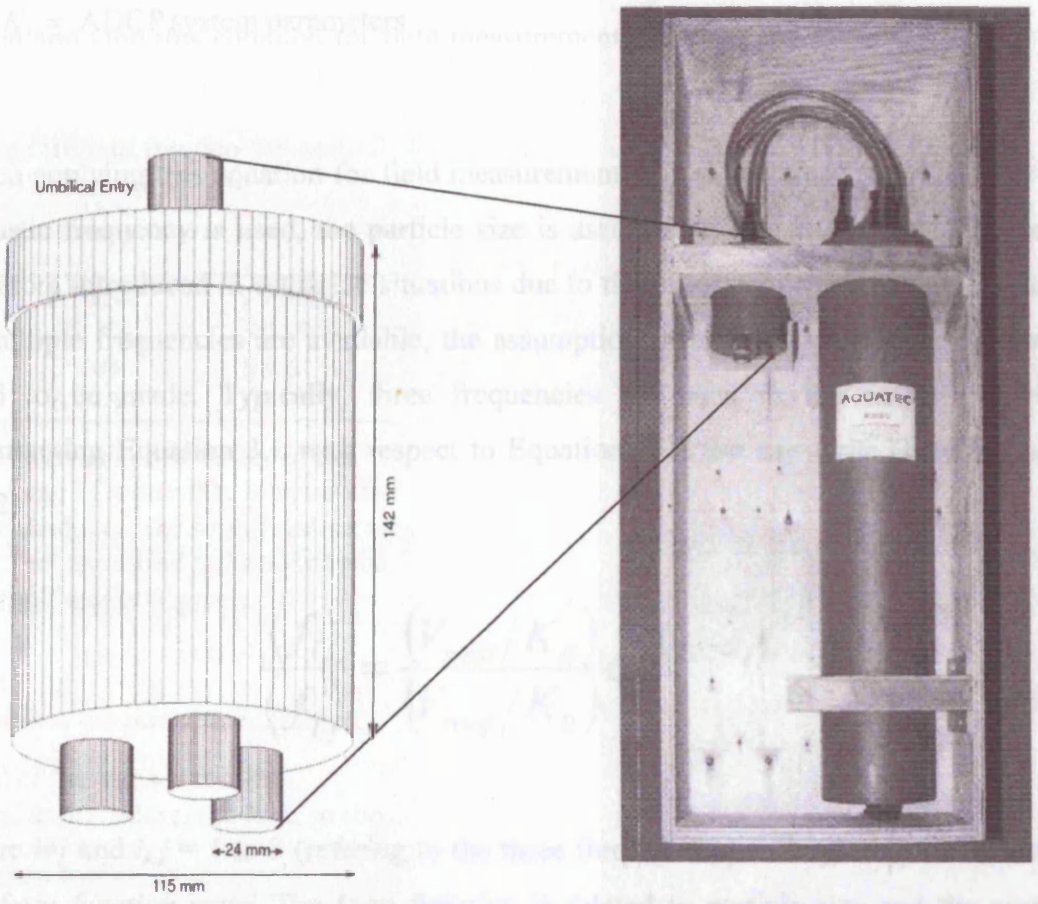

Figure 3.7 – The Aquatec multiple frequency Acoustic Backscatter System, with detail of the sensor head, showing the three transducers (Smerdon *et al*, 1998)

Particle sizing by acoustic methods can be explained using Equation 1.37, which is rewritten here in a slightly simplified form with the attenuation coefficients for water (α_w) and sediment (α_s) represented by one variable (α):

$$M_A(r) = \left\{ \frac{V_{rms} r}{K_s K_t} \right\}^2 e^{4r\alpha} \tag{3.1}$$

where :

$M_A(r)$ = suspended mass concentration at range r (kg m^{-3})

V_{rms} = recorded voltage from transceiver (V)

$\alpha = \alpha_w + \alpha_s$ = attenuation due to absorption by water and suspended sediment (m^{-1})

K_s = ADCP system parameters

K_t = ADCP system parameters

When applying this equation for field measurements of mass concentration, if only one acoustic frequency is used, the particle size is assumed to remain constant. Errors are therefore introduced in estuarine situations due to the process of flocculation. However, if multiple frequencies are available, the assumption of constant particle size does not need to be made. Typically, three frequencies are used in the range 1-5 MHz. Rearranging Equation 3.1 with respect to Equation 1.38 we can write (Hay & Sheng, 1992):

$$\frac{\langle f_i \rangle}{\langle f_j \rangle} = \frac{\left(V_{rmsi} / K_{ti} \right)}{\left(V_{rmsj} / K_{tj} \right)} e^{2r(\alpha_i - \alpha_j)} \tag{3.2}$$

where $i \neq j$ and i, j = 1 to 3 (refering to the three frequencies) and $\langle f_i \rangle / \langle f_j \rangle$ is known as the *form function ratio.* The form function is related to particle size and the acoustic frequency. Empirical relationships based on laboratory experiments using different sized particles have been derived in order to represent the relationship between size and form function (Sheng & Hay, 1988; Crawford & Hay, 1993; Thorne *et al*, 1993; Thorne & Hanes, 2002). One example of such an expression is given by Thorne & Hanes (2002), written as:

$$f = C_0 \left\{ \frac{k_f x^2}{1 + k_f x^2} \right\} \tag{3.3}$$

$$C_0 = 1.1\left\{1 - 0.25\exp\left[-((x-1.4)/0.5)^2\right]\right\}\left\{1 + 0.37\exp\left[-((x-2.8)/2.2)^2\right]\right\} \tag{3.4}$$

$$\chi = \frac{1.1(4/3)k_\alpha x^4}{\left[1 + 1.3x^2 + (4/3)k_\alpha x^4\right]} \tag{3.5}$$

where:

$k_f \approx 1.1$

$k_\alpha \approx 0.18$

$x \approx ka$

In Figure 3.8, the form function (f) calculated using Equation 3.3 plotted against ka, where k is the wavenumber ($=2\pi f/c$) and a is the particle diameter. By comparing the form function ratios for each of the three frequencies it is possible to estimate the mean particle diameter. For example, using frequencies of 1 MHz, 2.25 MHz and 5 MHz, Hay & Sheng (1992) were able to estimate particle sizes in the range 50-170 μm with an accuracy of 10-20%.

Despite providing reasonably accurate results, the main drawback with this approach is that the useable region of the form function is limited to a narrow range of values for ka. Hence, a wide range of acoustic frequencies are required. However, Figure 3.8 shows that for $ka>2$, the form function tends towards unity, whereas for very small values of ka, the form function tends towards zero, thus introducing errors into the calculation (Thorne & Hanes, 2002). For acoustic wavelengths, the main constraint for particle sizing is the lower size limit, which requires the use of higher frequencies. However, the higher acoustic frequencies are attenuated very rapidly in water and the maximum useable frequency is between 10-15 MHz, which may be used to measure particle sizes down to 25 μm (Lynch *et al*, 1994).

Particle concentration levels must also be high enough in order to calculate the mean size with reasonable accuracy. Furthermore, this method cannot distinguish the entire particle size distribution, and the results are therefore a function of the mean particle size. This means that it is only useful for distributions that are unimodal and Gaussian in shape and errors may be introduced if the distribution is multimodal. The system is also expensive. For example, the Aquatec ABS system costs ~£20k (Aquatec Electronics Ltd., pers. comms.).

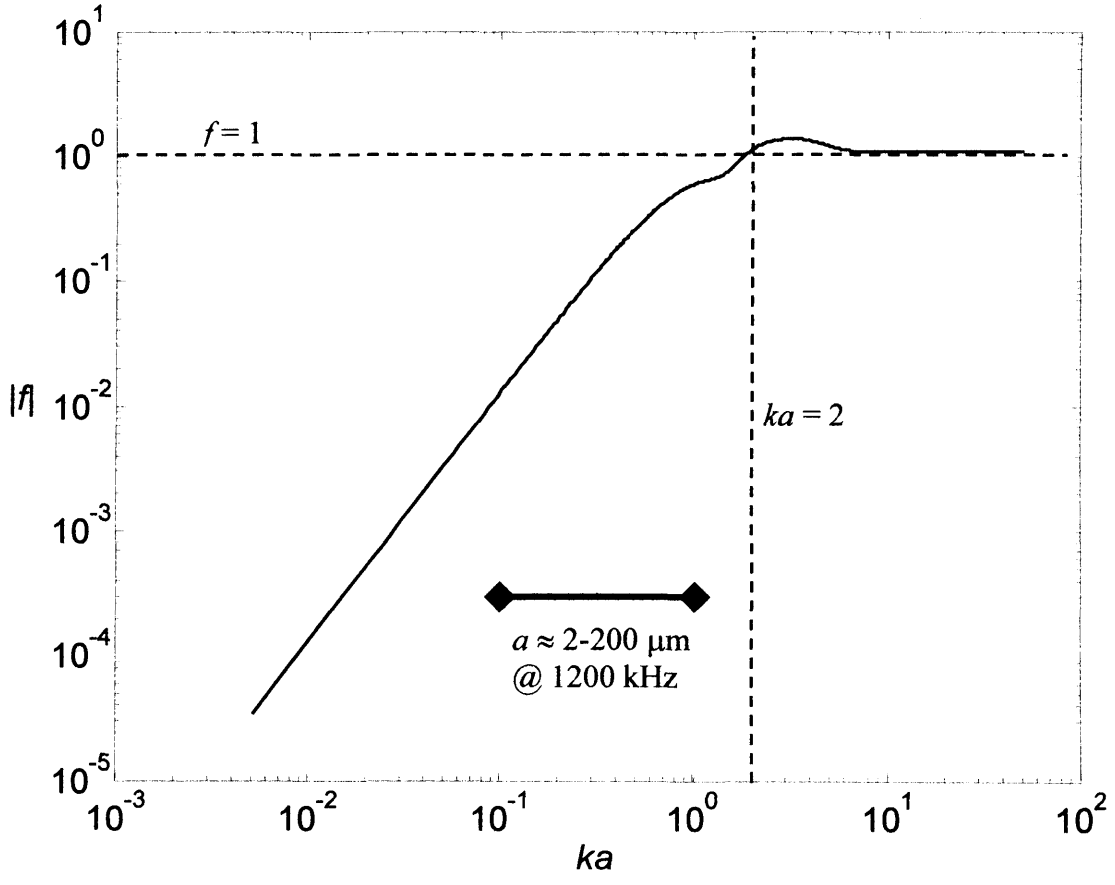

Figure 3.8 – Variation of the backscatter form function (f) with ka (k = wavenumber, a = particle radius) calculated using Equation 3.3.

3.6 Model-dependent inversion techniques

If it is assumed that the sediment concentration depth-profile follows a simple model, such as the Rouse profile (Equation 1.16), the mean particle size may be estimated from the measured concentration. Lynch & Agrawal (1991) describe this method as *model-dependent inversion*, and it is usually used as a simple way of determining the *in situ* settling velocity (e.g. Clarke & Elliott, 1998; Ciffroy *et al*, 2000; van der Ham & Winterwerp, 2001). However, by applying Stokes' Law, an equivalent particle size may also be obtained (Lynch & Agrawal, 1991; Lynch *et al*, 1994).

In order to explain how this method is used, it is necessary to recall the Rouse approximation for sediment concentration profiles, given in Equation 1.16. Figure 3.9 shows the calculated sediment concentration gradient for several different settling velocities, with the reference concentration (C_a) and the shear velocity (u_*) set at constant values of 100 mgl^{-1} and 0.01 ms^{-1}, respectively. As can be seen the calculated near-bed concentrations approximate to a straight line when plotted on a log-log scale, the gradient (P) being equal to:

$$P = \frac{w_s}{\beta \kappa u_*} \tag{3.6}$$

where:

w_s = particle settling velocity

β = Prandtl number (approximated to 1)

κ = von Karman constant (= 0.41)

u_* = shear velocity

From Equation 3.6, to determine the *in situ* settling velocity, the near-bed concentration gradient (P) and the shear velocity (u_*) need to be measured. Measurement of the concentration gradient may be achieved using acoustic or optical instrumentation (see Section 1.4), or by direct water samples. The shear velocity may be estimated by taking current measurements near to the bed and fitting a log velocity profile, usually by a

least-squares technique, as described by Equation 1.15 (Lynch *et al*, 1994). By comparing the calculated and measured concentration gradients, an estimate of the average *in situ* settling velocity may then be determined. By applying Stokes' Law (Equation 1.13), the settling velocity may then be converted to an estimate of the mean particle size.

The main problem with this method is that it relies on the validity of both the Rouse Profile and Stokes' Law. However, it is increasingly being applied as a simple method for determining the *in situ* settling velocity for the parameterisation of sediment transport models (Clarke & Elliott, 1998; Ciffroy *et al*, 2000; van der Ham & Winterwerp, 2001).

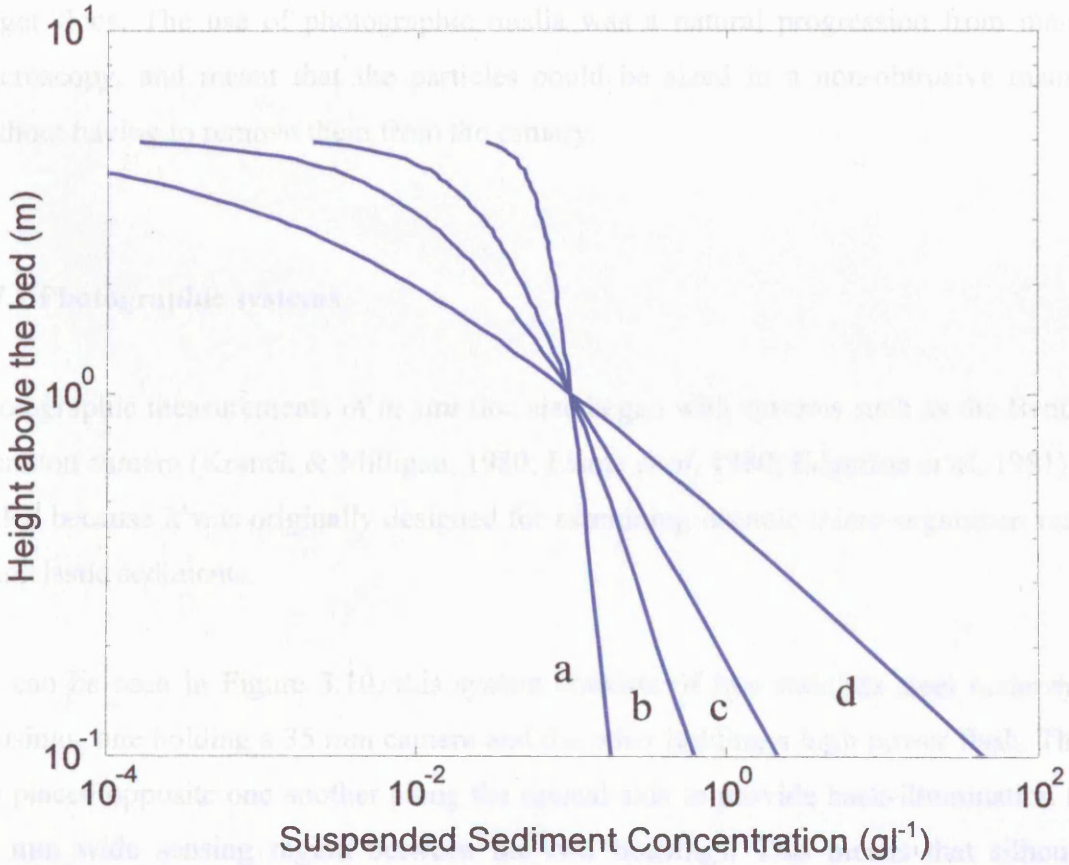

Figure 3.9 – Rouse profiles calculated from Equation 1.16 with a variety of settling velocities: **a** = 1, **b** = 3, **c** = 5, **d** = 10 mm s^{-1}. The reference concentration (C_a) and shear velocity (u_*) are set to be constant at 100 mgl^{-1} and 0.01 ms^{-1} respectively.

3.7 Imaging Systems

A problem with all of the above methods is the fact that they rely largely on theory to determine the particle size. Camera systems, however, have the advantage that they allow the user to see what is being measured as well as allowing shape measurements to be made. Over the last twenty years there have been rapid improvements in the use of imaging techniques for particle size analysis. Up until the early 1980s particles were counted and sized manually by viewing a sample under a microscope (e.g. Schubel, 1969; Gibbs *et al*, 1983). However, removing suspended particles from their natural environment tends to induce floc break-up (Gibbs & Konwar, 1983; Eisma *et al*, 1990). Despite methods of reducing this problem with devices such as the small volume microsampler (SVPM; Schubel & Schiemer, 1972; Archambault *et al*, 2001) it is preferential in estuarine situations to obtain *in situ* images due to the fragility of the larger flocs. The use of photographic media was a natural progression from manual microscopy, and meant that the particles could be sized in a non-obtrusive manner, without having to remove them from the estuary.

3.7.1 Photographic systems

Photographic measurements of *in situ* floc size began with systems such as the Benthos Plankton camera (Kranck & Milligan, 1980; Eisma *et al*, 1980; Edgerton *et al*, 1981), so called because it was originally designed for examining oceanic micro-organisms rather than clastic sediments.

As can be seen in Figure 3.10, this system consists of two stainless steel underwater housings, one holding a 35 mm camera and the other holding a high power flash. These are placed opposite one another along the optical axis to provide back-illumination to a 40 mm wide sensing region between the two housings. This means that silhouette images of the particles may be taken as they pass through the field of view of the camera. The field of view is circular, with a 7.4 cm diameter, and the depth of field is 4 cm. The minimum resolution of the system is approximately 100 μm.

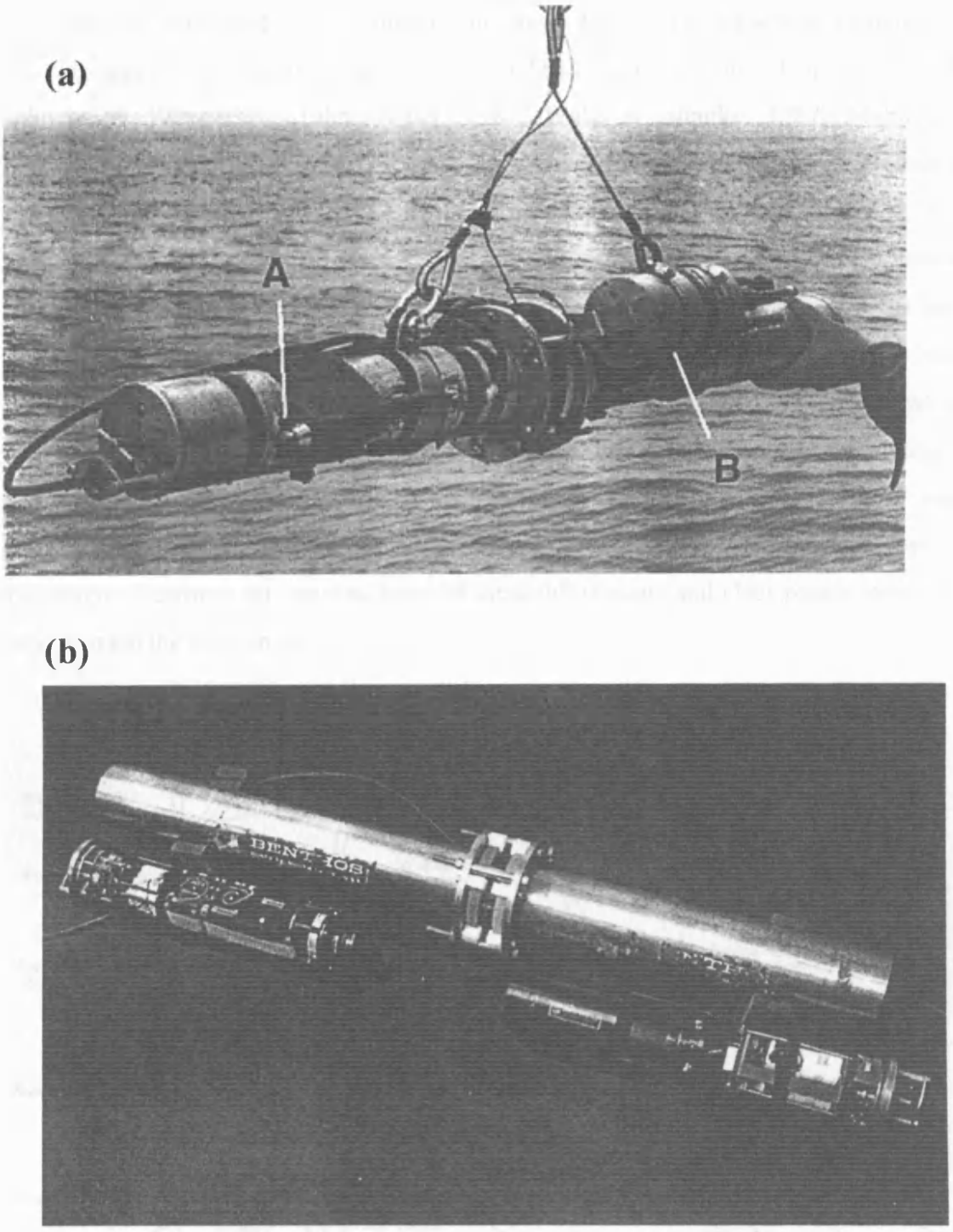

Figure 3.10 – (a) The Benthos Plankton Camera (Milligan, 1996), and (b) its internal workings.

Since the development of this instrument, there have been numerous camera-based systems specifically designed for *in situ* particle sizing underwater (Honjo *et al*, 1984; Johnson & Wangersky, 1985; Asper, 1987; Wells & Shanks, 1987; Maldiney & Mouchel, 1995; Pfeiffer, 1996; Thomsen *et al*, 1996). Figure 3.11 shows a system that was first developed by Wells & Shanks (1987) then improved by Knowles & Wells (1996) called the In Situ Aggregate Analysis Camera (ISAAC). This used a standard Nikon 35 mm camera with a 1:2.8 magnification lens giving size range from 20 μm to several millimetres. Rather than using back-illumination, this system used lateral illumination whereby a *sheet* of light was projected perpendicular to the optical axis thus reducing the number of out of focus particles in the image by only illuminating the particles within the depth of field. The resultant images therefore showed bright particles against a dark background. This illumination was supplied by two synchronised strobes on opposite sides of the field of view, and clear plastic strips were used to form the light sheet.

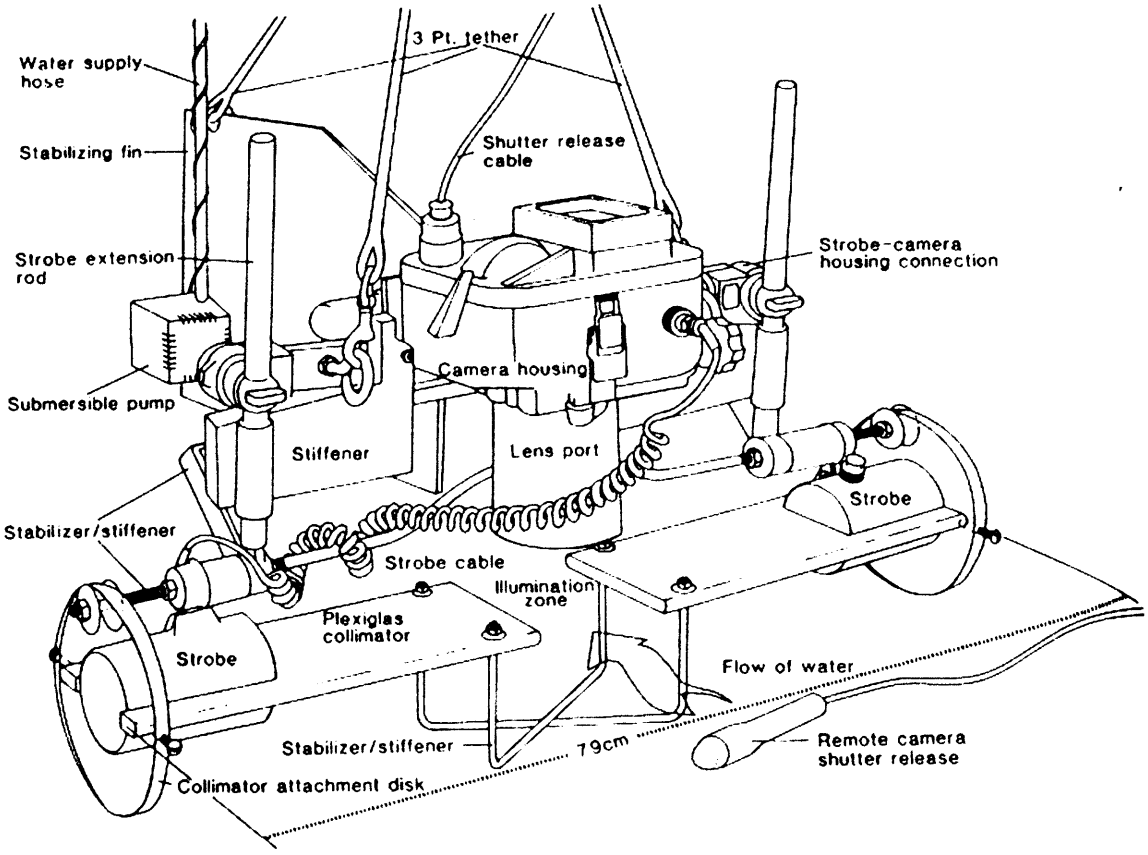

Figure 3.11 - ISAAC (Knowles & Wells, 1996).

All such camera systems suffer from a common problem when looking at estuarine particles, in that they have a restricted size range of about two orders of magnitude. As explained in Section 1.3.1, it is well documented that particle size can vary from a micron to several millimetres. An obvious remedy would be to use two cameras at different magnifications. A system which did just this, hence increasing the resolution and size range, was an *in situ* camera system developed by the Netherlands Institute of Sea Research (Eisma *et al*, 1990) shown in Figure 3.12a. Because of its wide size range, this camera system has probably become the most successful of all its competitors to date. In principle, this system is very similar to the original Benthos Plankton camera except that it uses two professional Nikon F3 cameras instead of one. One camera has a 1:1 magnification lens system for particle sizes ranging from ~100 μm to a few millimetres, the other camera has a 1:10 lens system for observing particles as small as ~3.5 μm. Each camera has a flash unit pointing directly towards the lens with a water flow aperture of 32 mm in between. For the 1:1 camera, the flash duration is 20-30 μsecs at 38 Joules per flash, while the 1:10 camera has a flash duration of 2-3 μsecs at 2 Joules per flash. The high-speed flashes are required in order to allow particles to be imaged without blurring at flow speeds of up to 1 ms^{-1}. Since, a particle moving at this flow speed would travel 1 μm in 1 μsec, a high-speed flash is essential.

A similar system called the Floc Camera Assembly (FCA) shown in Figure 3.12b has subsequently been developed by Heffler *et al* (1991). This also has two cameras with minimum resolutions of 50 μm and 250 μm. Although the minimum resolution is not as good as Eisma's system, it has the added capability of being able to measure settling velocities by incorporating a stilling tank.

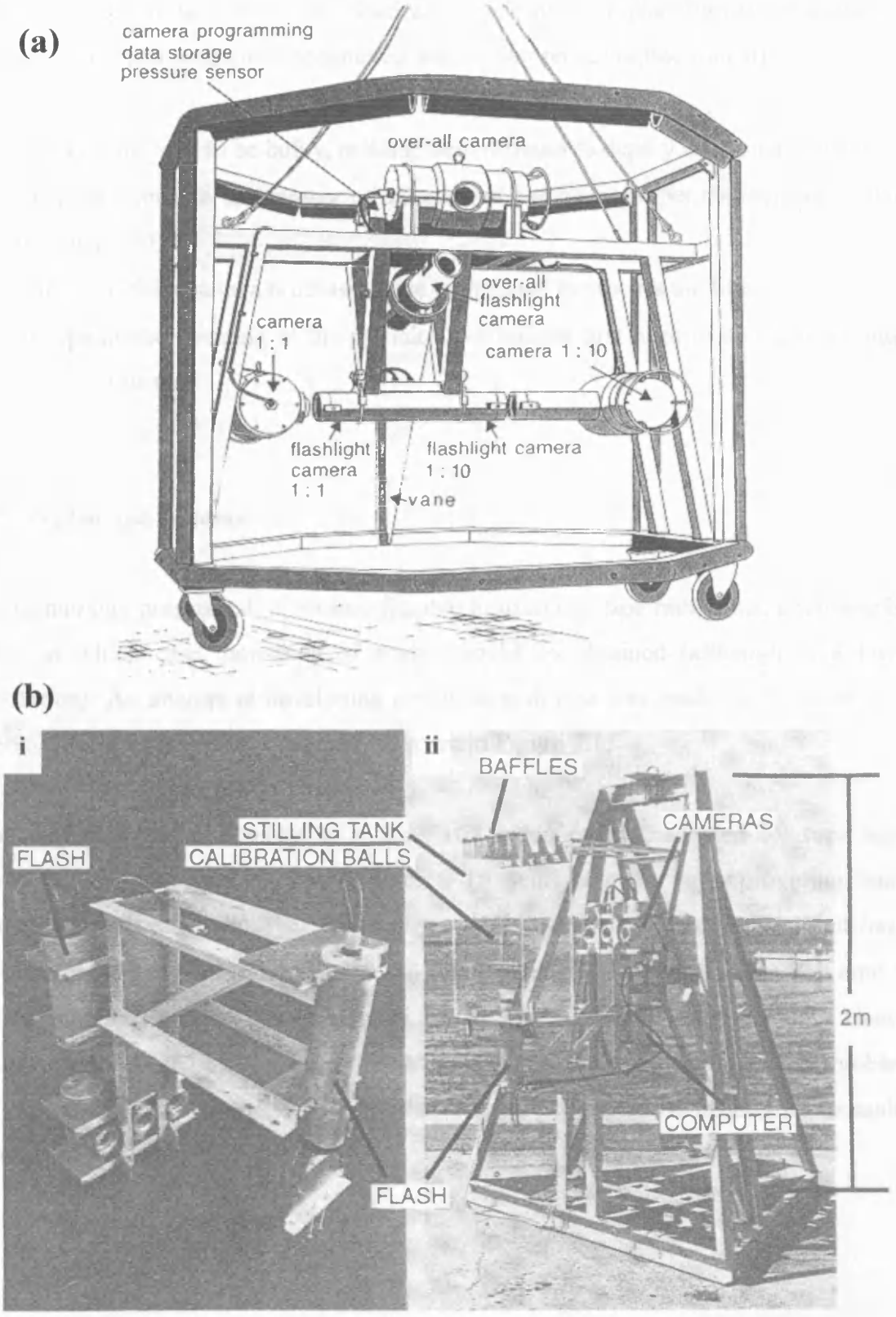

Figure 3.12 – Multiple camera systems (a) The camera system designed at the Netherlands Institute of Sea Research (Eisma *et al*, 1990). (b) The Floc Camera Assembly (i) detail of the three cameras and flash unit, (ii) full deployment rig, with stilling tanks (Heffler *et al*, 1991).

Each of the camera systems described above use photographic film to take snapshot images. The main problems encountered when using photographic film are:

- The systems tend to be bulky, making them difficult to deploy from small boats
- There is a limit to the number of images that can be taken per deployment (usually less than 250)
- There is a delay in data processing due to the need to process the film
- For automatic counting of the particles, the images first need to be digitised into a computer format

3.7.2 Videotape systems

As technology progressed, it became feasible to use videotape rather than photographic film, in which case thousands of images could be obtained (although at a lower resolution). An attempt at developing a videotape device was made by Thomsen *et al* (1996). The apparatus they designed is shown in Figure 3.13.

Basically this system consists of a Sony Hi8 video camera, adapted for time lapse imaging, in a waterproof housing with a 10 Watt halogen lamp providing back-illumination. The simplicity of this design means that it is relatively cheap, but has a poor resolution of approximately 150 μm (mainly because images are recorded onto S-VHS videotape) with a field of view of 2.5 cm and a depth of field of 4 cm. Hence, only large flocs can be observed. The use of a halogen lamp also introduces the problem of power requirement, and it is likely that a generator would be needed for extended periods of fieldwork.

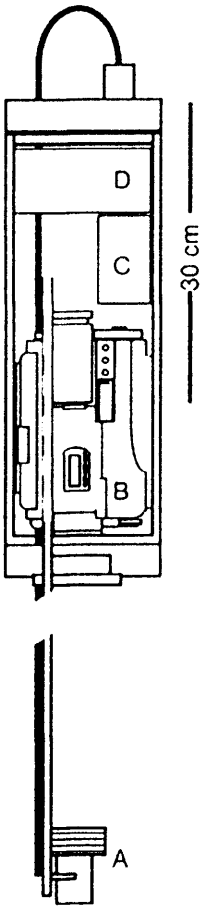

Figure 3.13- Video camera system from Thomsen *et al*, 1996.

3.7.3 Digital imaging systems

With advances in computer processing capabilities, and the introduction of cheap, off the shelf, framegrabbers and large memory storage capacity, it has recently become unnecessary to use any kind of photographic film. Instead, images may be digitised directly from the video output of the camera and stored on a computer hard drive, or on digital tape. This has the affect of reducing both the cost and the size of the instrument as well as reducing the processing time of the images. Such a system was made by Maldiney & Mouchel (1995) who took the novel approach of using an endoscope connected to a CCTV camera in order to look at small particles (Figure 3.14a).

By using an endoscopic lens system, the minimum size resolution for this device is reasonably good at 6 μm but this is at the expense of the largest viewable size, which is only 400 μm. Another problem is that the image is distorted significantly by aberrations caused by the endoscope optics, particularly in the region near the edges of the image. The use of a halogen light source has also proved to be a problem at high particle concentrations because it does not provide enough illumination, and has high power requirements. Also, because it is a constant light source, *smearing* of the particles has been observed at high current speeds due to motion blur.

Another system that uses both S-VHS recording and digital storage of images is described by Pfeiffer (1996) and is shown in Figure 3.14b. This is called the Video Multi-Sensor System since it is combined with a current and salinity meter. To overcome the previous problem of motion blur, this camera uses a flash light source, which is synchronised with the CCD camera (similar in principle to the original Benthos Plankton Camera described earlier). A translucent glass diffuser is fitted in front of the flash to provide a white background against which the particles are imaged. To vary the amount of light provided by the flash, an adjustable aperture has been placed between the flash and the diffuser screen. The magnification of the lens system in this device is approximately 6:1 giving a minimum resolution of ~120 μm and a field of view of 4x3 cm.

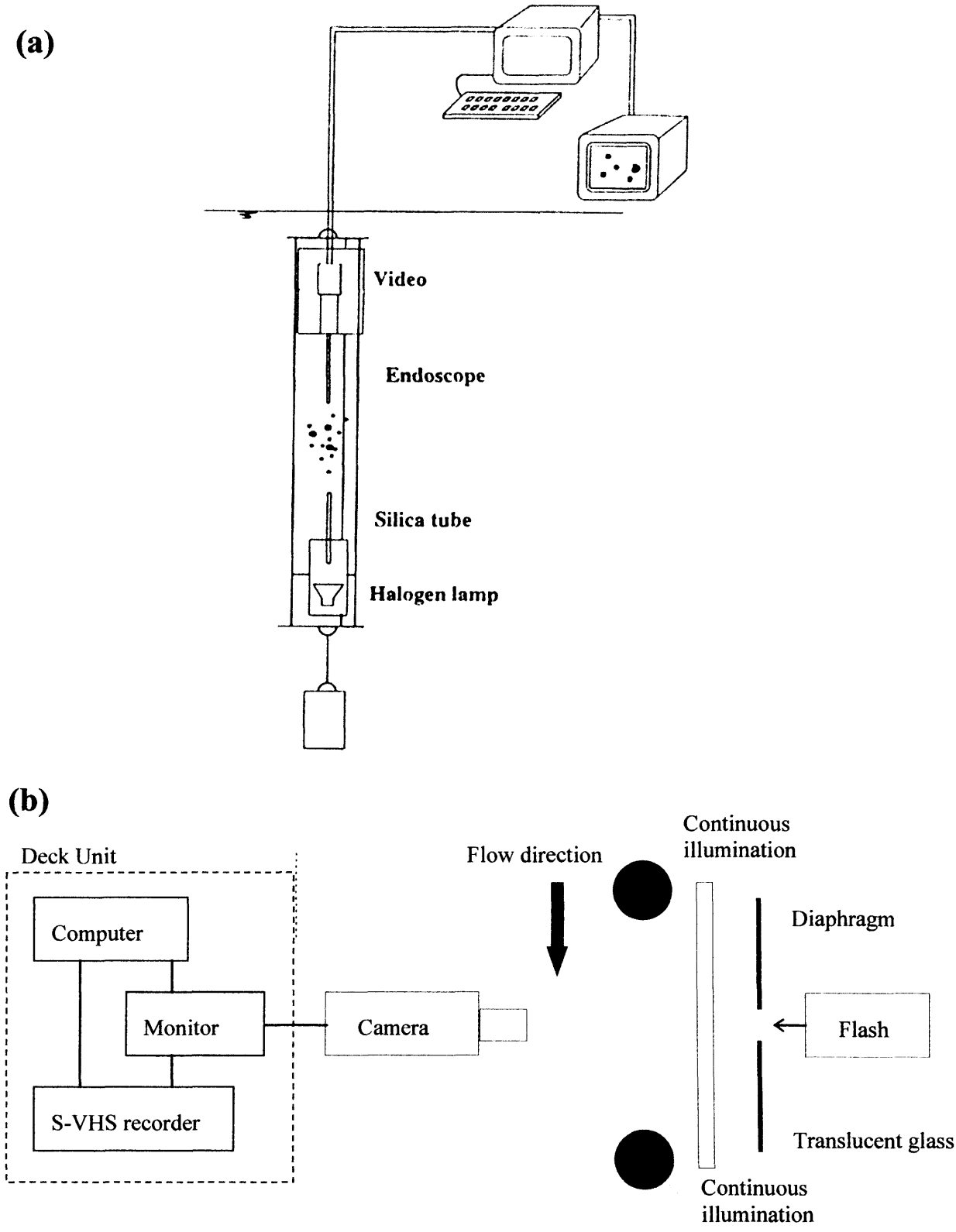

Figure 3.14 – In situ digital imaging systems: (a) Endoscope video system (Maldiney & Mouchel, 1995). (b) VMSS configuration – adapted from Pfeiffer (1996).

Here it is worth noting that several digital imaging systems have been developed for the visualisation and recognition of oceanic plankton [e.g. Critter-Cam, Bergeron *et al* (1988); ROV deployed video, Paffenhofer *et al* (1991); Ecoscope, Kils (1992); Video Profiler, Gorsky *et al* (1992); Video Plankton Recorder, Davis *et al* (1992, 1996)]. The most recent, and technically advanced, of these systems is the Video Plankton Recorder (Figure 3.15), which has been successfully used for monitoring zooplankton biomass in Georges Bank 100km south-east of Cape Cod (Davis *et al*, 1996; Gallager *et al*, 1996; Norrbin *et al*, 1996; Benfield *et al*, 1996, 1998; Ashjian *et al*, 2001). The instrument hardware consists of two to four video cameras, with a range of optics to allow images of particles in the size range of 10 μm to several centimetres. The cameras are synchronised to a red-filtered 80 W xenon strobe with a microsecond flash duration. Images are then sent by optical cable to a computer on the ship. Software has been developed to automatically segment the images in real-time. In this way, regions of interest containing possible particles or plankton are stored to hard disk as binary images. Manual sizing and recognition of plankton species is then carried out using a 'point and click' program written in MATLAB (Davis *et al*, 1996). This system is very expensive and would be too large for use in many estuaries. However, it is possible that a scaled down version of this system could be used for the purpose of particle size, as well as shape, analysis in estuaries.

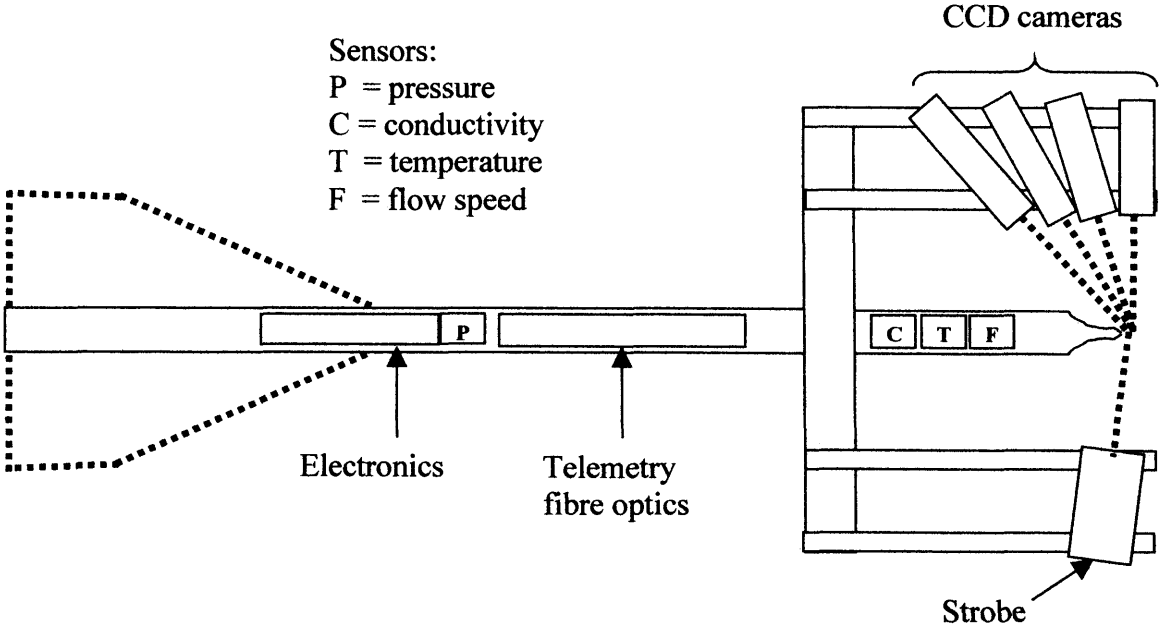

Figure 3.15 – The Video Plankton Recorder (adapted from Davis *et al*, 1992)

3.7.4 Sizing and settling velocity video systems

Recently, some *in situ* video camera system designers have attempted to incorporate a settling tube arrangement so that they can also measure the particle settling velocity (Fennessy & Dyer, 1996; Van Leussen & Cornelisse, 1993; Sternberg *et al*, 1996). By measuring the settling velocity, as well as the size, it is also possible to make *in situ* measurements of particle density. An example of such a device was designed by Van Leussen & Cornelisse (1993) called the VIS (Video In Situ).

As can be seen in Figure 3.16a this incorporates a *baffle* system in order to reduce turbulence in the settling column (as with the FCA design described previously) and a sheet of light (0.4 mm thick) to reduce the depth of field. A 25 mm lens is combined with a 15 mm extension ring to provide ~1:1 magnification. Hence, the overall field of view is 9x6 mm with a pixel size of 10x15 mm. Its small size means that it can be used in a *free-float* mode so that depth profiles of size and settling velocity may be obtained, reportedly in currents of up to $1ms^{-1}$ (Van Leussen & Cornelisse, 1993). Results from this system (Figure 3.16b) confirm the strong relationship between particle size and settling velocity. More recently, Van der Lee (2000) used this system to measure temporal variations in floc size and settling velocity in the Dollard estuary (The Netherlands). Settling velocity was observed to vary throughout a tidal cycle, but several problems with the system were. First, the minimum resolution was calculated to be 85 μm. By using a higher magnification camera Van der Lee showed that up to 15% of the suspended volume was below this size, so an overestimation of the mean floc size was determined. Second, particles that were only partly within the light sheet appeared to be smaller than their actual size, and in some cases the reflected light from a particle saturated the image, thus making the particle appear larger than actual size. Third, measurements of settling velocity were complicated by the presence of turbulence within the settling tube, thus reducing the accuracy of the particle density calculation. Despite these problems, it was estimated that the system had an error of approximately 10-20% for both floc size and settling velocity.

A similar system, with the same size resolution is the In Situ Settling Velocity instrument (INSSEV) designed by Fennessy *et al* (1994). INSSEV differs from other settling tubes by incorporating a two-chamber system in order to reduce turbulence. As

can be seen in Figure 3.17a, suspended particles are captured in a volume of water in the upper chamber by closing two doors. After waiting for turbulence to decay, a sliding door opens to allow the particles to settle through the lower chamber, which contains filtered water at a slightly higher salinity to prevent mixing. A video camera then monitors the particles as they settle, thus allowing simultaneous measurements of settling velocity and size. Results from INSSEV (Figure 3.17b) show that the effective density of particles tends to fall as the flocs get larger. This is due to their fractal nature and results in slower velocities than Stokes' Law predicts.

Sternberg *et al* (1996), developed a bottom-mounted system for measuring settling velocity. This system (Figure 3.18a) consists of a Sony Hi8 video camera, which views particles settling within a square sectioned column, again with baffles at the top to reduce turbulence. Results from this device were comparable with the INSSEV system (Figure 3.18b).

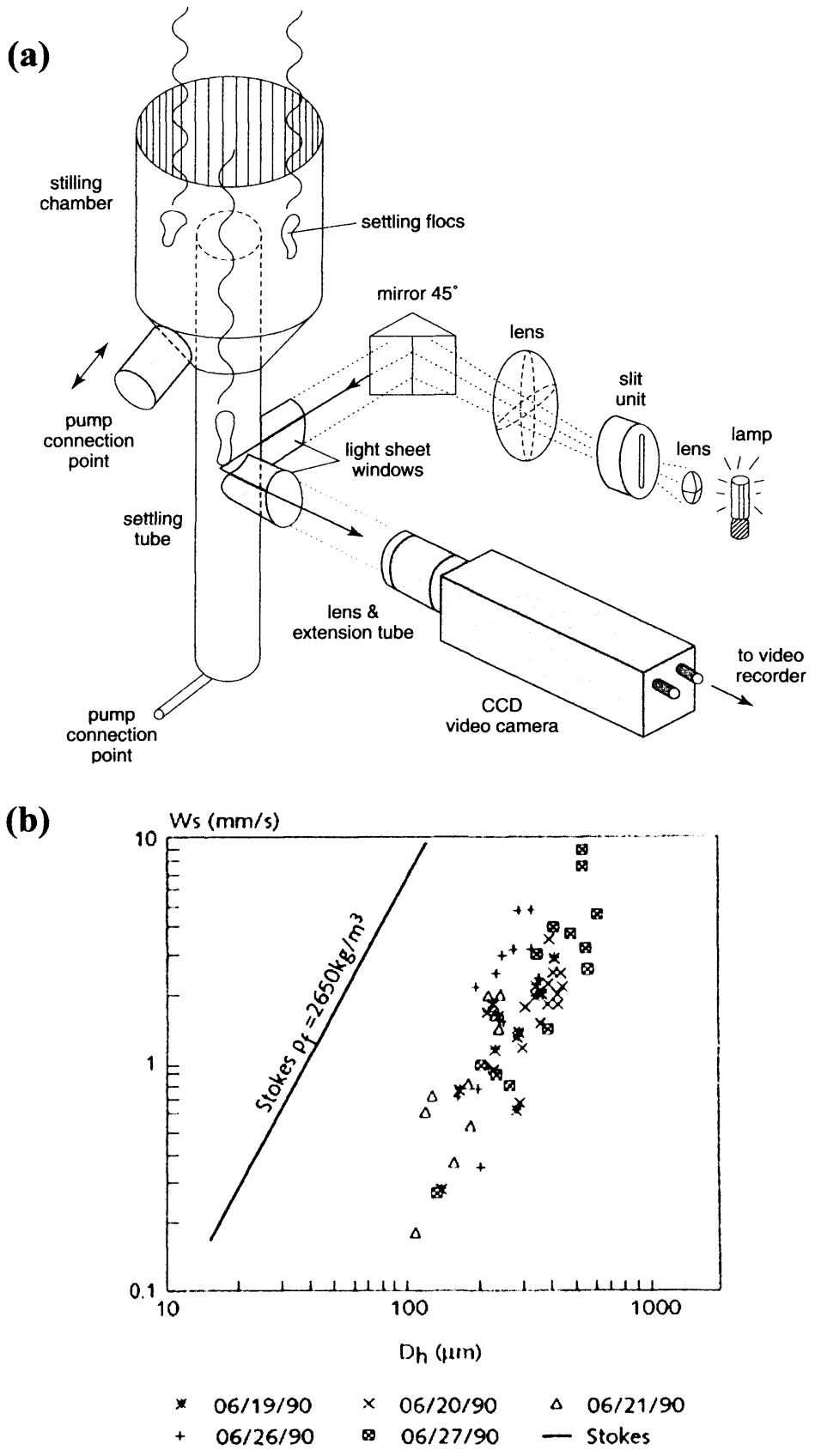

Figure 3.16 – (a) Video In Situ (VIS), (b) results from VIS (Van Leussen & Cornelisse, 1993).

(a)

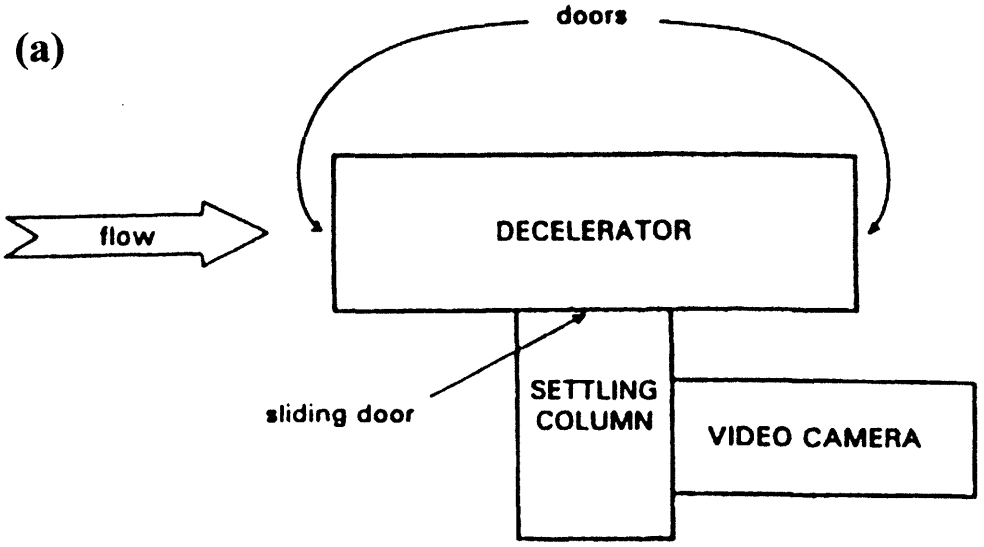

(b)

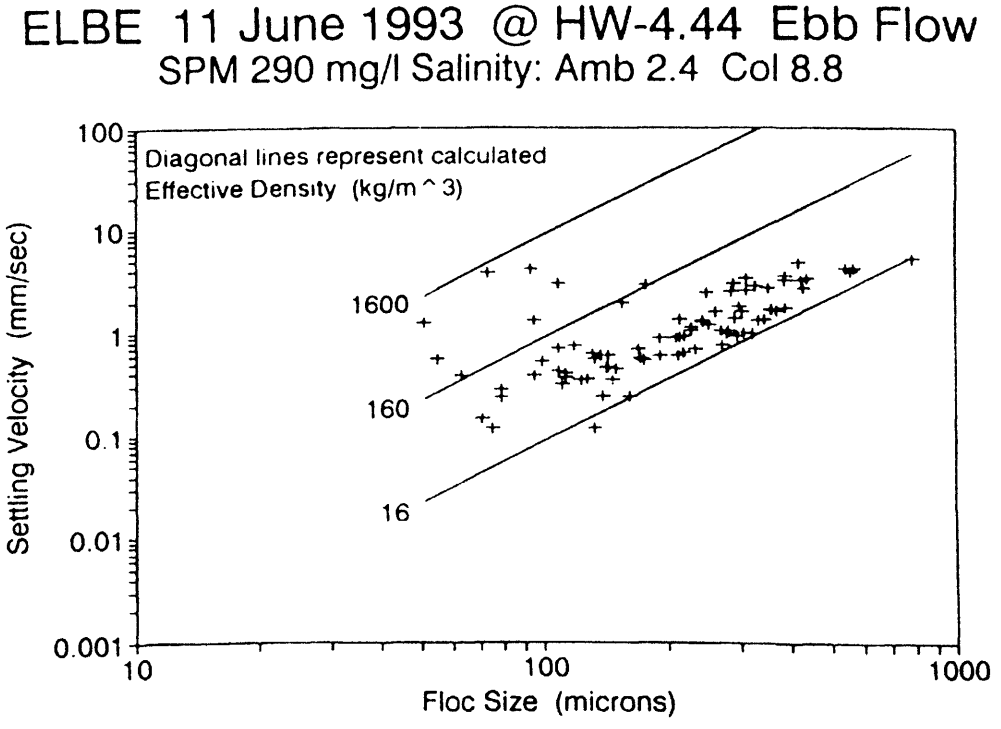

Figure 3.17 – (a) In Situ Size and Settling Velocity system (INSSEV) (Fennessy *et al*, 1994), (b) Results from INSSEV (Fennessy & Dyer, 1996).

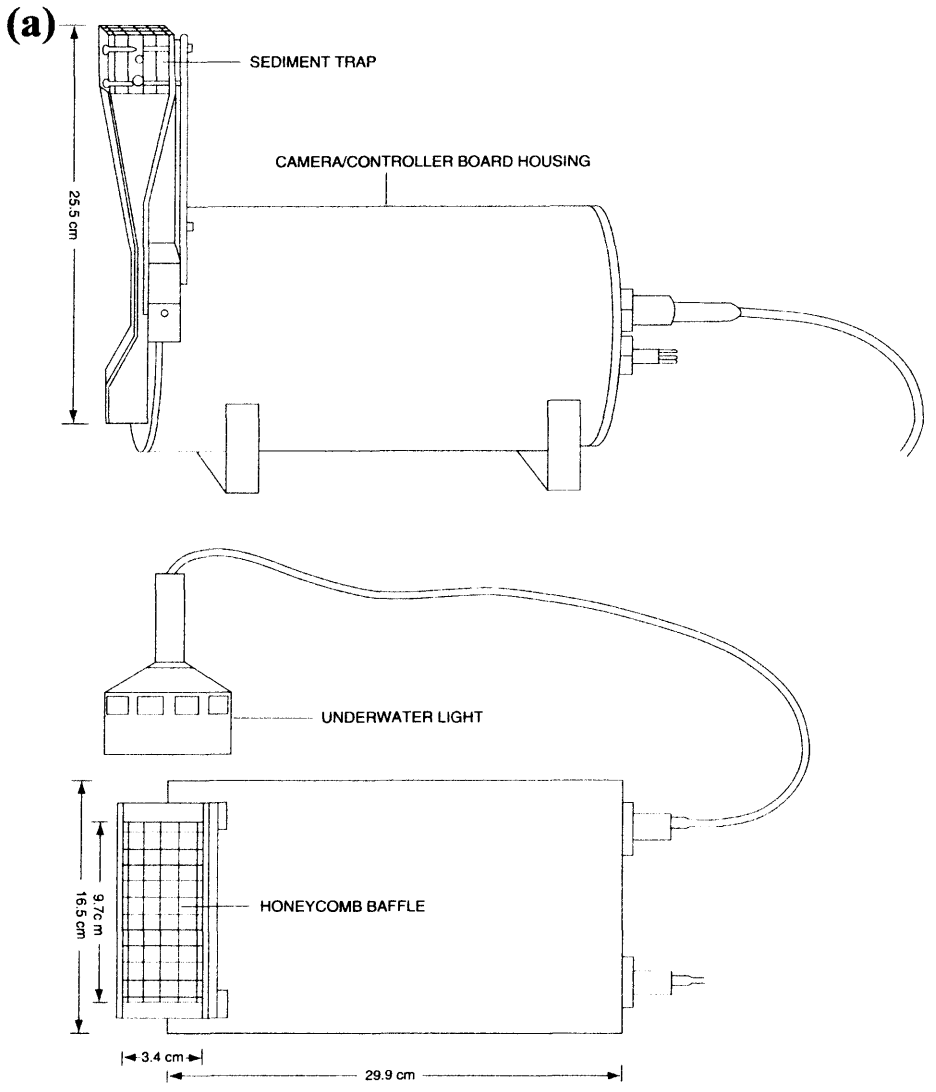

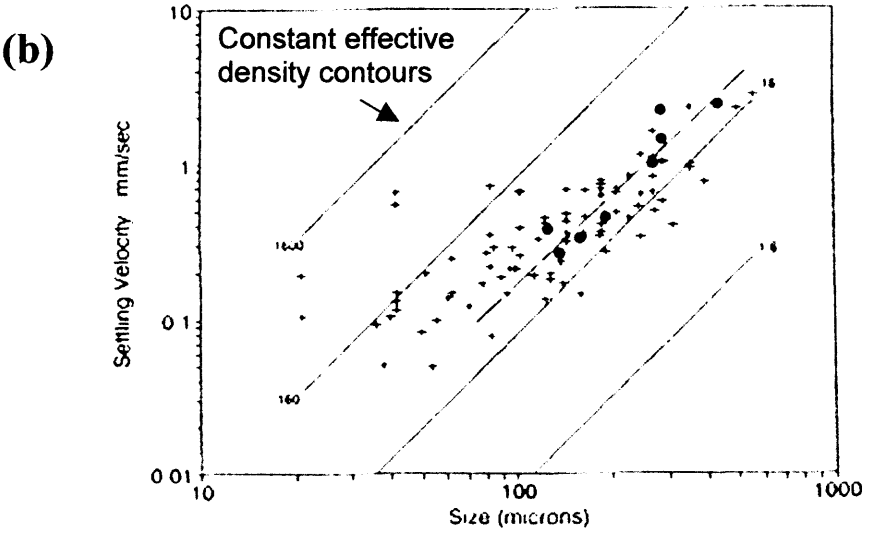

Figure 3.18 – (a) Automated settling velocity sediment trap (Sternberg *et al*, 1996), (b) Results from this system (•) compared with INSSEV results (+).

3.7.5 Holographic imaging systems

A less common method of particle sizing in the marine environment is holographic imaging. This method has some distinct advantages over the use of normal focal plane imaging systems, and has therefore been developed by a number of researchers as a means of particle sizing and plankton identification (Knox, 1966; Stewart *et al*, 1973; Hefflinger *et al*, 1978; Carder, 1979; Carder *et al*, 1982; Katz *et al*, 1984; O'Hern *et al*, 1988; Foster & Watson, 1997; Hobson *et al*, 1997; Katz *et al*, 1999).

Standard focal plane photographic systems have two main limitations. First, the particle size range is restricted by the pixel size, lens optics and field of view, thus requiring two or more cameras to monitor the full size distribution. Second, the total number of particles viewed in one image is limited by the depth of field, which needs to be small in order to prevent imaging of overlapping particles. Many images are usually needed to build up a good statistical representation of the particle size population. By using holographic techniques, both these problems can be overcome. Holographic imaging is in fact a combination of laser diffraction and imaging techniques, and is capable of simultaneously viewing a large volume of water (>1 litre) with a high resolution (~10 μm). A full explanation of the theory of far-field holography (see Hariharan, 1996) is beyond the scope of the present study. However, a brief explanation is required in order to understand the benefits and pitfalls of this method.

There are two types of holography used for recording underwater images, *in-line* and *off-axis* recording. In-line holography, is the simplest and most commonly used of the two methods for viewing small objects in suspension (e.g. Carder *et al*, 1982; Hobson *et al*, 1997; Katz *et al*, 1999). In this situation a single collimated laser beam, expanded to several centimetres diameter, is used to illuminate both the object and the holographic film, as shown in Figure 3.19a. An image of the diffracted light is therefore formed on the film. This is basically the same set up as a laser diffractometer, but without the Fourier Transform lens for refocusing the beam to a point. A limitation is that the object size must be small (as with laser diffraction), the maximum particle size being dictated by the far field (Fraunhofer) condition (Hariharan, 1996). This states that the distance (z) from the object to the hologram should be greater than the square of the largest particle dimension divided by the wavelength of light (i.e. $z > d^2/\lambda$). This method is

therefore not suited to viewing large objects. However, the images are very high-resolution, making this a suitable method for observations of marine plankton and suspended particles. In order to replay the images, the processed hologram is re-illuminated by a laser (Figure 3.19b) creating two 3D images of the scene, one virtual and one real. The real image can then be viewed either by focusing a CCD camera at different points within it, or by progressively moving a CCD without a lens through the whole image. The particles may then be counted and sized in a similar manner to a normal imaging system. Optical aberrations, such as astigmatism and coma, caused by the replaying of the hologram in air rather than water, are overcome by using a replay laser wavelength that is equal to the recording wavelength divided by the refractive index of the water (Foster & Watson, 1997). For this reason, most underwater holograms are recorded with a red beam (694 nm) and replayed with a green beam (522 nm).

Off-axis holograммetry is slightly more complicated. In this case, the laser beam is split into two separate beams, one to illuminate the objects, and a second reference beam to illuminate the holographic photo plate. This has the advantage of being able to view objects at higher concentrations, but at the expense of the resolution (>140 μm) due to increased aberrations (Foster & Watson, 1997; Hobson *et al*, 1997). This method is therefore less appropriate for particle sizing in estuaries and is not discussed further.

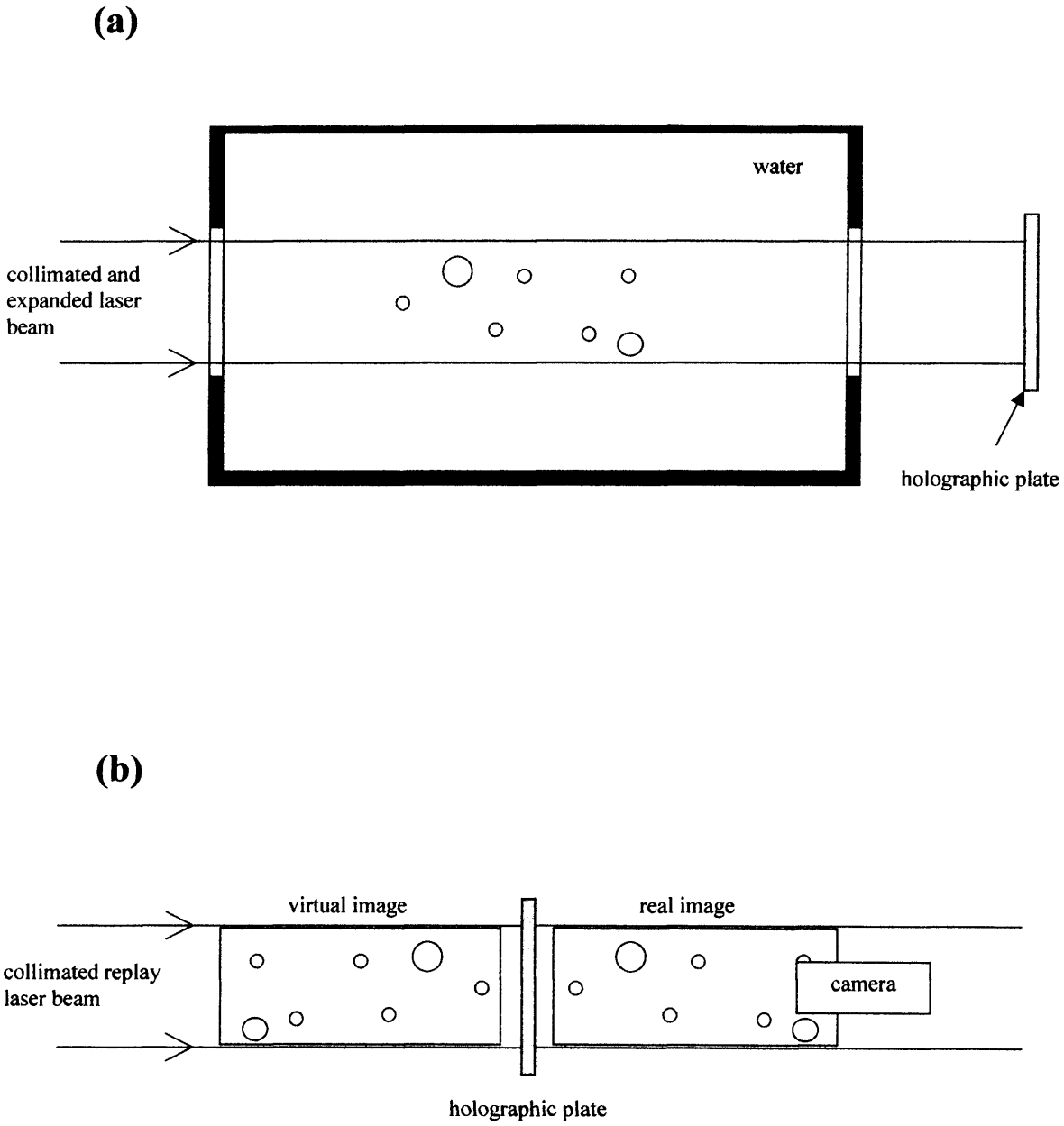

Figure 3.19 – In-line hologrammetry (a) Recording, (b) Playback, showing the virtual and real images. As shown, a camera may be passed through the 3D image to record 2D slice images for particle sizing (redrawn from Foster & Watson, 1997).

Due to its potential advantages for particle imaging, attempts to use holography for plankton detection in the laboratory were started in 1960s and 1970s (Knox, 1966; Stewart *et al*, 1973; Hefflinger *et al*, 1978). Carder (1979) adapted the idea for observing microscopic particles in the laboratory, and later developed a submersible particle velocimeter for *in situ* measurements of particle size and settling velocity (Carder *et al*, 1982). This system, shown in Figure 3.20a, was primarily limited by laser power (it used a 2 mW, He-Ne laser) which meant that the sample volume was only a few millimetres wide, containing very few particles. Katz *et al* (1984) and O'Hern *et al* (1988) then developed another system which used a more powerful pulsed ruby-laser for sizing and counting of particles and bubbles in waters off Catalina Island, CA. Similar systems have also been designed specifically for *in situ* monitoring of plankton (Foster & Watson 1997; Hobson *et al*, 1997).

The most recent example of a submersible holocamera, used to detect particle characteristics and motions in the ocean, is described by Katz *et al* (1999), and is shown in Figure 3.20b. The cylindrical sampling volume in this system is 6.3 cm in diameter and its length can be varied from 10 to 68 cm, giving a total volume of between 400-2000 cm^3. The resolution is reported to be ~10 μm. This system is also capable of three-dimensional velocity measurements using Holographic Particle Image Velocimetry, HPIV (Katz *et al*, 1999). By this method, the velocities of the particles may be determined by obtaining two images in rapid succession (~1 ms interval), the displacement between the two images is then related to the velocity.

The main disadvantage of holographic imaging is its complexity, and hence its cost. Also, the fact that there are three stages to the particle sizing process (i.e. hologram recording, playback and image processing) makes this method very time consuming.

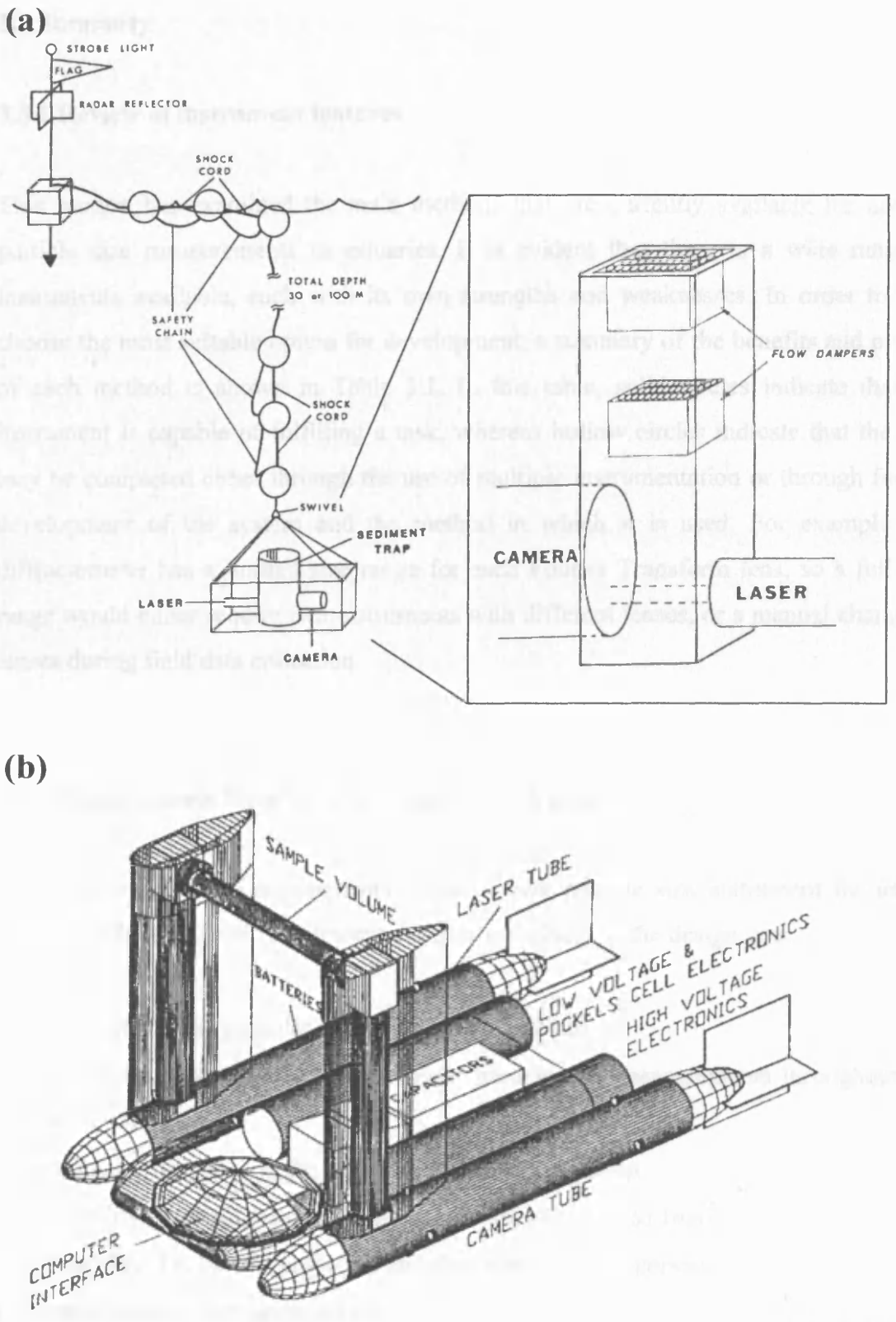

Figure 3.20 – Submersible holocamera systems: (a) The system developed by Carder et al (1982), with a detail to highlight the use of flow dampers, (b) The towable system developed by Katz *et al* (1999).

3.8 Summary

3.8.1 Review of instrument features

This section has examined the main methods that are currently available for making particle size measurements in estuaries. It is evident that there is a wide range of instruments available, each with its own strengths and weaknesses. In order to help choose the most suitable option for development, a summary of the benefits and pitfalls of each method is shown in Table 3.1. In this table, solid circles indicate that the instrument is capable of fulfilling a task, whereas hollow circles indicate that the task may be completed either through the use of multiple instrumentation or through further development of the system and the method in which it is used. For example, the diffractometer has a limited size range for each Fourier Transform lens, so a full size range would either require two instruments with different lenses, or a manual change of lenses during field data collection.

3.8.2 Requirements for a low cost estuarine instrument

There are two tiers of requirements for an *in situ* particle size instrument for use in estuaries. The first level requirements, which are critical to the design, are:

- the ability to size particles in the range 1 to 5000μm
- the ability to obtain *in situ* underwater particle size measurements throughout the entire water column
- minimal disturbance to the flow to prevent floc break-up
- the ability to obtain measurements in flow speeds of up to $1 ms^{-1}$
- portability (i.e. battery powered) and deployable by one person
- cost of construction under £5,000
- the system must be non-hazardous to human health or the environment

The second tier requirements are those that are not vital to the design, but which would be preferable. These include:

- particle size distribution output, rather than merely average size
- automated output
- settling velocity measurements
- shape analysis
- large sample volume
- very high (and very low) SSC capability
- long-term deployable

From Table 3.1, several particle-sizing techniques can be immediately discarded since they do not meet the criteria for the first tier of requirements. The remaining sizing techniques are:

- Field settling tubes
- Model-dependent inversion
- Focal plane imaging techniques

The first two methods are heavily reliant on theory, since they both rely on Stokes' Law (Equation 1.13) for obtaining particle size. Model-dependent inversion also relies upon the assumption of the Rouse profile, making this method even less reliable. For this reason, these two methods are more useful for parameterisation of the settling velocity in sediment transport models.

On balance, it is apparent that the most cost effective and reliable method is to use a focal plane imaging system in terms of the main requirements for the design, as well as their flexibility for development (see Table 3.1). However, it is apparent that the main limitation with recently designed particle imaging systems is the fact that they can only measure a narrow size range and small sample volume. However, it is possible to overcome these problems by using several cameras such as in the photographic systems of Eisma *et al* (1990) and Heffler *et al* (1991), as well as taking multiple images as with the Video Plankton Recorder (Davis *et al*, 1992). These types of system also have the added benefit that particle shape may be determined.

With respect to measurement of settling velocity, despite the obvious advantages in data collection for sediment transport modelling, there are two main complications when trying to measure *in situ* settling velocity:

- Ambient water circulation is difficult to eliminate entirely, even for systems fixed to the bed, so the measured settling velocities may be inaccurate.
- The mechanical nature of such designs means that they are liable to failure, have high power requirements and tend to cost more to build.

	Critical requirements					Preferred additional capabilities								
Technique	*In situ* sizing	Low cost	Small boat deployable	Use in $>1ms^{-1}$ flows	Wide size range (i.e. 0.01-1mm)	Entire size distributio n output	Automated output	Settling velocity	Not based on theory*	Shape analysis	Large sample volume	High SSC capability ($>1gl^{-1}$)	Low SSC capability ($<0.01gl^{-1}$)	Long term measure-ment
Coulter Counter		●		●	○	●	●					○	●	
Field settling tube	○	●	○	●	○	●		●			●	○	○	
Laser diffractometer	●		●	●	○	●	●	●			●	○	○	●
Time-of-transition	●		●	●	●	●	●		●			●		○
Multi-frequency acoustic backscatter	●		●	●	○		●	●			●	●		●
Model-dependent inversion	○	●	●	●	●	○		●			●	●	●	●
In situ imaging:														
Photography	●	●		●	○	●		●	●	●	○	○	○	
Video tape	●	●	○		○	●		●	●	●	○	○	○	
Digital	●	●	○	●	○	●	●	●	●	●	○	○	○	○
Holography	●		○	●	●	●		●	●	●	●		●	

Table 3.1 – Inherent capabilities (●) and possible capabilities with adaptation (○) of the various estuarine particle size measurement techniques. (* The category 'Not based on theory' refers specifically to the theoretical assumption that the particles are solid spheres).

4. InSiPID: Instrument Design

4.1 Overview

The particle-sizing instrument developed as part of the current project has been named the In Situ Particle Imaging Device (InSiPID). The system (Figure 4.1 and Figure 4.2) consists of two cameras, each with its own strobe light source. Each camera and strobe is encased in a waterproof housing to allow it to operate to a depth of 15m. Snapshot images of the analogue video signal are digitised directly to computer memory using a framegrabber. Standard monochrome framegrabbers produce images with an 8-bit greyscale depth resolution (i.e. each pixel in the image is allocated a greyscale value of between 0 (black) and 255 (white)). Once the images are digitised, counting and sizing of the particles is carried out using image-processing software. Rather than carrying out on-line processing of the images, it was decided that a more cost-effective option would be to use an off-line approach whereby the captured images are written to a hard disk for subsequent post-processing and analysis. This method also allows for manual detection of faulty images, which may corrupt the derived data.

Eight main components are fundamental to the design of the particle sizing system:

- Camera
- Lens system and calibration
- Light source
- Waterproof housing
- Computer and framegrabber
- Data communication and power supply
- Data acquisition software
- Image processing software

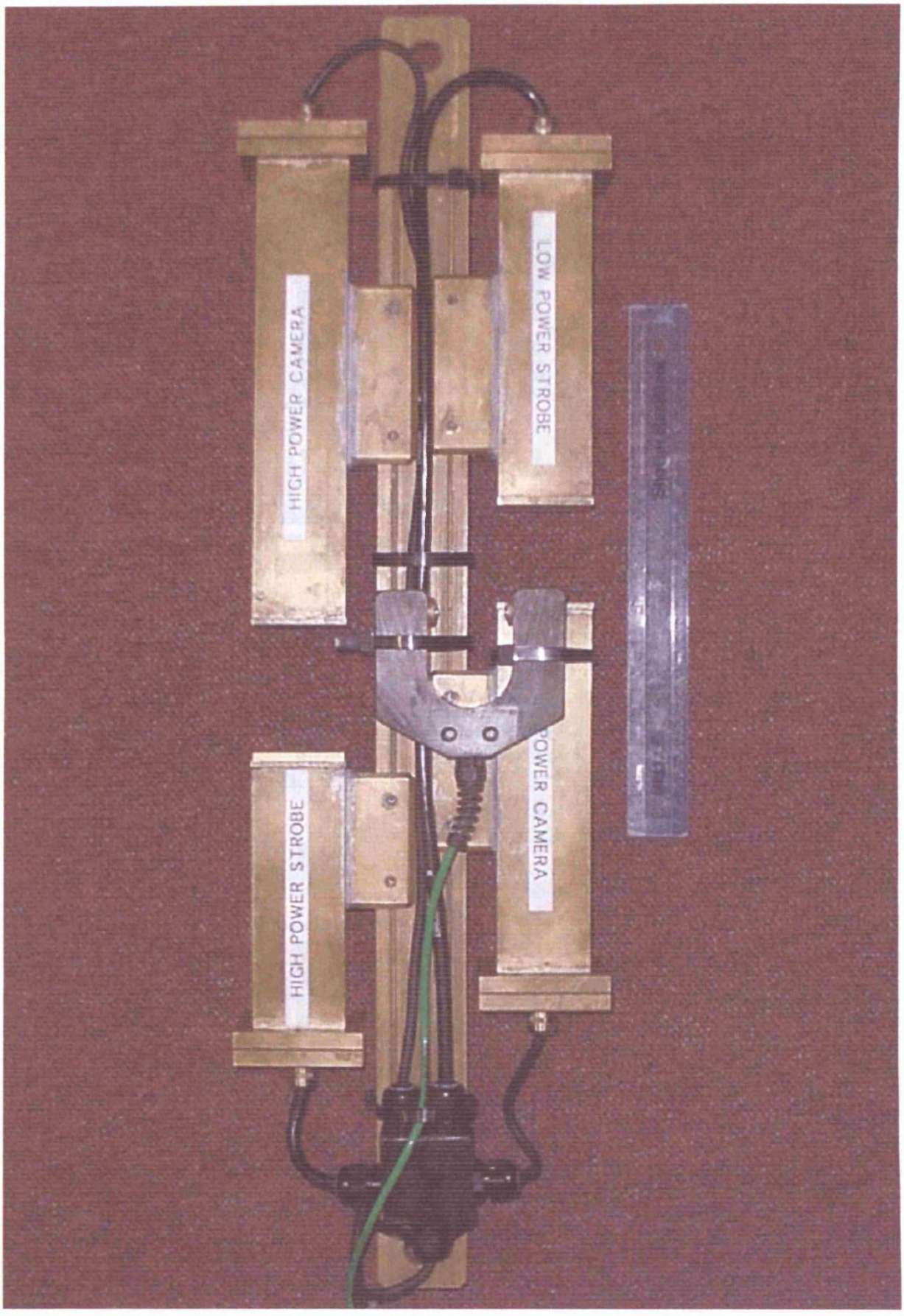

Figure 4.1 - In Situ Particle Imaging Device (30cm rule for scale).

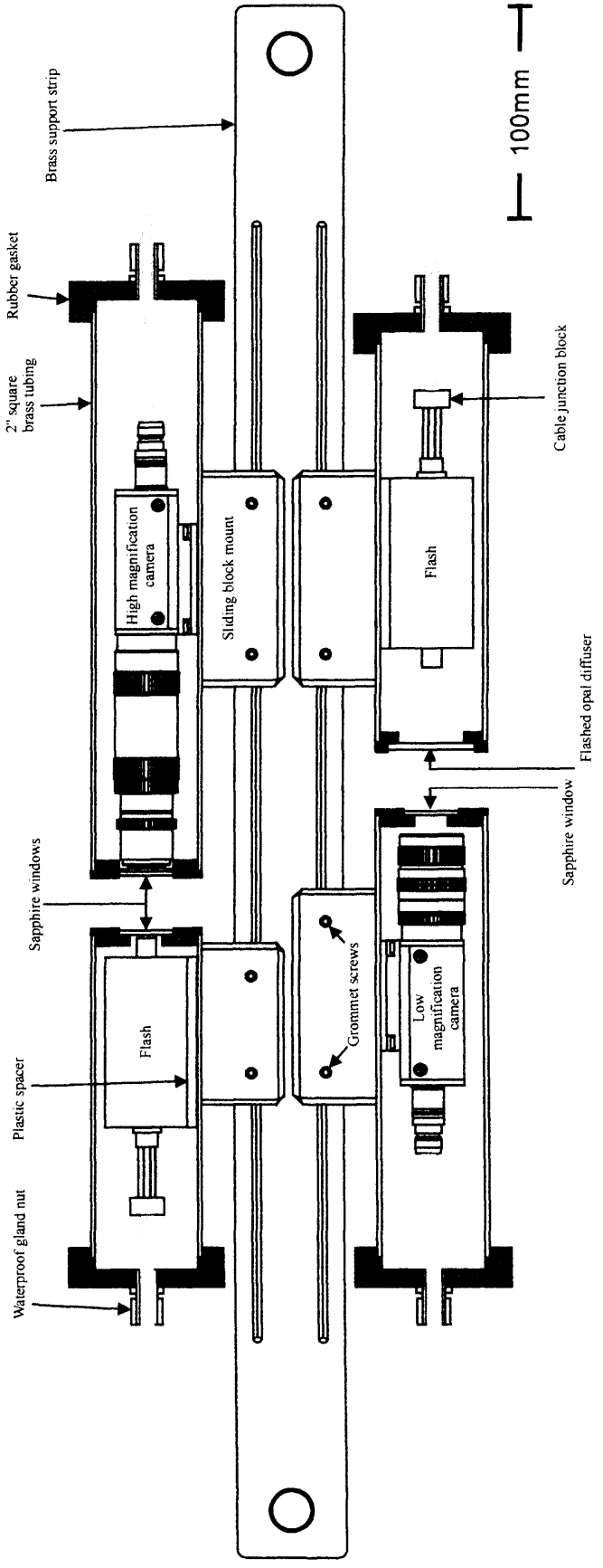

Figure 4.2 - Cut away diagram of INSIPID housing showing main electronic components.

4.2 Hardware components

4.2.1 Camera

It was decided early on in the design process that the most suitable method for particle sizing in relation to cost, ease of manufacture, and suitability for field use, was to use a Charge-Coupled Device (CCD) camera based system. One of the primary system requirements is for the device to measure the size of particles in the range of a few microns to over a millimetre. However, the resolution and overall size of standard CCD arrays means that only a limited range of sizes can be viewed at a single magnification. The minimum resolution is limited by the pixel size, and the maximum viewable particle size is limited by the overall size of the array. At best, with a standard CCD array it is possible to measure particle sizes within a total range of about two orders of magnitude. This problem may be overcome by using either of the following:

- a customised CCD sensor that is much larger than a standard sensor
- a standard CCD camera with a zoom lens
- two cameras at different magnifications

The first option would allow both the larger and smaller particles to be imaged using a single camera. However, apart from the high cost of having such a sensor built, the array size would need to be approximately 20 times larger than standard, which would dramatically increase the computer processing time for each image. The second option would be more problematic to engineer since mechanised zoom lens have relatively high power requirements and are also liable to malfunction during field deployment. In addition, such lenses are more expensive than the cost of a second camera. These considerations lead to the chosen solution which is to use two separate cameras at different magnifications: one to view small particles from between 5-250μm, and the other to view larger particles from 50-2500μm (allowing some overlap for joining the two size distributions). This is similar in principle to the technique adopted by Eisma *et al* (1990) and Heffler *et al* (1991) for their photographic systems (Section 3.7.1), and Davis *et al* (1992) for the Video Plankton Recorder (Section 3.7.3). On balance, this is the most cost effective and reliable of the possible options.

A further consideration was whether or not to use a camera with a fast electronic shutter so that moving particles could be viewed without motion smear. However, cameras with microsecond shutter speeds are not widely available and therefore tend to be expensive. They are also larger in size. Section 4.2.3 discusses this problem further, and explains how motion blur has been overcome by using a flash light source.

The most suitable commercially available camera for building the particle-sizing instrument is the Sony XC-55 camera shown in Figure 4.3. Although the requirements for the high and low magnification systems are slightly different, it was decided that the same camera should be used in both cases, primarily to reduce the complexity of the design.

The main reasons for choosing the XC-55 camera are:

- **Analogue output** – Analogue cameras allow the transfer of images over long cable lengths without the loss of signal, they are also smaller and cheaper than their digital counterparts.
- **Monochrome images** - Since measurements of the particle colour are not needed, a monochrome camera has been used, thus providing high-resolution images at a low cost.
- **Low light sensitivity** - The XC-55 camera has a good minimum light sensitivity of 0.5 lux in comparison to other devices. This makes it useful for the present application because it allows a low powered light source to be used.
- **Small pixel size** - The CCD array consists of 659x494 individual square pixels, which are only 7.4x7.4 μm in size. Hence, the overall array size is 4.9x3.7 mm, conventionally known as a 1/3" array. Older cameras usually have a 2/3" array with larger pixels. The smaller pixel size on the XC-55 camera is beneficial because it means that a less powerful lens system is needed to resolve small particles. In addition, the fact that the pixels are square simplifies the implementation of image processing algorithms for the detection and sizing of particles.
- **Small dimensions** - Compared to other cameras with a similar specification, the XC-55 is relatively compact. The camera dimensions are 75x29x29 mm and it weighs only 110 g. Since two cameras are being used, this reduces the size of the overall system considerably.

- **Progressive scan capability** - In most standard CCD cameras, the pixel array is scanned twice on alternate lines to gain a single interlaced image. This causes problems when viewing moving objects since the second scan is taken fractionally after the first resulting in *striping* of the image. The XC-55 camera uses progressive scanning whereby all the pixels in the array are read in one sweep, thus eliminating this problem.
- **12V DC power supply** – Since the camera system is ultimately intended for use in the field it is vital that it can be powered from a battery. This camera requires 10.5-15 V DC, which makes it ideal for use with a standard car or boat battery. The camera also only draws 150 mA (i.e. 1.8 W) thus helping to reduce the overall power requirements of the system.

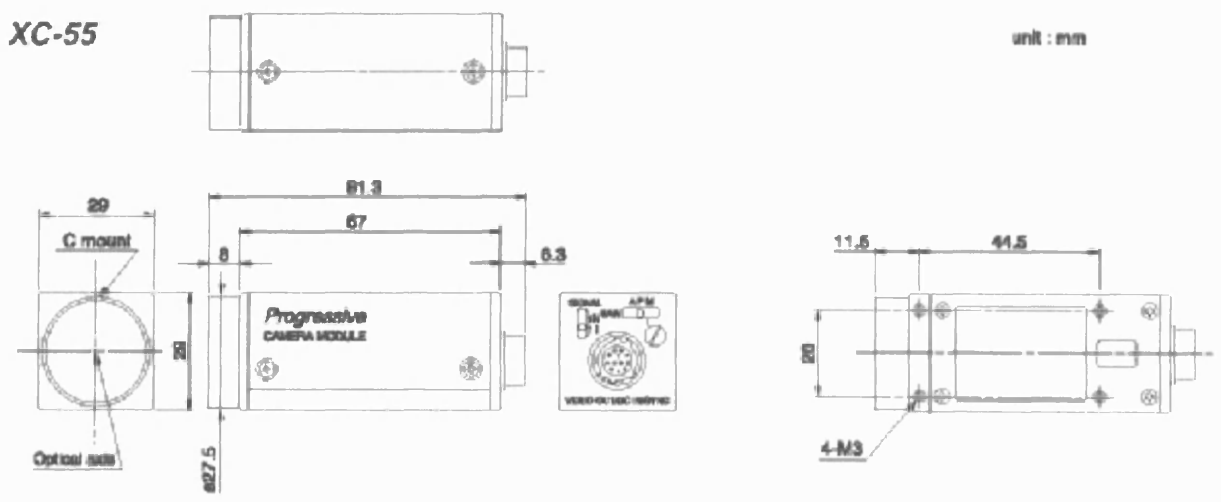

Figure 4.3 - The Sony XC-55 Progressive scan CCD camera.

4.2.2 Lens system and calibration

High-resolution system

For the high-resolution system, magnification is achieved by using a Nikon 20:1 M Plan extra-long-working-distance microscope objective lens. Standard microscope objectives have a maximum working distance of about 2 mm. This particular Nikon objective lens is chosen because it has a much greater working distance of 20 mm, achieved by using larger aperture optical components. This is important for two reasons. First, the camera needs to be sealed in a waterproof housing, thus requiring a window between the front of the lens and the water. Second, the focal point needs to be several millimetres from the outside face of the window where fluid shear is likely to be lower and, hence, where floc break-up will be minimised.

The lens is rated for use with a 210 mm microscope barrel for full magnification but by using a shorter barrel length (83.5 mm from the base of the lens to the CCD array) a magnification of approximately 9:1 is obtained (Figure 4.4a). This results in slightly poorer quality images, but it was deemed more important to keep the size of the housing within manageable limits.

Figure 4.5a shows an image taken of a 50 μm graticule line using the high powered lens. Figure 4.5b is the binary image formed after applying a threshold to the image (determined using the InSiPID segmentation software described in Section 4.3.3). The left and right graticule lines in the binary threshold image are made up of 29262 and 28917 pixels respectively. Since the image height is 480 pixels, the average width can be calculated to be 60.963 and 60.244 pixels, giving an overall average of 60.603, which compares visually with the pixel profile taken across the left line (Figure 4.5c). Hence, each pixel in the image is equivalent to 0.825x0.825 μm (i.e. 0.681 μm^2). According to the Rayleigh Criterion (Van Der Hulst, 1989), the minimum resolution of a system is said to be diffraction-limited when the first diffraction minimum of the image of one source point coincides with the maximum of another, where the diffraction angle $\sin\theta \approx \lambda/d$. This results in the minimum resolution being approximately equal to the wavelength of light used as the source illumination. Assuming a wavelength of 0.65 μm is used (i.e. that of red light), the diffraction limit is therefore within the size of one

pixel. Therefore, theoretically, the resolution of this system is limited by the pixel resolution. However, due to blurring of the images, a minimum pixel count of 18 is applied, thus giving a practical minimum resolution of ~4 μm. The upper limit of the particle size range is determined by the field of view. Since the number of pixels in the image and the pixel size is known, the field of view can be calculated to be 528x396 μm.

High magnification optical systems, particularly those with long working distances, have an unavoidably small depth of field (as is the case for standard microscopes). The depth of field of the high-resolution system used here is only of the order of a few tens of μm. At first this was considered to be a problem since it would provide a very small sample volume. However, it does have the advantage that, by providing a very narrow depth of field, the likelihood of particles overlapping one another in the image is reduced. This necessitates the processing of a large number of images in order to gain a representative sample of the true particle size distribution, but simplifies the analysis of the images.

Low-resolution system

The low-resolution system is fitted with a standard 12 mm Cosmicar/Pentax c-mount lens. This was combined with a 5 mm extension ring spacer to give a magnification of approximately 1:2.5 (Figure 4.4b), which enables the system to view particles up to a few millimetres in diameter. An image of a graticule taken with this lens system is shown in Figure 4.6a. The circle in the image has a diameter of 1 mm and is also shown in binary form, as a close up image (Figure 4.6b). The circle is made up of 2287 pixels. The area of each pixel, P, can be calculated from:

$$P = \frac{\pi r^2}{n} \tag{4.1}$$

where:

r = true radius of the calibration circle (μm)

n = number of pixels in the circle image

The true area of a 1000 μm diameter circle is 7.85×10^{-5} μm and therefore the area of each pixel is calculated to be $P = 343.419$ μm^2 (i.e.18.532x18.532 μm). The good quality of the low power images means that a minimum particle size of 9 pixels has been applied. This results in the low power system having a minimum resolution of ~63 μm, and a field of view of 11.86x8.90 mm.

The working distance of the low power lens system is 14 mm from the lens hood with the focus set to infinity, and the depth of focus is approximately 10 mm. The combination of both a wide field of view and large depth of field pose a slight problem because the light source element is imaged in the background. The following section describes how this problem was overcome.

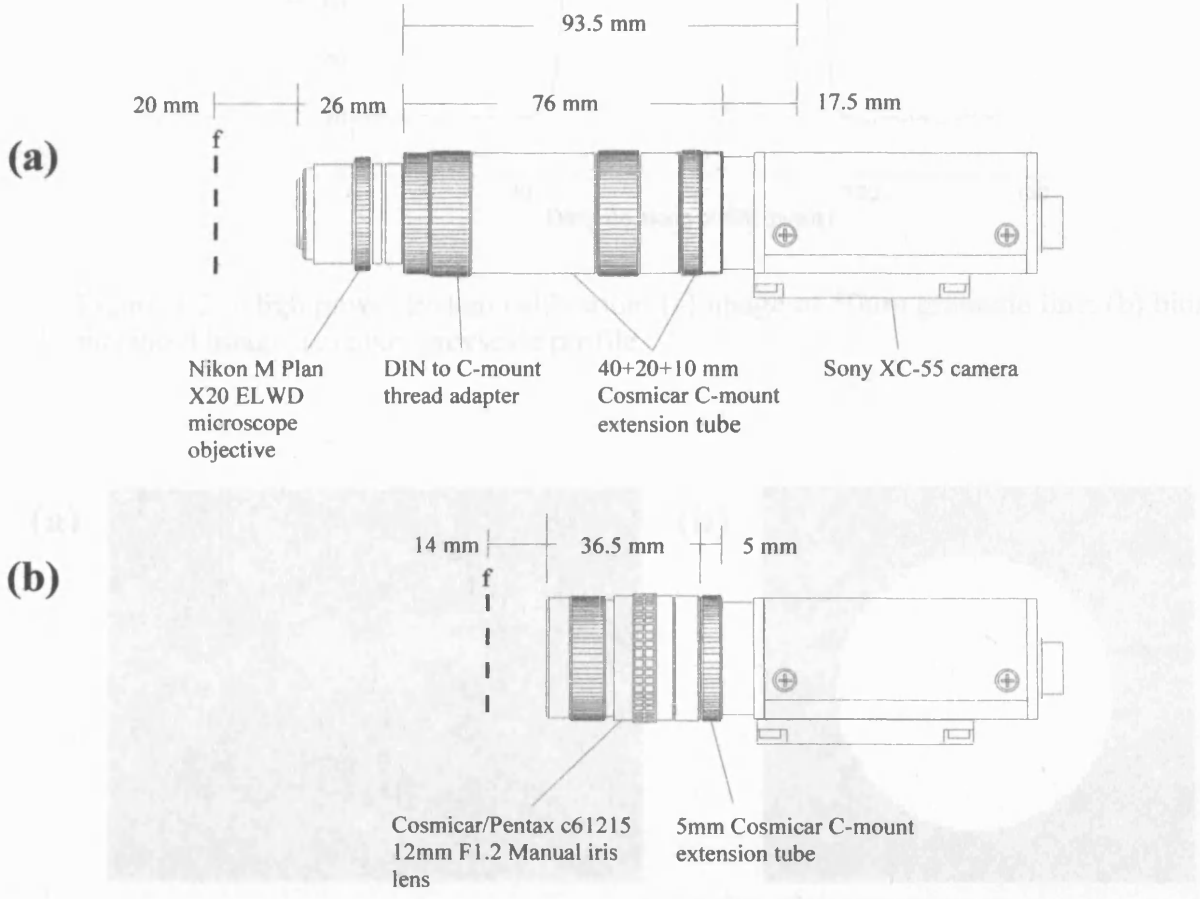

Figure 4.4 - The lens magnification systems: (a) high magnification - 9:1; (b) low magnification - 1:2.5.

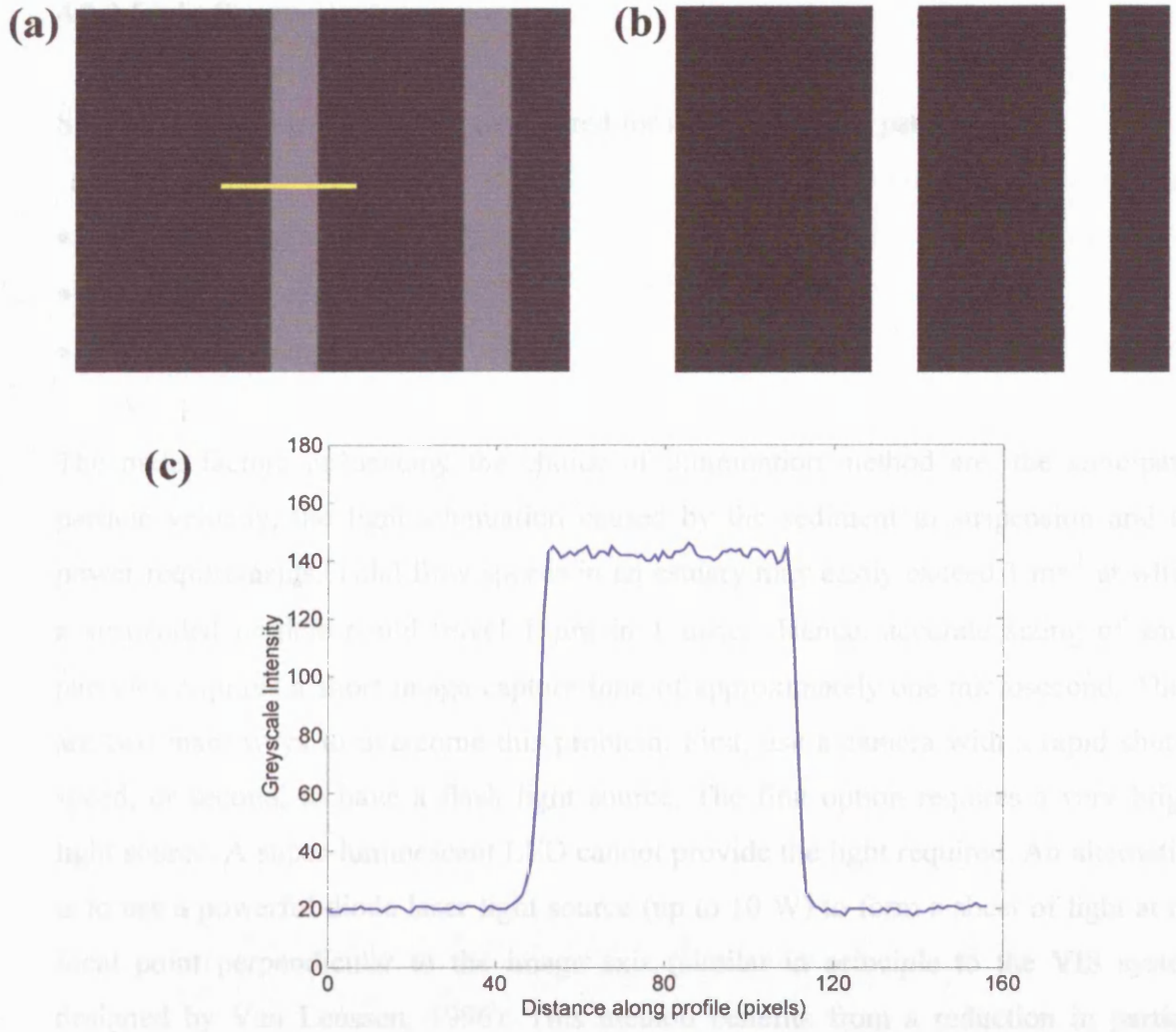

Figure 4.5 - High power system calibration: (a) image of 50μm graticule line; (b) binary threshold image; (c) pixel greyscale profile.

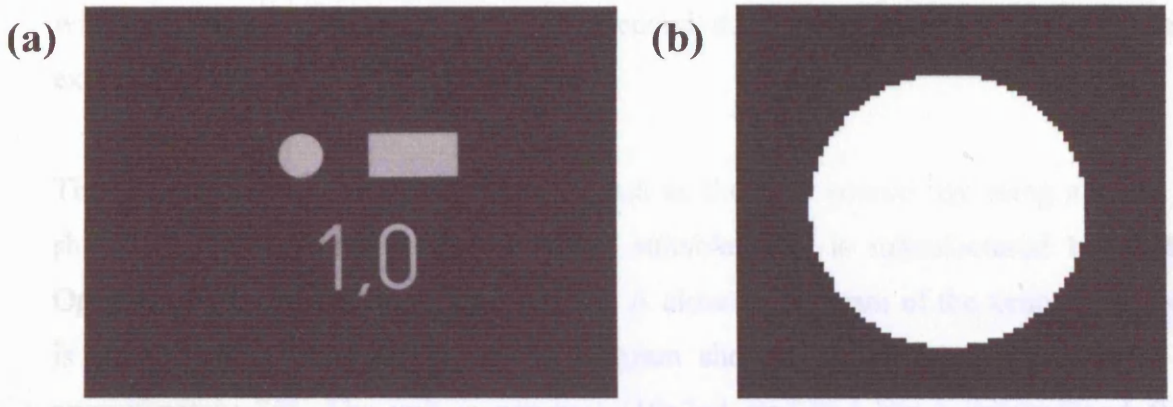

Figure 4.6 - Low power system calibration: (a) image of a 1 mm graticule marking with the low power camera; (b) binary close up of the circle.

4.2.3 Light Source

Several options were originally considered for illuminating the particles:

- Light Emitting Diode (LED)
- Laser light sheet
- Xenon flashlamp

The main factors influencing the choice of illumination method are: the anticipated particle velocity, the light attenuation caused by the sediment in suspension and the power requirements. Tidal flow speeds in an estuary may easily exceed 1 ms^{-1} at which a suspended particle could travel 1 μm in 1 μsec. Hence, accurate sizing of small particles requires a short image capture time of approximately one microsecond. There are two main ways to overcome this problem. First, use a camera with a rapid shutter speed, or second, to have a flash light source. The first option requires a very bright light source. A super-luminescent LED cannot provide the light required. An alternative is to use a powerful diode laser light source (up to 10 W) to form a sheet of light at the focal point perpendicular to the image axis (similar in principle to the VIS system designed by Van Leussen, 1996). This method benefits from a reduction in particle overlap within an image. However, using such a powerful laser creates a number of safety issues, and the design would have needed to provide heat sinking to prevent the diode from overheating. Power requirements would also be relatively high. Therefore, this option was discounted. As mentioned previously, another problem is that cameras with electronic shuttering of one microsecond duration tend to be specialised and expensive.

The chosen option was to use a xenon flash as the light source. By using a flash, no shuttering of the camera is required. A suitable unit, is manufactured by EG&G Optoelectronics (RSL-2100-1; Figure 4.7). A close up diagram of the xenon flash bulb is given in Figure 4.8 along with a diagram showing the solid beam angle to be approximately 25°. The unit is compact (10x3x4 cm) and has a microsecond flash duration, with ~40 mJ of energy per flash, covering a wide spectrum of wavelengths from blue to infrared (Figure 4.9). It is powered from a 12 V DC supply, which is useful for field operation, and has a TTL trigger to allow synchronisation to the cameras. A

separate flash unit is used for each camera system, rather than splitting the light, thus reducing the need for expensive, fragile optics.

Diffusers have been incorporated into both systems in order to create a uniform image background. For the low magnification system, a non-granular background illumination is achieved by using a flashed opal diffuser, mounted at a distance of 35 mm from the strobe bulb. Since the beam half-angle is approximately 25°, this creates a uniformly distributed back-light region with a diameter of ~30 mm, which is sufficient for covering the entire field of view of the low magnification system. The high magnification system is fitted with a ground glass diffuser since this attenuates the beam to a lesser degree. The depth of field of this system is small enough to prevent imaging of the diffuser itself.

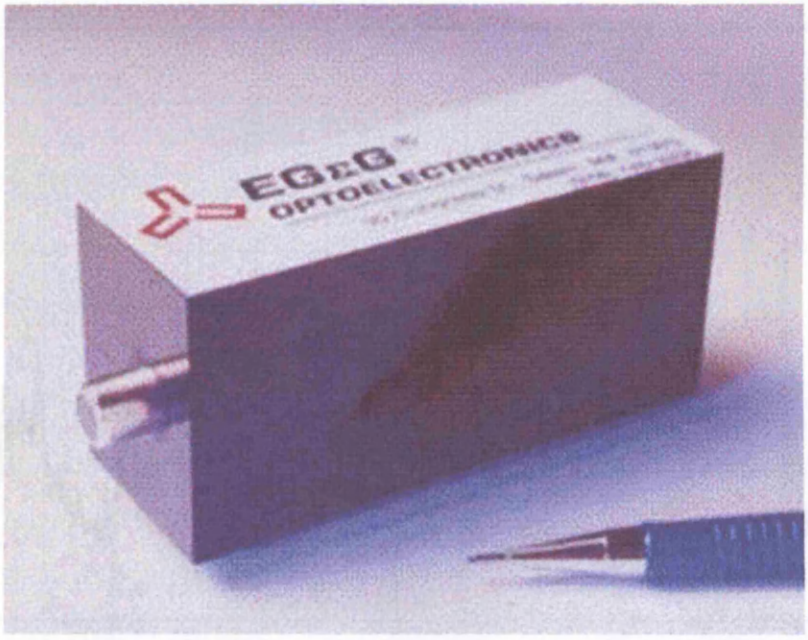

Figure 4.7 - The EG&G miniature microsecond xenon flash unit.

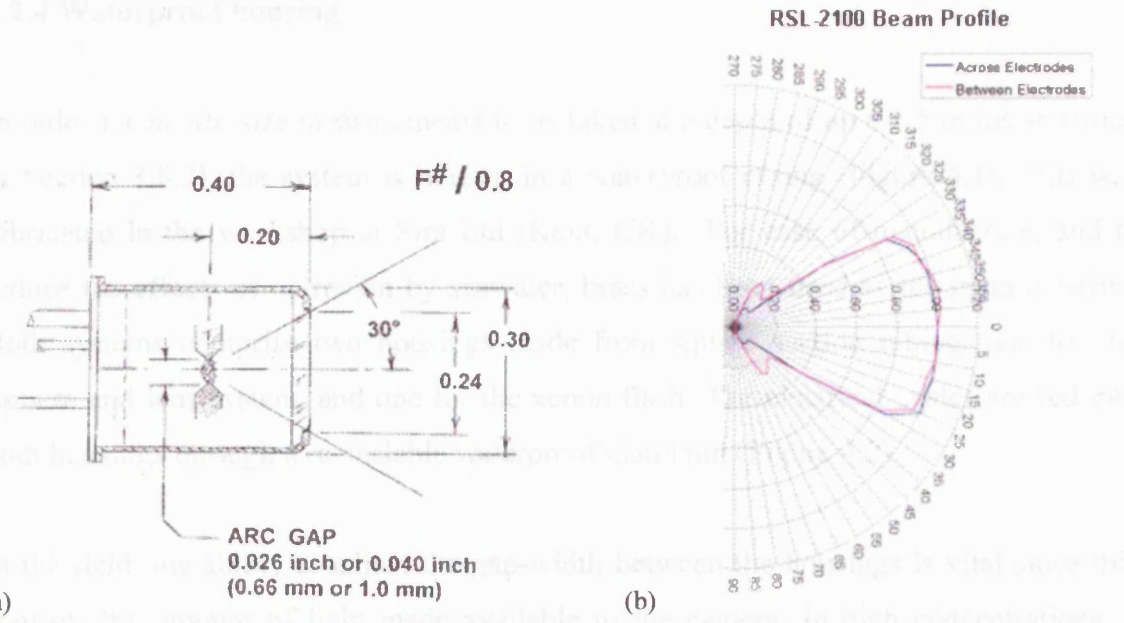

Figure 4.8 - (a) The RSL-2100-1 flash bulb (units in inchs); (b) Beam Profile.

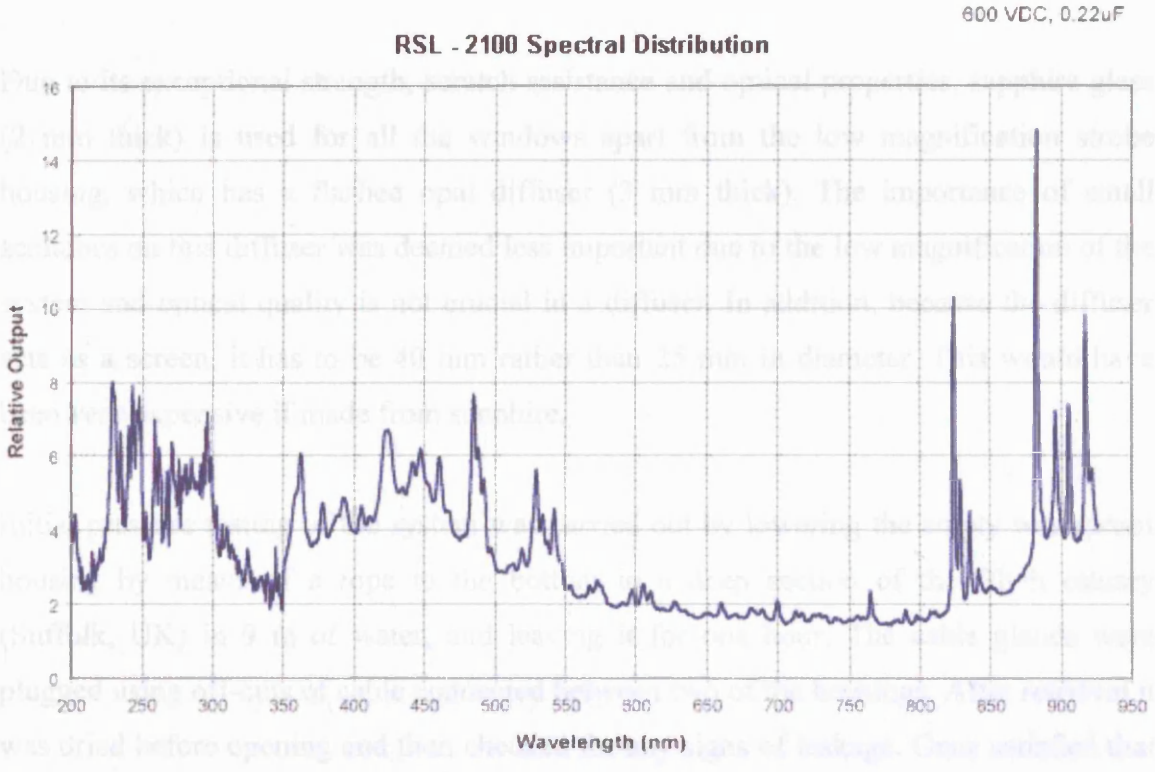

Figure 4.9 - Typical beam spectrum characteristics of the miniature flash (Manufacturers' data).

4.2.4 Waterproof housing

In order for *in situ* size measurements to be taken at a depth of up to 15 m (as specified in Section 3.8.2), the system is housed in a waterproof casing (Figure 4.1). This was fabricated in the workshop at Sira Ltd (Kent, UK). For ease of manufacture, and to reduce the effects of corrosion by seawater, brass has been used as the main material. Both systems comprise two housings made from square section tubing, one for the camera and lens system, and one for the xenon flash. The electrical cables are fed into both housings through a re-sealable waterproof gland nut (Figure 4.2).

In the field, the ability to adjust the gap-width between the housings is vital since this controls the amount of light made available to the camera. In high concentrations, a smaller gap is needed due to stronger attenuation of the beam. To solve this, the housings are fixed in position on a rigid brass strip using lock nuts, which can be loosened thus allowing both houses to be slid in either direction (thereby altering the gap-width).

Due to its exceptional strength, scratch resistance and optical properties, sapphire glass (2 mm thick) is used for all the windows apart from the low magnification strobe housing, which has a flashed opal diffuser (3 mm thick). The importance of small scratches on this diffuser was deemed less important due to the low magnification of the system and optical quality is not crucial in a diffuser. In addition, because the diffuser acts as a screen, it has to be 40 mm rather than 25 mm in diameter. This would have been very expensive if made from sapphire.

Initial pressure testing of the system was carried out by lowering the empty waterproof housing by means of a rope to the bottom in a deep section of the Blyth estuary (Suffolk, UK) in 9 m of water, and leaving it for one hour. The cable glands were plugged using off-cuts of cable connected between two of the housings. After retrieval it was dried before opening and then checked for any signs of leakage. Once satisfied that there was no water entering the housing, the camera and strobe components were refitted into the housing. Although further pressure testing is required in order to verify that the casing can withstand greater pressures, the depth of the Blyth estuary does not exceed 9 m, and therefore this is satisfactory for the current project.

4.2.5 Computer and framegrabber

During the initial stages of the design of the camera system, a Pentium III 450 MHz desktop PC, fitted with a Matrox Pulsar video capture card, was used for digitising the images. In order to grab images from each camera, a program was written in the C programming language, which incorporated the Matrox Imaging Library (Mil-Lite) software. The full program code is given in Appendix A. Clearly this computer set-up is not ideal for use in the field, and therefore a portable system was developed, the details of which are outlined below.

When considering the options available, the possibility of using a laptop computer system was investigated. However, all but the most expensive laptops do not support PCI card framegrabbers and currently there are no available PC-card (PCMCIA) framegrabbers that provide TTL triggers outputs, or which can be used with multiple, progressive scan cameras. Some currently available laptops are provided with a docking station. Essentially, these are add-on boxes that allow PCI cards to be used with laptop computers. However, tests with a docking station and a Matrox Pulsar framegrabber were unsuccessful due to compatibility problems. Docking stations are also bulky and tend to have high power requirements since they are designed desktop use.

The most suitable option in terms of cost and development time has been to use components that comply with the 'PC/104-*plus*' standard (PC/104-*plus* Embedded Consortium, 2001). These are low power stackable boards made to a compact size specification of roughly 10 cm x 10 cm. Most board manufacturers now offer this standard as an alternative to PCI cards. For the system proposed, a minimum of three components are needed, namely:

- a programmable CPU board
- a progressive scan compatible framegrabber
- a hard disk for storing images

A commercially available device, which satisfies these requirements, is the Matrox 4Sight II (Figure 4.10). Although this system is slightly more expensive than a laptop

computer (£2000 in the UK in 2004), it has several benefits that make it the most suitable option, namely:

- An integrated framegrabber with strobe outputs, and multiple progressive-scan camera capabilities.
- 12V dc power input, thus requiring no additional transformers or inverters.
- TV-output, allowing the use of a cheap television monitor, rather than a more expensive LCD panel.
- Standard PC operating system (i.e. Windows NT and Mil-Lite), allowing rapid software development and interoperability with desktop PCs.
- Room for additional PC/104-plus cards for future upgrades.

In this system, images are grabbed from both cameras and stored directly to hard disk for processing at a later date. This method is simpler than attempting to obtain real-time measurements of particle size, which requires rapid processing speeds. When saved in TIFF file format, the required memory for each image is approximately 300 KB. Compressing each file using a program such as PKZIP can approximately halve this. Consequently, a 6 GB hard drive holds about 40,000 compressed images (20,000 from each camera). To allow the 4Sight to be used in the field, it is housed in an aluminium flight case, fitted with waterproof connectors (Figure 4.11).

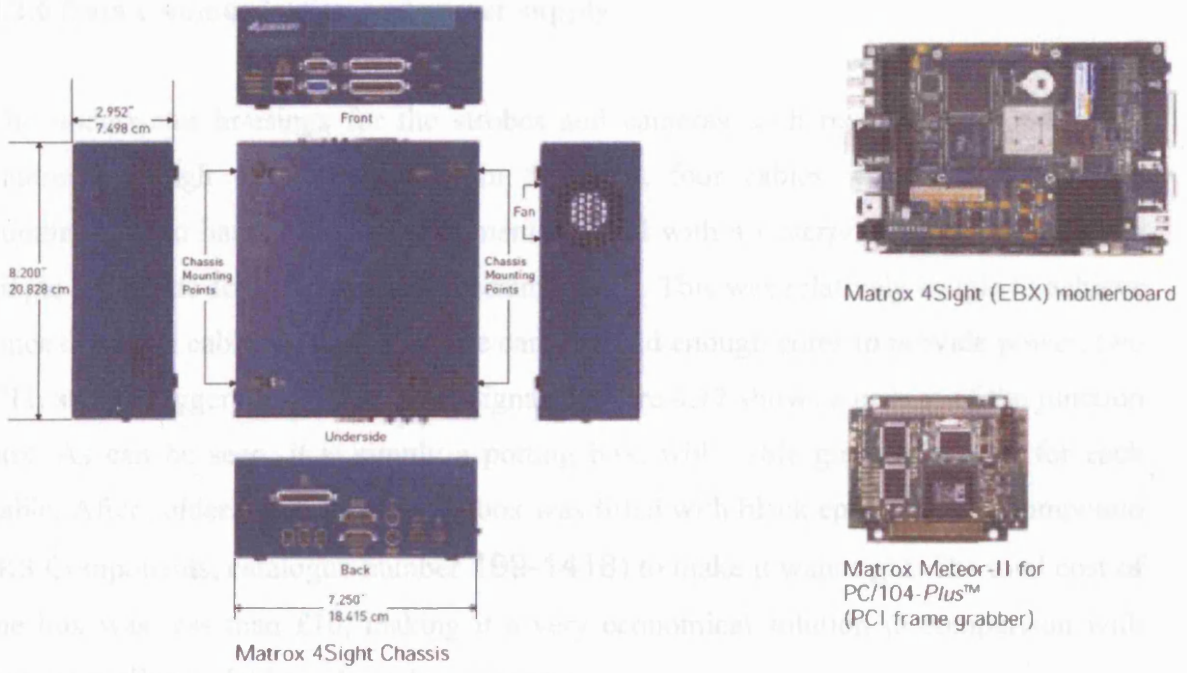

Figure 4.10 - The Matrox 4Sight II standalone imaging system (Matrox Imaging Ltd.; http://www.matrox.co.uk).

Figure 4.11 – Customised housing for computer components

4.2.6 Data communication and power supply

The underwater housings for the strobes and cameras each require a separate cable entering through the cable gland. In the field, four cables would have been too cumbersome to handle, so the instrument is fitted with a waterproof junction to split a single cable into four cables at the instrument end. This was relatively simple to achieve since the 25 m cable supplied with the cameras had enough cores to provide power, two TTL strobe triggers and two camera signals. Figure 4.12 shows a picture of the junction box. As can be seen, it is simply a potting box, with cable glands attached for each cable. After soldering the cables, the box was filled with black epoxy potting compound (RS Components, catalogue number 199-1418) to make it watertight. The total cost of the box was less than £10, making it a very economical solution in comparison with commercially available underwater connectors.

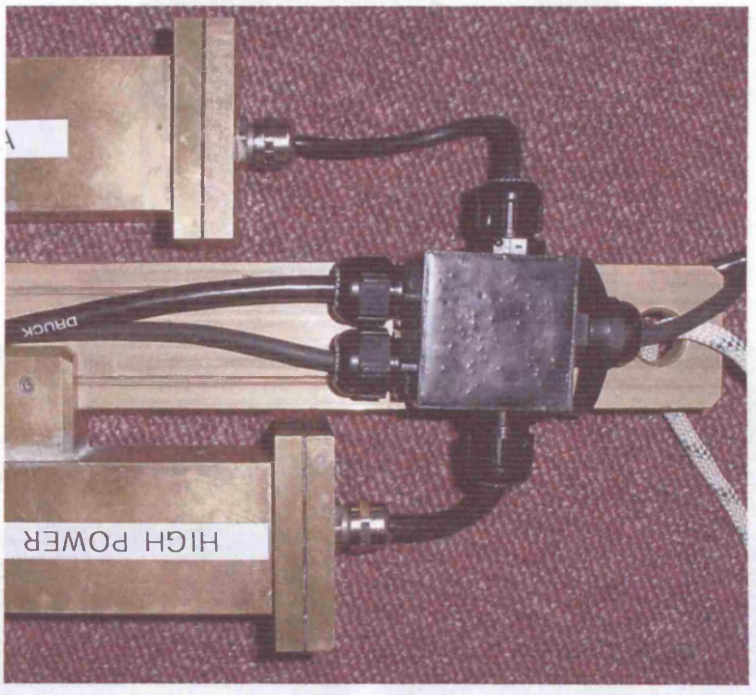

Figure 4.12 – Close up of underwater junction box for splitting cables

4.2.7 Additional instrumentation

In order to incorporate additional instrumentation into the system, an analogue to digital converter (ADC) has been added. A 12-bit ADC from Quasar Electronics™, has been used which connects to the parallel port of the 4SightII (Figure 4.13a). This has the capability of receiving 8 single ended analogue inputs and 4 digital inputs. The software written to collect data using this ADC is presented in Appendix A.

Two additional instruments are included in the current InSiPID configuration. These are a Druck™ pressure sensor (PTX 1830 series) for recording depth below the surface (Figure 4.13b), and a Partech™ transmissometer (IR40C) for recording turbidity (Figure 4.13c).

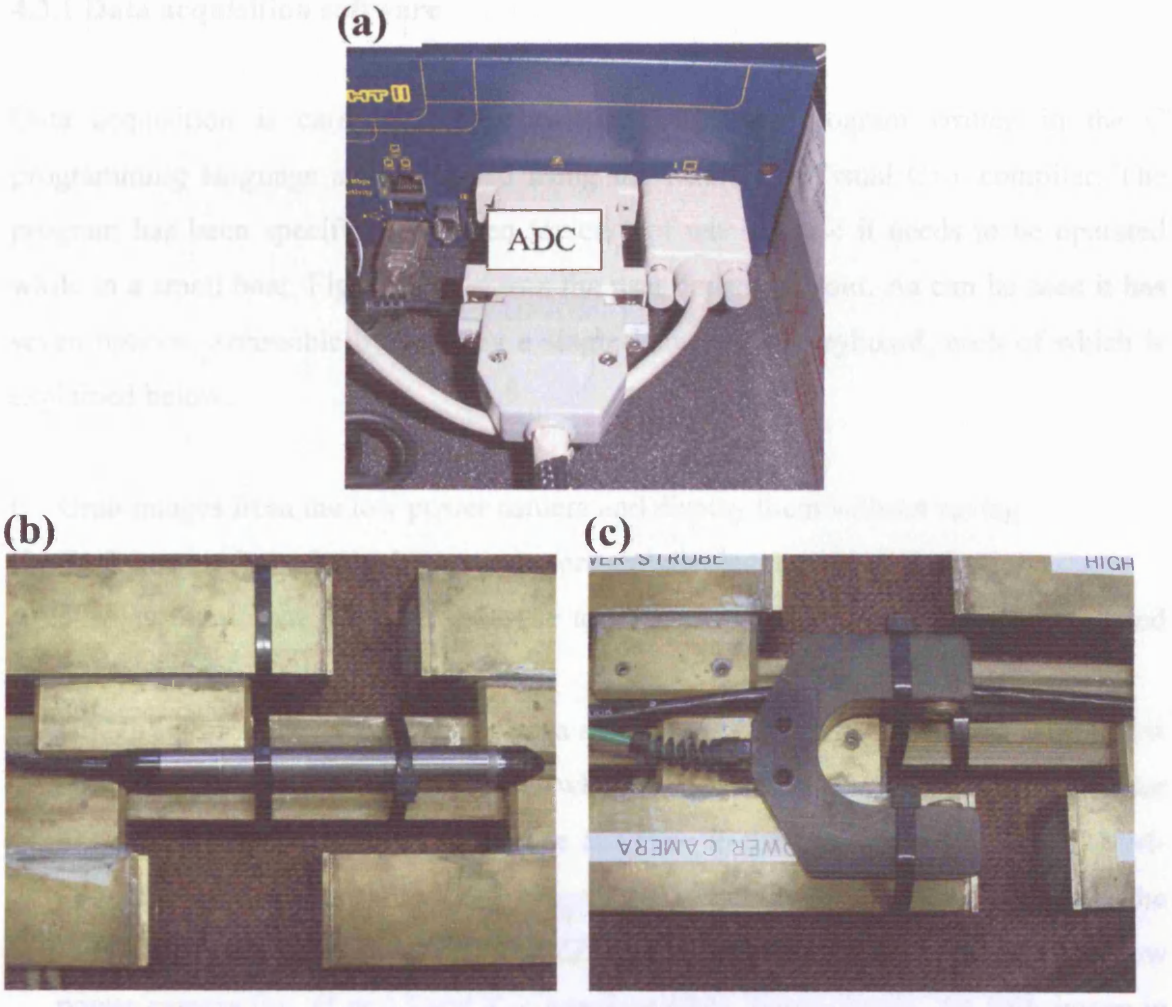

Figure 4.13 – Additional instrumentation: (a) Quasar Electronics parallel port ADC; (b) Druck pressure sensor; (c) Partech IR40 transmissometer.

4.3 Software components

As mentioned in Section 4.2.5, the collection of data is carried out in two stages. First, the images are saved digitally to hard disk, along with the data from the pressure sensor and transmissometer. Second, the images are processed to find the particle size distribution. Using this method, it is possible to use MATLAB (version 6.0; Mathworks, 1998) off-line for the image processing, even though the processing speed is slow in comparison to compiled C or Fortran code. The MATLAB image processing add-on toolbox costs approximately £250, whereas a dedicated image-processing package would have cost around £3000. Two separate pieces of software have therefore been written for the acquisition and subsequent analysis of the images (Appendix A).

4.3.1 Data acquisition software

Data acquisition is carried out via a Win32 Console program written in the C programming language and compiled using the Microsoft Visual C++ compiler. The program has been specifically written for ease of use because it needs to be operated while in a small boat. Figure 4.14 shows the user console layout. As can be seen it has seven options, accessible by pressing a single letter on the keyboard, each of which is explained below:

L Grab images from the low power camera and display them without saving.

H Grab images from the high power camera and display them without saving.

A Display the output from the analogue to digital converter (i.e. pressure sensor and transmissometer output).

G Grab a set of images from each camera and save to hard disk. At the start of the first set of images a new folder is created which stores the image files. Each new folder has a unique name containing the date and time in the following format: YY-MM-DD-HH-MM-SS. The individual images are saved in TIFF format and have the following filename layout XXX_Y_ZZZ.tif, where X = set number, Y = high or low power camera (i.e. H or L) and Z = image number. For example, the fifth image in the first set from the high powered camera would be 001_H_005.tif.

N Create a new folder to store the image sets. Before continuing, the user is asked by the program whether to compress all the images in the current profile folder to a single file (images.zip). The compression is performed using a command line version of Winzip™ (http://www.winzip.com/wzcline.htm).

S Change the settings. This allows the user to define:

(a) The hard drive partition to which to save the image folders.

(b) The ratio of images grabbed from the low and high magnification cameras.

(c) The number of iterations of this grab ratio.

(d) The pause time between each image (with a minimum of 0.1 s).

(e) Whether or not to use dummy images (used for software debugging when the cameras are not connected).

Q Quit from the program. If not already done so, the user is asked whether to compress the images in the last profile folder.

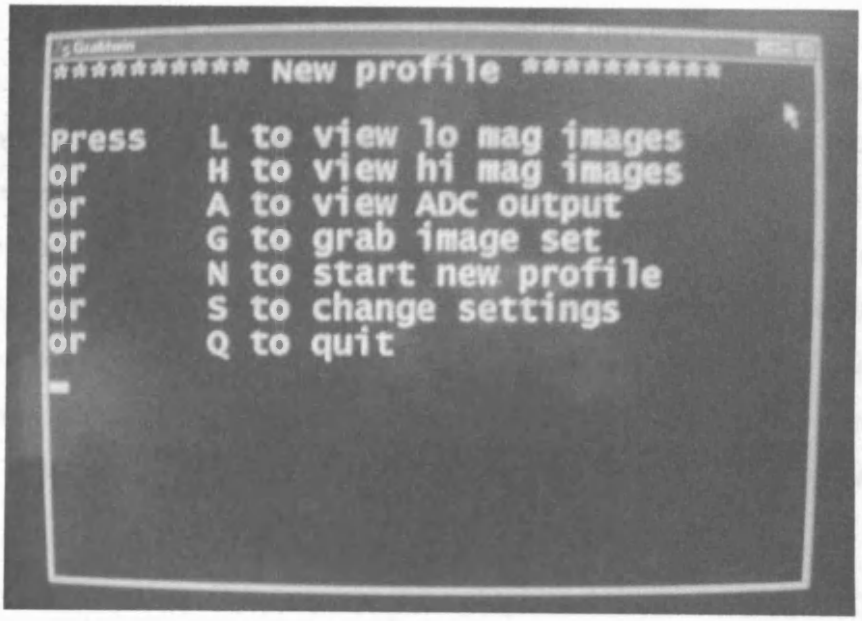

Figure 4.14 – User console window for data acquisition.

After saving the digitised images to a TIFF format file on the computer hard disk, the particles are counted using an image-processing program written in the MATLAB programming language, and utilising specialised routines provided in the Image Processing Toolbox. Elements of the approach and the algorithms used are outlined below.

4.3.2 Noise filtering

Reference image subtraction

The main image processing stages are shown as a sequence of images (Figure 4.20 to Figure 4.27). The first stage of the image processing is to remove any possible sources of noise (*RemoveNoise.m* in Appendix A). Much of the unwanted noise is removed from the high and low-resolution test images (Figure 4.20) by subtracting a reference image (Figure 4.21), which is simply the average of all the images in each set. The resultant image is therefore assumed to correspond to the permanent light intensity. By subtracting the reference image from each consecutive test image and then rescaling from between 0 to 255, the resultant image (Figure 4.22) should theoretically only contain the time varying components (i.e. the suspended sediment).

A problem with this procedure becomes apparent when there are no particles in the test image (i.e. when the raw image is almost identical to the reference image). When this occurs, the resultant image after subtraction of the reference and rescaling is essentially a noise image. If this image is passed onto the counting and sizing routine in the program, it results in an apparent abundance of very small particles in the water, whereas in fact they are merely amplified electrical noise. A simple method for detecting such images has been devised based on the fact that any particles in the image will result in negative pixel values after subtracting the reference (before rescaling). The program has therefore been modified to look for instances where the minimum difference between the reference and real image exceeds a critical negative value, defined as:

$$\left|(I-R)_{\min}+\bar{I}-\bar{R}\right|>T_c \tag{4.2}$$

where:

$(I-R)_{\min}$ = minimum pixel intensity difference between test and reference images

$\bar{I}$ = mean intensity in test image

$\bar{R}$ = mean intensity in reference image

T_c = critical test threshold value to be exceeded

After carrying out a number of visual tests with over 100 images, the threshold value (T_c) was set to -13 grey levels which corresponds to ~5% of the greyscale range (MATLAB uses a scale of 0 to 1, rather than 0 to 255, so the actual value used is -0.05).

On rare occasions, it is possible for the captured image to appear completely black (although in reality the image is never completely black due to noise). This may occur if the strobe has failed to flash, or if it has lost synchronisation with the camera. It may also happen if a large object obscures the image entirely. These *dropout* images are useless since they contain no particle data, and may cause problems in the referencing routine. A dropout test is therefore applied to each image. In this test, the modal pixel value of each image is determined and, if it is below a threshold value, the image is discounted. The chosen threshold value is 0.05 (i.e. 13 grey levels). Such images are detected by the program during the making of the reference image (*MakeRef.m*), and a list of good images is then passed on to the rest of the program.

High frequency filtering

All digitised images contain some high frequency electronic noise. Much of this noise is introduced as the signal travels through the cable from the camera to the framegrabber. Since this system uses a 25 m cable, Gaussian noise is clearly present in the images (Figure 4.15a). Therefore, a low pass filter is applied to each image. This filter uses a pixel-wise adaptive Wiener method (Gonzalez & Woods, 2002) based on statistics estimated from a local neighbourhood of each pixel. For each MxN neighbourhood (η) around each pixel ($a(n_1,n_2)$), the local mean (μ) and variance (σ^2) is estimated as given below:

$$\mu = \frac{1}{NM} \sum_{n_1,n_2 \in \eta} a(n_1, n_2) \tag{4.3}$$

$$\sigma^2 = \frac{1}{NM} \sum_{n_1,n_2 \in \eta} a^2(n_1, n_2) - \mu^2 \tag{4.4}$$

In this case the smallest neighbourhood block size of 3x3 was used. These estimates are then used to create a pixel-wise Wiener filter of the following form:

$$b(n_1,n_2)=\mu+\frac{\sigma^2-\nu^2}{\sigma^2}\left(a(n_1,n_2)-\mu\right) \tag{4.5}$$

where ν^2 is the noise variance. If the noise variance is not given, the average of all the local estimated variances is used instead. An example of how this improves the image quality for the low-resolution system is shown in Figure 4.15b and in the sequence of images in Figure 4.23.

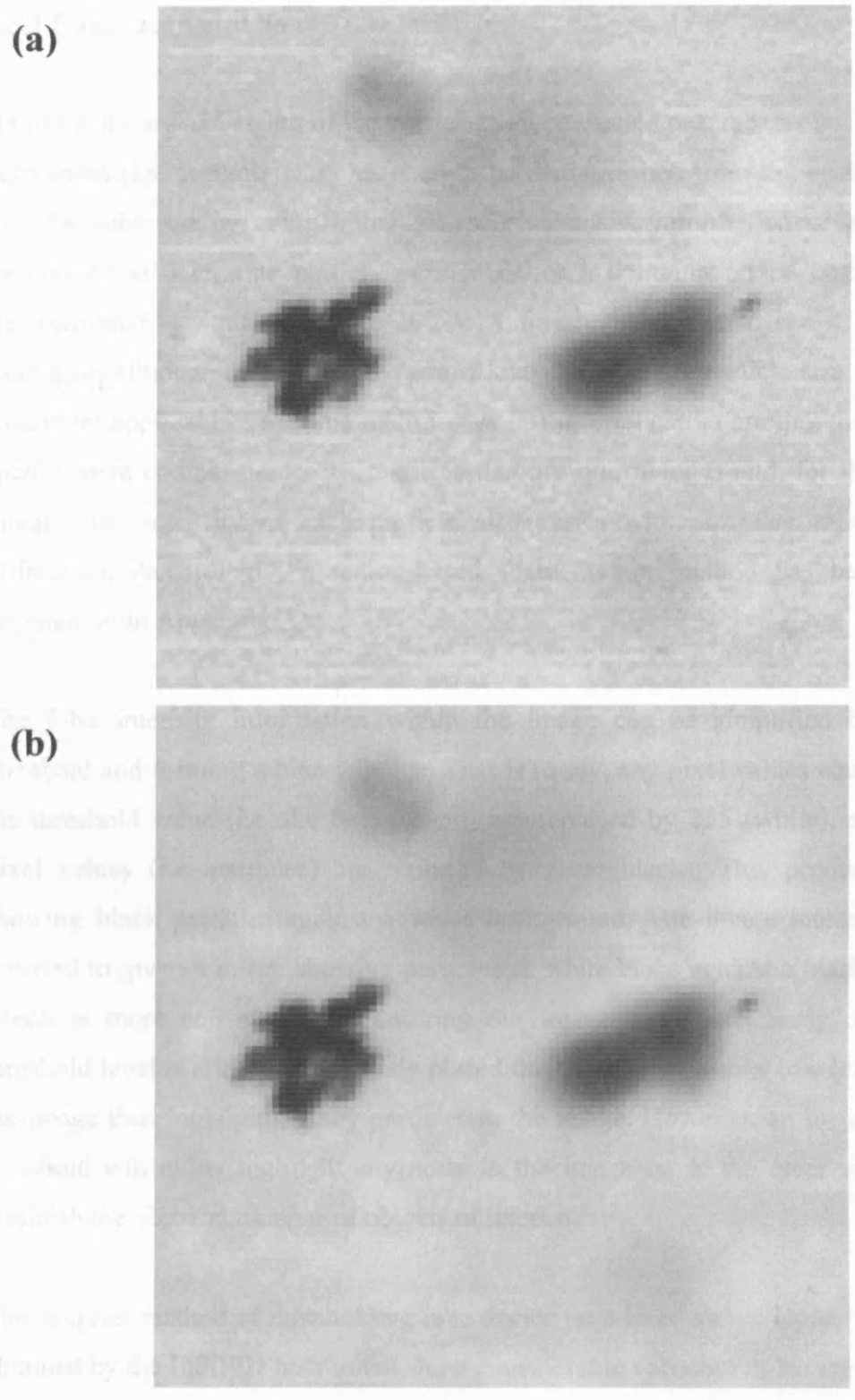

Figure 4.15 – 100x100 pixel sub-sample of a low-resolution image (a) before filtering; and (b) after applying Wiener filter, showing a reduction in the image 'graininess'. Although this appears minimal to the naked eye, it greatly reduces the detection of false particle edges in the segmentation stage.

4.3.3 Image segmentation

Before counting and sizing of the particles can be carried out, the test image needs to be segmented (i.e. separate particles need to be distinguished from the background). This may be achieved by using either the pixel intensity information or edge detection techniques to determine particle perimeters, or a combination of both known as a 'region-based' technique (Jähne, 2002). A fourth method is to use a 'model-based' technique, although these require *a priori* knowledge of the particle size and shape and so are not applicable here. The main issues in this application are that the images from each camera contain numerous particles that are out of focus and, for the high power images, the intensity of each particle also varies with size due to the effects of diffraction. Accordingly, a region-based segmentation method has been developed (*segment.m* in Appendix A).

The 8-bit intensity information within the image can be simplified by applying a threshold and forming a binary image. That is to say, any pixel values equal to or above the threshold value (i.e. the background) are replaced by 255 (white), and any lower pixel values (i.e. particles) are replaced by zero (black). This produces an image showing black particles against a white background. The image intensities are then inverted to give an image showing particles as white blobs against a black background, which is more convenient for carrying out image analysis. Clearly, the choice of threshold level is critical. A correctly placed threshold will remove low level noise from the image thus highlighting any particles in the image. However, an incorrectly chosen threshold will either highlight any noise in the image or, at the other extreme, might diminish the size and number of objects of interest.

The simplest method of thresholding is to decide on a fixed value. However, the images obtained by the InSiPID instrument show considerable variation in background intensity due to varying particle concentrations and the presence of out of focus particles. Therefore, an automated method of thresholding has been developed. There are many different methods of automatically determining the correct threshold, the most common of which fall into the following categories:

(1) Histogram shape-based methods where the peaks, valleys and curvatures of the histogram are analysed (Rosenfeld & De la Torre, 1983; Sezan, 1985; Olivo, 1994; Carlotto, 1997).
(2) Clustering-based methods where the grey levels are clustered in two parts as background and foreground (object) by modelling as two Gaussian distributions (Ridler & Calvard, 1978; Trussel, 1979; Otsu, 1979; Kittler & Illingworth, 1986; Yanni & Horne, 1994; Leung & Lam, 1996), or by comparing their entropies (Pun, 1981; Kapur *et al*, 1985; Li & Lee, 1993; Shanbag, 1994; Yen *et al*, 1995; Brink & Pendock, 1996; Sahoo *et al*, 1997; Pal, 1996; Li & Tam, 1998; Cheng *et al*, 1999).
(3) Object attribute-based methods, which measure the similarity between the grey-level and the binary image, such as shape, texture, edges, number of objects or fuzzy similarity (Rosenfeld, 1984; Tsai, 1985; Pal & Rosenfeld, 1988; Toriu *et al*, 1990; Cheng & Tsai, 1993; Hertz & Schafer, 1993; O'Gorman, 1994; Huang & Wang, 1995; Pikaz & Averbuch, 1996).

Histogram and clustering-based methods are essentially the same since they analyse the intensities of the individual pixels to determine a global threshold value (i.e. they are pixel-based techniques). Both methods assume that, for an image containing opaque particles with back-illumination, the histogram of the pixel intensities should show a bimodal distribution with two distinct maxima: one for the particles and another for the background (Jähne, 2002). The optimum threshold is the lowest point between these two distributions. Histogram methods attempt to locate this point by geometric analysis of the greyscale histogram itself, whereas clustering based methods use a more statistical approach. Both methods are useful where there are two distinct peaks in the histogram. However, in many applications the distributions are difficult to distinguish from one another, especially where there are many small objects in the image (Jähne, 2002). This was the case with the InSiPID images due to the presence of out of focus particles.

Otsu (1979) gives a commonly used example of a clustering-based threshold method. By this method, the threshold value is determined by minimising the intraclass variance of the thresholded black and white pixels. Figure 4.17b shows the application of this method to a low-resolution InSiPID image (Figure 4.17a). It is apparent that the estimated threshold level (T=172) is too high resulting in the inclusion of some

background intensity. This method is clearly not suitable for distinguishing regions of the image that are in focus.

Consequently, it was decided to develop a thresholding method using a combination of an object attribute method (based on edge sharpness) and histogram analysis. Toriu *et al* (1990) developed a method of determining the correct threshold using edge coincidence, later developed further by Hertz & Schafer (1993). In this method a thinned edge field is obtained from the greyscale image and is then compared with the edge field derived from the binary threshold image. The threshold is then iteratively adjusted until there is maximum coincidence between the images (Figure 4.18). Coincidence is measured using the edge measure, which is a count of the number of common edges (*CE*), with a penalty for excess original edges (*EO*) and excess thresholded image edges (*ET*), given as:

$$Em = \frac{CE}{CE + EO + ET} \tag{4.6}$$

where:

Em = edge measure
CE = coincident edges
EO = excess original edges
ET = excess thresholded image edges

A problem with this method, however, is that it is relatively time consuming since the location of the edge measure maximum is not known and many iterations may be required to converge on a suitable global threshold value. This is of particular importance here since the InSiPID instrument is designed to record about 1000 images per depth profile, and hence processing time becomes an issue. The method also applies only a single global threshold value. The resultant threshold is therefore an approximation for the entire image, and biases may be introduced if there is variation in the intensity of the particles. Figure 4.17c shows the outcome of applying the threshold determined by this method. In this example, the edge threshold gradient is 0.07. It can be seen that much of the detail is extracted from the image, but out of focus regions are also included and poorly contrasted particles are ignored. Therefore, an edge coincidence method has been developed whereby several thresholds are applied and in

focus particle information is extracted at each level. In this way, particles with poor contrast may be identified. The fully automated segmentation process consists of the following stages: (1) Dark-side edge detection; (2) analysis of the edge pixel greyscale intensities to obtain threshold values; (3) multiple binary thresholding; and (4) removal of out of focus particles at each threshold.

First, an edge detection image is obtained by means of a two-dimensional convolution of the input greyscale image array with a sliding operator matrix. For the low power system, a 3x3 sliding operator Sobel filter (Gonzalez & Woods, 2002) is used (Figure 4.16a). For the high magnification system, the poorer quality of the images has necessitated the use of a 21x21 sliding operator Gaussian filter (Figure 4.16b), which detects more blurred particle edges and is less sensitive to noise. The sliding operators are applied in two iterations in the x and y directions, thus obtaining both the vertical and horizontal edges. A series of visual tests were carried out in order to determine a suitable value for the edge strength thresholds for both filters, which are applied whilst locating the edge gradient maxima. Values of 0.07 and 0.35 have been set for the Sobel and Gaussian edge detectors respectively.

A simple modification that has been applied to both edge detectors has been developed for this application in order to maximise the coincidence of the edge pixels and the thresholded image pixels. This process, referred to as *dark-side edge thinning,* is achieved during the thinning of the edge gradients. Normally during the edge detection process, single thickness local maxima are located in order to create the final edge image from the edge gradient image. This results in edge pixels that are distributed on either side of an edge feature. With dark-side edge thinning, however, the second highest local maxima are also located, resulting in a double thickness edge. The double edge image is then used to retrieve the corresponding pixel intensities from the greyscale image through masking. Since it is known that the objects in the image are dark, the side of the double edge with the maximum greyscale value is then discarded, resulting in a single thickness edge with the pixels selected over the dark side of the edge. A histogram of the edge pixel intensities with normal thinning (Figure 4.19b) shows that much of the background intensity in the entire image (Figure 4.19a) is discarded. The additional use of dark-side edge thinning clearly reduces the intensities further (Figure 4.19c). It is now assumed that the peaks in this histogram correspond to the main features in the image, and hence these are the locations of the thresholds.

To extract these peaks, the histogram is first smoothed using an approximated eleven-element Gaussian filter, with a standard deviation of 1.5. This is applied to the histogram in both directions in order to prevent a shift in the position of any peaks. The maxima are then obtained from the histogram (Figure 4.25) and the greyscale intensities of all the maxima are then used as threshold values, above which image intensity information is rejected. Any thresholds not within the range of 50 to 200 are discarded since these are unlikely to contain any particle data and may contain noise.

It was found that the low contrast of the high-resolution images resulted in greater noise levels, which occasionally caused large noise peaks in the histogram. Most of this noise appeared as bright horizontal streaks in the image. Therefore, for the choice of the high-resolution binary threshold values, only the vertical edges are used.

The final stage in the segmentation process is to remove out of focus particles from the binary image. At each threshold value, particles are chosen according to the coincidence ratio (R_e) between their perimeter pixels in the binary image (Figure 4.26) and the corresponding edge detected pixels (Figure 4.24). The low and high-resolution systems have been assigned minimum edge coincidence ratios of 0.3 and 0.15 respectively. The lower ratio for the high power images is necessary due to the poorer focus, and hence reduced chance of pixel coincidence (in this case both the vertical and horizontal edges are used in both systems). For each suspected particle in the current threshold image, if the edge coincidence ratio is greater than that in the previous threshold (and greater than the minimum), the particle is kept. In effect, a spatially varied threshold is applied. After removal of any out of focus particles not satisfying this criterion, each consecutive binary threshold image is combined with the previous one. Once all the thresholds have been applied, the resultant binary image (Figure 4.27) contains particle information ready for sizing and counting. As seen in Figure 4.17d, unlike the method of Otsu (1979) or Toriu *et al* (1990), this method is capable of ignoring out of focus particles, yet retains most of the important particle information.

(a)

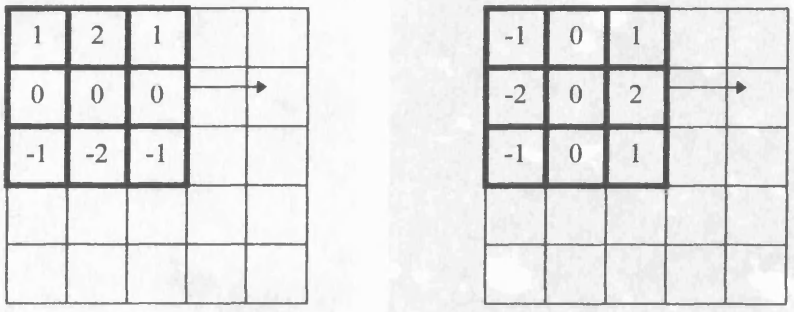

Horizontal edges Vertical edges

(b)

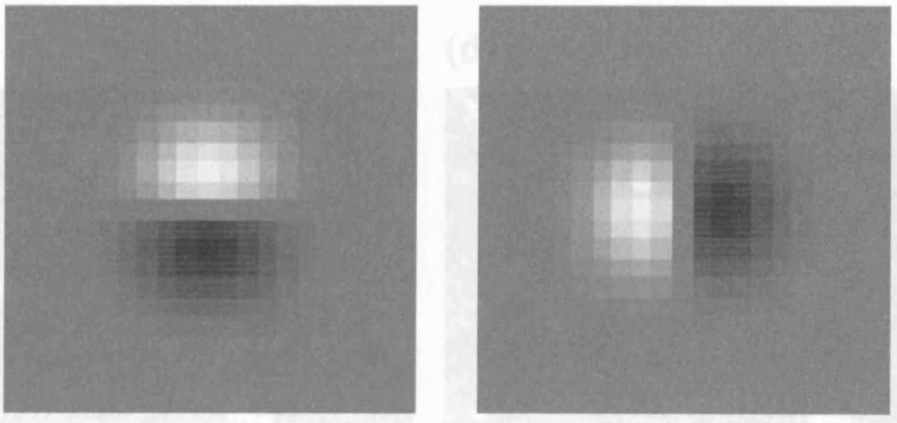

Figure 4.16 – The edge detection operators: (a) schematic diagram of the implementation of a 3x3 Sobel operator used for the low power images; (b) normalised greyscale image of the 21x21 Gaussian edge detection operator (standard deviation = 2) used for the high power images: (i) horizontal edges, (ii) vertical edges.

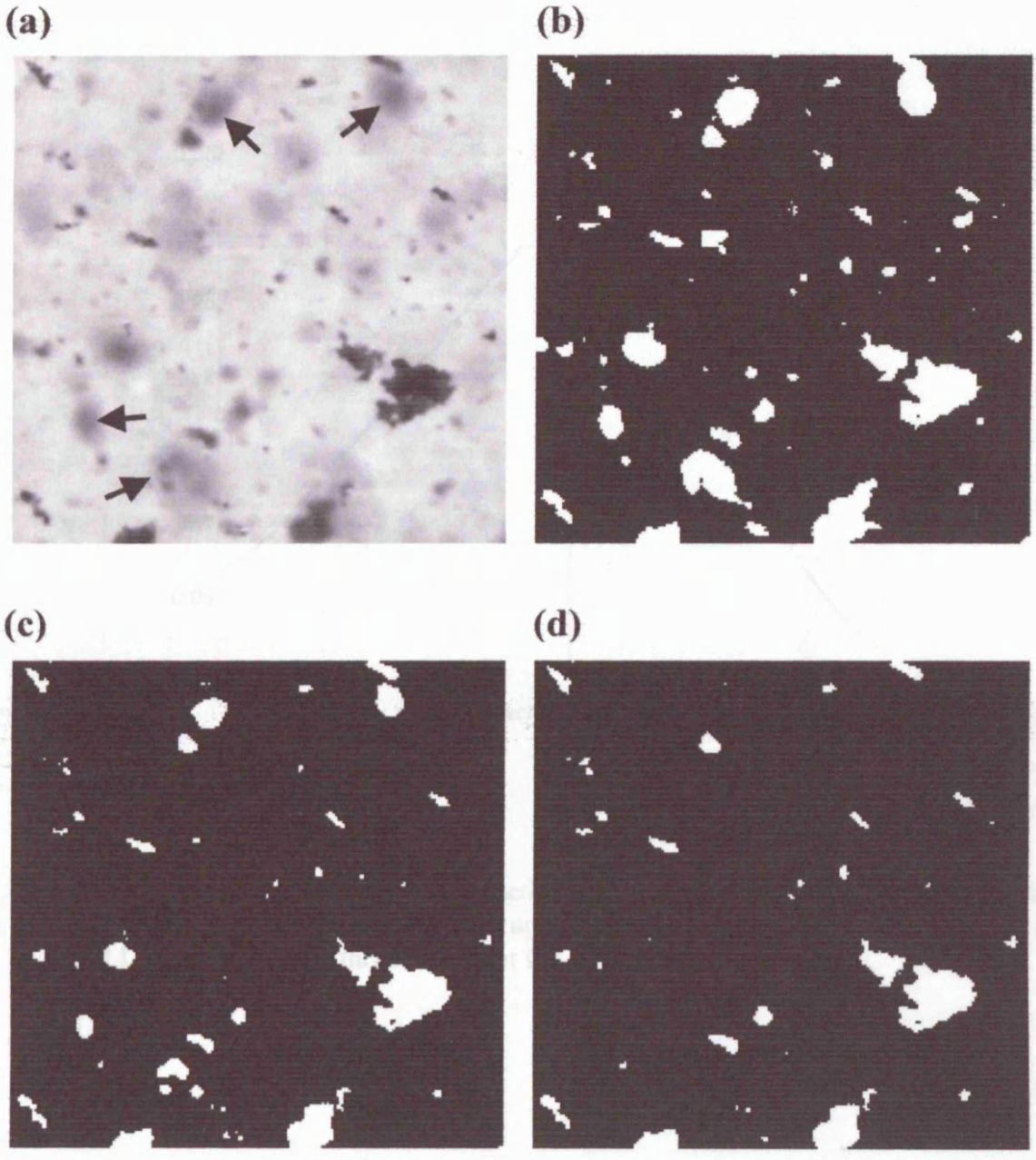

Figure 4.17 - Binary thresholding of a low-resolution image using various thresholding techniques – (a) Subset of original image, with arrows indicating some out of focus particles; (b) histogram/cluster-based method of Otsu (1979), T=172; (c) iterative edge coincidence method of Toriu *et al* (1990), T=153; (d) dark-side edge pixel intensity method with removal of out of focus particles (presented here).

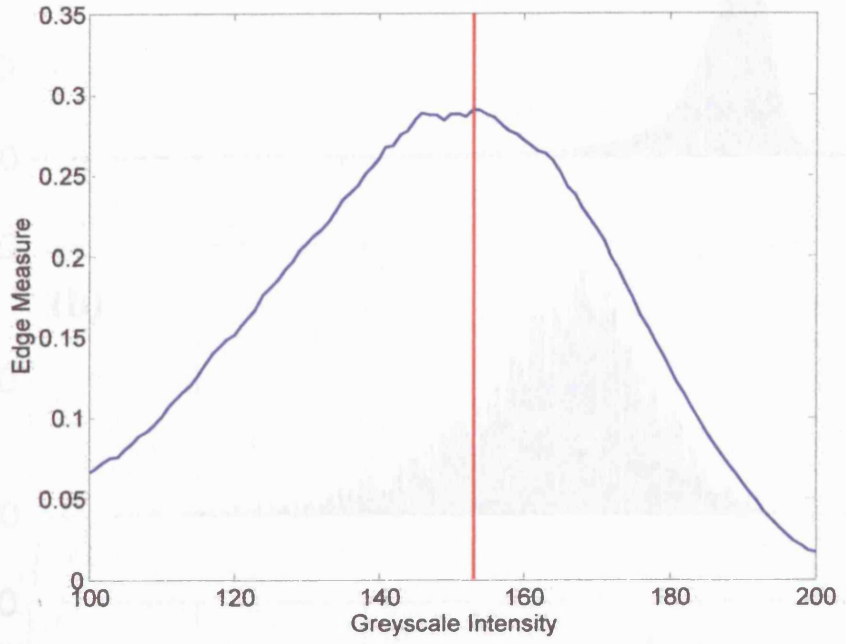

Figure 4.18 - Iterative edge measure method of Toriu *et al* (1990) for finding the threshold according to edge coincidence, applied to the low-resolution image shown in Figure 4.17a, with the edge threshold set at 0.07, resulting in T_{max}=153.

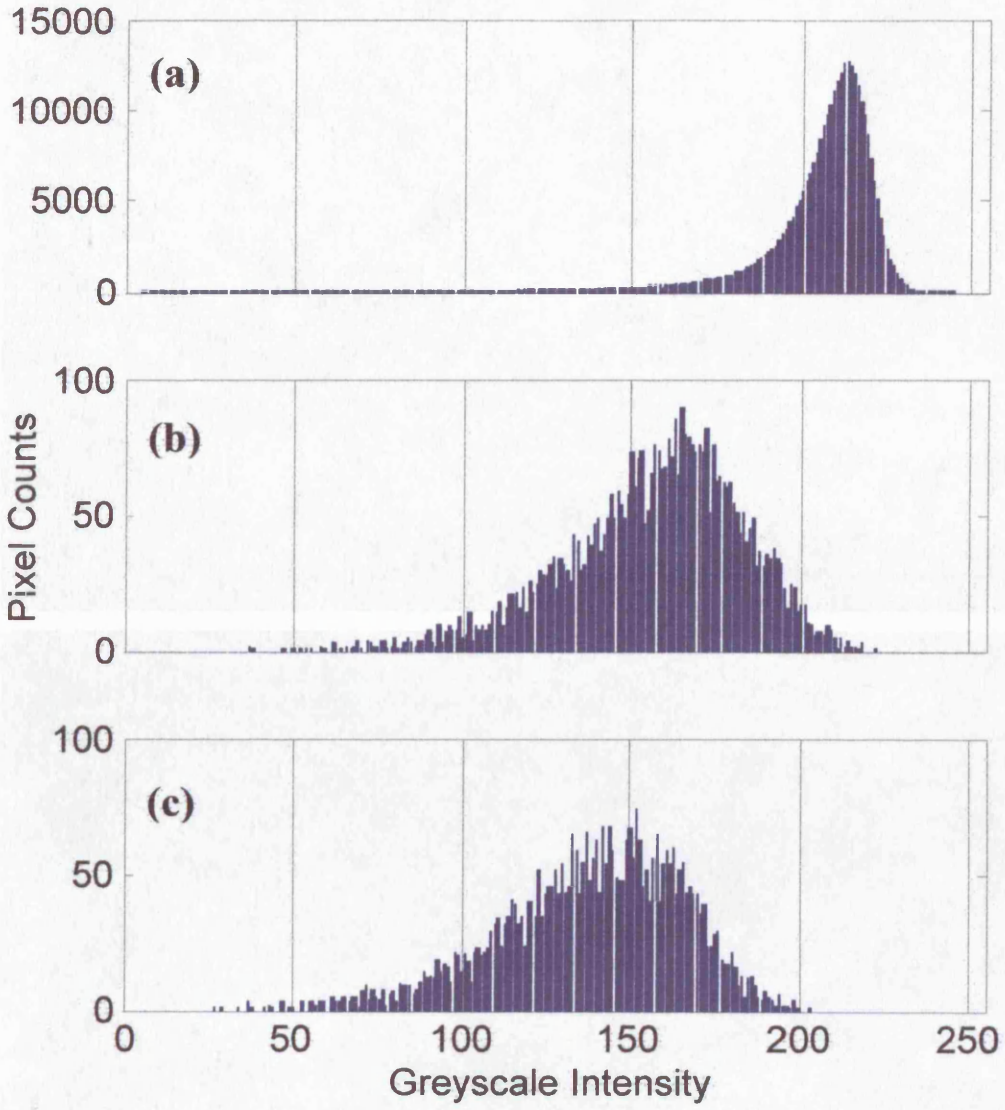

Figure 4.19 - Greyscale pixel intensity histograms for: (a) entire image, showing lack of double peak; (b) edges obtained using normal edge thinning (edge threshold = 0.07); (c) edges obtained using dark-side edge thinning (edge threshold = 0.07).

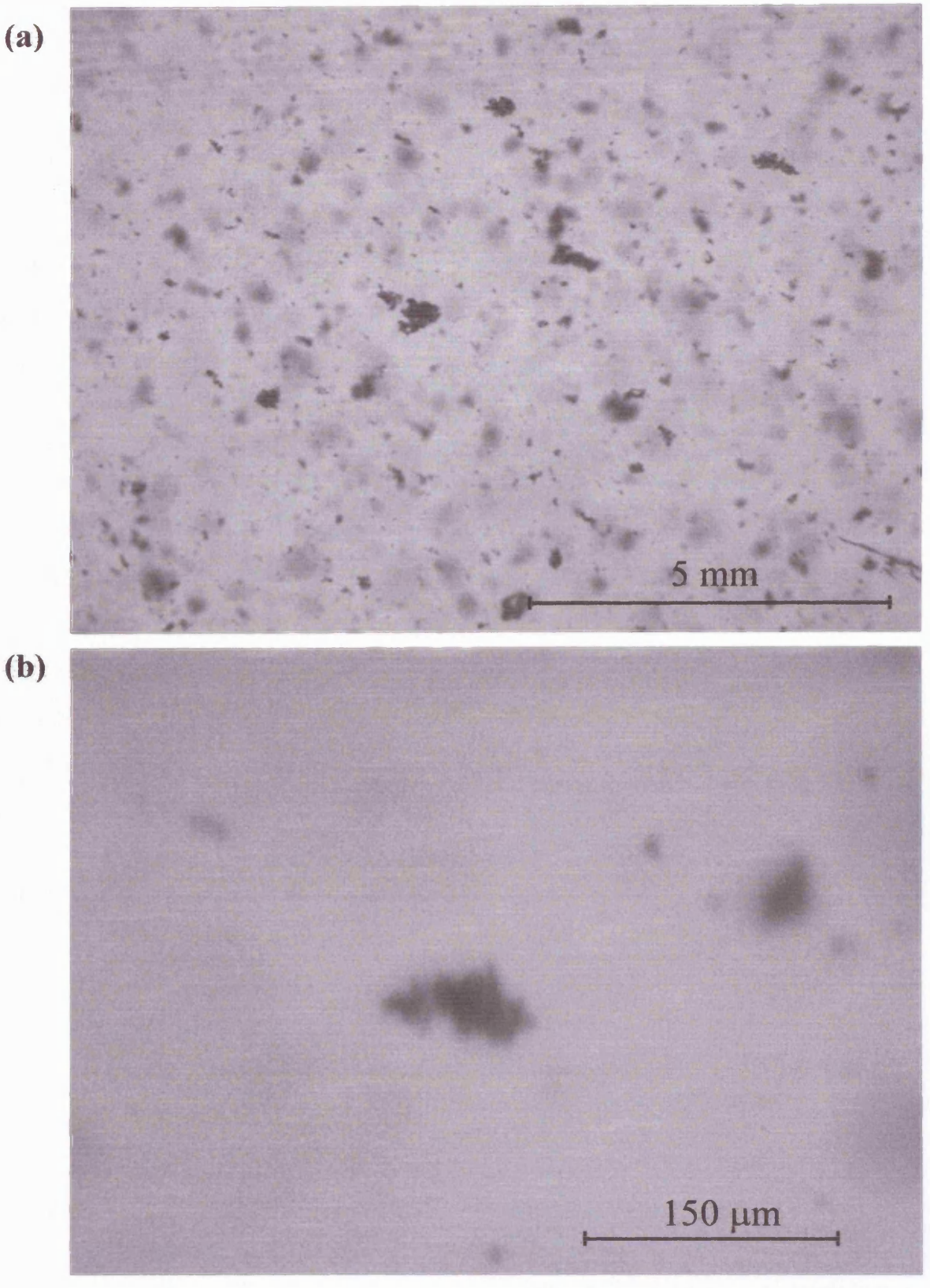

Figure 4.20 - Raw images: (a) low-resolution system; (b) high-resolution system.

(a)

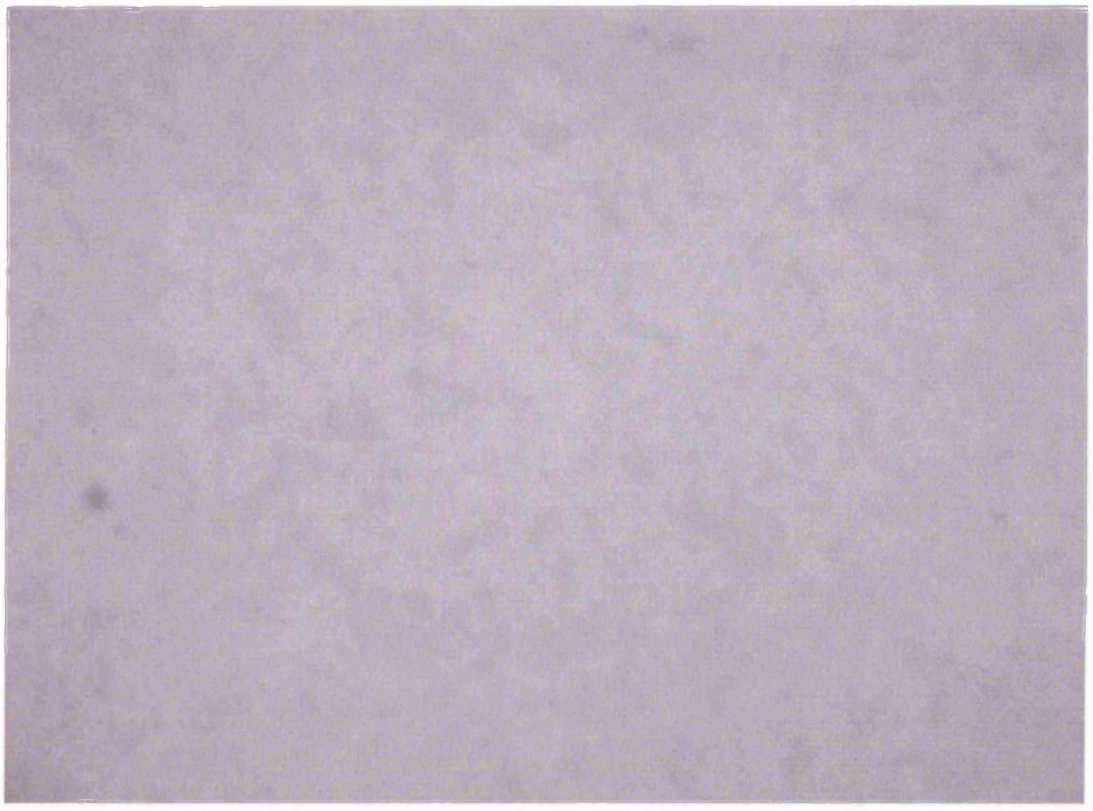

(b)

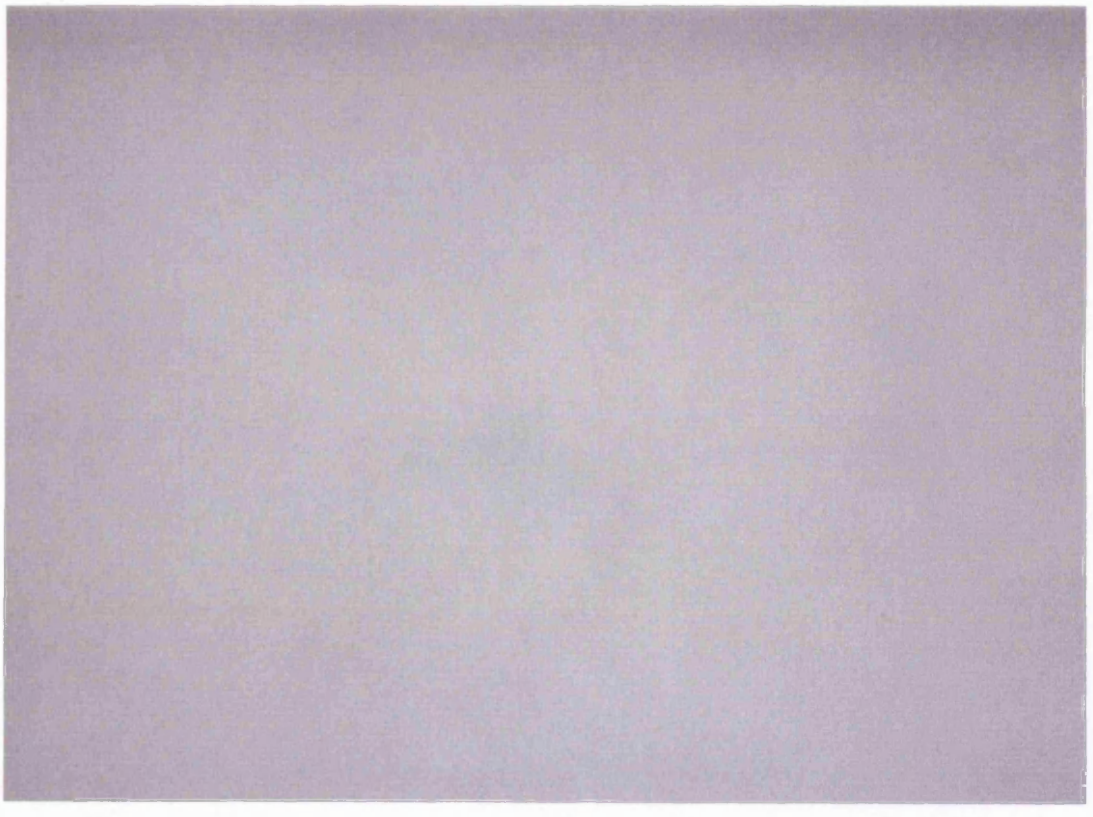

Figure 4.21 - Reference images: (a) low-resolution system; (b) high-resolution system.

(a)

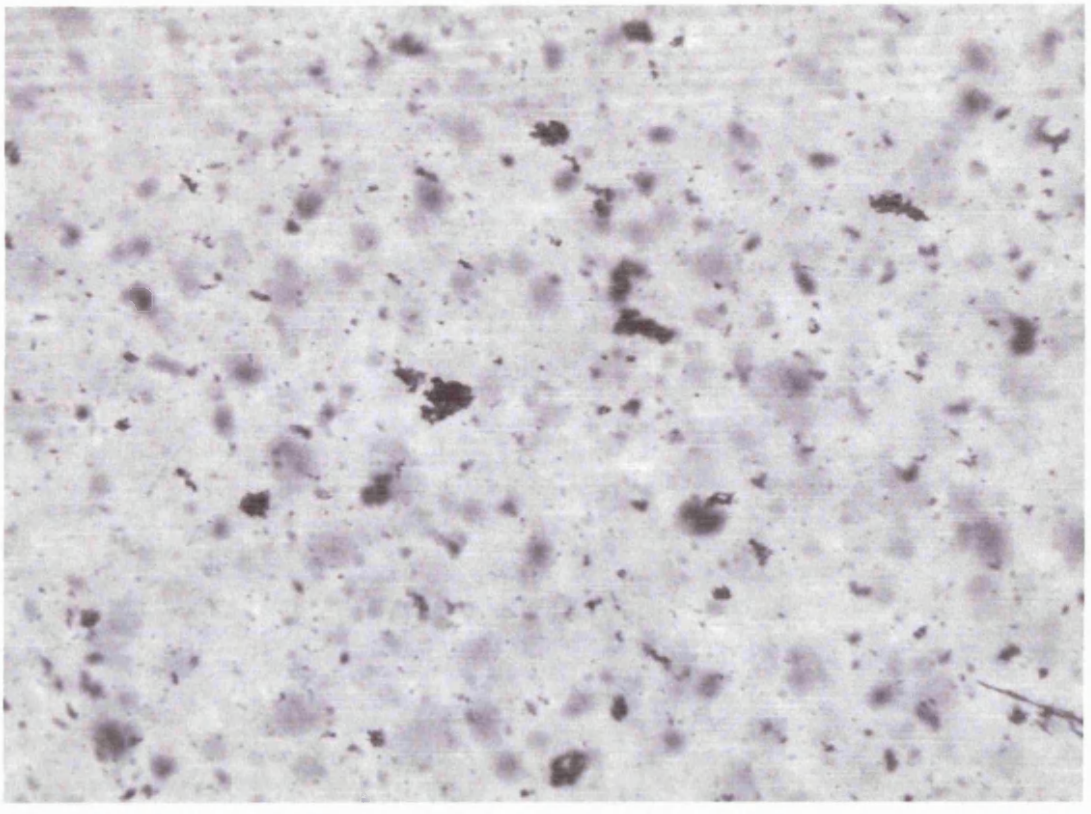

(b)

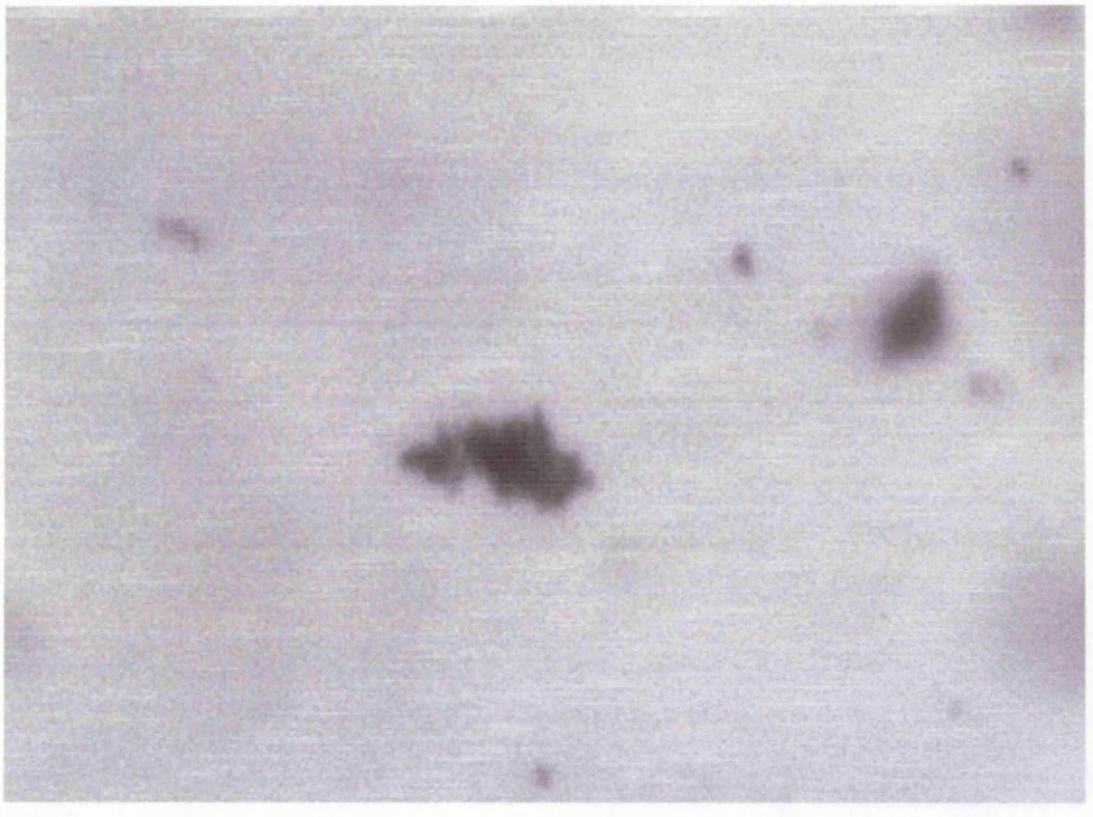

Figure 4.22 - Raw minus reference images, rescaled from 0 to 255: (a) low-resolution system; (b) high-resolution system.

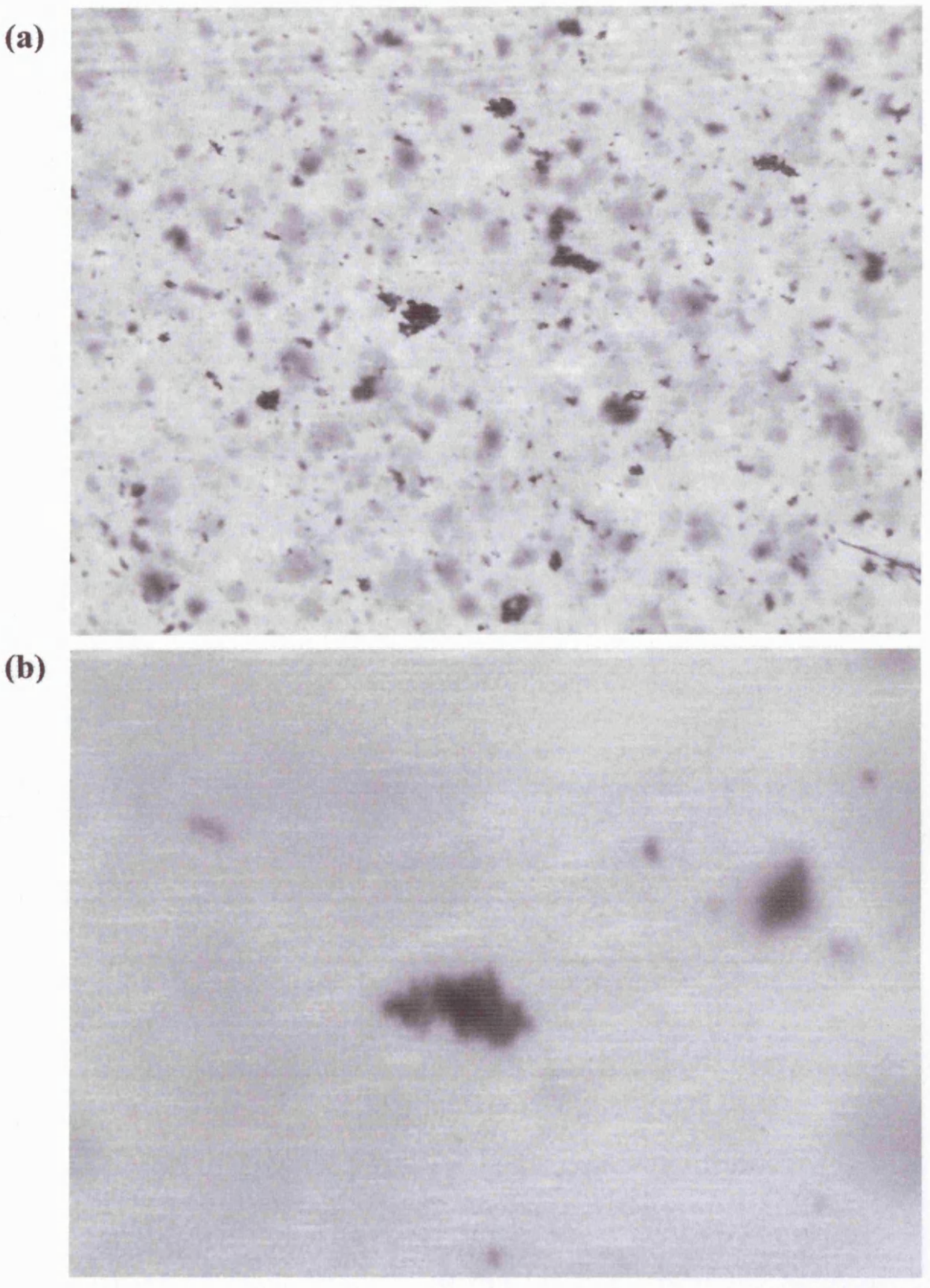

Figure 4.23 - High frequency filtered images: (a) low-resolution system; (b) high-resolution system.

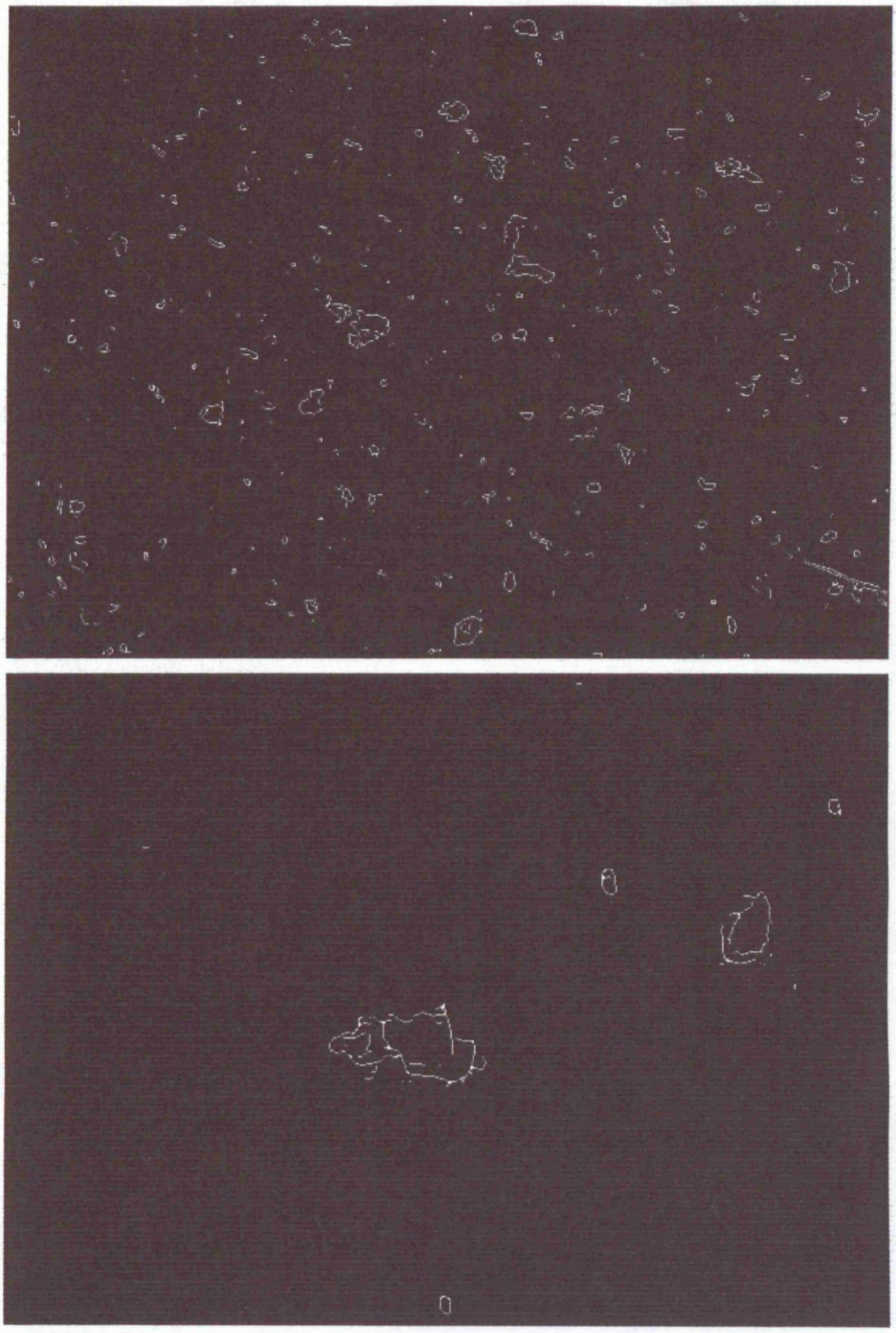

Figure 4.24 - Edge detection images: (a) low-resolution image, using a 3x3 Sobel dark-side edge detector, with an edge gradient threshold of 0.07; (b) high-resolution image, using a 21x21 Gaussian edge detector, with an edge gradient threshold of 0.35.

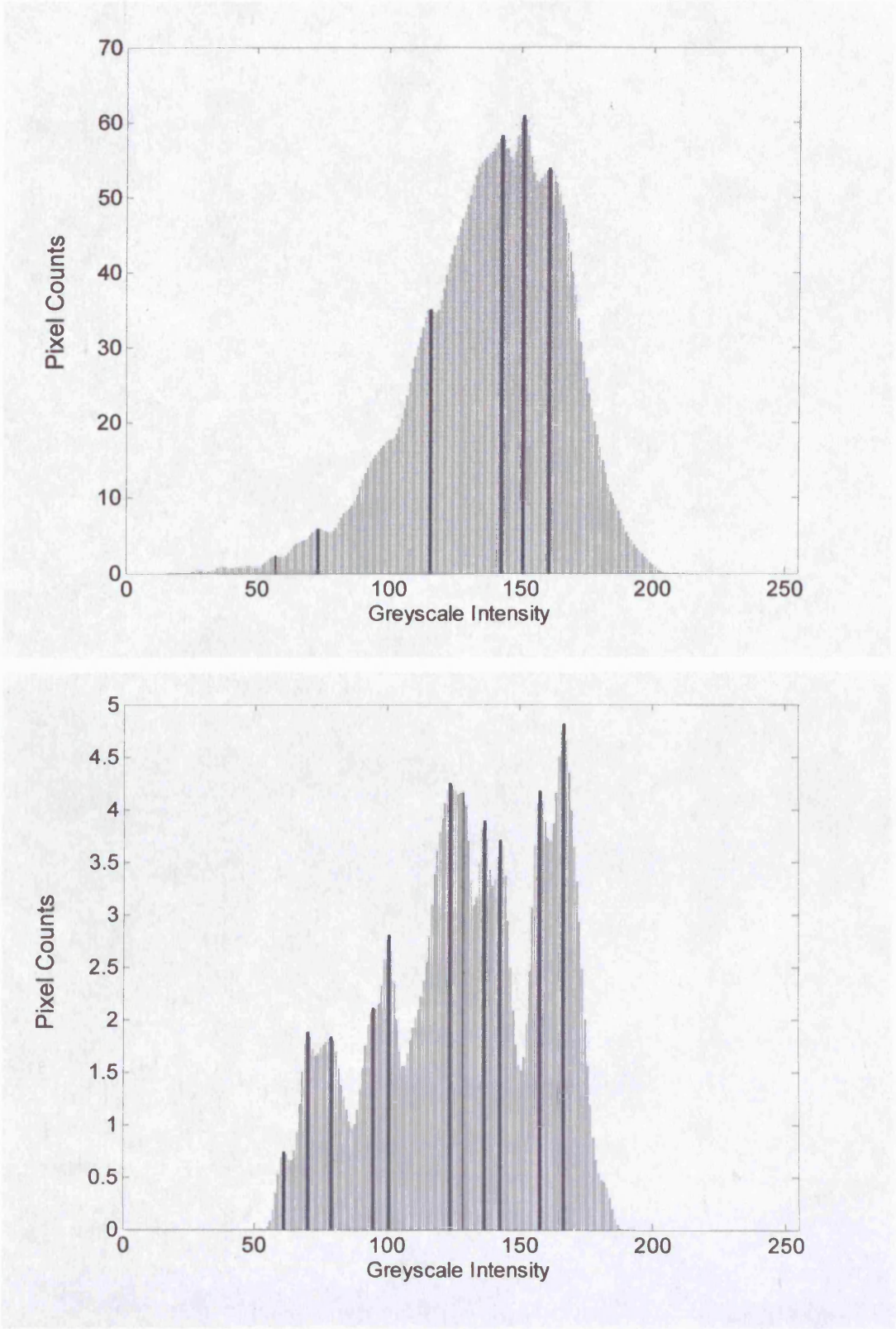

Figure 4.25 - Histogram of edge pixel intensities, showing the located maxima within the predefined range of 50 to 200 grey levels: (a) low-resolution image, with size maxima; (b) high-resolution image with eleven maxima.

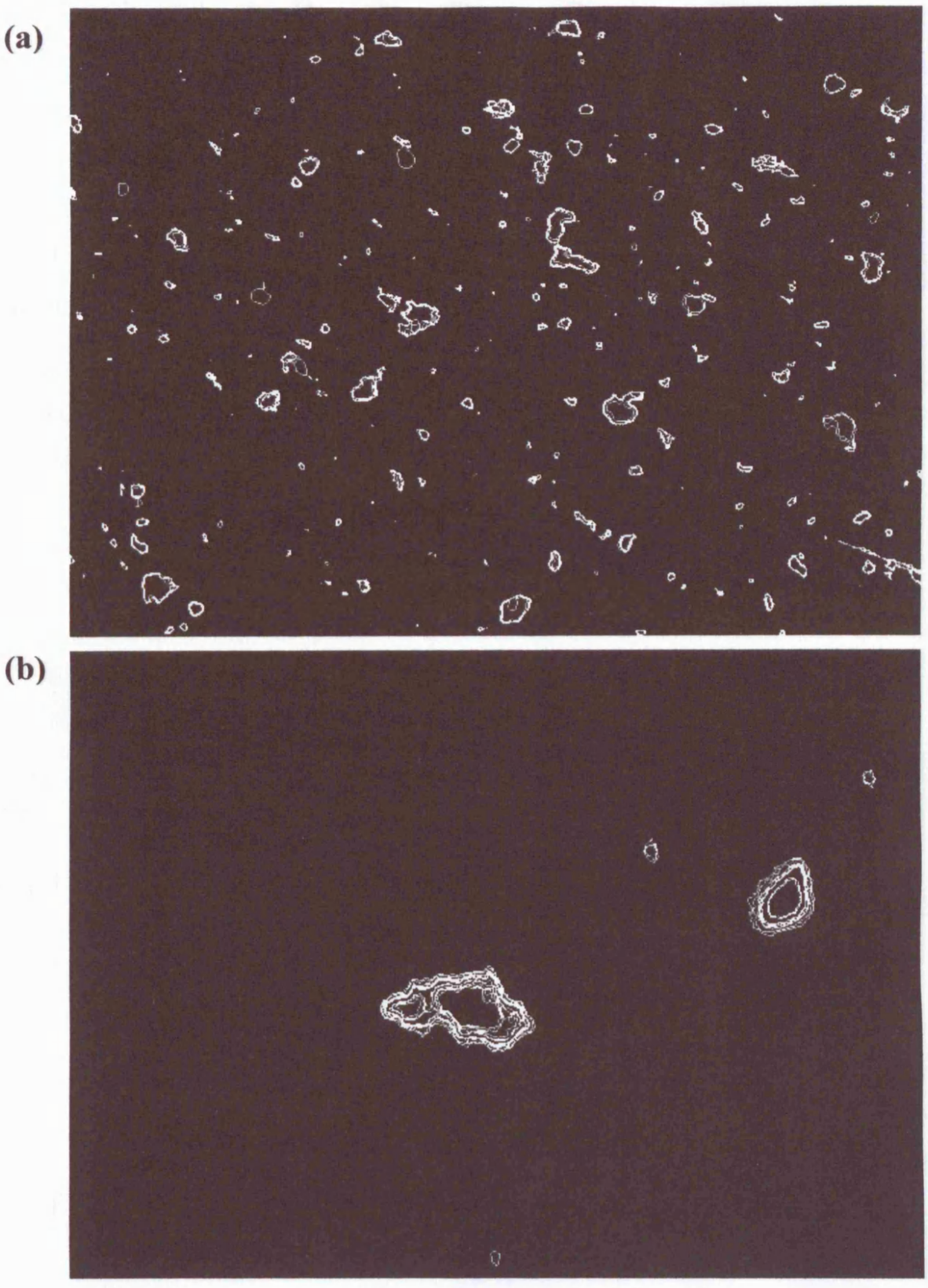

Figure 4.26 - Perimeters of the binary images for each threshold (shown here as a single image): (a) low-resolution system; (b) high-resolution system.

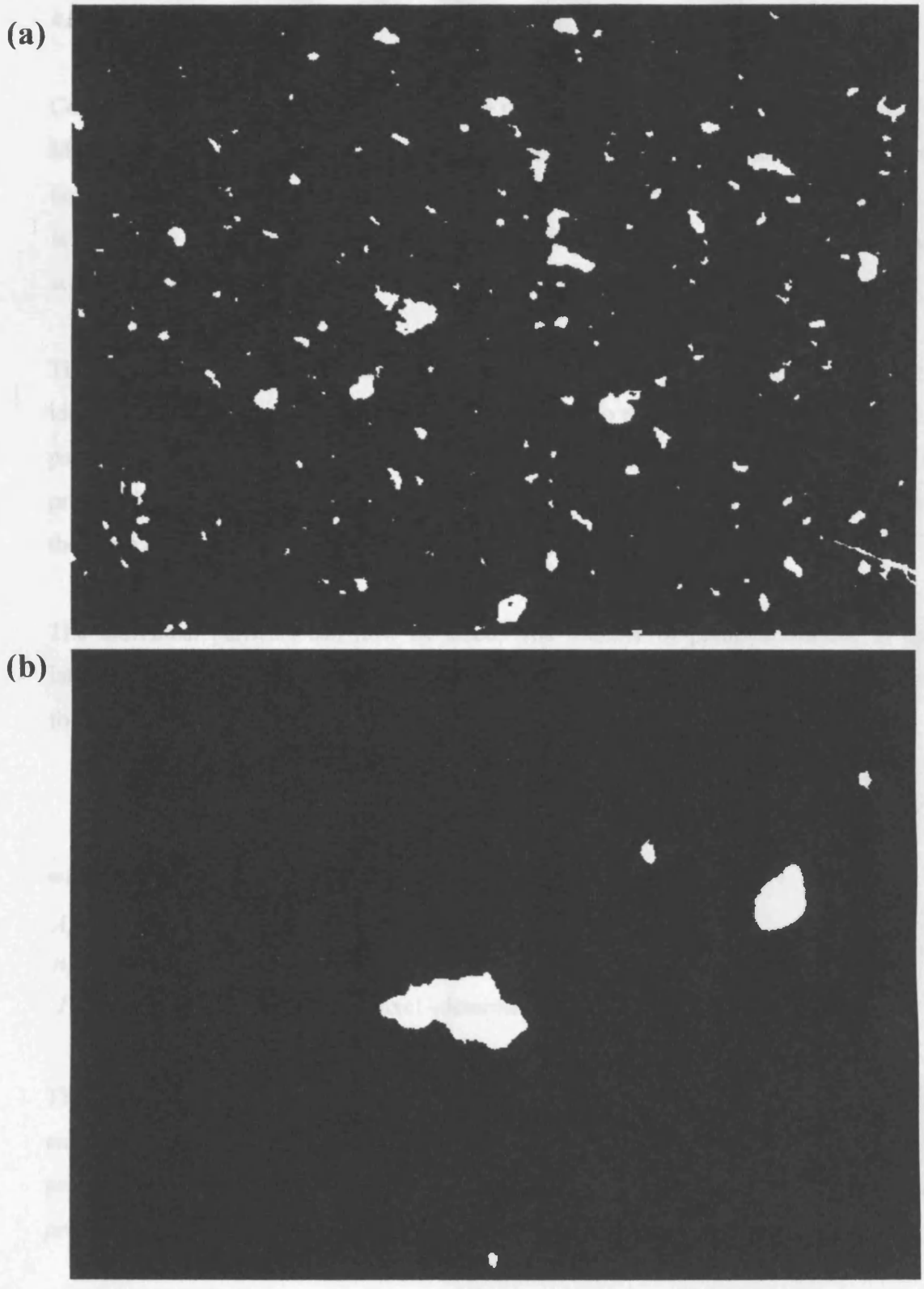

Figure 4.27 - Final image, produced by the logical combination of each binary threshold image. Out of focus particles are removed at each threshold according to the edge coincidence (R_e) between the edge image and the binary perimeter image: (a) low-resolution image (R_e= 0.3); (b) high-resolution image (R_e = 0.15).

4.3.4 Particle sizing

Counting objects in the final binary image proved relatively straight forward since the MATLAB image processing toolbox has numerous functions for manipulating binary images. After the previous processing steps have been carried out, the remaining image is in binary form, with white particle regions on a black background, as shown schematically in Figure 4.28a.

The next step is to label each region of white pixels with a separate number in order to identify it as a separate particle (Figure 4.28b). Due to the restricted field of view, any particles that are touching the outermost pixels of the image are ignored in the labelling process because they cannot be accurately measured. The total number of particles is therefore equivalent to the largest label value.

The individual particles can now be sized. The number of pixels contained in each labelled region is equivalent to the *projected area* of the particle, calculated using the following formula:

$$A_i = n_i P \tag{4.7}$$

where:

A_i = projected area of the ith particle (μm^2)
n_i = number of pixels in the group
P = equivalent area of a single pixel - determined from calibration (μm^2)

The equivalent area for a single pixel (P) has already been determined to be 343.419 and 0.681 for the low and high magnification systems respectively (Section 4.2.2). The particles are then assumed to be spherical (i.e. have a circular profile) and the *equivalent projected diameter of a sphere* (d_i) is calculated by using the following formula:

$$d_i = 2.\sqrt{\frac{A_i}{\pi}} \tag{4.8}$$

(a)

0	0	1	0	0	0	0	0	0
0	1	1	0	1	1	1	0	0
0	1	0	0	0	0	0	0	0
0	0	0	0	0	1	0	1	0
0	0	1	0	0	1	1	1	0
0	1	0	0	1	0	1	1	0
0	0	0	0	0	0	0	0	0

(b)

0	0	0	0	0	0	0	0	0
0	0	0	0	1	1	1	0	0
0	0	0	0	0	0	0	0	0
0	0	0	0	0	2	0	2	0
0	0	3	0	0	2	2	2	0
0	3	0	0	2	0	2	2	0
0	0	0	0	0	0	0	0	0

Figure 4.28 – Schematic diagram of particle counting and sizing process: (a) Binary image showing white particles; (b) labelling of individual particles, ignoring any particles with pixels touching the perimeter of the image (grey).

Table 4.1 gives the particle size calculation stages for the schematic example in Figure 4.28b, using the low-resolution calibration (P=343.419).

Particle label	*Number of pixels*	*Projected area - using low power calibration (μm^2)*	*Equivalent projected diameter of a sphere (μm)*
1	3	958.5	34.93
2	8	2556	57.05
3	2	639	28.52

Table 4.1 - Calculation of the equivalent diameter of a sphere for the particles in Figure 4.28b.

4.3.5 Particle shape analysis

By using basic size parameters such as length, breadth, perimeter and area it is possible to define shape in several different ways such as: aspect ratio, form factor and roundness (Gonzalez & Woods, 2002). The option to use any of the following shape parameters has been included in the image processing software.

- Aspect ratio
- Form factor
- Roundness
- Convexity
- Fractal dimension

Apect ratio:

The aspect ratio (σ_a) of a particle is simply defined as:

$$\sigma_a = \frac{\text{Length}}{\text{Breadth}} \tag{4.9}$$

Form factor:

Form factor (σ_f) is a very common measure of shape and is defined as:

$$\sigma_f = 4\pi \frac{\text{Area}}{[\text{Perimeter}]^2} \tag{4.10}$$

Roundness:

A roundness (σ_r) of one is a perfect circle and decreases for elongated shapes. It is defined as:

$$\sigma_r = \frac{4}{\pi} \frac{\text{Area}}{[\text{Length}]^2} \tag{4.11}$$

More complicated shape descriptions include parameters such as *convexity* and *fractal dimension.*

Convexity:

For convexity to be determined, the perimeter length of the *convex hull* first needs to be calculated. The convex hull is defined as the smallest convex polygon that can contain the region (included in the *imfeature* function in MATLAB). Once this is found, the convexity is defined as:

$$\sigma_c = \frac{\text{Convex Perimeter}}{\text{Perimeter}} \tag{4.12}$$

Any indentations in the particle will therefore result in a convexity of less than one.

Fractal Dimension:

A very useful shape measurement for classifying estuarine aggregates is the fractal dimension, because it relates to the compactness, and therefore the density, of the particles. There are various different methods of determining the fractal dimension. For determining the fractal dimension of a single particle, the *structured walk* method is often used (Addison, 1997). By this method, the fractal dimension is calculated by *walking* around the perimeter of a particle boundary for a fixed number of pixels,

known as the *step size*. A straight line is then drawn between the start and end pixel (Figure 4.29). The length of this line (the *step length*) is then determined.

By walking around the entire perimeter, the particle is approximated by a polygon. The average step length is then calculated by dividing the polygon's perimeter length (i.e. the sum of all the step lengths) by its number of sides. The process is then repeated at various step sizes and the results plotted on a log-log graph of polygon perimeter length versus average step length, i.e. a Richardson plot (Addison, 1997). As the step size decreases, the polygon perimeter length increases as finer detail is measured. The fractal dimension (F_D) is then calculated from the slope (m) of this graph as:

$$F_D = 1 - m \tag{4.13}$$

The larger the fractal dimension, the larger the complexity of the boundary shape. This provides an idea of the compactness of the particle.

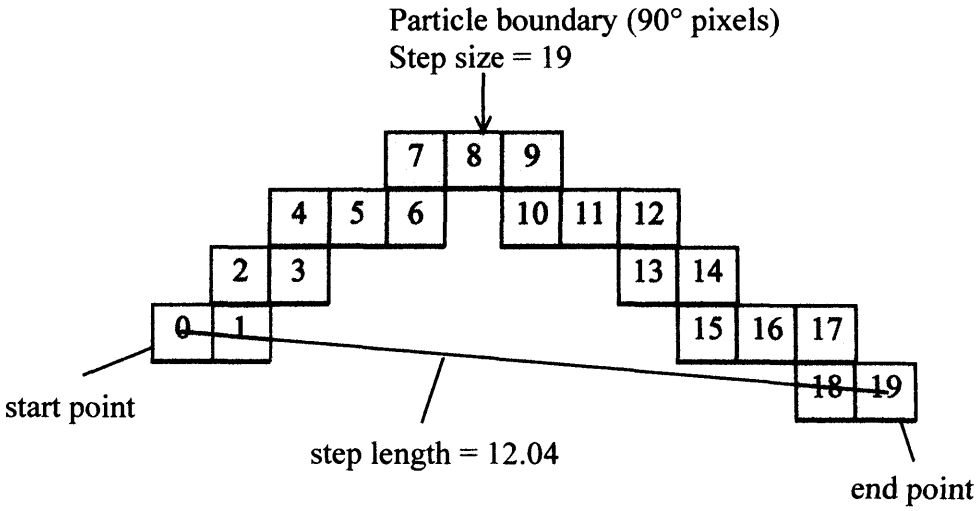

Figure 4.29 - Determining step length from step size for a section of a particle boundary.

The boundary method, however, is very time-consuming due to the large number of iterations involved for each particle. It is also inaccurate when individual particles are represented by only a few pixels. A more efficient method is to calculate the fractal dimension as a function of the length-area relationship of the particles (Chen & Eisma, 1995; Bellouti *et al*, 1997). This is calculated from the log-log plot of the major axis area against length for all the particles in the image (Figure 4.30). The 2-D fractal dimension is then obtained from the slope of the least-squares fit through these data. Using this method, the resultant fractal dimension is the statistical average for all the particles in the image, or set of images. In this case, a fractal dimension of 2 suggests spherical, compact objects whereas lower values suggest greater porosity, with a value of 1 being equal to a straight line.

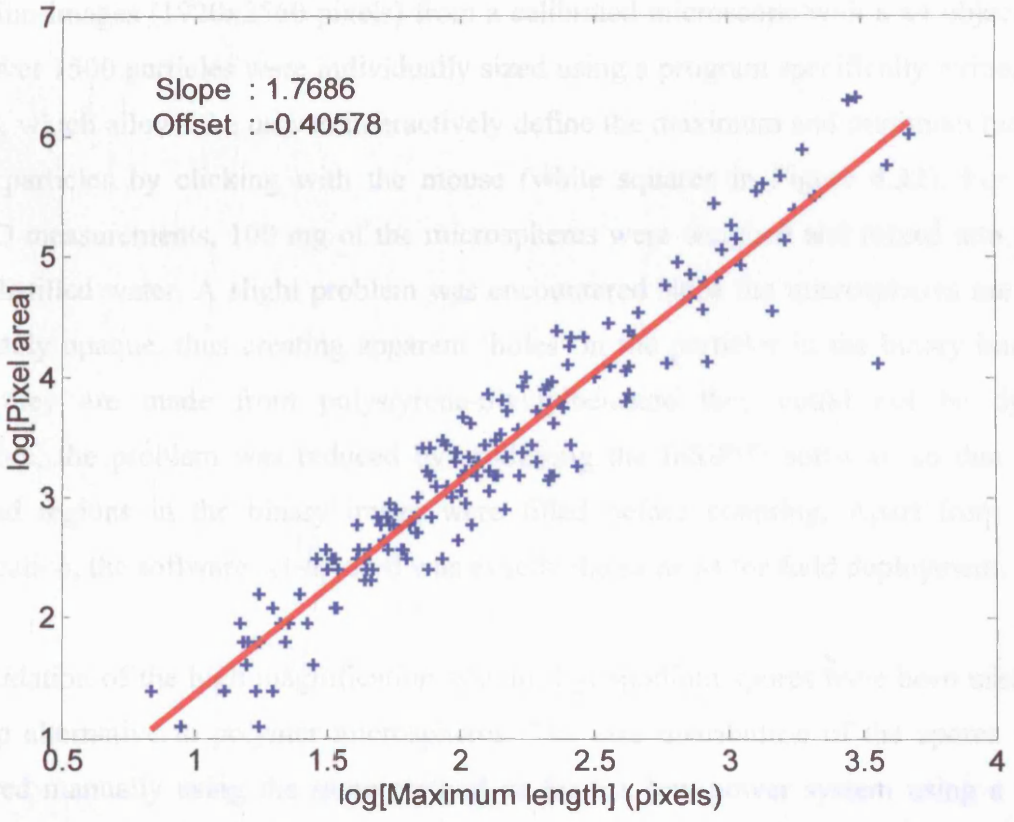

Figure 4.30 – Fractal dimension calculation for the low-resolution binary image shown in Figure 4.27 (F_D=1.77).

4.4 Laboratory assessment and validation

4.4.1 Test method

Testing of the InSiPID instrument was carried out in the laboratory using known size standards. An experiment was set up (Figure 4.31) whereby a small sample volume of water could be placed directly between the camera and the strobe without the need for extra windows, which may have caused errors due to refraction.

For the low magnification system, neutrally buoyant polystyrene-divinylbenzene microspheres were used (Figure 4.32a) with a quoted size range of 149-350 μm and a mean size of 250 μm (Bangs Laboratories, Inc, USA – catalogue code BB04N). These were chosen because of the uniform size distribution and relatively low cost. In order to validate this quoted value, the microspheres were sized manually by obtaining high-resolution images (1920x2560 pixels) from a calibrated microscope with a x4 objective lens. Over 1500 particles were individually sized using a program specifically written in Matlab, which allows the user to interactively define the maximum and minimum radius of the particles by clicking with the mouse (white squares in Figure 4.32). For the InSiPID measurements, 100 mg of the microspheres were weighed and mixed into 500 ml of distilled water. A slight problem was encountered since the microspheres are not completely opaque, thus creating apparent 'holes' in the particles in the binary image. Since they are made from polystyrene-divinylbenzene they could not be dyed. Therefore, the problem was reduced by modifying the InSiPID software so that any enclosed regions in the binary image were filled before counting. Apart from this modification, the software set-up used was exactly the same as for field deployment.

For validation of the high magnification system, Lycopodium spores have been used as a cheap alternative to polymer microspheres. The size distribution of the spores was measured manually using the same method as for the low power system using a x10 objective lens (Figure 4.32b). Lycopodium spores come in tablet form. Each tablet weighs about 92 mg and contains approximately 12,500 spores. Twelve tablets were first dissolved in a few millilitres of methanol. A drop of safranin was then added in order to dye the spores to aid in visualisation. Most of the methanol was then evaporated off from the spore suspension and approximately 200 ml of distilled water was added to make up the final test suspension.

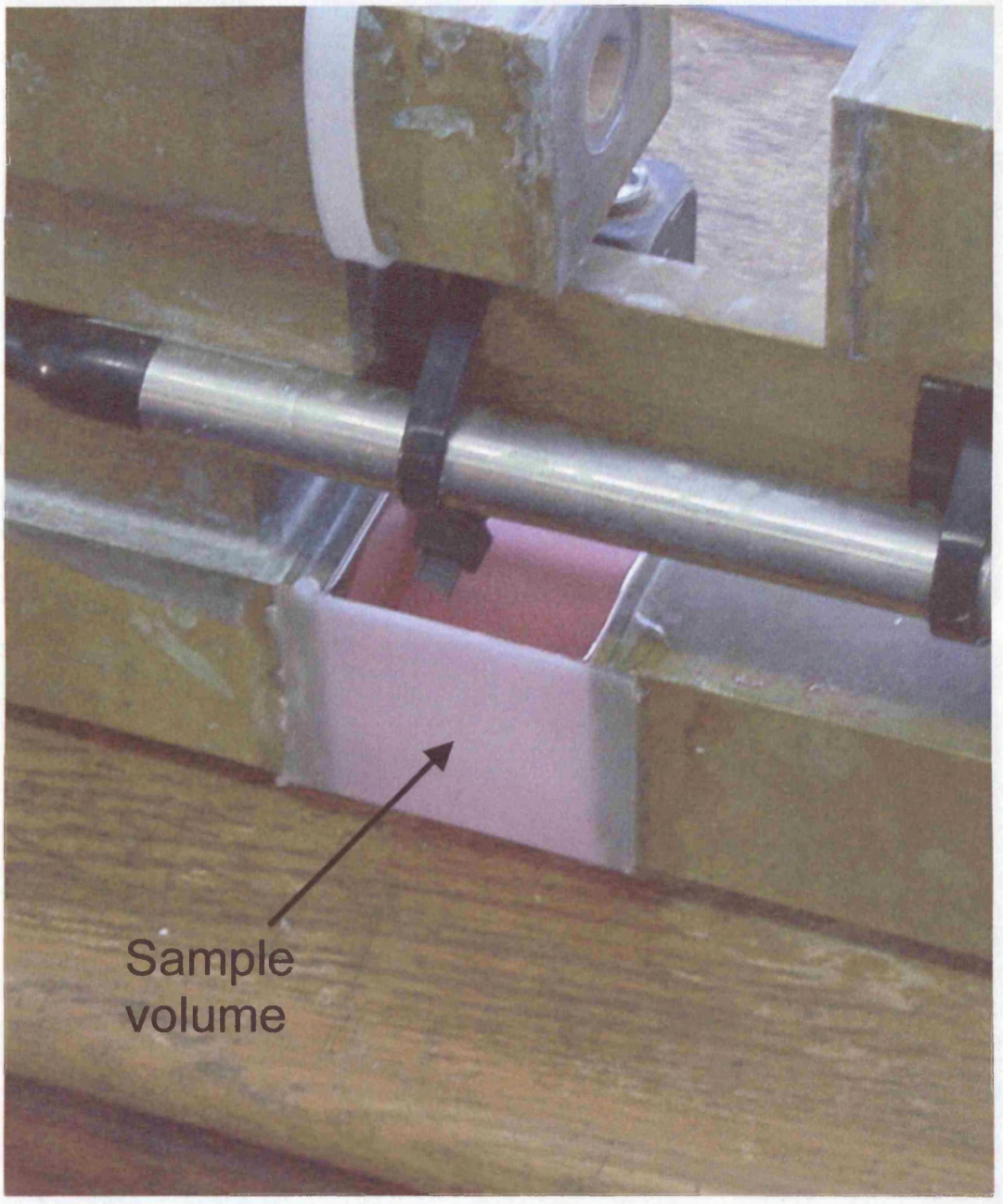

Figure 4.31 – Test set-up, showing the sample volume between the high power camera and strobe housing.

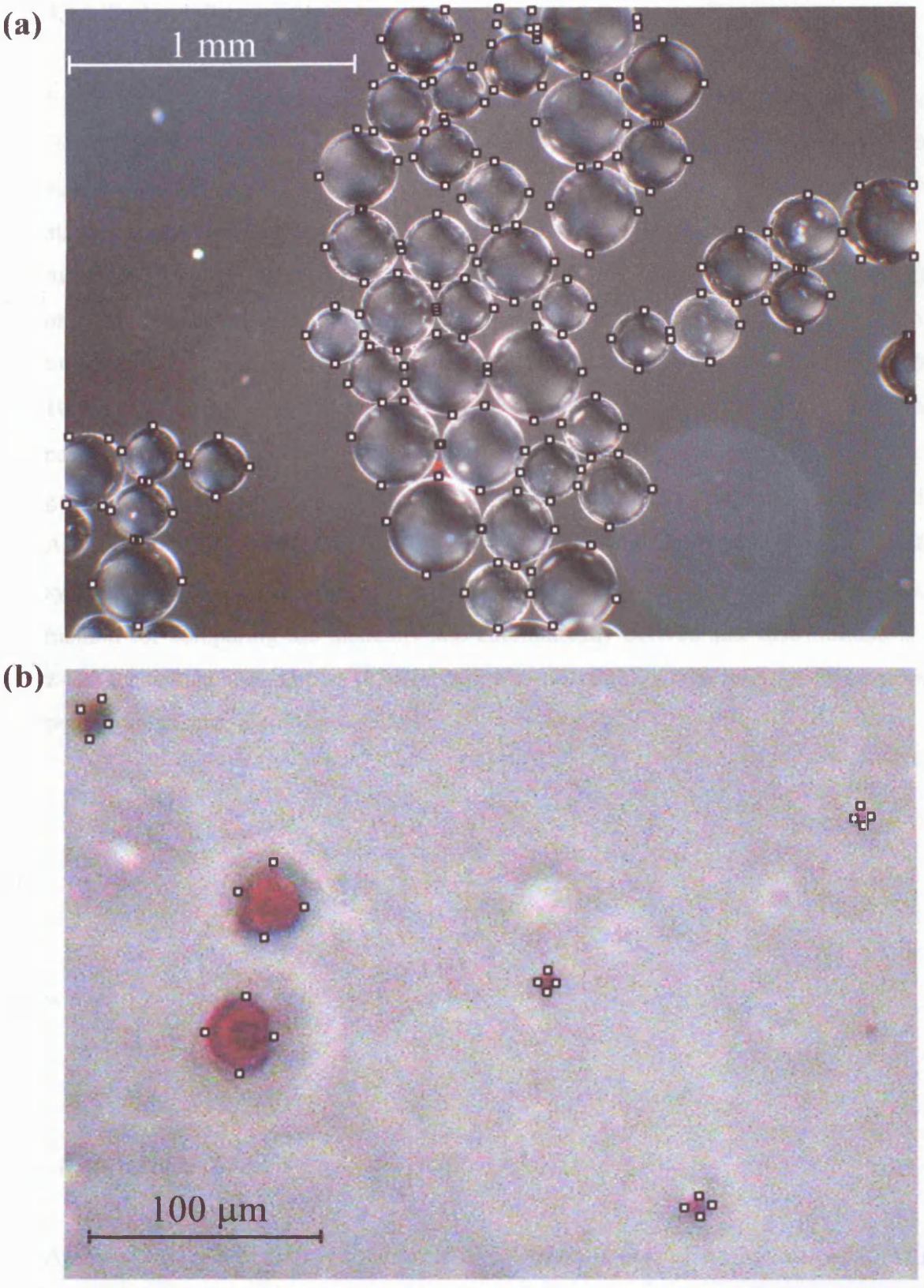

Figure 4.32 – Manual sizing using calibrated microscope images (see scale): (a) Polymer microspheres; (b) Lycopodium spores (subsection of a whole image)

4.4.2 Test results

Examples of the test images and derived binary images are given in Figure 4.33 and Figure 4.34 for the low and high magnification systems respectively. Test result particle size distributions for the two systems are shown in Figure 4.35 and Figure 4.36. The statistical analysis is summarised in Table 4.2. There is good agreement between the manually counted and automatic InSiPID size distributions. For sediment transport modelling, the most important parameter is the median diameter (D_{50}). For the microspheres, the difference between the manually obtained and InSiPID median size is 10.4 μm, giving a relative error of just 4% (using a number distribution and linear particle size scale). For the lycopodium spores the median size difference is -1.2 μm, giving a larger relative error (due to the smaller size range) of approximately 11%. Assuming full-scale readings of 3000 and 300 μm for the low and high magnification systems respectively, this provides an accuracy of ± 0.3-0.4% FS for either system. A method for comparing the manually and automatically derived size distributions is the z-test for unmatched samples (Chalmers & Parker, 1986), which tests for differences in population means, and formulated as:

$$z = \frac{\bar{x}_A - \bar{x}_B}{\sqrt{\frac{\sigma_A^2}{n_A} + \frac{\sigma_B^2}{n_B}}} \qquad (4.14)$$

where:

$\bar{x}$ = sample means
σ^2 = sample variances
n = number of observations
A, B = samples A and B

Applying this test to the microsphere and Lycopodium data gives z-values of 4.347 and 2.071 respectively, corresponding to two-tailed p-values of <0.001 and <0.05. This suggests that the comparisons between the means of the distributions are 99.9% and 95% significant for the low and high magnification systems respectively.

For the microsphere measurements, a slight spreading of the distribution to larger diameters is observed in the automated results. This is highlighted by the larger standard deviation for the InSiPID data of 60.3 μm as opposed to 49.7 μm for the manual observations and the larger mean and median diameters. This can be explained due to the fact that touching particles are not differentiated by the program since the system is designed to measure flocs rather than spheres. As the low power camera has a relatively large depth of field, coincidence between particles is relatively common, thus resulting in a proportion of the particle sizes being overestimated. The manually counted particles on the other hand were visually differentiated and, as a result, the median and mean particle sizes are slightly smaller.

This problem is less apparent for the high magnification system due to the small depth of field, thus reducing the chance of particle overlap. There is in fact a slight bias towards smaller size ranges for the insipid instrument, although this could be accounted for by innaccuracies in the manual counting process which was found to be more difficult for the smaller objects in the microscope images due to a slight blurriness of the particle edges (Figure 4.32b). This is a possible reason for the lower significance in the z-test for the high power system.

	Low magnification (Polymer microspheres)		High magnification (Lycopodium spores)	
	Manual	InSiPID	Manual	InSiPID
Observations	1696	643	1570	1533
Median	256.6	267.0	11.1	9.9
Mean	253.4	265.0	13.5	12.9
Maximum	400.6	400.6	66.2	74.1
Minimum	65.4	93.5	2.4	4.1
Standard Dev.	49.7	60.3	8.4	9.0
z-test:				
z	4.347		2.071	
p-value	<0.001		<0.05	

Table 4.2 – Statistical comparison between manually counted and automated InSiPID size distributions.

Overall, the test results presented in Table 4.1 show that the InSiPID is an effective instrument for accurately sizing suspended particles. In accordance with the aims and objectives set out in Chapter 2, the system offers a wide range of capabilities in comparison to other particle sizing techniques. First, a major advantage of this system is the ability to measure the full particle size distribution in the range of 4 to 3000 μm, which is achieved through the use of two cameras at different magnifications.

Second, by directly viewing the particles without relying upon theory of light scattering or particle settling velocity, the system is less susceptible to errors. This capability also allows measurements to be made of particle shape as well as size.

Third, by using microsecond strobed illumination and direct digitisation of the video signal, the system can rapidly obtain a sufficiently large number of images to accurately determine the full particle size distribution, even at flow speeds of up to 1 ms^{-1}.

Fourth, the system is designed to be field portable and waterproof to a depth of 9 m. In situ particle size measurements can be therefore be made from a small boat as opposed to other systems which are generally deployed from large research ships. Thus it is possible to deploy the instrument in shallow estuarine regions, such as over mudflats at high tide. The testing of these capabilities is described in the case study in the following chapter.

Finally, the system has been developed at cost of under £5000 making it a considerably cheaper option compared to laser diffraction and acoustic backscatter techniques. In addition, the system offers the possibility for future development of the software and computer hardware, with minimal additional cost and resources.

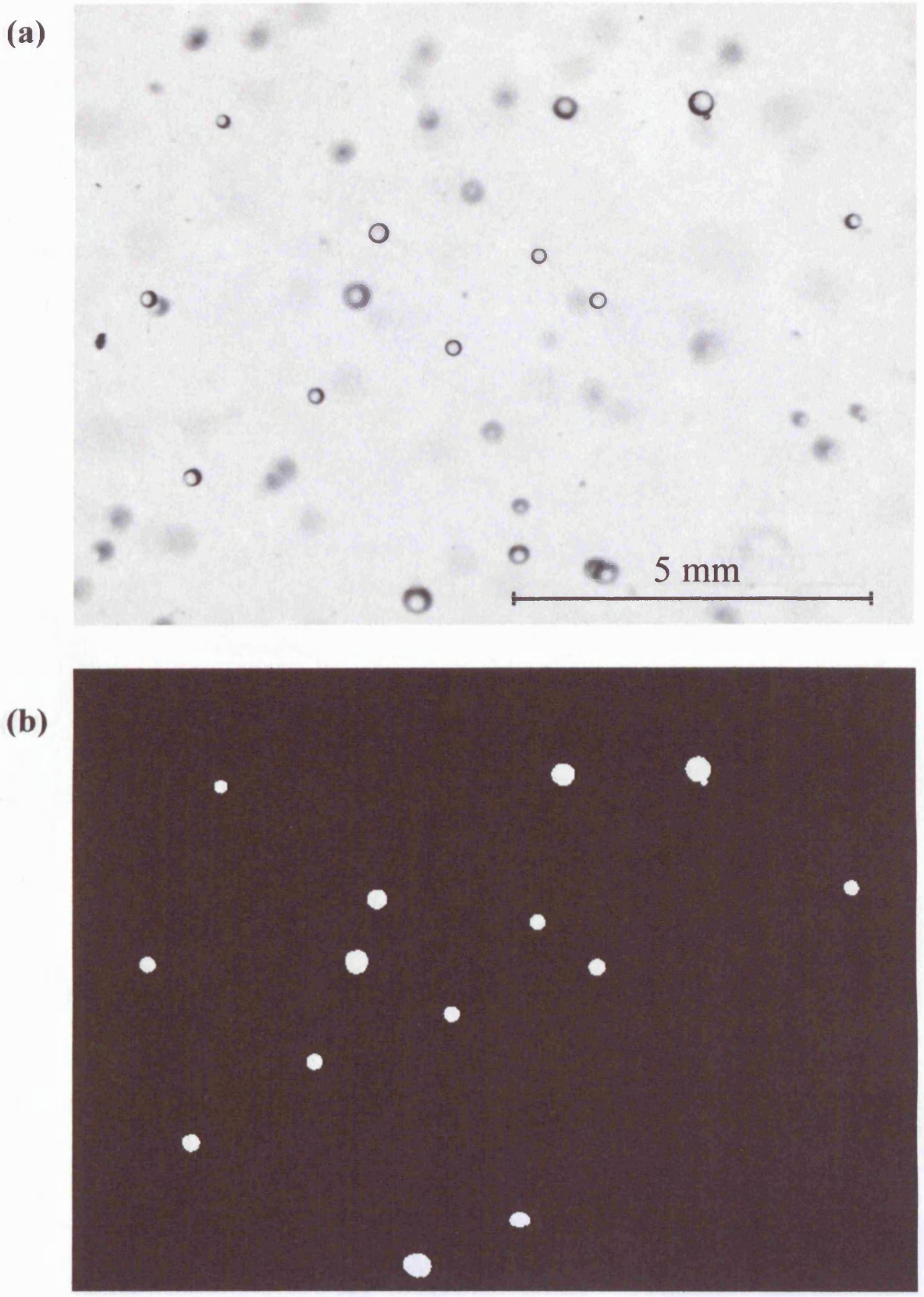

Figure 4.33 – Low-magnification images of the polymer microspheres: (a) greyscale image (after noise removal); (b) Binary image using InSiPID software with region filling to account for transparent spheres.

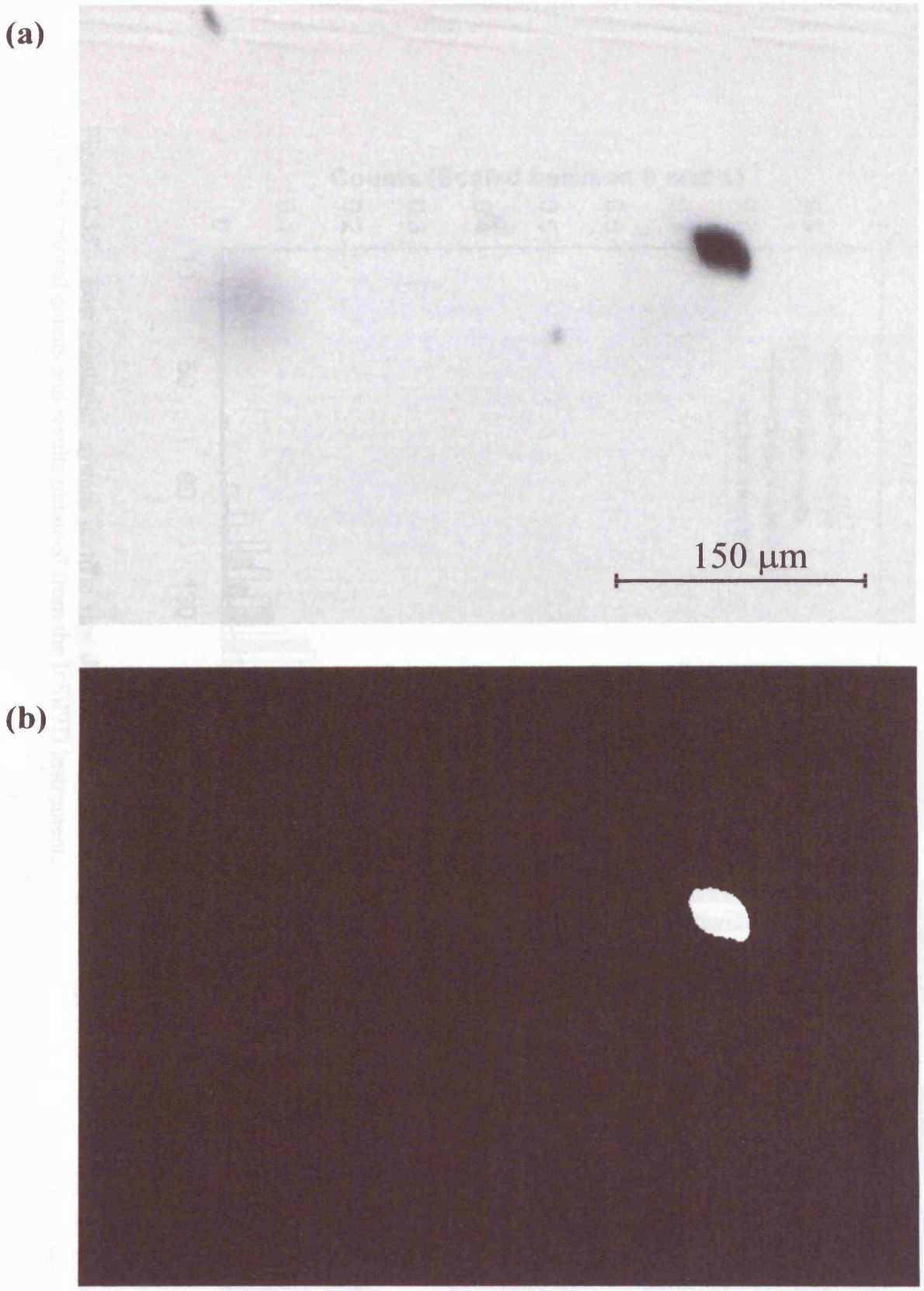

Figure 4.34 – High-magnification images of a lycopodium spore: (a) greyscale image (after noise removal); (b) Binary image using InSiPID software.

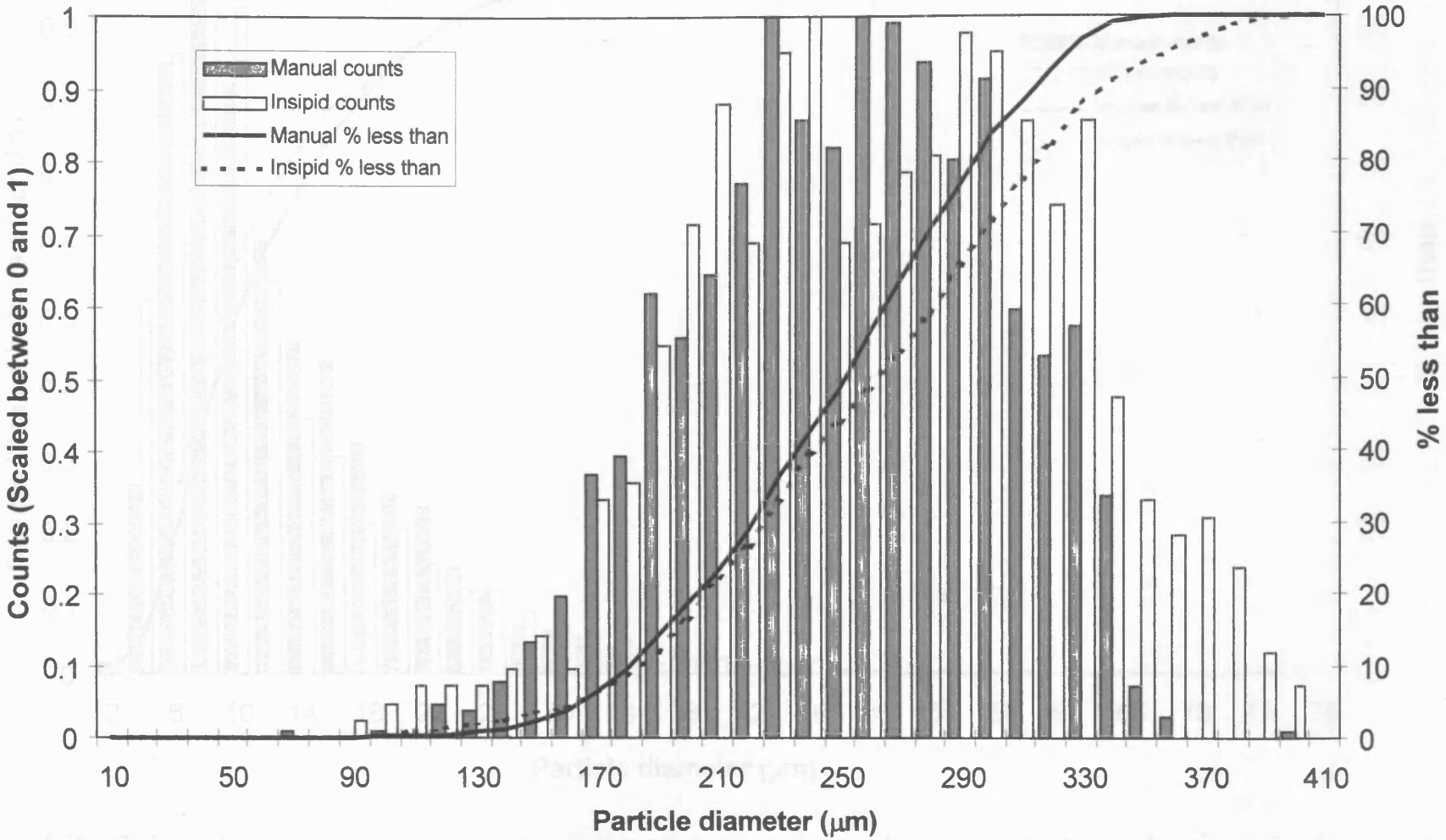

Figure 4.35 – Low-resolution system particle size distribution results using neutrally buoyant microspheres (histogram bin size = 10), showing manual counts and results obtained from the InSiPID instrument.

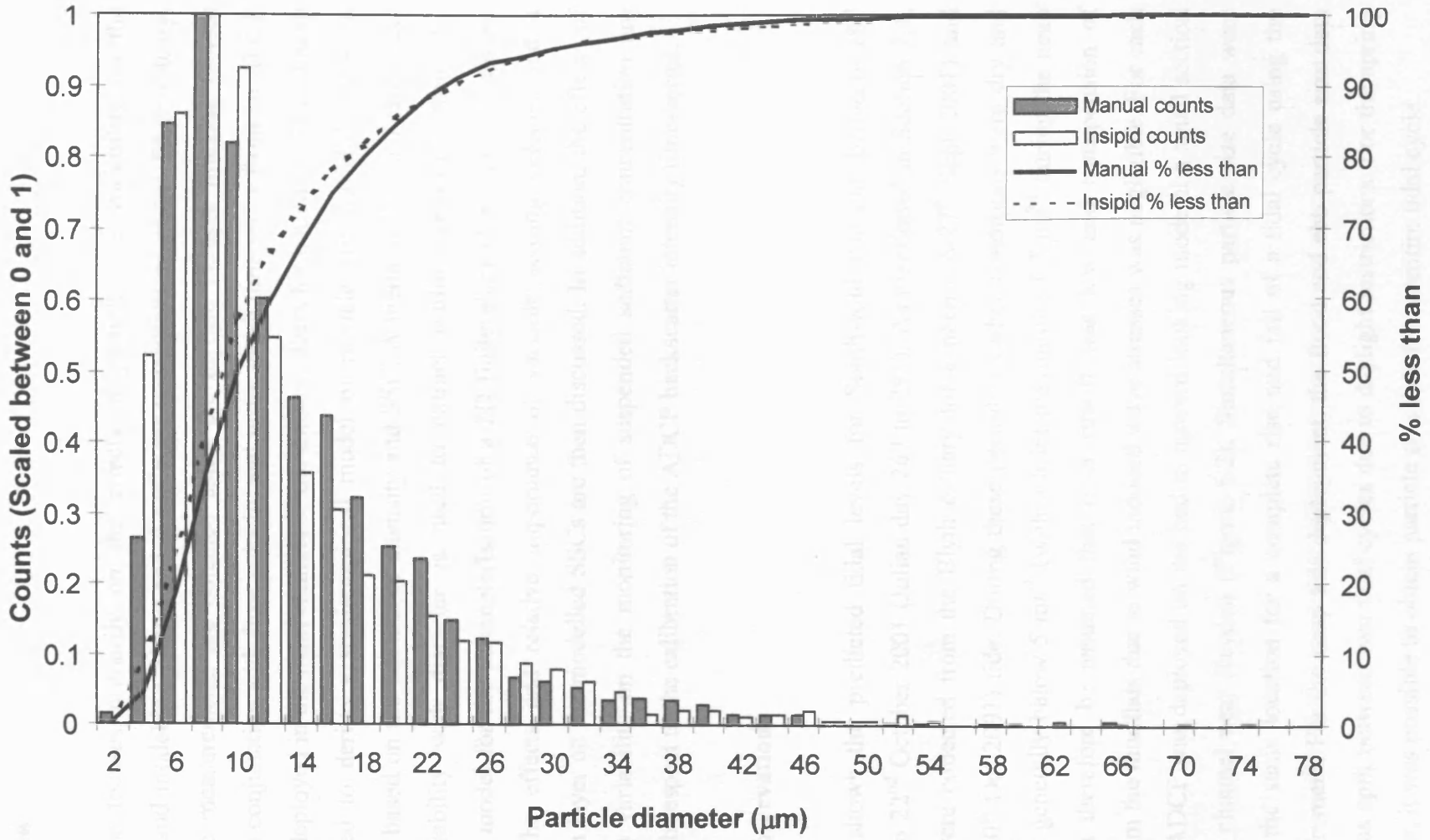

Figure 4.36– High-resolution system particle size distribution results using Lycopodium spores (histogram bin size = 2), showing manual counts and results obtained from the InSiPID instrument.

5. Monitoring and modelling of particle size and sediment transport: Blyth estuary case study

5.1 Overview

This chapter focuses primarily on the effects of particle size variability on the monitoring and modelling of suspended sediment concentrations in the Blyth estuary. Particle size measurements are obtained using the In Situ Particle Imaging Device (InSiPID) in conjunction with flow velocity and water depth time series from an ADCP instrument deployed in the main channel of the estuary. Data for both a spring and neap tide are used to derive a semi-empirical model of particle size variability due to flocculation based on the turbulence intensity and SSC. A theoretical model of particle density variability with diameter is used to extract settling velocities from the flocculation model for the parameterisation of a 2D finite element model of sediment transport. The effects and relative importance of variable settling velocity and a resuspension layer on the modelled SSCs are then discussed. In addition, the effects of particle size variability on the monitoring of suspended sediment concentration are assessed with respect to the calibration of the ADCP backscatter intensity time-series.

5.2 Field Observations

Figure 5.1 shows the predicted tidal levels for Southwold harbour between 18th September to 22nd October 2001 (Julian day 267 to 294). As mentioned in Section 2.4, field data were collected from the Blyth estuary for a neap (26-27th Sept 2001) and spring (19-20th Oct 2001) tide. During these periods weather conditions were dry and wind speeds generally below 5 ms^{-1} (with a brief maximum of 7 ms^{-1} during the neap tide). It can therefore be assumed that river runoff was low and resuspension of sediment from the mudflats due to wind induced wave stresses was negligible. For each survey, the ADCP was deployed on the bed in upward looking mode at a small section of the main channel near Reydon (Figure 5.2). Simultaneous particle size data were collected at the same location for a complete rise and fall of a tidal cycle using the InSiPID instrument. For the neap tide deployment, the flood and ebb particle size data collection was split between two tidal cycles due to daylight restrictions. For the spring tide, however, it was possible to obtain particle size data for an entire tidal cycle.

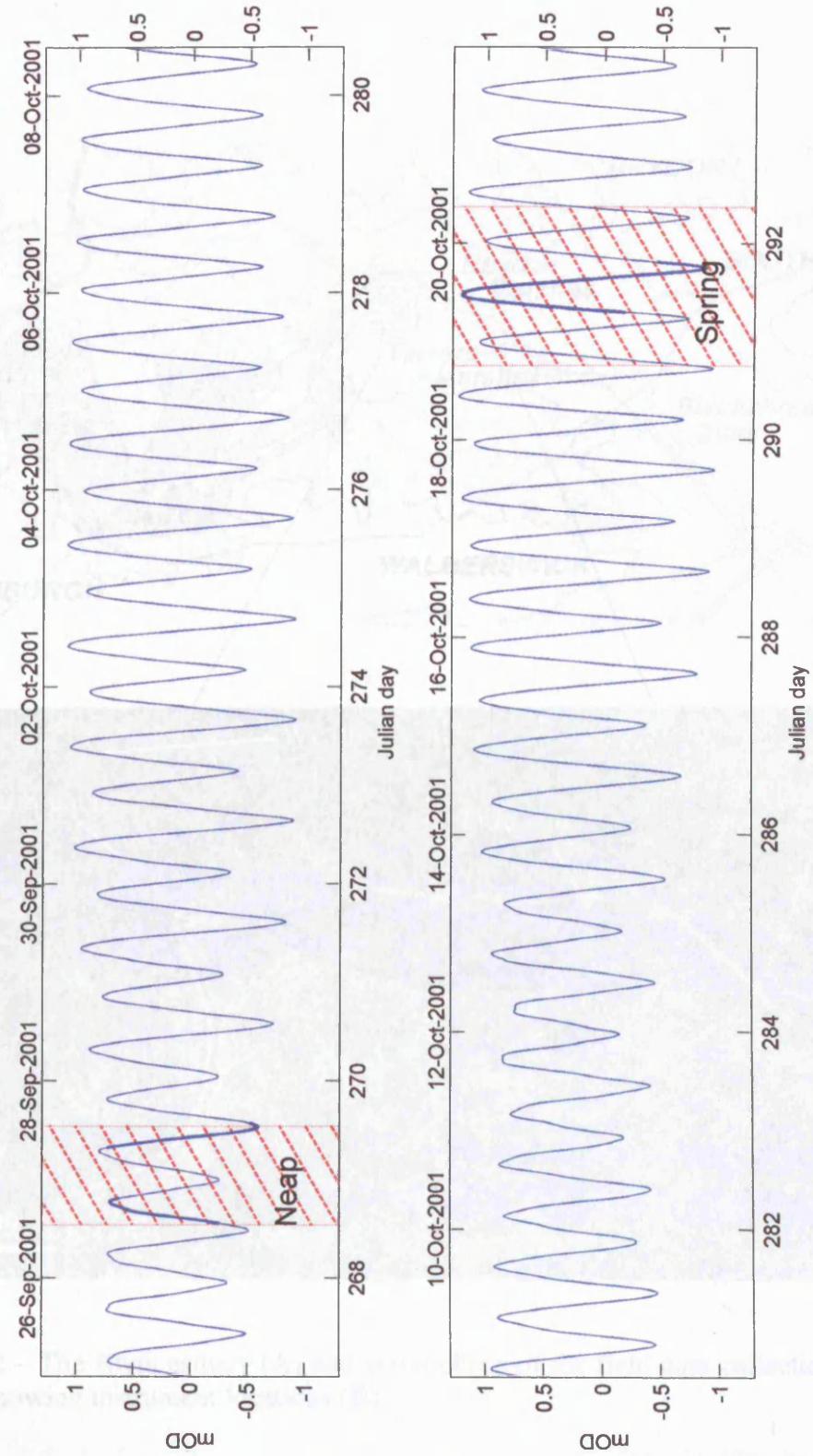

Figure 5.1 – Predicted tides for Southwold harbour between September 25th and October 22nd showing ADCP deployment periods (hatched regions) and the InSiPID data collection periods (bold line)

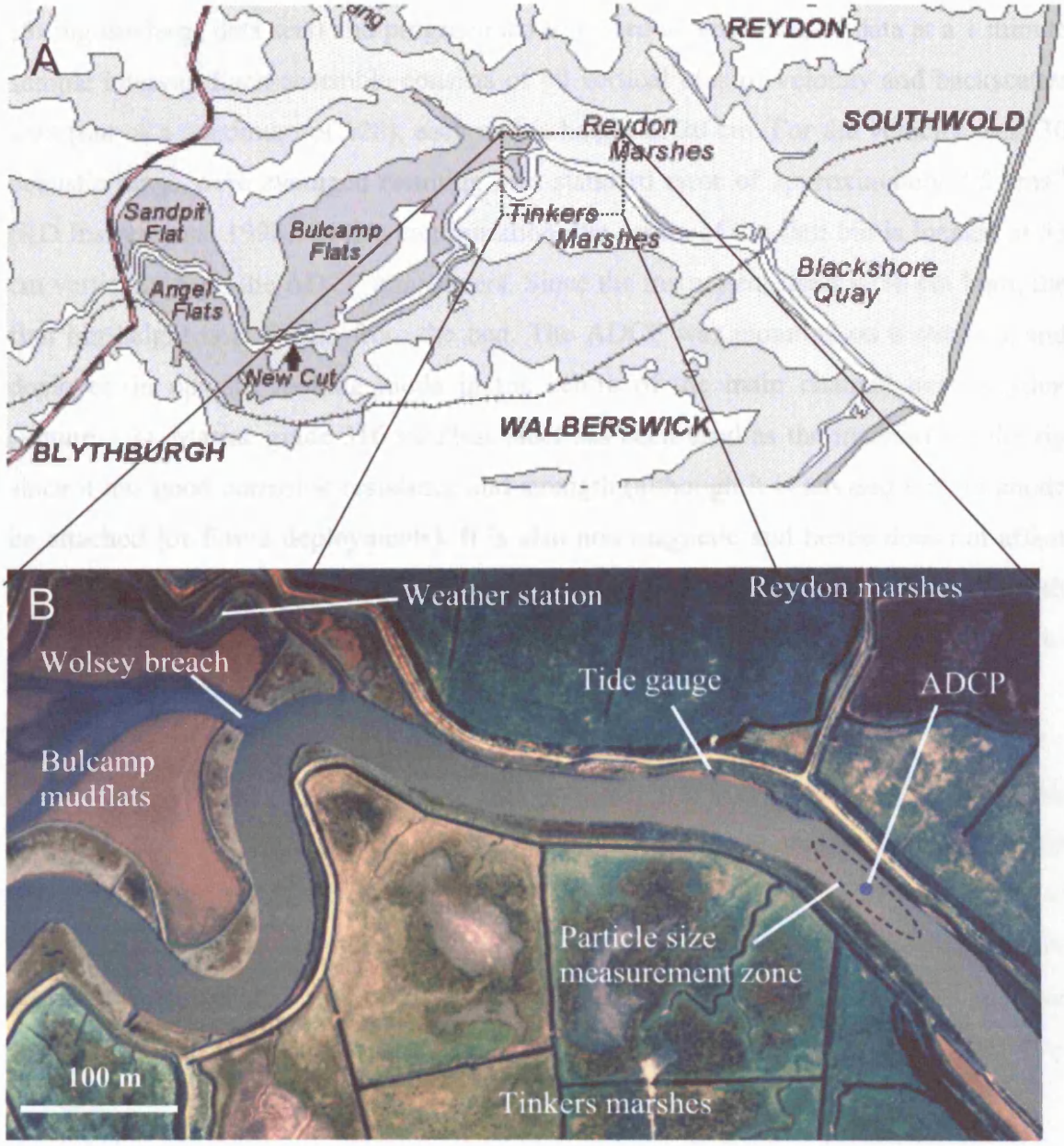

Figure 5.2 – The Blyth estuary (A) and aerial photo of the field data collection site near Reydon showing instrument locations (B).

5.2.1 ADCP time-series

Prior to both deployments, the ADCP was fitted with a 10 Mb PCMCIA flash-disk (for storing the large data sets) and programmed to record an ensemble of data at a 1 minute sample interval. Each ensemble consists of 40 vertical bins of velocity and backscatter data (out of a maximum of 128), each with a height of 20 cm. For the velocity data, 30 acoustic pings were averaged resulting in a standard error of approximately 2.5 cms^{-1} (RD Instruments, 1998). In this configuration, the centre of the first bin is located at 53 cm vertically from the ADCP transducers. Since the instrument itself is 38 cm high, the first bin height is at 91 cm from the bed. The ADCP was mounted on a steel rig and deployed in upward looking mode in the centre of the main channel near Reydon (Figure 5.2). Marine grade 316 stainless steel has been used as the material for the rig since it has good corrosion resistance and strength (although it is advised that an anode be attached for future deployments). It is also non-magnetic and hence does not affect the ADCP on-board compass. The ADCP was secured to the frame with four M8 titanium bolts and flange nuts (stainless steel bolts were found to be susceptible to corrosion by electrolysis).

The velocity (Figure 5.3) and range-scaled backscatter data (Figure 5.4) obtained from the ADCP for the spring and neap tide deployments show that the water column remains homogenously mixed, with no layering of flow velocity visible. Water level data from the ADCP integral pressure sensor is also plotted in these figures. Acoustic measurements cannot be made near to the water surface due to reflection of the acoustic signal from the water-air interface and also from resonant backscatter effects caused by bubbles which are formed by wave action (Zedel *et al*, 1996).

The depth mean current speed (Figure 5.8B and Figure 5.9B) was calculated from the velocity components using a power law profiling technique. This is achieved using a modified form of Manning's formula for open channel flows, to give the following equation (Chen, 1991; Simpson & Oltmann, 1990):

$$u = a' z^b \qquad (5.1)$$

where:

z = height above the bed (m)

u = current velocity at height z from the bed (ms^{-1})

$a' = 9.5u_* / z_0$ (s^{-1})

u_* = shear velocity (ms^{-1})

z_0 = bottom roughness height (m)

b = power exponent (1/6)

In this formula, the term a' is not known. It must therefore be obtained from the shape of the ADCP velocity profile data using the antiderivative of the power law (RD Instruments, 1999), written as:

$$a' = \frac{D_a (b+1) \sum_{i=Z_1}^{Z_2} u_i}{Z_2^{b+1} - Z_1^{b+1}} \qquad (5.2)$$

where:

D_a = ADCP range bin thickness (0.2 m)

Z_1 = Distance from the channel bed to the first (deepest) good bin (m)

Z_2 = Distance from the channel bed to the last (shallowest) good bin (m)

Using Equation 5.2, the antiderivative is calculated for the range bins located between the heights in the water column for which the ADCP can collect data, i.e. from the first bin at a fixed height above the instrument (Z_1) to the nearest bin to the water surface that is unaffected by reflectance (Z_2). The antiderivative is then applied over the top and bottom regions of the water column using Equation 5.1 to give a full velocity profile, from which a depth mean velocity magnitude is calculated (Figure 5.8B and Figure 5.9B).

The depth mean velocity data show that the flow is ebb dominated for both the neap and spring ebb tides, with maximum recorded speeds of 0.72 and 1.16 ms^{-1} respectively. Maximum speeds during the flood were 0.64 and 0.97 ms^{-1}.

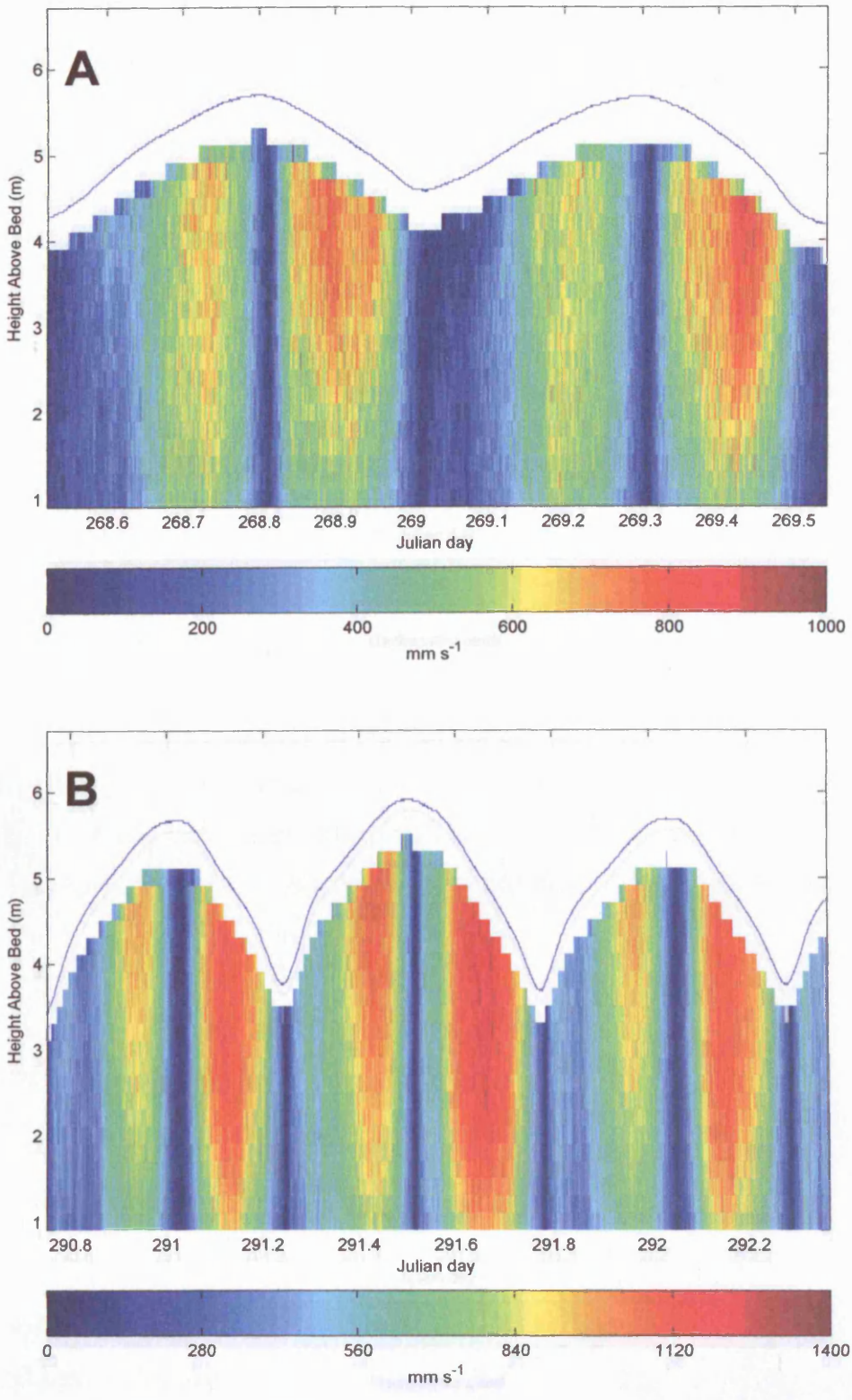

Figure 5.3 - Upward looking ADCP velocity magnitude profiles at Reydon field site for neap tide (A) and spring tide (B) deployments (note the difference in velocity scale and the deployment duration between the two plots). The water surface is also plotted from the ADCP's integral pressure sensor.

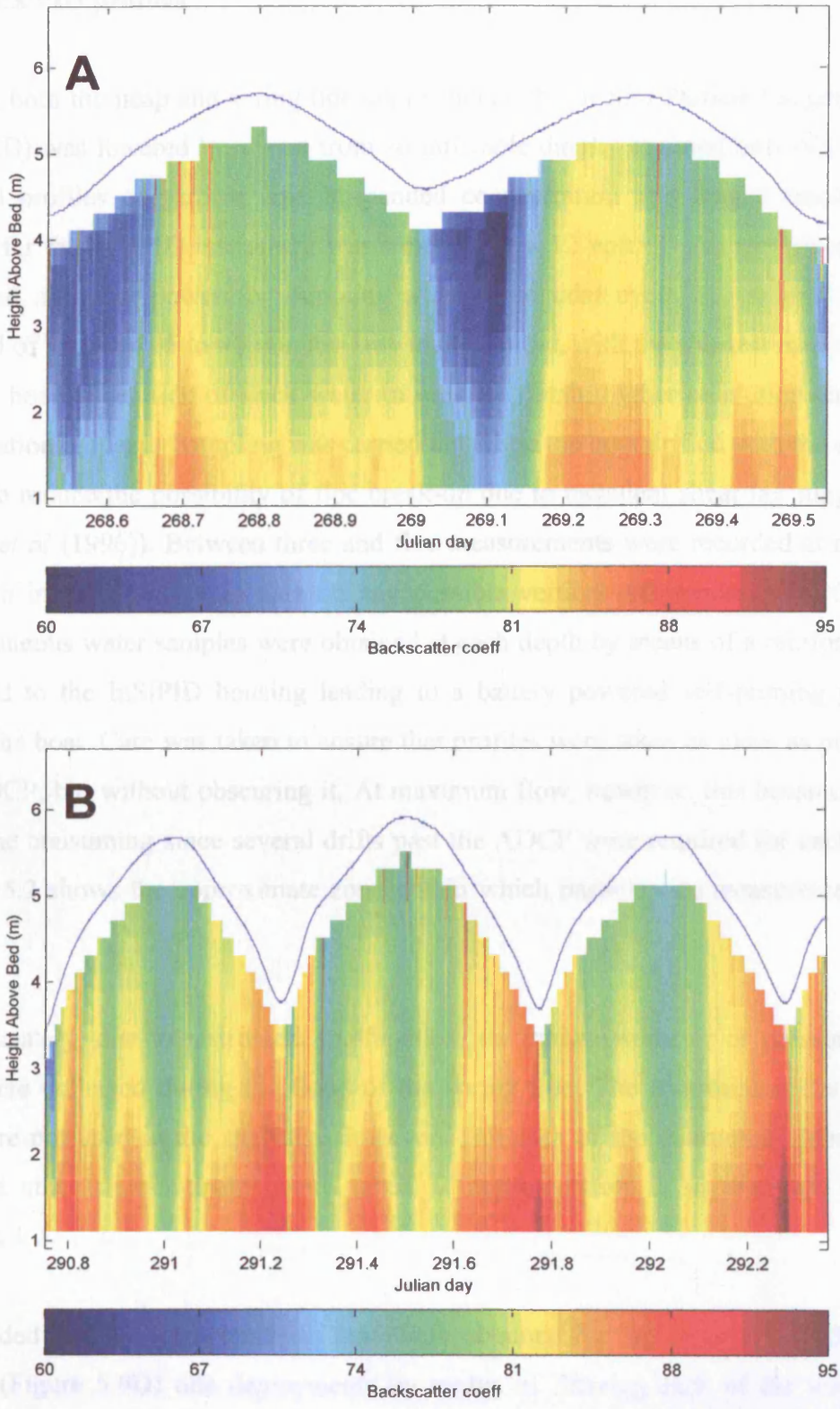

Figure 5.4 - ADCP backscatter coefficient at Reydon, corrected for beam spreading and attenuation, for the neap (A) and spring (B) tide deployments (note that the colour bar scaling is the same for each plot).

5.2.2 InSiPID profiles

During both the neap and spring tide deployments, the In Situ Particle Imaging Device (InSiPID) was lowered by a rope from an inflatable dinghy at timed intervals to obtain vertical profiles of particle size, suspended concentration and optical transmittance. Power for the InSiPID instrument was supplied by a 12 volt, 75 Ah car battery, which provided adequate power for sampling a complete tidal cycle. A variable sampling interval of between 15 to 40 minutes was implemented, with the shortest intervals taken half an hour either side of slack water in order to obtain higher resolution data on the flocculation process. Sampling was carried out while the boat drifted with the current in order to reduce the possibility of floc break-up due to turbulent shear (as suggested by Eisma *et al* (1996)). Between three and five measurements were recorded at roughly 1 m depth intervals to obtain data on any possible vertical differences in particle size. Simultaneous water samples were obtained at each depth by means of a reinforced hose attached to the InSiPID housing leading to a battery powered self-priming pump on board the boat. Care was taken to ensure that profiles were taken as close as possible to the ADCP, but without obscuring it. At maximum flow, however, this became difficult and time consuming since several drifts past the ADCP were required for each profile. Figure 5.2 shows the approximate zone within which particle size measurements were taken.

Unfortunately, due to instrument malfunction, no transmissometer or pressure sensor data were collected during the flood of the spring tide. The transmissometer data are therefore not used in the analysis. However, estimates of the instrument depth can be inferred since measurements were taken at approximately 1 m intervals from the surface.

Suspended sediment concentration data were obtained for the neap (Figure 5.8D) and spring (Figure 5.9D) tide deployments by means of filtering each of the water bottle samples using pre-weighed 47 mm GF/C filter papers (Whatman International Ltd, Cat. No. 1822 047). After drying, the filters were reweighed to determine the mass of sediment per unit volume of water to a precision of 10^{-4} g. Each data point is plotted separately with a trend line of the average of all the samples for each profile, which is considered to be approximately equal to the depth mean concentration. For the neap

tide, mean depth-averaged concentrations for the flood and ebb are 40.2 and 38.1 mgl^{-1} respectively, with maximums of 88.2 and 47.9 mgl^{-1}. Higher concentrations are observed during the spring tide, with mean depth-averaged values for the flood and ebb of 81.6 and 73.5 mgl^{-1} respectively, and maximums reaching 113.7 and 139.3 mgl^{-1}.

Generally, both particle size and SSC were found to be reasonably constant with depth for each deployment (Figure 5.6 and Figure 5.7) except around slack water when the combined effects of settling and resuspension result in larger sizes and higher concentrations near to the bed. This suggests that the sampling technique is internally consistent and shows that the water column is vertically well mixed for most of the time. At no point in the data are the concentrations high enough to form fluid mud (Section 1.3.3).

Figure 5.5 - Deploying the In Situ Particle Imaging Device at Reydon

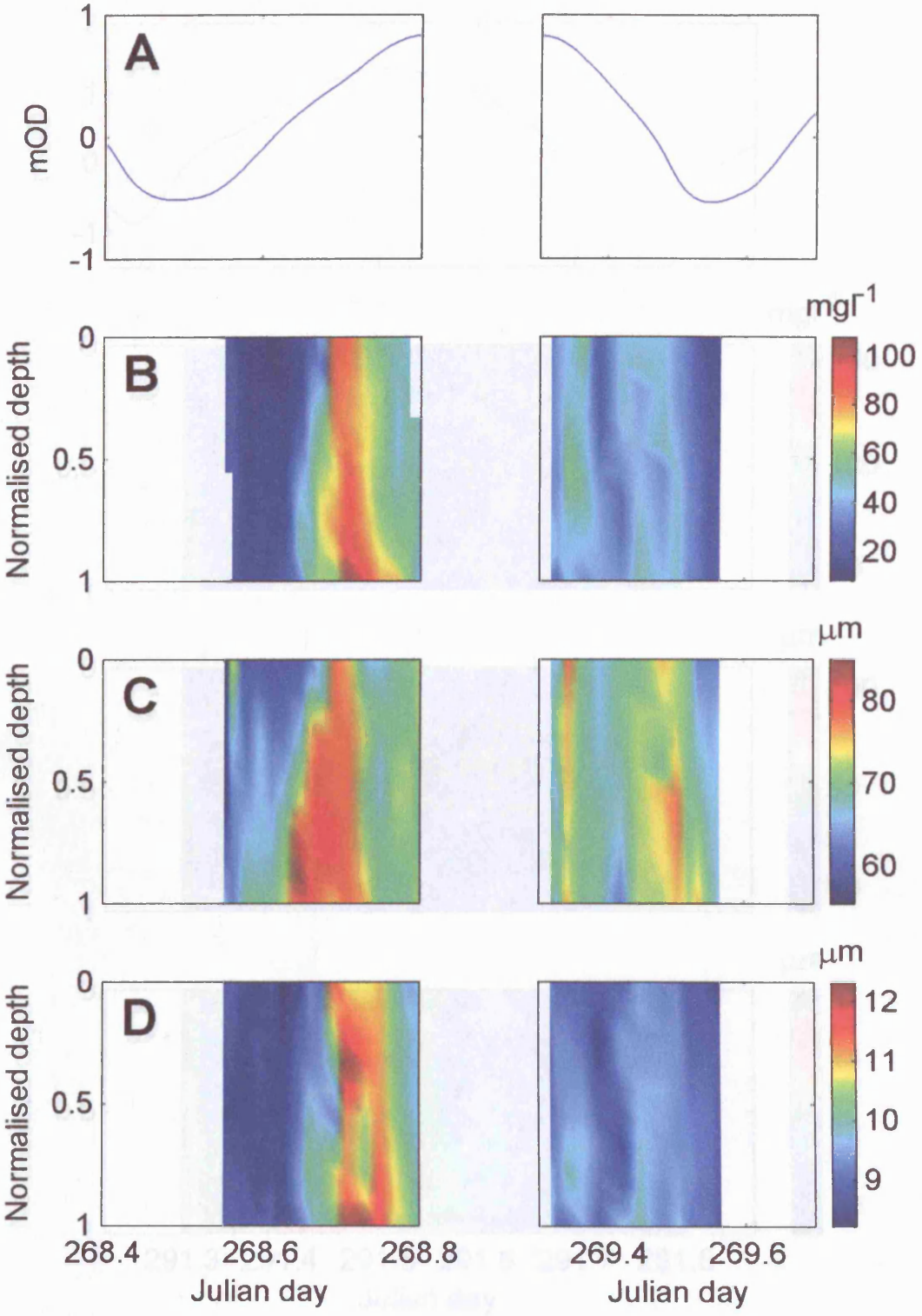

Figure 5.6 - Neap tide depth profile time series data showing the water level (A), suspended sediment concentration from water samples (B), low magnification D_{50} (C) and high magnification D_{50} (D). Note that depths are normalised.

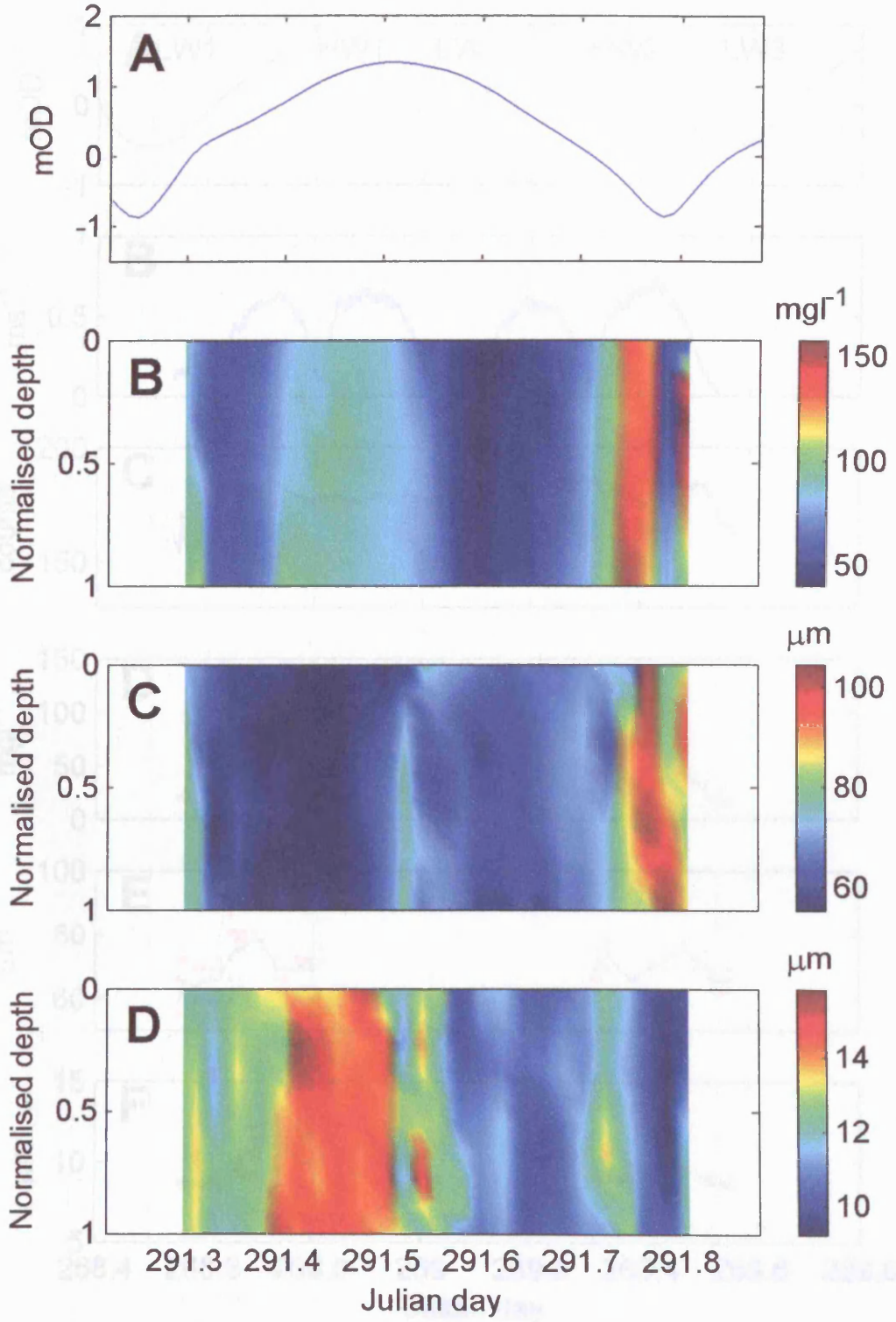

Figure 5.7 - Spring tide depth profile time series data showing the water level (A), suspended sediment concentration from water samples (B), low magnification D_{50} (C) and high magnification D_{50} (D). Note that depths are normalised.

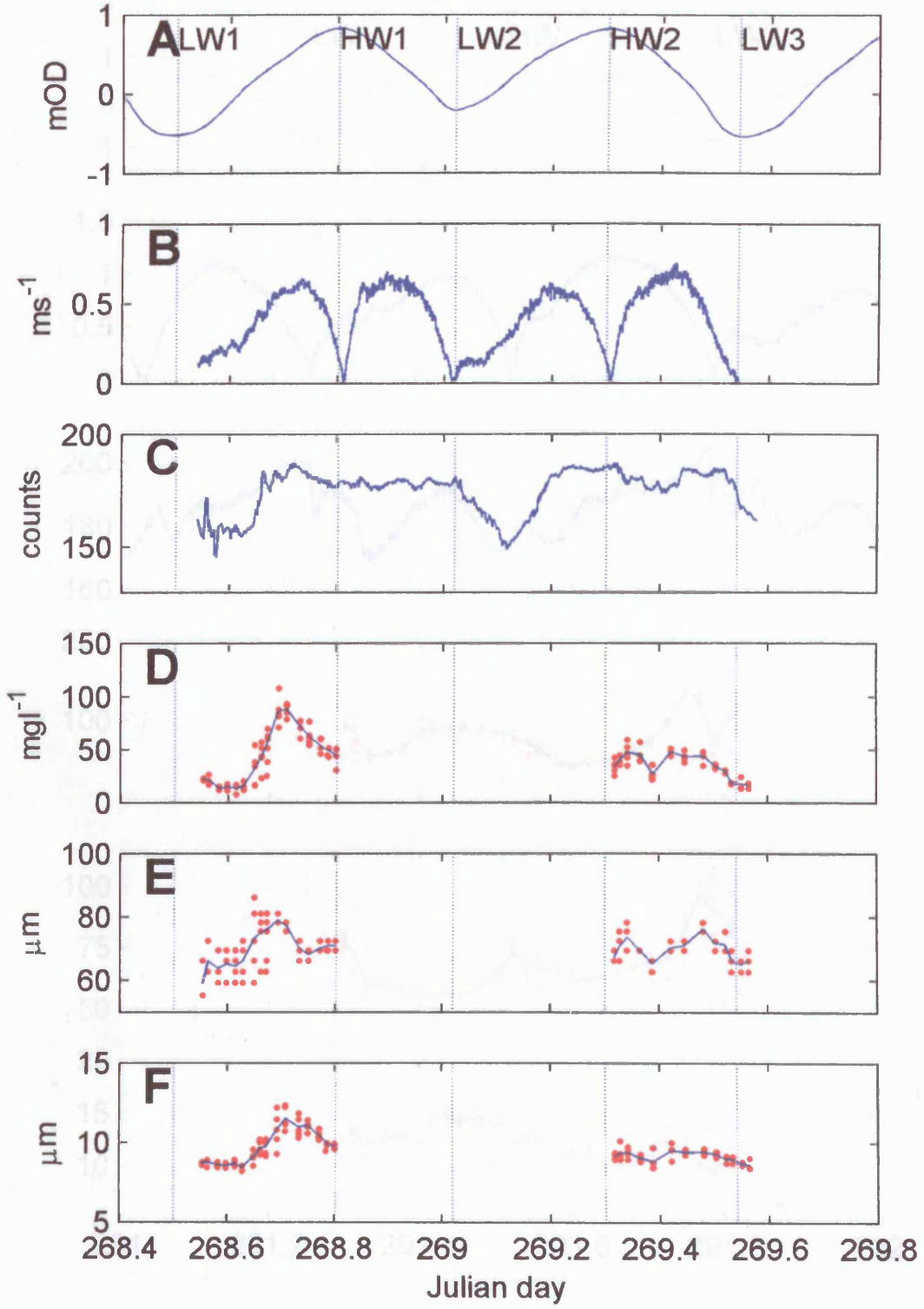

Figure 5.8 – Neap tide depth averaged data set for Reydon showing tide gauge water level (A), ADCP depth mean current speed from power law (B), ADCP bin 2 beam average backscatter (C), suspended sediment concentration from water samples (D), low magnification D_{50} (E) and high power D_{50} (F). In D to F, dots represent individual samples and the trend line represents the assumed depth average.

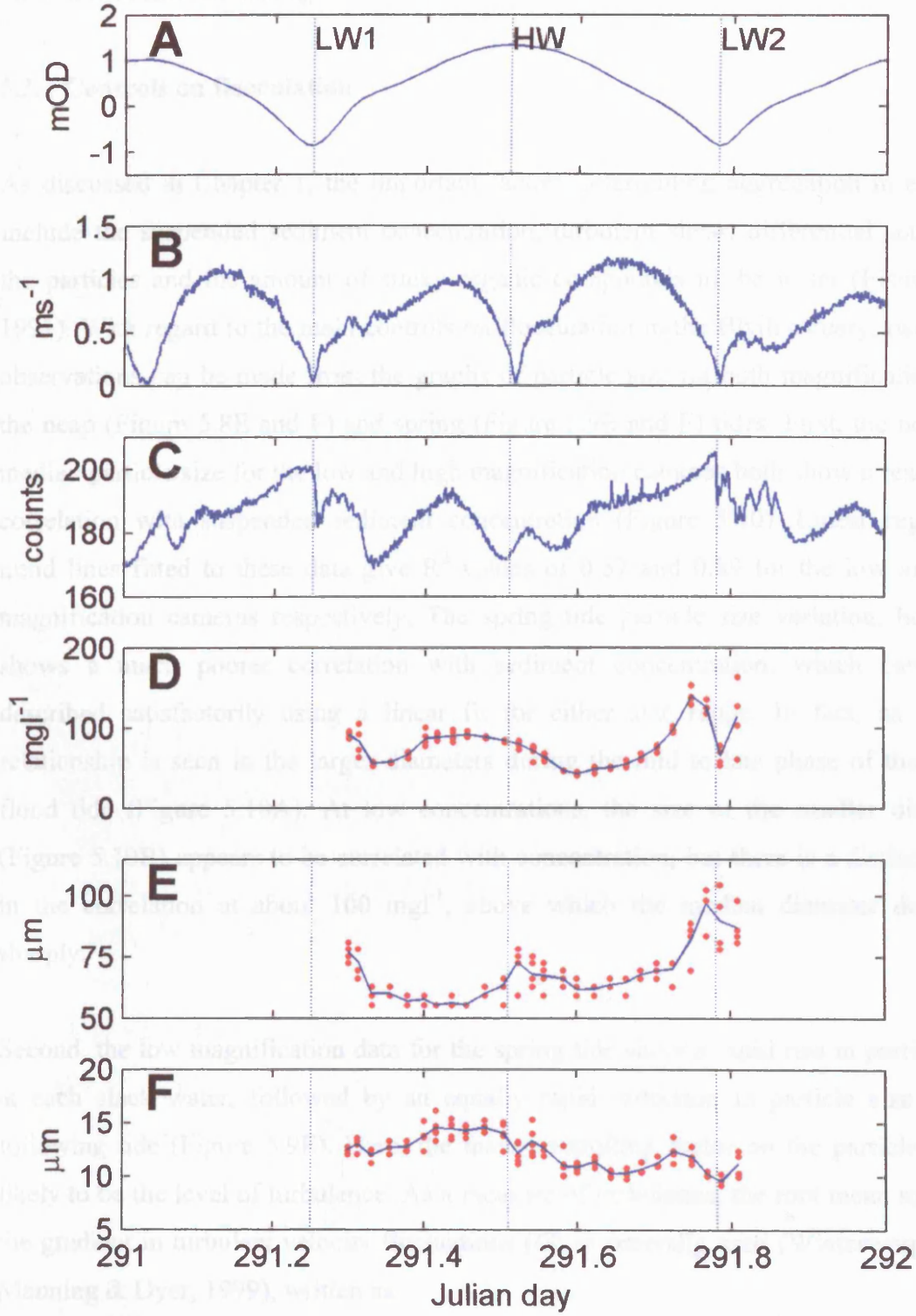

Figure 5.9 – Spring tide depth averaged data set for Reydon showing tide gauge water level (A), ADCP depth mean current speed from power law (B), ADCP bin 2 beam average backscatter (C), suspended sediment concentration from water samples (D), low magnification D_{50} (E) and high power D_{50} (F). Note the distinct peaks in particle size in (E) at slack water.

5.3 Particle size modelling

5.3.1 Controls on flocculation

As discussed in Chapter 1, the important factors determining aggregation in estuaries include the suspended sediment concentration, turbulent shear, differential settling of the particles and the amount of sticky organic compounds in the water (Eisma *et al*, 1991). With regard to the main controls on flocculation in the Blyth estuary, two initial observations can be made from the graphs of particle size (at both magnifications) for the neap (Figure 5.8E and F) and spring (Figure 5.9E and F) tides. First, the neap tide median particle size for the low and high magnification cameras both show a reasonable correlation with suspended sediment concentration (Figure 5.10). Linear regression trend lines fitted to these data give R^2 values of 0.57 and 0.89 for the low and high magnification cameras respectively. The spring tide particle size variation, however, shows a much poorer correlation with sediment concentration, which cannot be described satisfactorily using a linear fit for either size range. In fact, an inverse relationship is seen in the larger diameters during the mid to late phase of the spring flood tide (Figure 5.10A). At low concentrations, the size of the smaller diameters (Figure 5.10B) appears to be correlated with concentration, but there is a distinct break in the correlation at about 100 mgl^{-1}, above which the median diameter decreases sharply.

Second, the low magnification data for the spring tide show a rapid rise in particle size at each slack water, followed by an equally rapid reduction in particle size on the following tide (Figure 5.9E). Here, the main controlling factor on the particle size is likely to be the level of turbulence. As a measure of turbulence, the root mean square of the gradient in turbulent velocity fluctuations (G) is generally used (Winterwerp, 2002, Manning & Dyer, 1999), written as:

$$G = \left(\frac{\varepsilon}{\upsilon}\right)^{1/2} = u_* \left(\frac{|u|}{\upsilon} \cdot h\right)^{1/2} \qquad (5.3)$$

where:

ε = turbulent kinetic energy dissipation rate (m^2s^{-3})

υ = kinematic viscosity of water (m^2s^{-1})

h = water depth (m)

$|u|$ = depth mean current speed (ms^{-1})

u_* = shear velocity (ms^{-1})

Assuming the channel bed has a Manning friction coefficient (n) of 0.02 (as used by French (2001) in the 2D hydrodynamic model of the estuary), the shear velocity can be calculated using the data from the ADCP as (Delo, 1988):

$$u_* = \frac{|u| n \sqrt{g}}{h^{1/6}} \tag{5.4}$$

where:

n = Manning friction coefficient ($sm^{-1/3}$)

g = gravitational acceleration (ms^{-2})

Using the particle size data obtained from just the low power camera for the spring tide, a reasonable log relationship is obtained with the level of turbulence (Figure 5.11A). Differences are observed between the flood and the ebb phases of the spring tide, thus requiring two curves to be fitted to the data. The curves appear to be differentiated between the mid to late phase of the spring flood tide (after resuspension at the start of the flood) and the rest of the spring tide data. However, both curves are internally consistent with R^2 values of 0.58 and 0.85 respectively. Reasons for the differences in the two curves for flood and ebb are discussed later.

For the neap tide, the low magnification particle size data show a very different relationship to that of the spring tide data. At low values of G, the particle size increases proportionally with turbulence until a threshold is reached (between 15 to 30 s^{-1}), above which the diameters start to diminish with any further increase in G. A similar relationship is also apparent in the high magnification data for the spring ebb tide (Figure 5.11B). To highlight this, a quadratic polynomial has been fitted through the spring ebb data, giving a reasonable correlation (R^2 = 0.61). This is consistent with the

findings of Manning & Dyer (1999) who suggest that a small amount of turbulence is required for flocculation to occur, but above a certain threshold, the turbulent energy induces floc break-up. This observation may also be explained by the fact that, during periods of low turbulence, there is less sediment in suspension, thus resulting in smaller flocs.

In summary, the trends shown in Figure 5.10 and Figure 5.11 suggest that the floc size is dependent upon both the turbulence intensity and SSC. Up to this point, however, the particle size data from the two InSiPID cameras (each viewing different size ranges) have been assessed separately. Clearly, a better understanding of the size variability can be obtained if a single value of median diameter is calculated for the full particle size range by joining the size distribution data from each camera (discussed in the following section). A single value for D_{50} is also required for the development of a mathematical flocculation model, which can be used to test and quantify the theoretical model.

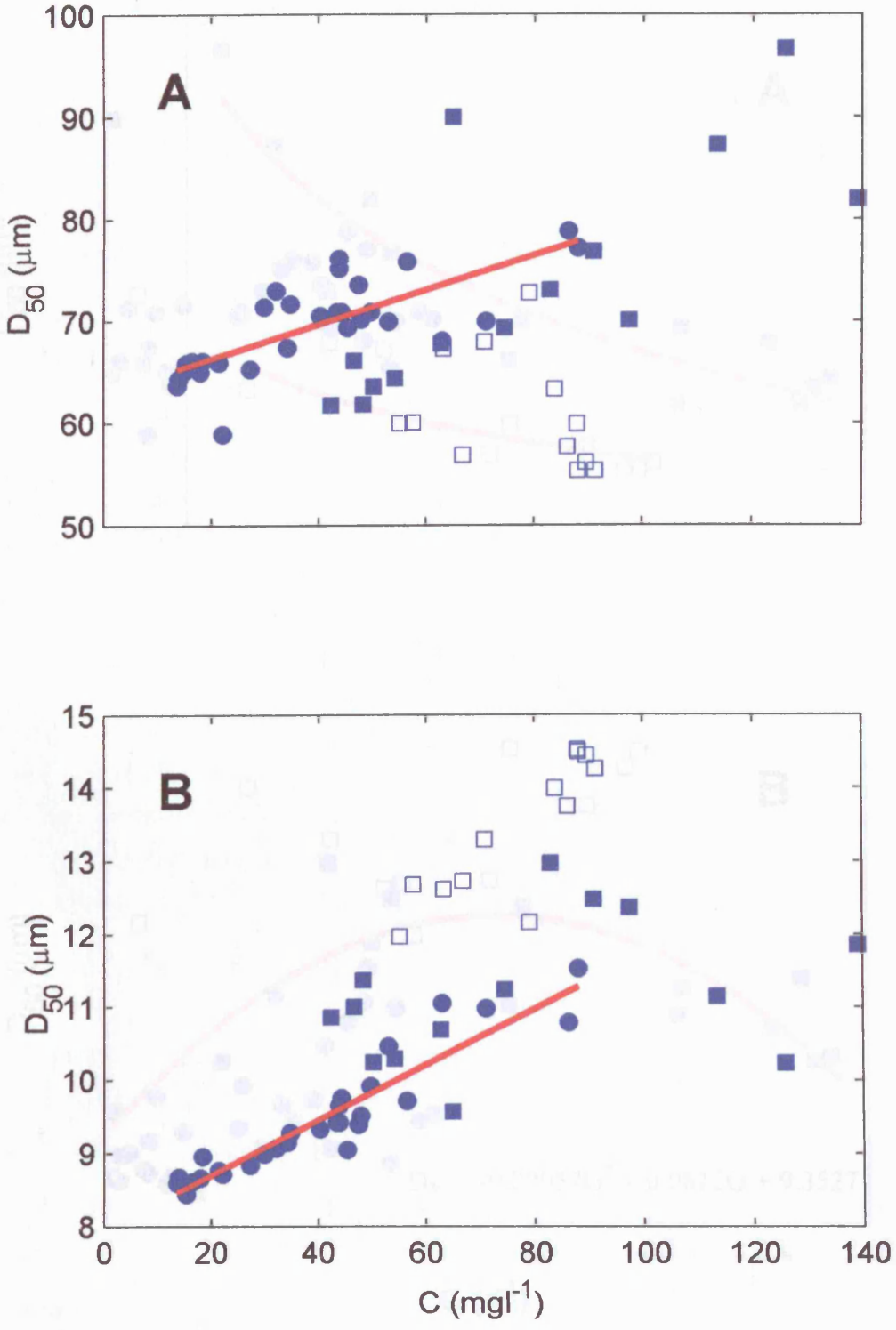

Figure 5.10 – Depth mean D_{50} vs suspended sediment concentration for the entire data from the low (A) and high (B) magnification systems. Circles mark the neap tide data and squares mark the spring tide. Flood spring tide data are represented by unfilled markers. The regression lines are fitted through the neap tide data in both graphs.

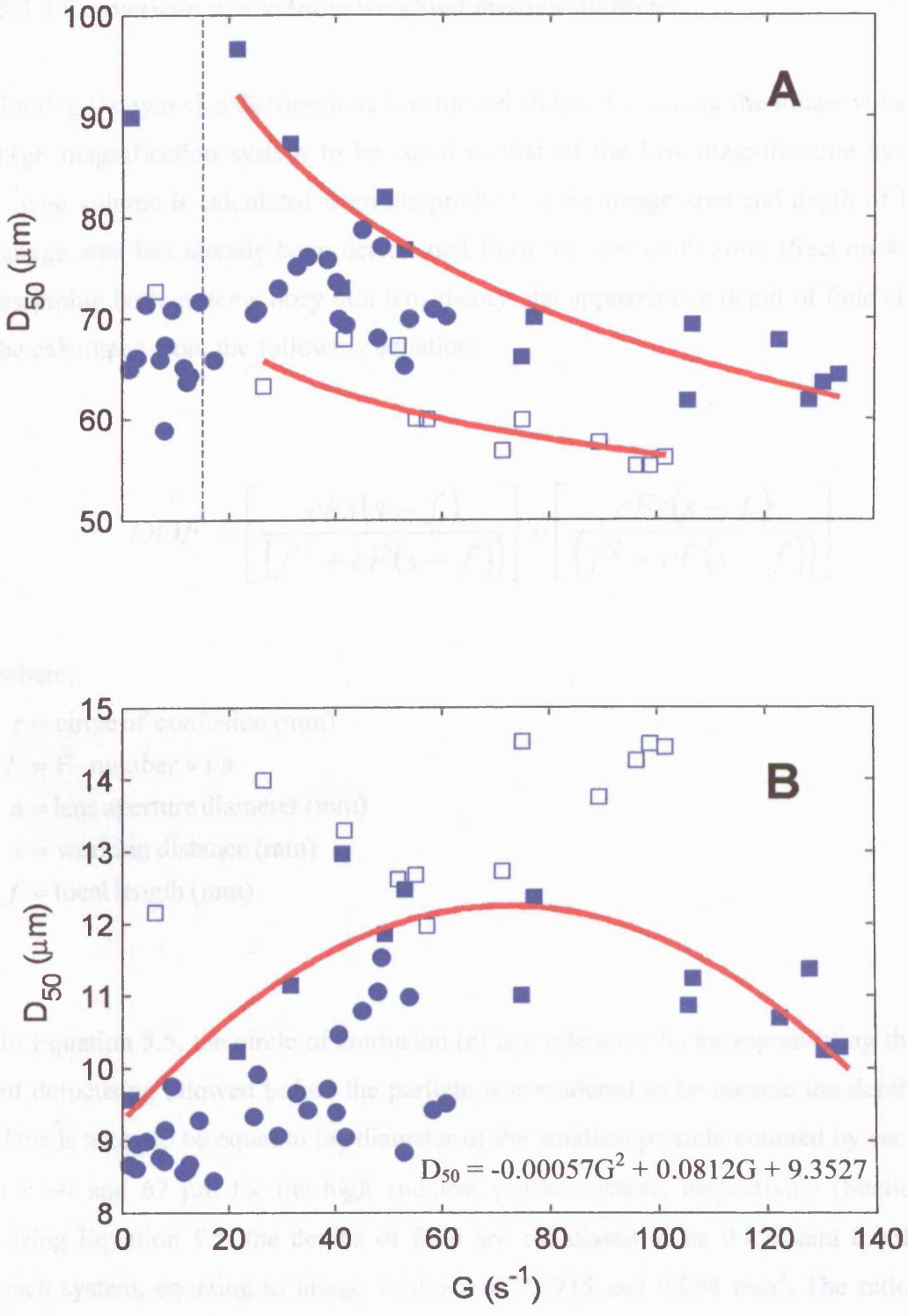

Figure 5.11 - Depth mean D_{50} vs turbulence parameter (G) for the entire data from the low (A) and high (B) magnification systems. Circles mark the neap tide data and squares mark the spring tide. Flood tide spring data are represented by unfilled markers. The two log regression lines in graph A are fitted through the spring tide flood (dashed curve) and ebb (solid curve). The quadratic polynomial in graph B is fitted through the spring ebb data (solid squares).

5.3.2 Conversion to a volume weighted median diameter

Joining the two size distributions is achieved simply by scaling the image volume of the high magnification system to be equal to that of the low magnification system. The image volume is calculated from the product of the image area and depth of field. The image area has already been determined from the size calibration (Section 4.2.2) and, assuming both systems obey thin lens theory, the approximate depth of field (*DOF*) can be calculated from the following equation:

$$DOF = \left[\frac{cFs(s-f)}{(f^2 + cF(s-f))}\right] + \left[\frac{cFs(s-f)}{(f^2 - cF(s-f))}\right] \qquad (5.5)$$

where:

c = circle of confusion (mm)
F = F - number ≈ f/a
a = lens aperture diameter (mm)
s = working distance (mm)
f = focal length (mm)

In Equation 5.5, the circle of confusion (c) is a tolerance factor representing the amount of defocusing allowed before the particle is considered to be outside the depth of field. This is taken to be equal to the diameter of the smallest particle counted by each system, i.e. ~4 and 62 μm for the high and low power systems respectively (Section 4.2.2). Using Equation 5.5, the depths of field are calculated to be 0.890 and 0.038 mm for each system, equating to image volumes of 93.915 and 0.008 mm^3. The ratio between the low and the high magnification image volumes is therefore approximately 11700:1.

The particle size data from the high magnification system are now multiplied by the ratio between the two volumes to provide a single size distribution. Any particle counts in the overlapping size bins are averaged. The resultant number distributions are then converted to a volume weighted size distribution by multiplying the counts in each range bin by the equivalent volume for that diameter. Figure 5.13B and Figure 5.14B

shows the resultant median diameter calculated from the volume weighted size distribution for the neap and spring tide respectively. The general shape of the graph is very similar to the number distributions obtained from just the low power camera system, but with an increase in the size range.

5.3.3 Floc density

For sediment transport studies, the use of a mass weighted median diameter is preferential since it describes the size of 50% of the mass of the sediment in suspension. Conversion from a volume to a mass weighted distribution requires knowledge of the particle density. However, no direct measurements of particle density are available for the period of data collection. In addition, the fractal nature of the flocs causes a decrease in density with increasing size (Gregory, 1997), thus a single value is not suitable. As discussed in Section 1.3.1, Winterwerp (1998) presents a method of estimating the floc density from fractal theory of natural aggregates using an adapted form of Stokes' Law (Equation 1.13) for the particle settling velocity (assuming a Reynolds number, $Re = w_s d / \nu < 1$), written as:

$$w_s = \frac{\alpha}{18\beta} \frac{(\rho_s - \rho_w) g}{\eta} d_p^{3-n_f} d_f^{n_f - 1} \tag{5.6}$$

where:

α, β = particle shape parameters (= 1 for spherical particles)
n_f = fractal dimension of flocs
d_p = diameter of the primaryparticles (μm)
d_f = diameter of the flocs (μm)

Since estuarine flocs have an average fractal dimension of n_f = 2 (Kranenburg, 1994; Winterwerp, 1998, 2002) it can be seen that the settling velocity becomes linearly proportional to particle diameter, i.e. $w_s \propto d^1$ and, hence, the floc effective density ($\rho_e = \rho_s - \rho_w$) is inversely proportional floc diameter, i.e. $\rho_e \propto d^{-1}$.

This can be demonstrated more simply by plotting diameter versus the effective density for a variety of floc sizes on a log-log plot (Gregory, 1997; Lagvankar & Gemmell, 1968; Tambo & Watanabe, 1979). The effective density (ρ_e) can be obtained experimentally using Stokes' Law (Equation 1.13) by measuring the size and settling velocity of each floc. Assuming the water density remains constant, a linear regression is fitted to the data to produce a power relationship of the form:

$$\rho_e = Bd^q \tag{5.7}$$

where:

$\rho_e = \rho_f - \rho_w$ = effective density of floc (kgm^{-3})
d = floc diameter (m)
B, q = power law constants

This method provides a simple relationship between particle size and density as shown in Figure 5.12. This is a composite graph of floc effective density variability from a number of different studies by various authors (McCave, 1975, 1984; Gibbs, 1985; Alldredge & Gotschalk, 1988; Al Ani *et al*, 1991; Kranck *et al*, 1993; Fennessy *et al*, 1994; Syvitski *et al*, 1995; Manning & Dyer, 1999; Sternberg *et al*, 1999). These data were obtained using video imaging of settling estuarine mud flocs in both the laboratory and the field. As can be seen, the slopes of the graphs are relatively consistent with each other and a linear fit to all the data provides an R^2 value of 0.713. The origin of this curve has been fixed at 5 μm (approximately the minimum size measured by InSiPID), at which it is assumed the maximum effective density is reached. Generally, it is assumed that estuarine flocs are composed of a 20:80 percent ratio of organic content to clay minerals (Fennessy *et al*, 1994; Manning & Dyer, 1999). Assuming densities of 2665 and 1030 kgm^{-3} for the clay mineral and organic content respectively, the maximum effective floc density is 1318 kgm^{-3}. The resultant power law constants B and q are 0.006907 and –0.996 respectively, thus showing that the particle density is inversely proportional to d. This confirms that a theoretical fractal dimension of 2 is a reasonable generalisation.

The derived power law equation is applied to each of the volume weighted size bins to provide a quasi-mass weighted distribution from which a new median diameter is determined (Figure 5.13C and Figure 5.14C). The mass and volume weighted median diameters are very similar, with only a minor reduction, which shows that the larger flocs contain the majority of the transported sediment mass, despite having a low density. It also suggests that the volume weighted distribution is a good first approximation to the mass weighted distribution.

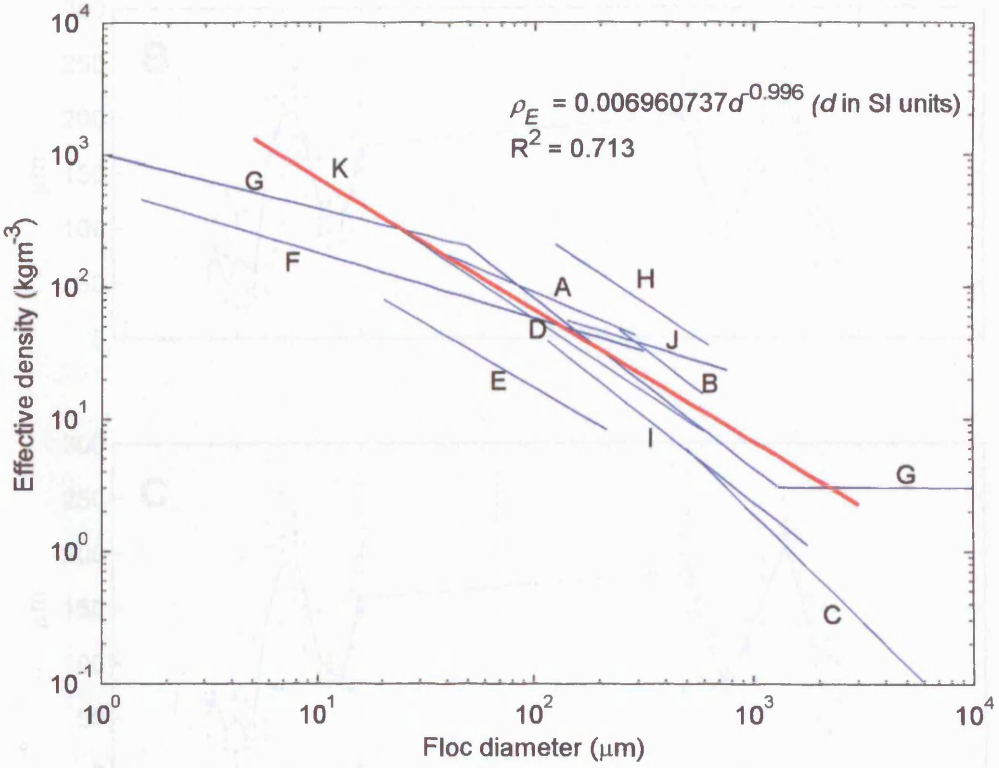

Figure 5.12 – Graph of floc diameter versus effective density, composed of data from a variety of authors: A = Manning & Dyer (1999); B = Al Ani *et al* (1991); C = Alldredge & Gotschalk (1988); D = Fennessy *et al* (1994); E = Gibbs (1985); F = McCave (1975); G = McCave (1984); H = Kranck *et al* (1993); I = Syvitski *et al* (1995); J = Sternberg *et al* (1999); K = linear regression through all data, forced through a fixed origin of 5 μm at an effective density of 1318 kgm^{-3} (see text for explanation).

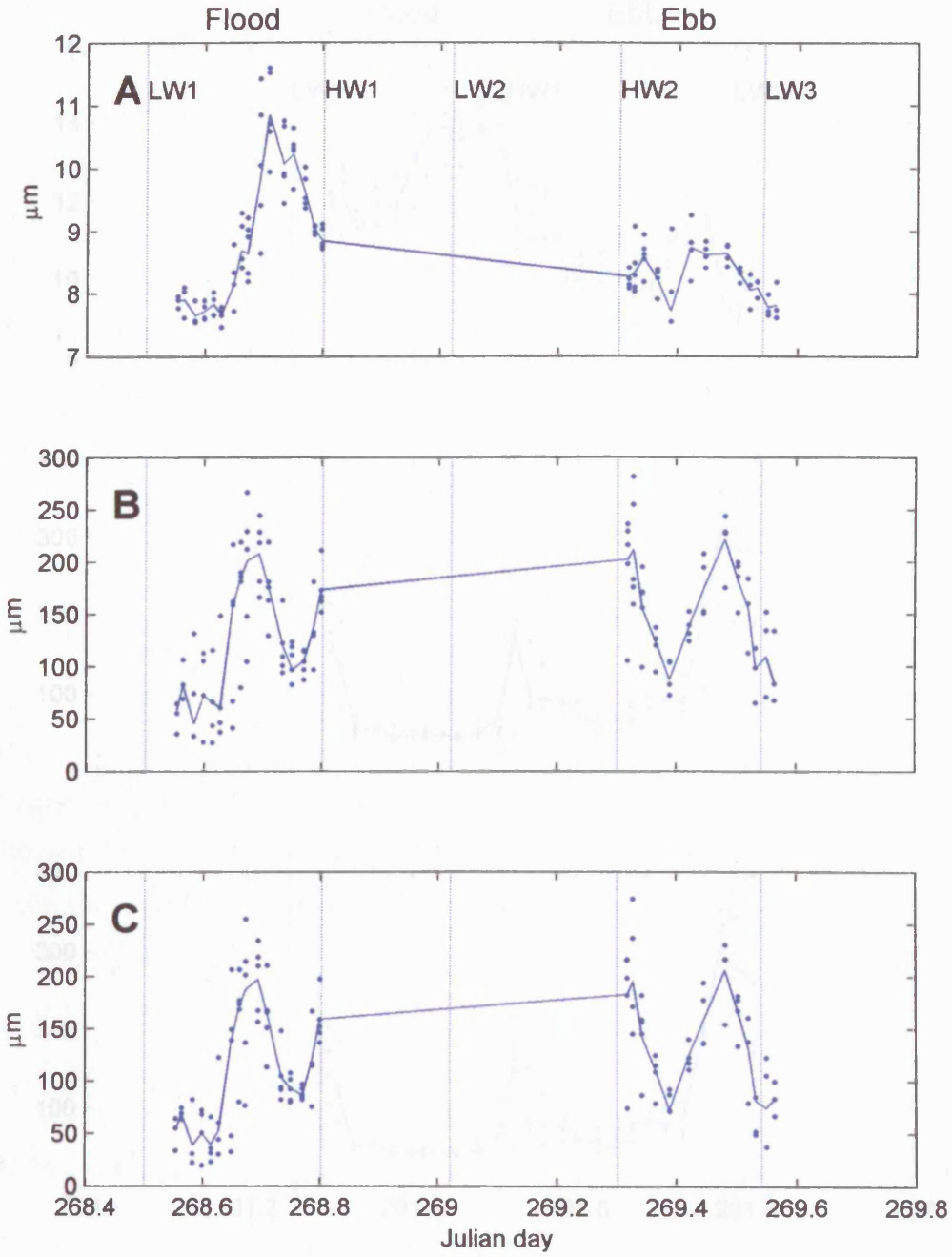

Figure 5.13 – Neap tide D_{50} calculated from a number (A), volume weighted (B) and quasi-mass weighted (C) particle size distribution from the combined camera data. The solid line represents the average for each vertical InSiPID profile (assumed to be equivalent to the depth average particle size).

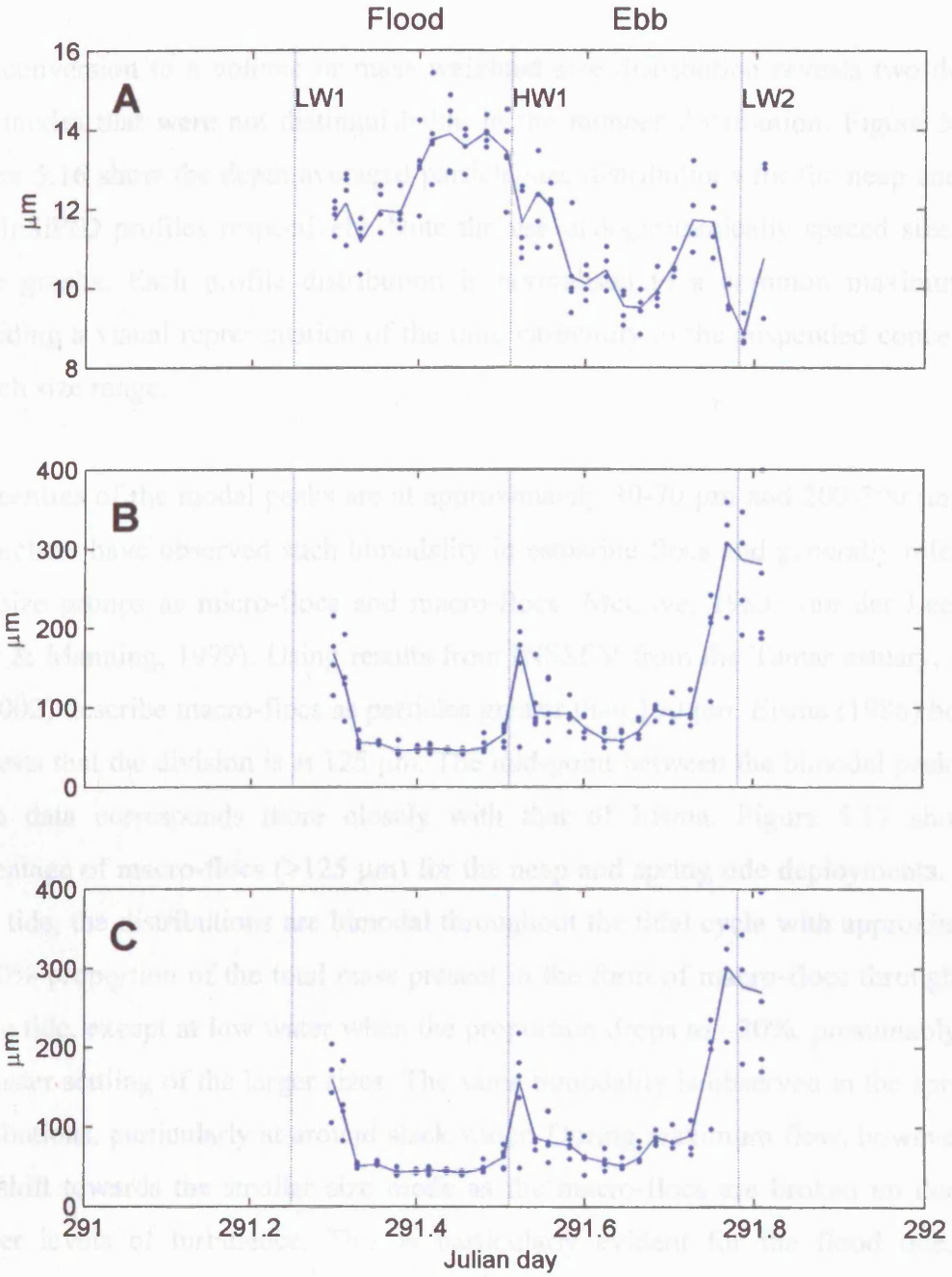

Figure 5.14 – Spring tide D_{50} calculated from a number (A), volume weighted (B) and quasi-mass weighted (C) particle size distribution from the combined camera data.

5.3.4 Particle sub-populations

The conversion to a volume or mass weighted size distribution reveals two dominant size modes that were not distinguishable in the number distribution. Figure 5.15 and Figure 5.16 show the depth averaged particle size distributions for the neap and spring tide InSiPID profiles respectively. Note the use of logarithmically spaced size bins in these graphs. Each profile distribution is normalised to a common maximum, thus providing a visual representation of the time variability in the suspended concentration at each size range.

The centres of the modal peaks are at approximately 30-70 μm and 200-300 μm. Other researchers have observed such bimodality in estuarine flocs and generally refer to the two size groups as micro-flocs and macro-flocs (McCave, 1983; van der Lee, 2000; Dyer & Manning, 1999). Using results from INSSEV from the Tamar estuary, Dyer *et al* (2002) describe macro-flocs as particles greater than 160 μm. Eisma (1986) however, suggests that the division is at 125 μm. The mid-point between the bimodal peaks in the Blyth data corresponds more closely with that of Eisma. Figure 5.17 shows the percentage of macro-flocs (>125 μm) for the neap and spring tide deployments. For the neap tide, the distributions are bimodal throughout the tidal cycle with approximately a 30-60% proportion of the total mass present in the form of macro-flocs throughout the whole tide, except at low water when the proportion drops to ~20%, presumably due to the faster settling of the larger sizes. The same bimodality is observed in the spring tide distributions, particularly at around slack water. During maximum flow, however, there is a shift towards the smaller size mode as the macro-flocs are broken up due to the greater levels of turbulence. This is particularly evident for the flood tide, which exhibits a near unimodal distribution of ~90% micro-flocs with almost a complete absence of any macro-flocs. This may be as a result of the advection of different particle sub-populations during the flood and ebb stages of the tide. The largest proportion of macro-flocs is observed during the slack water periods, with approximately 60% and 80% for the high and low water respectively.

The peaks in the distribution are more prominent during the spring tide because of the higher suspended sediment concentrations and levels of turbulence. Interestingly, the observed difference between neap and spring tide distributions compares with the

findings of McCave (1984) for marine snow (in the deep ocean) where particle size distributions near to the bed are more sorted into two modes due to active resuspension (equivalent to the spring tide situation) as compared to the less turbulent mid-water depths where flocculation due to differential settling leads to a flatter distribution (equivalent to the neap tide situation).

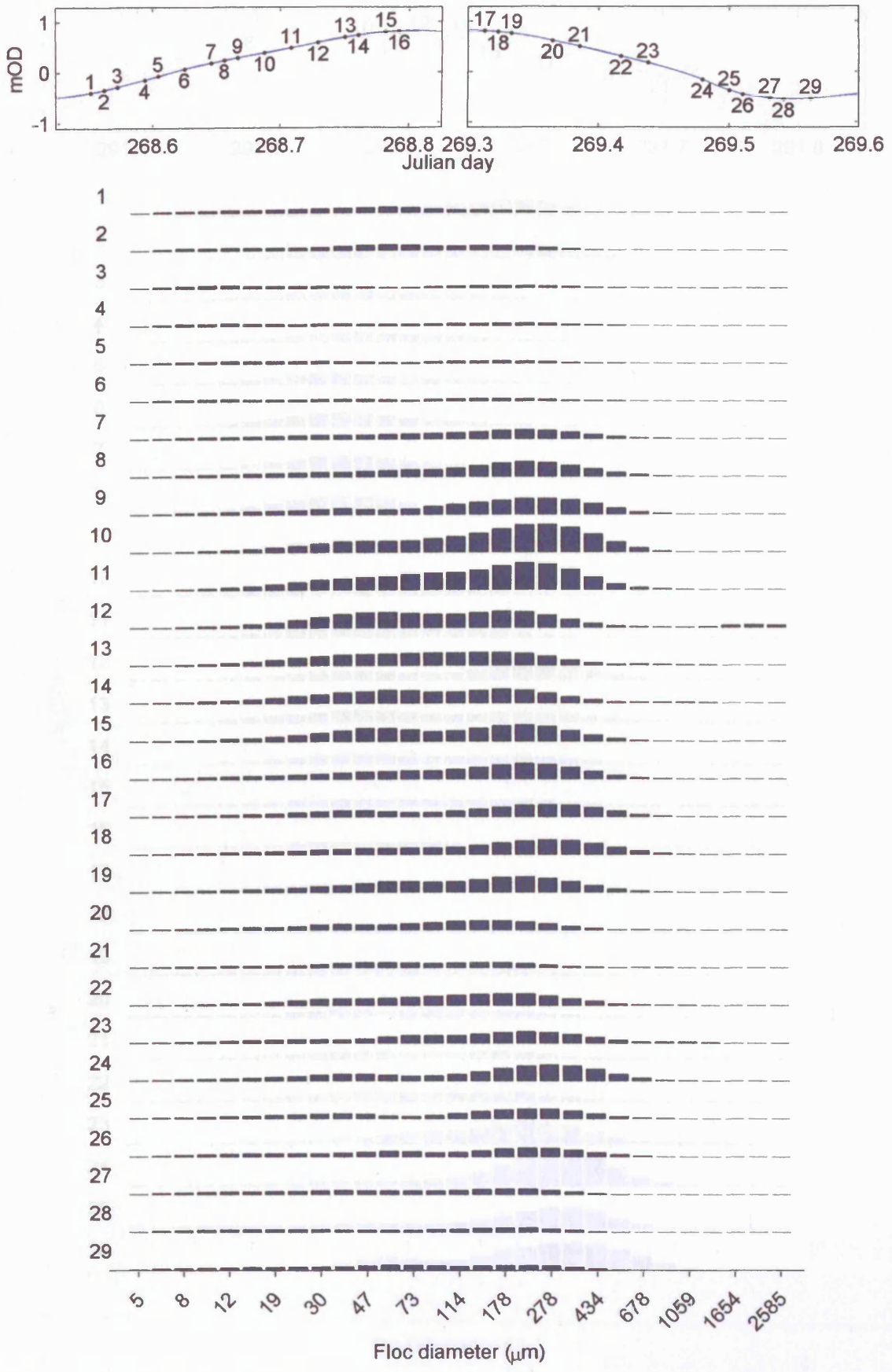

Figure 5.15 - Quasi-mass weighted, depth-averaged particle size distribution for each InSiPID profile (neap tide). Each graph is normalised to a common maximum mass.

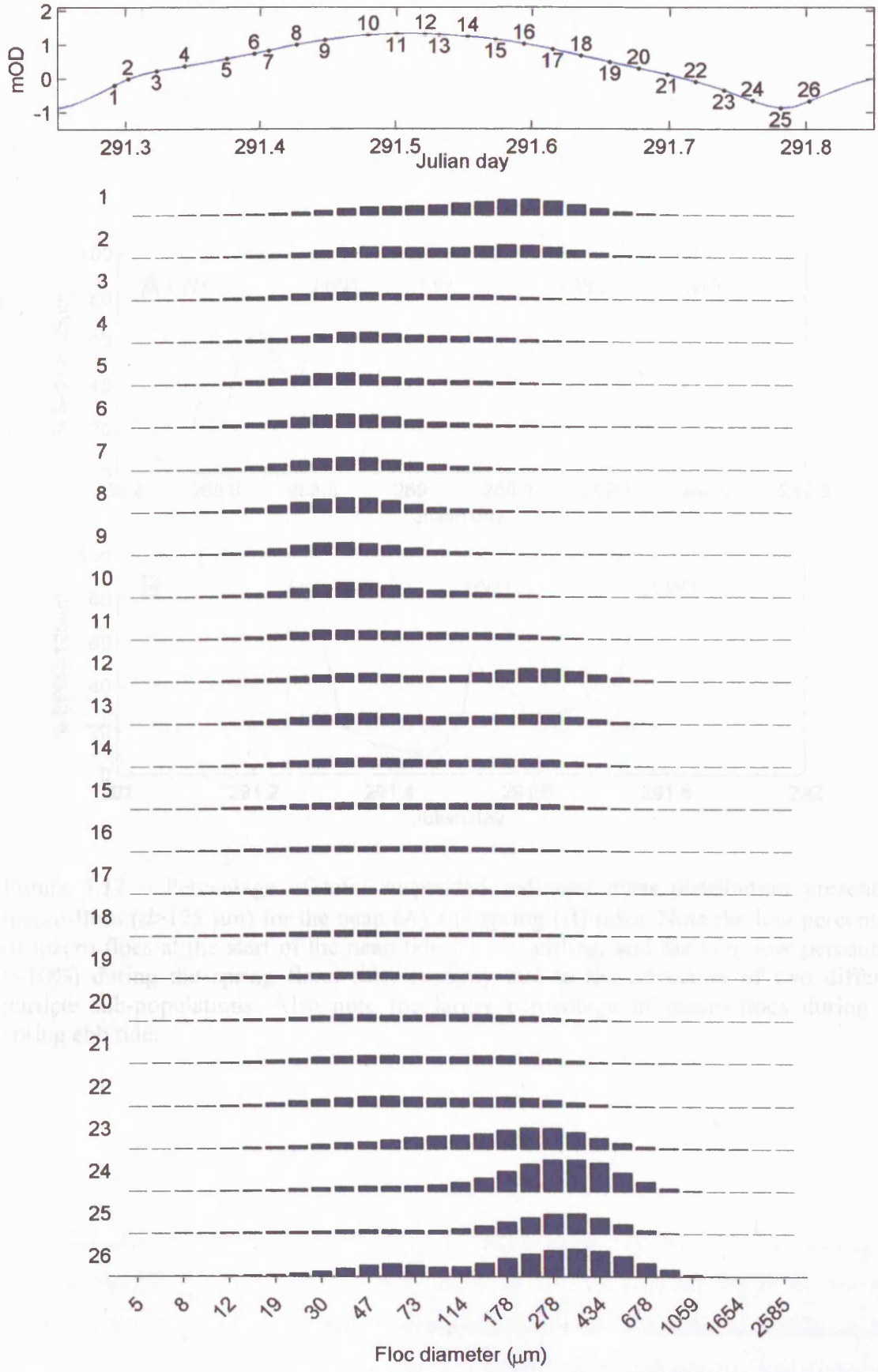

Figure 5.16 - Quasi-mass weighted, depth averaged particle size distribution for each InSiPID profile (spring tide). Each graph is normalised to a common maximum mass.

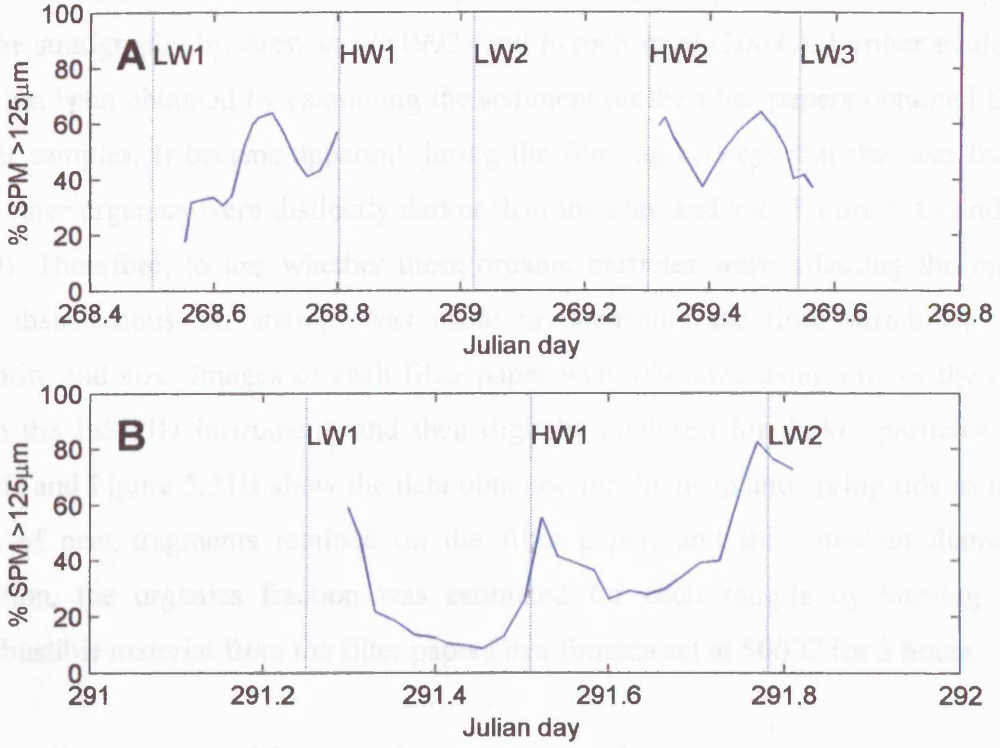

Figure 5.17 – Percentage of total suspended sediment mass distribution present as macro-flocs (d>125 µm) for the neap (A) and spring (B) tides. Note the low percentage of macro-flocs at the start of the neap tide due to settling, and the very low percentage (<10%) during the spring flood tide, possibly due to the advection of two different particle sub-populations. Also note the larger percentage of macro-flocs during the spring ebb tide.

Apart from the time-variability in floc size, it is possible that some of the observed bimodality in the particle size distributions is due to the presence of large organic material such as peat fragments, diatoms and algae. Field observations in the Blyth estuary show that the bottom sediment is predominantly composed of clay (deposited in marine conditions after inundation of the glacial valley by the rising sea levels during the Holocene) with spatially varied proportions of organic peat (substantiated by studies of the stratigraphy by Brew *et al* (1992) and French *et al* (2004)). Further evidence for this has been obtained by examining the sediment on the filter papers obtained from the water samples. It became apparent during the filtering process that the peat fragments and other organics were distinctly darker than the clay and silt (Figure 5.18 and Figure 5.19). Therefore, to test whether these organic particles were affecting the measured size distributions, an attempt was made to determine the time variability in their quantity and size. Images of each filter paper were obtained using one of the cameras from the InSiPID instrument, and then digitally analysed for darker particles. Figure 5.20B and Figure 5.21B show the data obtained for the neap and spring tide as the total area of peat fragments retained on the filter paper, and their median diameter. In addition, the organics fraction was estimated for each sample by burning off the combustible material from the filter papers in a furnace set at 500°C for 5 hours.

The median diameter of the imaged organic material is reasonably constant at about 175 μm for both the spring and neap tide, except during slack water when settling of the particles results in smaller median sizes. The total area of the large peat fragments on the filter papers varies in proportion to sediment concentration for both experiments. In addition, the larger peat fragments are likely to settle out rapidly as the flow velocity reduces, which is supported in Figure 5.20B and Figure 5.21B. This confirms that the large particle size mode measured by InSiPID during slack water periods is primarily due to flocculation of the clay particles.

The loss-on-ignition data (Figure 5.20C and Figure 5.21C) show that the percentage of organic material in suspension during the neap tide is between 10-30%, which is slightly higher than the spring tide percentage of 10-15%. A similar variability in total organics was observed by Winterwerp *et al* (2002) in the Tamar estuary, where the neap and spring tide percentages were 13-18% and 10-12.5% respectively. This suggests that there is less resuspension of denser inorganic particles during the neap tide, resulting in

a larger proportion of low-density organic material. During both the spring and neap tides, the percent organics increases during slack water as the clay particles settle out more quickly (particularly during the longer slack low water). In general, the total mass of organic material is proportional to the total suspended concentration. However, differences are observed on the neap mid-ebb, where there is larger variability in organic material that does not correspond to the total suspended load. The higher proportion of organic material during the neap tide may contribute to the presence of macro-flocs throughout the tidal cycle due to the sticky properties of organic compounds (Eisma *et al*, 1991) in addition to the lower turbulence intensities.

One method of determining changes in particle properties is to use shape analysis. For instance, the fractal dimension has been shown to represent the porosity, or density, of floc structure (Gregory, 1997). As discussed in Section 4.3.5, the depth mean fractal dimension was calculated from the log-log plot of maximum length versus particle area for the neap (Figure 5.20D) and spring tide data (Figure 5.21D). In theory, the fractal dimension should decrease as the structure of the floc becomes more porous due to the increased concavity of the particle perimeter. However, a problem with this method arises due to resultant 'fluffy' edges of the larger flocs, which cannot be imaged correctly by the InSiPID system due to defocusing and lack of image resolution, thus forming a more circular shaped object in the binary image. Consequently, the presence of flocs causes an apparent *increase* in the fractal dimension. In addition, the inherent limit of the pixel resolution means that smaller particles are not measured correctly, and must therefore be discarded. Due to the poor quality of the images, this method cannot be relied upon to give accurate measurements of fractal dimension. Despite this, the graphs of fractal dimension show a large difference in particle characteristics between flood and ebb of the spring tide, suggesting that there are indeed two particle sub-populations.

It may be concluded that the use of a single parameter (i.e. D_{50}) is not very appropriate for representing the particle size distribution. However, since the quasi-mass weighted D_{50} is an estimate of the size of 50^{th} percentile of the settling flux, it is still useful for determining the mean settling velocity of the sediment in suspension. In addition, the incorporation of a multimodal size distribution in the sediment transport model is complex and considered beyond the scope of this project.

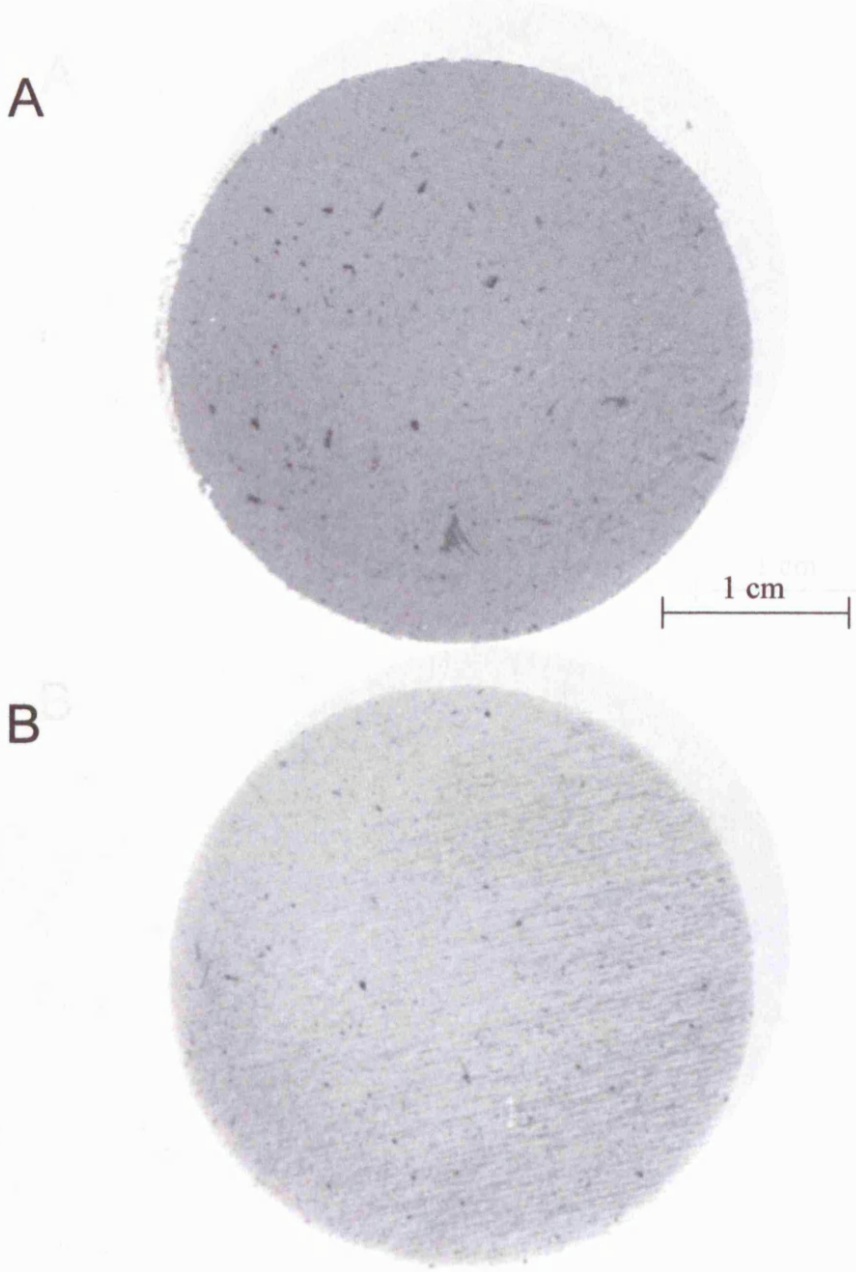

Figure 5.18 – Neap tide representative images of filter papers from the mid flood (A) and ebb (B) water samples. Note the presence of large organic material (seen as darker fragments)

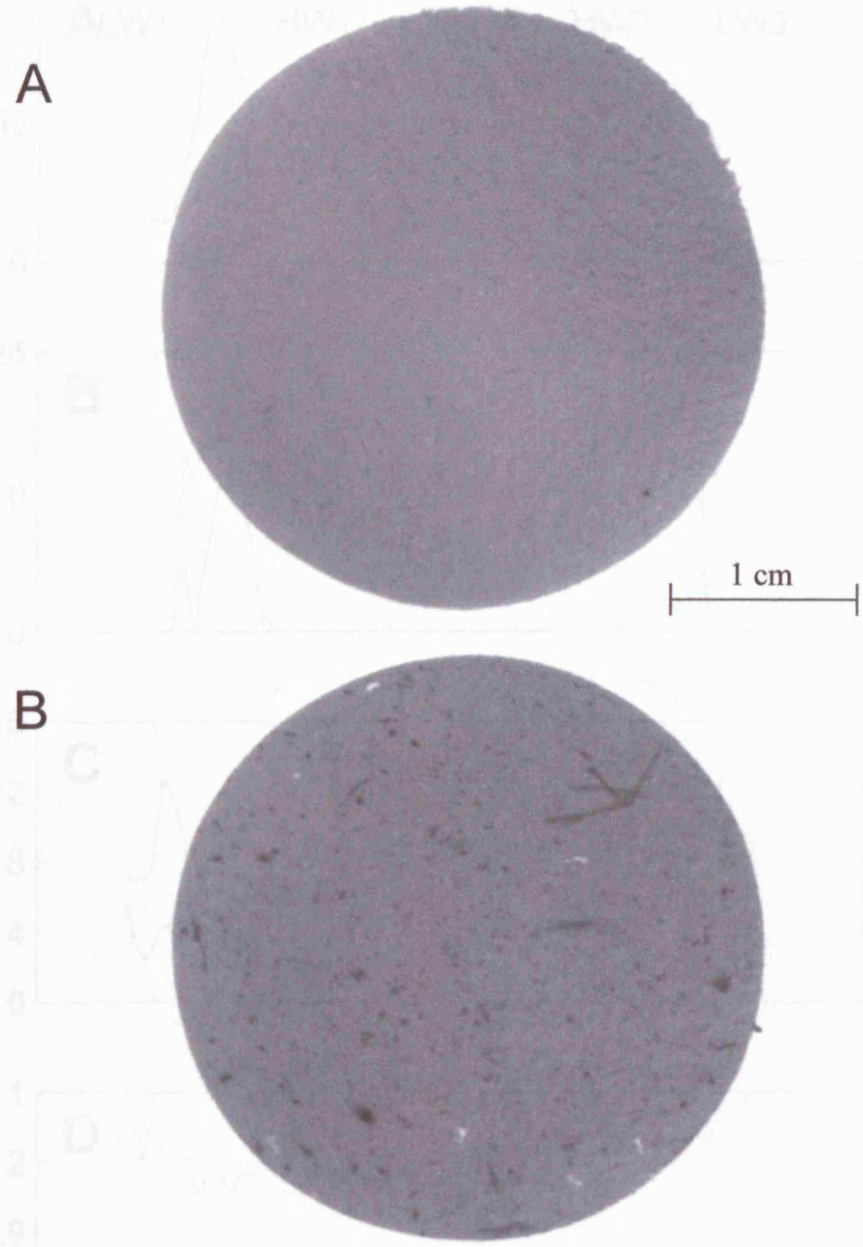

Figure 5.19 – Spring tide representative images of water sample filter papers taken during mid flood (A) and towards the end of the ebb (B). Note the darker colouration as compared to the neaps (indicating higher sediment concentrations) and lower proportion of organic material in the flood sample.

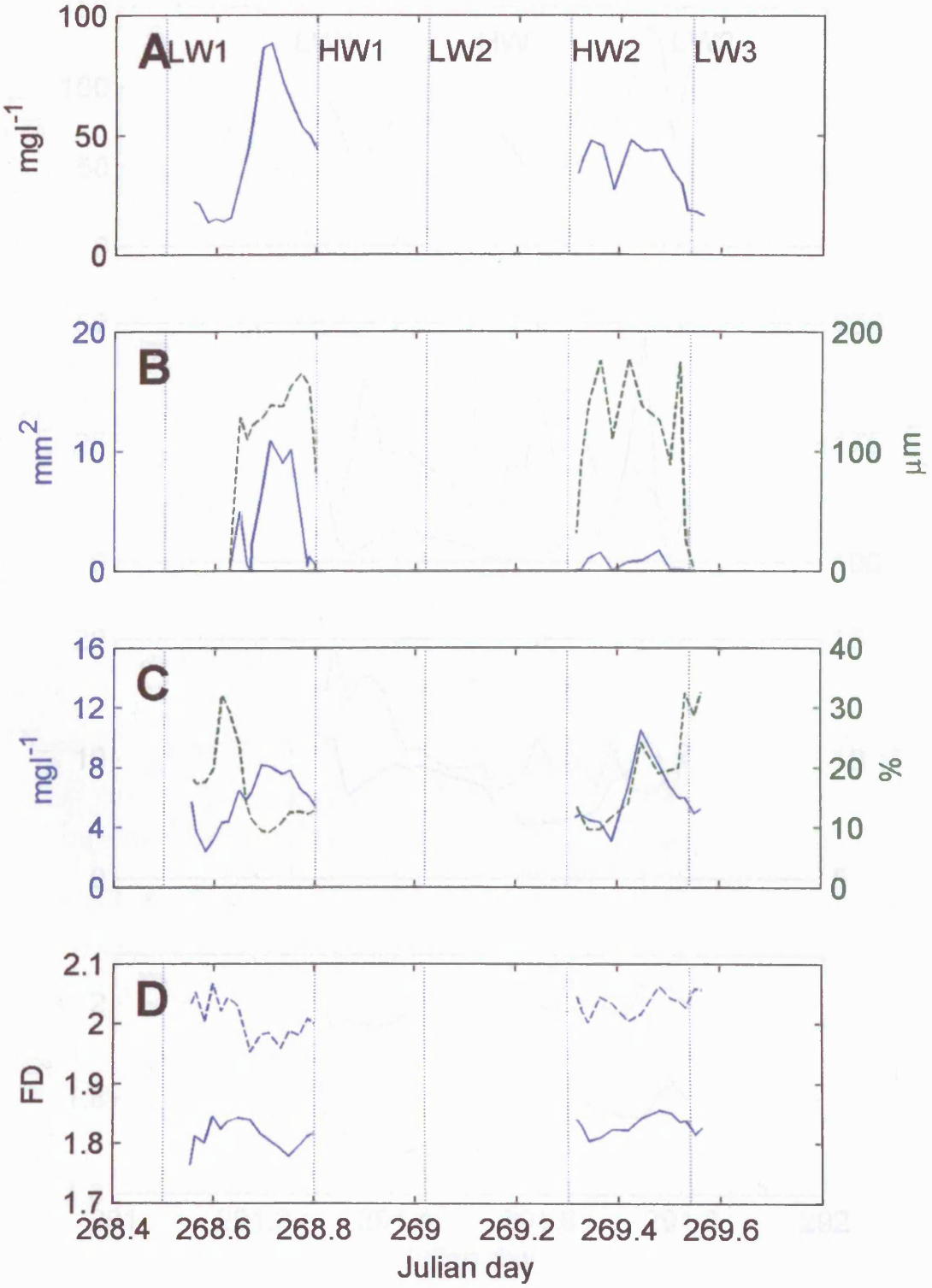

Figure 5.20 – Neap tide particle characteristics other than size: (A) total concentration, (B) total area (solid line) and D_{50} (dashed line) of organic particles on filter paper, (C) mass (solid line) and percentage (dashed line) loss on ignition, (D) fractal dimension from low (solid line) and high (dashed line) magnification cameras.

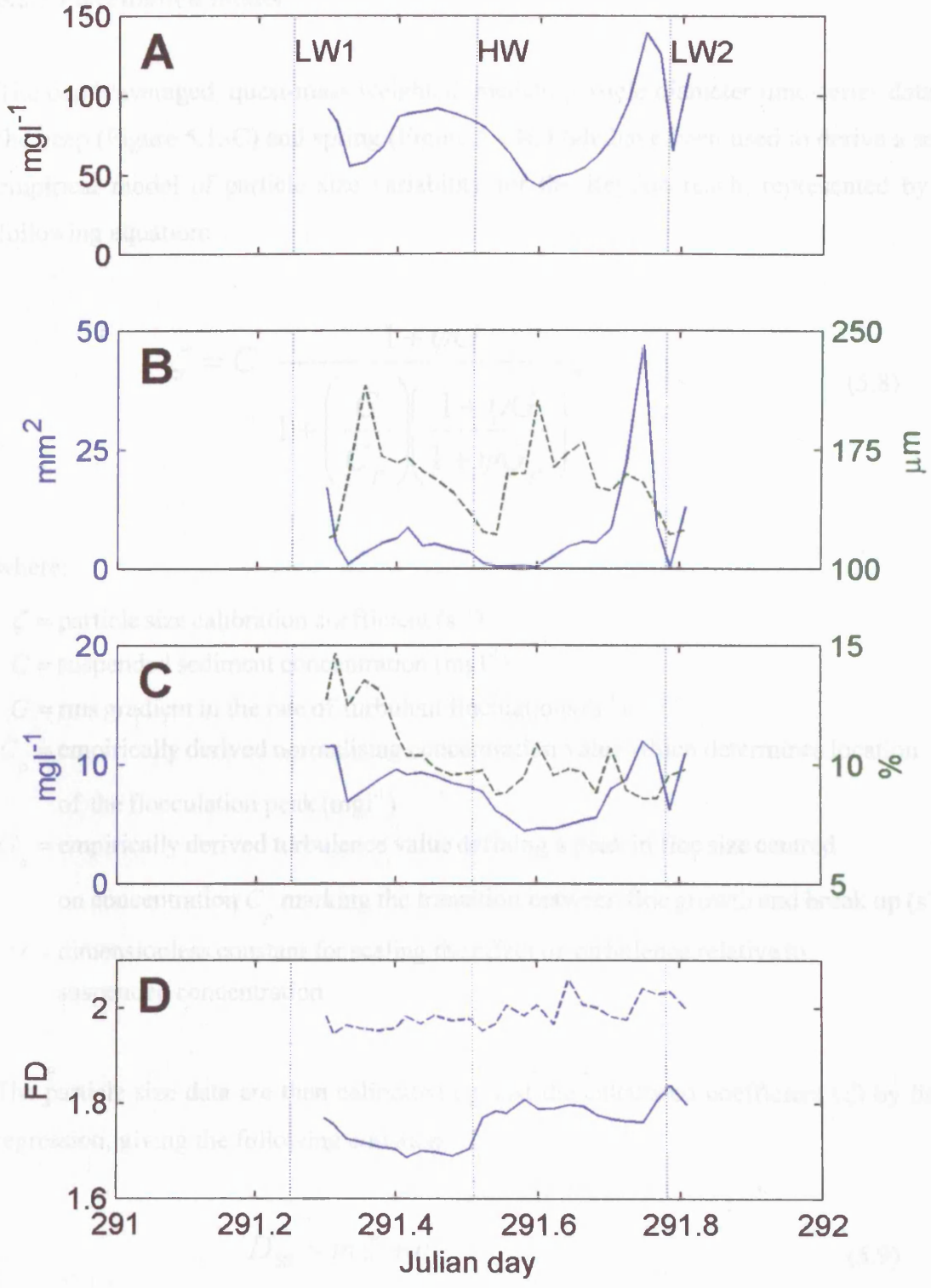

Figure 5.21 – Spring tide particle characteristics other than size: (A) total concentration, (B) total area (solid line) and D_{50} (dashed line) of organic particles on filter paper, (C) mass (solid line) and percentage (dashed line) loss on ignition, (D) fractal dimension from low (solid line) and high (dashed line) magnification cameras.

5.3.5 Flocculation model

The depth averaged, quasi-mass weighted, median particle diameter time-series data for the neap (Figure 5.13C) and spring (Figure 5.14C) tide have been used to derive a semi-empirical model of particle size variability for the Reydon reach, represented by the following equation:

$$\zeta = C \frac{1+\psi G}{1+\left(\frac{C}{C_p}\right)\left(\frac{1+\psi G}{1+\psi G_p}\right)^2} \tag{5.8}$$

where:

ζ = particle size calibration coefficient (s^{-1})

C = suspended sediment concentration (mgl^{-1})

G = rms gradient in the rate of turbulent fluctuations (s^{-1})

C_p = empirically derived normalising concentration value which determines location of the flocculation peak (mgl^{-1})

G_p = empirically derived turbulence value defining a peak in floc size centred on concentration C_p marking the transition between floc growth and break up (s^{-1})

ψ = dimensionless constant for scaling the effect of turbulence relative to suspended concentration

The particle size data are then calibrated against the calculated coefficient (ζ) by linear regression, giving the following equation:

$$D_{50} = m\zeta + c \tag{5.9}$$

where:

m = calibration slope

c = offset

This formulation is based upon the power law dissipation parameter function (Equation 1.22), originally suggested by van Leussen (1994) for estimating settling velocity. In this formulation, it is assumed that, at a fixed level of turbulence, the particle size increases proportionally with the suspended sediment concentration. The affect of turbulence (G) is two-fold. Low intensity turbulence acts to enhance the floc size by increasing the collision rate. This is supported by the Blyth field results and laboratory observations of Manning & Dyer (1999), which show that small amounts of turbulence are required to promote flocculation. Above a turbulence threshold, the flocs are broken up due to the increased shear induced by the micro-scale eddies. Bale *et al* (2002) use a similar approach to derive the following equation for particle size:

$$D_{50} = m\left[C^{x}\frac{1+aG}{1+bG^{y}}\right]+c \qquad (5.10)$$

where:

m, c = linear regression constants

a, b, x, y = empirically derived constants

This equation was derived from flume data using the Lasentec P-100 laser reflectance particle size instrument. The suspended concentration and G values were normalised by dividing by the mean value. It was found to represent 99.8% of the variance in particle size during the early to late phase of the decelerating current.

The new formulation presented in Equation 5.8 differs in two ways. First, it provides more control over parameterisation (especially in the case of a small number of size measurements at low turbulence) by using coefficients C_p and G_p. These coefficients have a physical value defining the location of the flocculation peak, which marks the transition from concentration dependent flocculation to turbulent induced floc break-up. Thus, the position of the flocculation peak can be controlled more intuitively and approximate values can be derived from the graphs of particle size versus both suspended concentration (Figure 5.10) and turbulence (Figure 5.11). For the Blyth estuary particle size data, the transitional point in the flocculation is estimated to occur at a concentration, C_p = 40 mgl^{-1} and turbulence parameter, G_p = 15 s^{-1}.

Second, the new model differs because the flocculation peak is not fixed at a constant value of G. The data obtained from the Blyth suggest that the location of the peak moves towards higher values of G as the suspended sediment concentration decreases. This is substantiated by the theoretical model of Dyer (1989), described in Section 1.3.1, which shows a similar spreading of the peak at lower suspended concentrations. If this is not taken into account, the modelled particle sizes for the neap tide are underestimated. A reason for this shift in the flocculation peak may be that the smaller particles are more compact and stronger, thus making them more resistant to turbulence. Eisma (1991) also suggests that the floc strength increases due to the presence of sticky organic compounds. This view is supported by the loss-on-ignition data (Figure 5.20C and Figure 5.21C), which suggest a larger percentage of organics is present during the neap tide, especially at low total suspended concentrations. In addition, at lower concentrations, particle collisions are less frequent and a greater amount of turbulence is therefore required to induce flocculation.

The relative influence of the level of turbulence on floc size in comparison with the suspended concentration is parameterised with an empirically derived constant (ψ). This has been iteratively determined by performing a series of linear regression fits of the model output versus the observed particle size for the entire data set for the spring and neap tide experiments. As shown in Figure 5.22, a maximum correlation is found at a value, $\psi \approx 0.055$.

Figure 5.23 shows the linear regression curves produced from the quasi-mass weighted median particle size data collected using the InSiPID system at Reydon plotted against ζ. The calibration of the particle size model for the spring tide data is found to differ between mid to late flood and the rest of the data of the with R^2 values of 0.726 and 0.91 respectively, suggesting that there is another factor affecting the particle size. The neap tide particle size correlation shows a larger amount of scatter ($R^2 = 0.613$) and, on first appearance, there is no obvious differentiation between flood and ebb. However, on closer examination, it appears that the data for the late phase of the neap flood tide (after the resuspension event) can be separated into the same category as the spring tide mid to late flood phase data (Figure 5.23B). This supports the theory that there are two sediment types advected on the flood and ebb tides and is beneficial since it allows the same calibrations to be used for the both tides. The sediment types are likely to be of

marine origin (i.e. introduced at the estuary mouth) and from within the estuary. Therefore, the two sediment types shall be referred to as *estuarine sourced* and *marine sourced* sediment from hereon. Using this distinction between the two sediment types, reasonable correlations are obtained using with R^2 values of 0.857 and 0.627 respectively.

The calculated variability in particle size with suspended concentration and turbulence can be visualised as a 2D surface plot (Figure 5.24A). The largest modelled floc sizes occur at high sediment concentrations and low turbulence. This is comparable to the multiple regression model presented by Manning & Dyer (1999) but differs in that it does not require knowledge of the particle settling velocity (which is used as a measure of the floc density). This is not required in the current model because an estimate of the floc density has already been used to provide a mass weighted median.

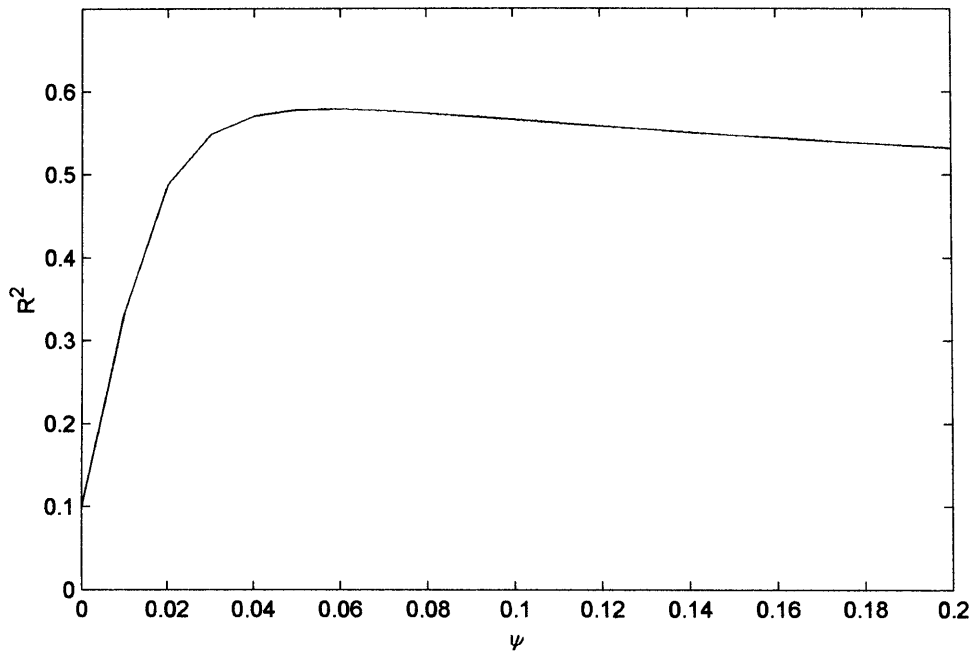

Figure 5.22 – Calibration of ψ by testing the modelled particle size against observations at a range of values using the linear regression R^2 values.

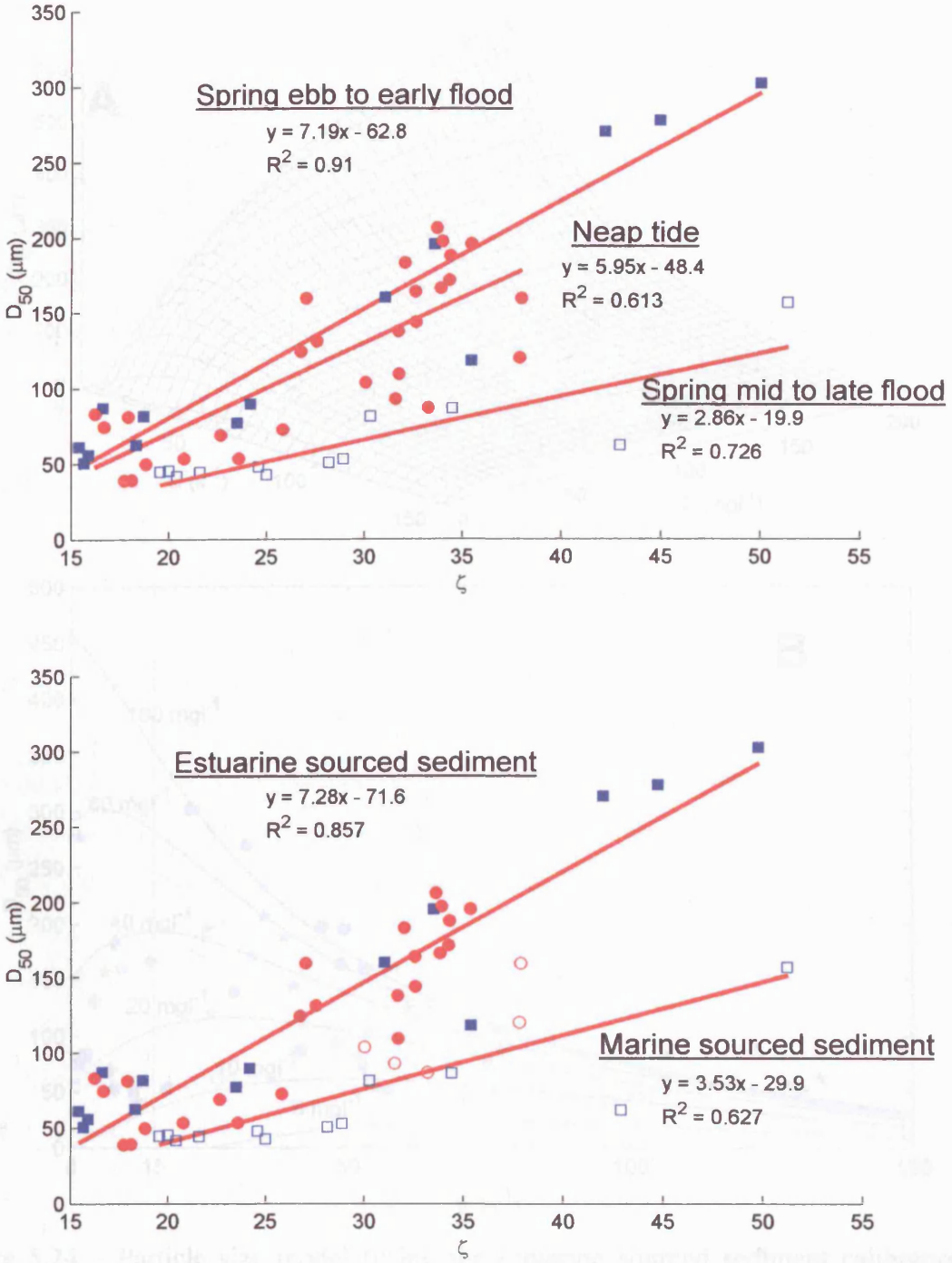

Figure 5.23 – Linear regression curves of particle size calibration coefficient (ζ) versus D_{50}. (A) Entire neap data and spring ebb and spring flood plotted separately. (B) Combined spring and neap tide calibrations, with late flood data plotted separately from rest of data, indicating the advection of different sub-populations of sediment during the flood and ebb.

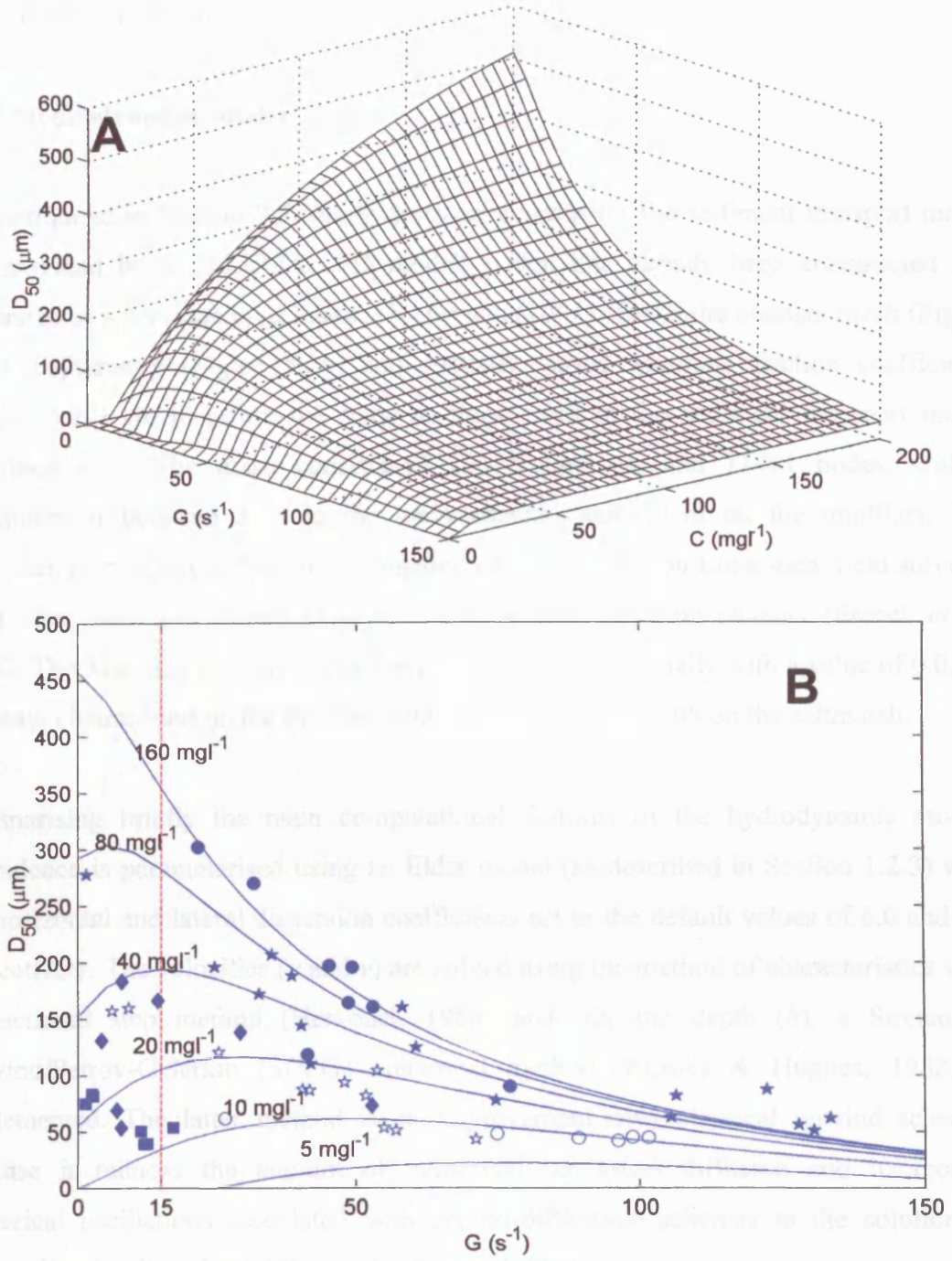

Figure 5.24 – Particle size model (using the estuarine sourced sediment calibration), showing: (A) 2D surface plot of calibrated D_{50} with suspended sediment concentration and turbulence parameter. (B) Modelled particle D_{50} versus turbulence parameter at a range of suspended concentrations. Observed particle size data are also plotted with symbols representing different concentrations (■=10-20; ♦ = 20-40; ★=40-80; ● = 80-160 mgl^{-1}). Mid to late flood tide data (after resuspension at the beginning of flood) are represented by unfilled markers (which are overestimated by the model using this calibration, particularly at higher values of G). Note the shift in the floc size peak towards higher turbulence with decreasing suspended concentration. The dashed line indicates the calibration point $G_p = 15\ s^{-1}$, which marks a peak in flocculation at $C_p = 40$ mgl^{-1}.

5.4 Sediment transport model

5.4.1 Hydrodynamic model

As mentioned in Section 2.5, the hydrodynamic data for the sediment transport model are provided by a TELEMAC-2D model, which has already been constructed and calibrated in a previous investigation by French (2001). The finite element mesh (Figure 5.25), bathymetry (Figure 5.26) and spatially varied Manning friction coefficients (Figure 5.27) are therefore the same as those used in the sediment transport model described here. The mesh consists of 22072 elements and 11461 nodes, with a resolution of between 3 m in the main channel and 60 m on the mudflats. The bathymetry was derived from a combination of high resolution Lidar data, field surveys, chart data, and over 23,000 echo soundings within the main channel (French *et al*, 2004). The Manning friction coefficients were defined regionally with a value of 0.02 in the main channel and on the mudflats and a higher value of 0.05 on the saltmarsh.

Summarising briefly the main computational features of the hydrodynamic model. Turbulence is parameterised using an Elder model (as described in Section 1.2.3) with the horizontal and lateral dispersion coefficients set to the default values of 6.0 and 0.6 respectively. The velocities (u and v) are solved using the method of characteristics with a fractional step method (Hervouet, 1986) and, for the depth (h), a Streamline Upwind/Petrov-Galerkin (SUPG) numerical method (Brooks & Hughes, 1982) is implemented. The latter method is an improvement over classical upwind schemes because it reduces the amount of numerical (or *false*) diffusion and overcomes numerical oscillations associated with central-difference schemes in the solution of convection-dominated fluid flows (Wilson *et al*, 2002).

For this application, the model was driven with tide data spanning each period of the neap and spring tide investigations applied at the mouth at a time-step of 2 seconds. Since no real data for tidal elevations at the mouth were available for these periods (Section 2.4), modelled elevations were used. Predicted levels for Southwold harbour entrance were derived from a harmonic analysis based on 12 months of data acquired in 1995-6 (French, pers. comm.). The predicted levels were then corrected for surge effects (caused by atmospheric pressure systems) using the smoothed residual between the

observed and predicted levels from Lowestoft, which is located approximately 19 km to the north of Southwold. The observed data for Lowestoft were obtained from the British Oceanographic Data Centre.

The hydrodynamic simulations were run at a timestep of 2 seconds for a period of 291000 seconds (3.4 days), spanning just over 6 tidal cycles. Results were saved at a 5 minute interval. Each simulation took approximately two days to run on a Sun Blade 2000 workstation.

Validation of the hydrodynamic model was carried out using the depth-averaged ADCP data and tidal level data from the temporary tide gauge at Reydon. The performance of the model at representing the tidal elevations and velocity magnitude is shown in Figure 5.28. The phasing of the high and low water is in accordance with observations. In general, the difference between the modelled and observed elevations are within 5 cm, although during the spring tide the model estuary does not seem to drain completely, resulting in maximum errors of about 15 cm at low water. Some of this error may be due to inaccuracies in the modelled tidal data at the mouth. In connection with this problem, the maximum ebb current speeds are attenuated slightly, with a maximum difference of -0.2 ms^{-1}. Despite this issue, the phasing and magnitude of the modelled current speeds are remarkably consistent with the observed data, and the overall model performance is considered acceptable for this application.

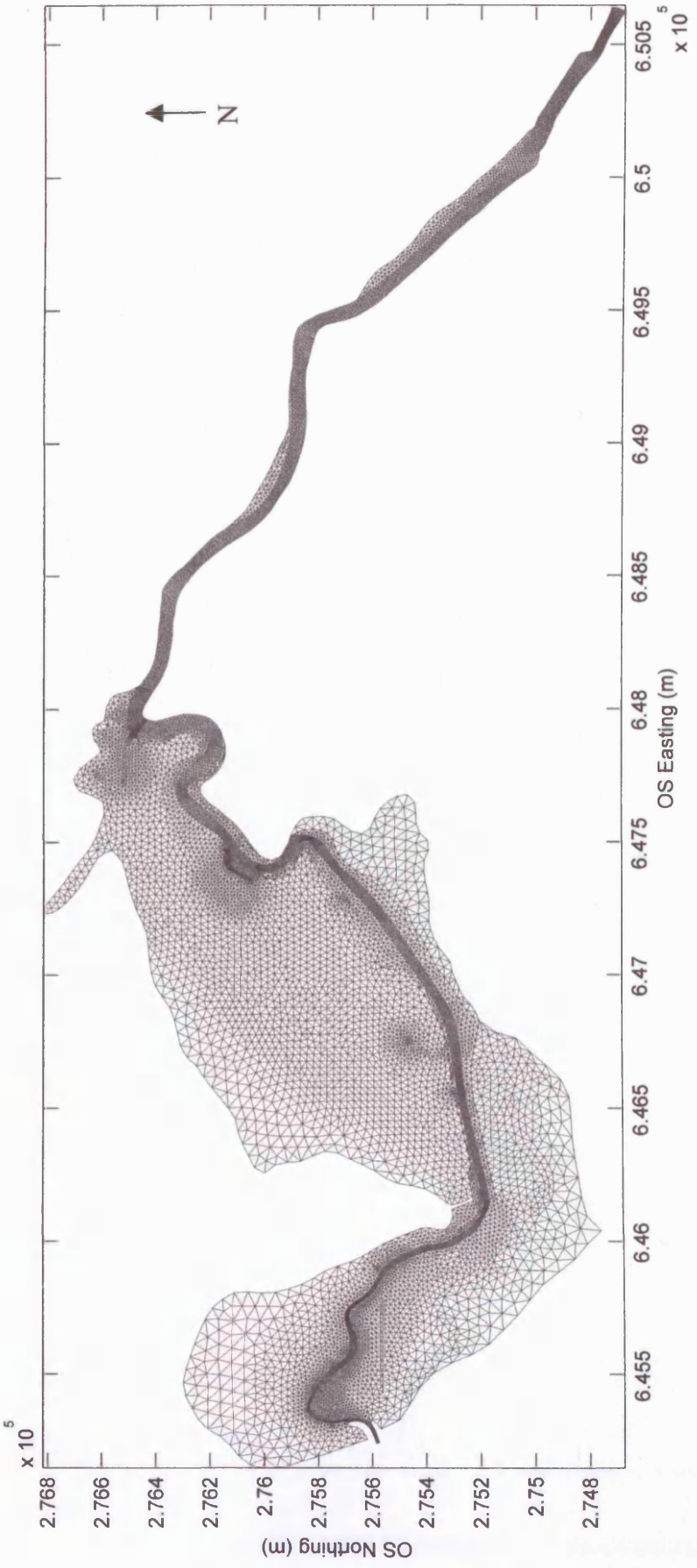

Figure 5.25 - Finite element mesh for the Blyth estuary model

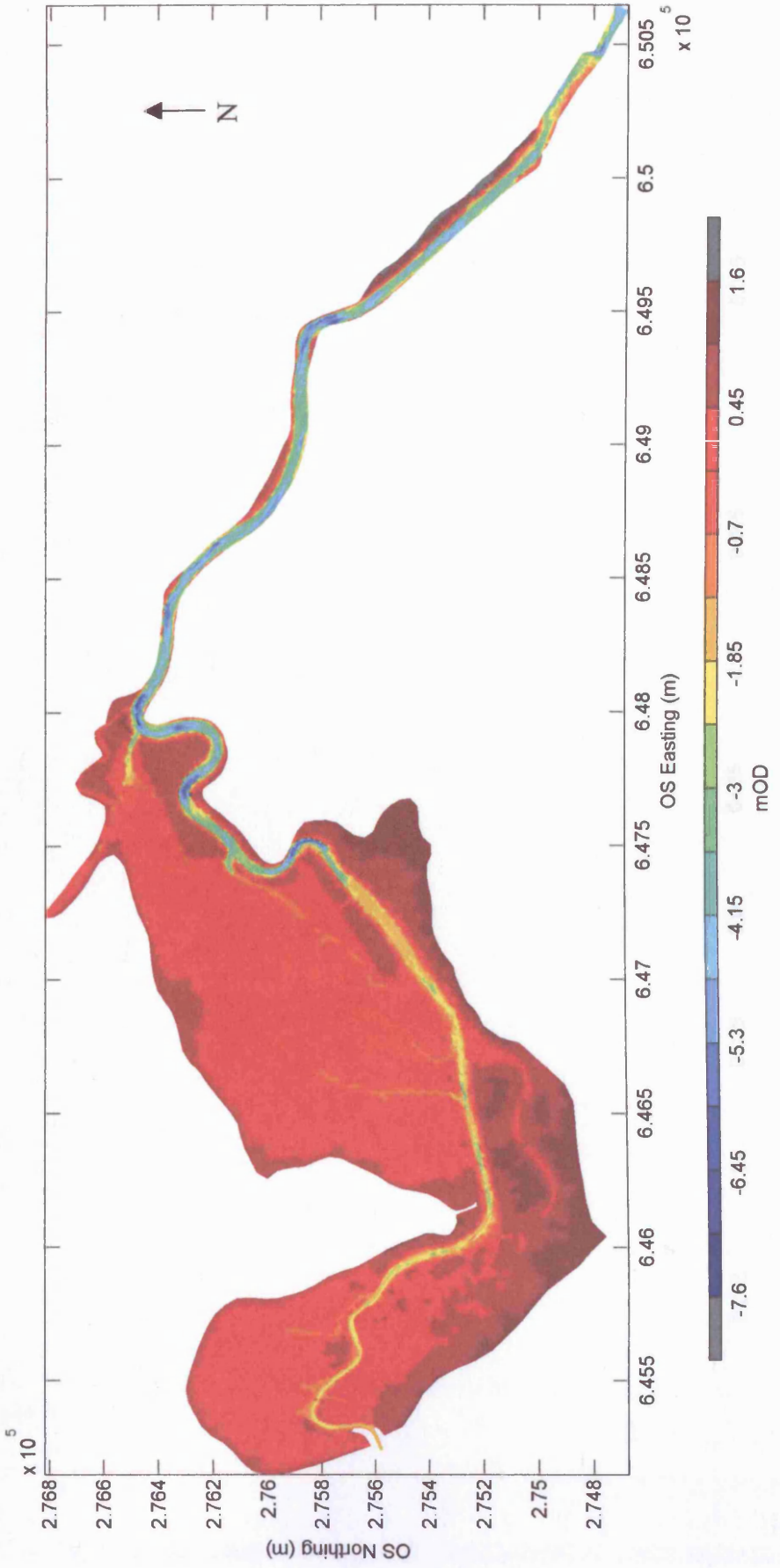

Figure 5.26 - Bathymetry for the Blyth estuary model

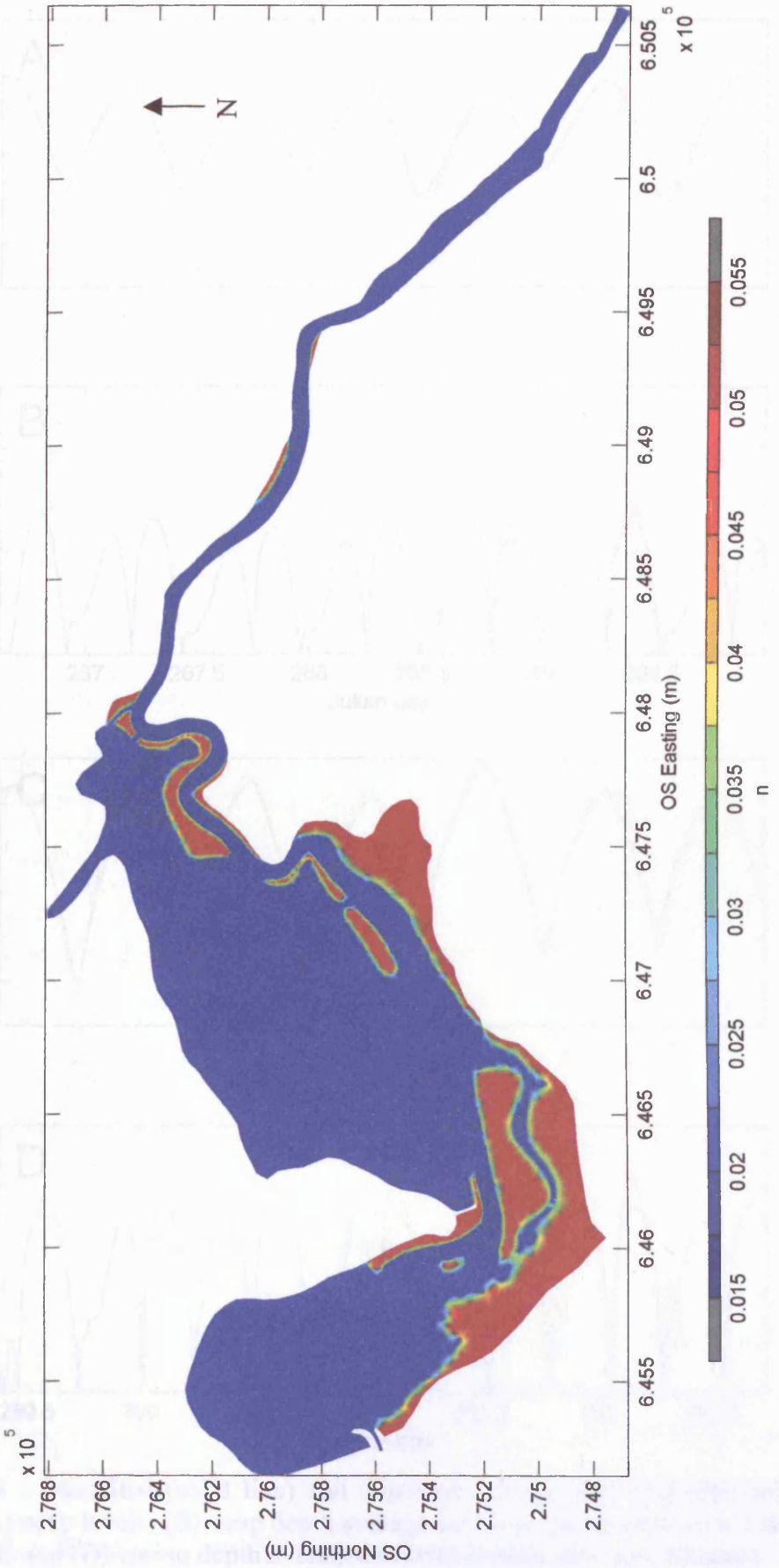

Figure 5.27 -Spatially varied Manning friction coefficients

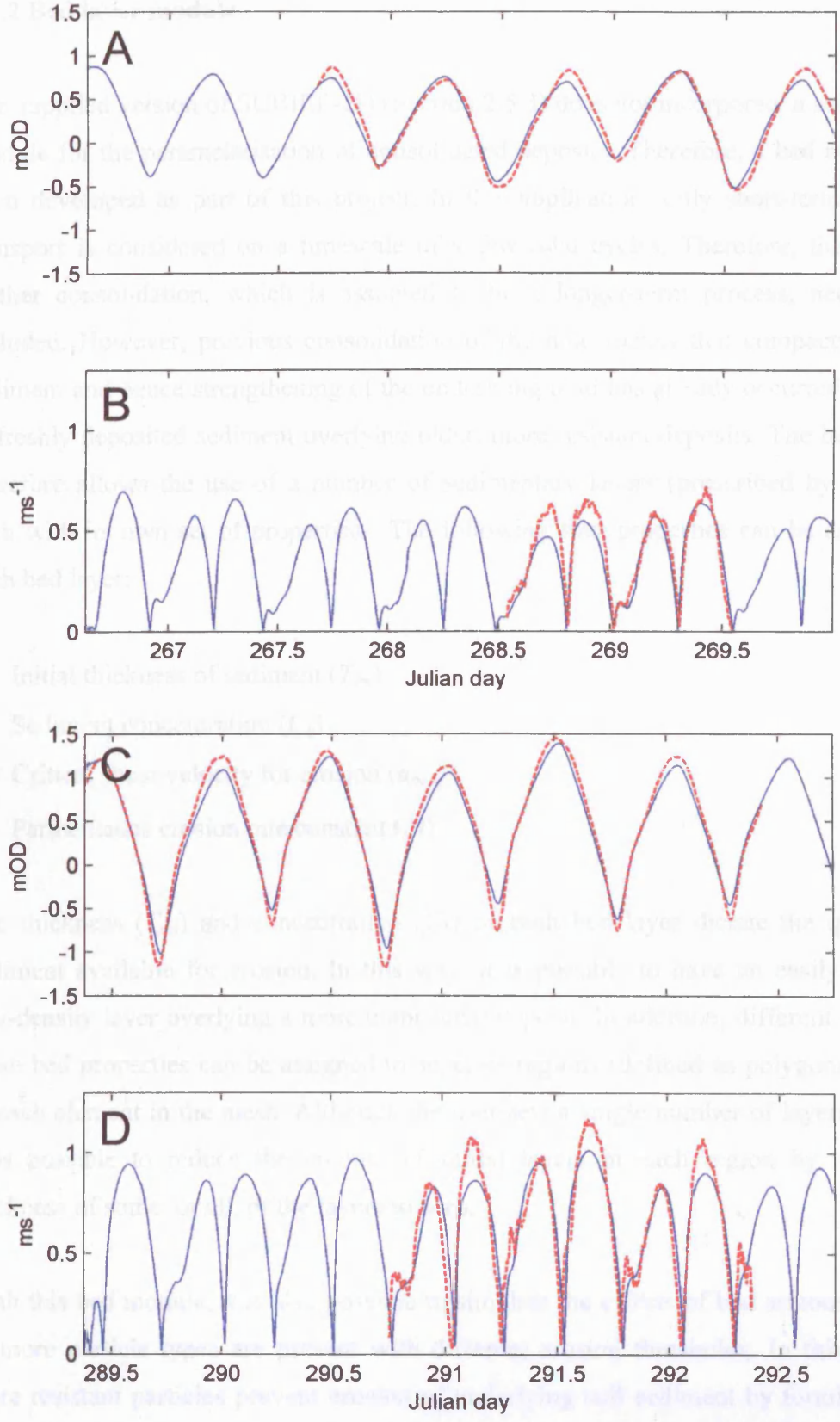

Figure 5.28 – Modelled (solid line) and observed (dotted line) hydrodynamic data at Reydon: (A) neap levels, (B) neap depth averaged current speeds (low pass filtered), (C) spring levels and (D) spring depth averaged current speeds (low pass filtered).

5.4.2 Bed layer module

The supplied version of SUBIEF-2D (Section 2.5.3) does not incorporate a suitable sub-module for the parameterisation of consolidated deposits. Therefore, a bed module has been developed as part of this project. In this application, only short-term sediment transport is considered on a timescale of a few tidal cycles. Therefore, the effect of further consolidation, which is assumed to be a longer-term process, need not be included. However, previous consolidation of the mud means that compaction of the sediment and hence strengthening of the underlying mud has already occurred, resulting in freshly deposited sediment overlying older, more resistant deposits. The bed module therefore allows the use of a number of sedimentary layers (prescribed by the user), each with its own set of properties. The following four properties can be assigned to each bed layer:

- Initial thickness of sediment (T_{ini})
- Sediment concentration (C_b)
- Critical shear velocity for erosion (u_{*ce})
- Partheniades erosion rate constant (M)

The thickness (T_{ini}) and concentration (C_b) of each bed layer dictate the quantity of sediment available for erosion. In this way, it is possible to have an easily erodable, low-density layer overlying a more compacted deposit. In addition, different values for these bed properties can be assigned to separate regions (defined as polygons) indexed to each element in the mesh. Although the user sets a single number of layers globally, it is possible to reduce the number of initial layers in each region by setting the thickness of some, or all, of the layers to zero.

With this bed module, it is also possible to simulate the effects of bed armouring if two or more particle types are present with different erosion thresholds. In this case, the more resistant particles prevent erosion of underlying soft sediment by forming a crust on the bed surface. This process is simulated by carrying out two passes through each time-step in the sediment transport model (Figure 5.29). During the first pass, it is assumed that erosion of the bed layers can occur unimpeded for all sediment classes. On the second pass, the depth of erosion is limited to the shallowest layer eroded to by any

tracer in the first run. A minimum armouring layer thickness can be defined before erosion of the next layer commences to prevent very small quantities of sediment from inhibiting erosion. This is supported by studies of bed armouring, which suggest an active layer thickness of 0.1-1 cm (Wiberg *et al*, 1994; Reed *et al*, 1999). However, bed armouring tends to occur in regions dominated by mixtures of sand, pebbles and mud deposits. Since the deposits in the Blyth are predominantly cohesive (Brew *et al*, 1992; French *et al*, 2004), only a single sediment type is used, and bed armouring is not considered further here.

At times of deposition, sediment is added to the top layer in the bed module (even if several layers have been eroded). Since consolidation over time is not modelled, fresh deposits never move into the lower, more resilient layers as in some models (Section 1.3.2), although this function could be added in the future for longer simulations.

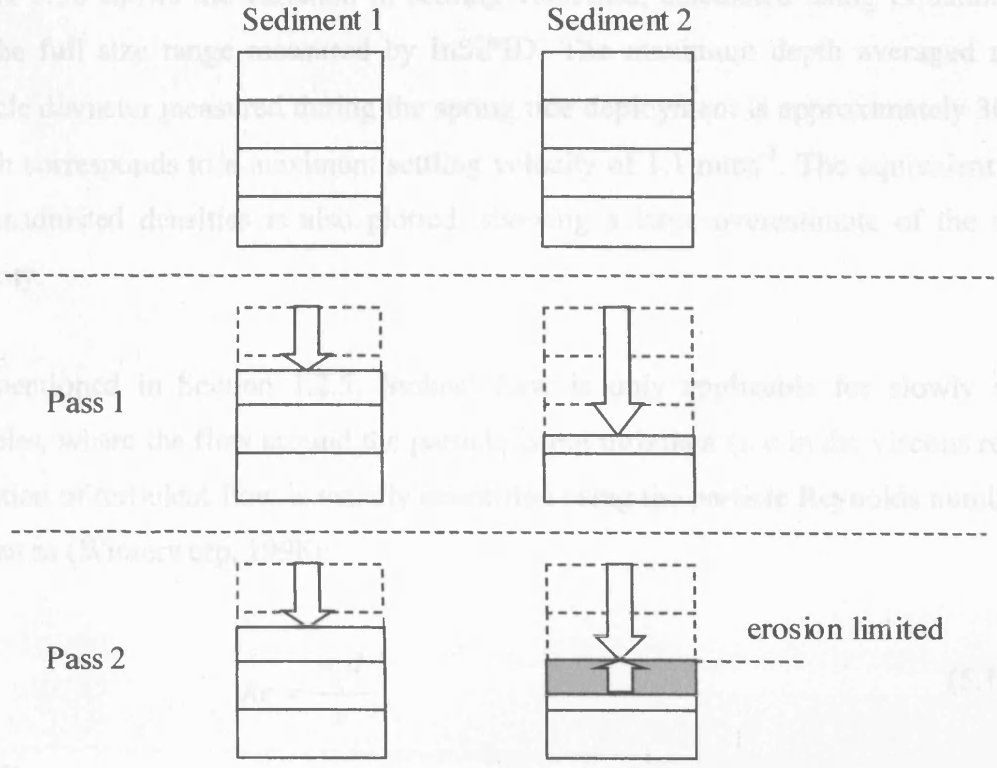

Figure 5.29 - Bed module erosion carried out in two passes for each time step to simulate bed armouring

5.4.3 Settling velocity module

A simple method has been derived for the parameterisation of time varying settling velocities in the sediment transport model, using the modelled particle size described in Section 5.3.5. By combining Stokes' Law for settling particles (Equation 1.13) with the model of floc density variation with size (Equation 5.7), the settling velocity (w_s) can be defined as:

$$w_s = \frac{1}{18}\frac{Bg}{\eta} d^{2+q} \tag{5.11}$$

In Equation 5.11, all the variables other than particle diameter (d) are constant and it can therefore be rewritten (in SI units) as:

$$w_s = 3.719\, d^{1.00448} \tag{5.12}$$

Figure 5.30 shows the variation in settling velocities, calculated using Equation 5.12, for the full size range measured by InSiPID. The maximum depth averaged median particle diameter measured during the spring tide deployment is approximately 300 μm, which corresponds to a maximum settling velocity of 1.1 mms^{-1}. The equivalent model for unadjusted densities is also plotted, showing a large overestimate of the settling velocity.

As mentioned in Section 1.2.5, Stokes' Law is only applicable for slowly settling particles, where the flow around the particle is not turbulent (i..e in the viscous regime). Initiation of turbulent flow is usually quantified using the particle Reynolds number, Re, written as (Winterwerp, 1998):

$$Re = \frac{w_s d}{v} \tag{5.13}$$

where:

v = kinematic viscosity of water (= 10^{-6} m^2s^{-1})

The flow is described as viscous for $Re < 1$. For a particle with a diameter of 300μm and a settling velocity of 1.1 mms^{-1}, Re = 0.33. Hence, Stokes' Law is applicable for the vast majority of the settling particles. From Figure 5.30, it is interesting to note that the high settling velocities observed for the unadjusted density curve lead to very high Reynolds numbers, which cannot be modelled accurately by Stokes' Law.

It is apparent that the influence of particle density on the maximum settling velocity is much greater than its influence on the conversion from a volume weighted to mass weighted median diameter (discussed in Section 5.3.2). Therefore, if the maximum settling velocity of 1.1 mms^{-1} produces undesired results in the model, it can be adjusted slightly in the calibration process without the need to change the equivalent maximum diameter. In this way, the slope of the graph in Figure 5.30 is altered (keeping the origin fixed, since the primary particles are assumed to be of constant density). This provides a simple method of calibrating settling velocity in the sediment transport model. The maximum settling velocity for a 300 μm particle with a Reynolds equal to 1 is 3.3 mms^{-1} (shown as the second adjusted curve in Figure 5.30). This therefore defines the maximum limit of any fine adjustment in the modelling process.

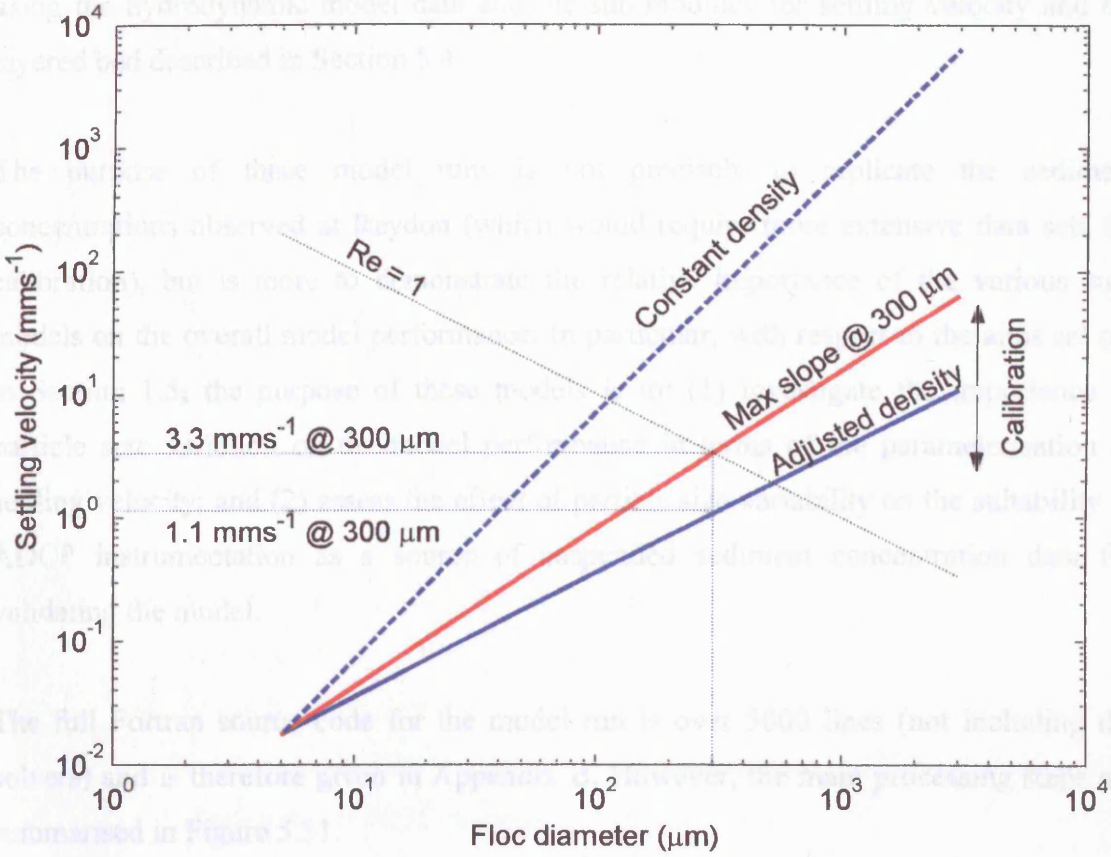

Figure 5.30 – Modelled settling velocity versus particle size using Stokes' Law, showing constant density model (dashed line) and adjusted density curves (solid lines). The dotted curve defines the maximum settling velocity before initiation of turbulent flow (Re = 1) around the settling particles for each size. Fine-tuning of the settling velocity curve can be performed during the sediment transport model calibration phase by adjusting the maximum settling velocity (and hence the slope of the graph) as shown. The two adjusted density curves are for the empirically derived density model (1.1 mms^{-1}) and the maximum settling velocity for applicability of Stokes' Law (3.3 mms^{-1}) both determined from the largest value of D_{50} measured in the Blyth estuary (300 μm).

5.5 Sediment transport simulations

A number of sediment transport model simulations were carried out with SUBIEF-2D using the hydrodynamic model data and the sub-modules for settling velocity and the layered bed described in Section 5.4.

The purpose of these model runs is not precisely to replicate the sediment concentrations observed at Reydon (which would require more extensive data sets for calibration), but is more to demonstrate the relative importance of the various sub-models on the overall model performance. In particular, with respect to the aims set out in Section 1.5, the purpose of these models is to: (1) investigate the importance of particle size variation on the model performance in terms of the parameterisation of settling velocity; and (2) assess the effect of particle size variability on the suitability of ADCP instrumentation as a source of suspended sediment concentration data for validating the model.

The full Fortran source code for the model run is over 5000 lines (not including the solvers) and is therefore given in Appendix B. However, the main processing steps are summarised in Figure 5.31.

MODEL INITIALISATION

- Read the geometry and boundary conditions files.
- Apply initial bed deposits and suspended concentrations for each node.
- Initialise the depositional and erosional fluxes to zero.

STEP THROUGH THE HYDRODYNAMIC RESULTS FILE

- Read the next hydrodynamic timestep record and linearly interpolate to a shorter timestep if required.
- Apply the suspended concentrations at the boundaries for each tracer.

SUB-LOOP TWICE THROUGH ALL THE TRACERS

On first sub-loop, for each mesh node:

- Solve for the suspended concentration for each tracer using the erosional and depositional fluxes calculated on the previous timestep.
- Explicitly calculate the new erosion flux for each tracer and determine the deepest bed layer eroded to by any tracer (L_{max}). N.B. the bed model elevations are NOT modified on this sub-loop.

On second sub-loop, for each mesh node:

- Explicitly re-calculate the erosion flux for each tracer, limiting the sediment supply to L_{max} calculated in the first sub-loop.
- Calculate the settling velocity for each tracer using the total concentration (i.e. sum of all the tracers) calculated on the first sub-loop and the individual particle size calibrations.
- Implicitly calculate the depositional flux between this and the next hydrodynamic loop using the derived settling velocity.
- Apply the erosional and depositional fluxes to the bed model elevations.

Figure 5.31 - Sediment transport model computation steps. Note the inclusion of a sub-loop for calculating the maximum erosion layer and total concentrations.

5.5.1 Model 1 – Basic parameterisation

In this model, the estuary is divided up into a number of distinct sedimentary zones, namely: the sub-tidal channel; intertidal mudflats; and saltmarsh (Figure 5.32). A fourth zone is also included in the main channel near to the estuary mouth to allow the parameterisation of a non-erodable bed. This accounts for natural armouring of the bed in this region due to the high shear stresses (French, 2001).

Zone No.	Description	Initial thickness of sediment, T_{ini} (m)	Critical shear stress for erosion, u_{*ce} (ms^{-1})
1	Saltmarsh	0	0.05
2	Intertidal mudflats	0.1	0.02
3	Subtidal channel	0.1	0.02
4	Harbour mouth	0	0.02

Table 5.1 – Bed parameterisation for the basic model run (for both springs and neaps)

The spring and neap tide simulations are initialised with a suspended sediment concentrations set globally to a nominal value of 75 and 50 mgl^{-1} respectively. A single layer of sediment deposit is initialised across most of the domain with a thickness (T_{ini}) of 0.1m and a concentration (C_b) of 500 kgm^{-3}. The two exceptions are on the saltmarsh (where no erosion is expected due to the presence of vegetation and low flow intensities) and at the harbour mouth (where the bed material is immobile). In both these zones, T_{ini} is set to zero.

On the saltmarsh, the critical shear velocity for erosion (u_{*ce}) is parameterised with a relatively high value of 0.05 ms^{-1} (τ_b = 2.6 Nm^{-2}) in order to prevent re-erosion of any settled material. Thus, the saltmarsh acts as a perfect sediment sink. Elsewhere, u_{*ce} is set to 0.02 ms^{-1} (τ_b = 0.4 Nm^{-2}), which is approximately equal to the mean shear velocity for all the nodes in the subtidal zone during the spring tide simulation (calculated from the hydrodynamic model output data using Equation 5.4).

Above the defined values of u_{*ce}, erosion is initiated according to the Partheniades formula (Equation 1.11). The erosion rate constant, M, was determined during the

calibration phase of the model and set globally to 0.00004 $kgm^{-2}s^{-1}$. Although this value for M is twice the original value determined by Partheniades for muds (Partheniades, 1965), it is within the range of values used by other researchers in numerical sediment transport models (e.g. Mulder & Udink, 1991 = $5e^{-5}$; Cancino & Neves, 1999a,b = $5e^{-5}$; Roberts *et al*, 2000 = $4e^{-5}$; van der Ham & Winterwerp, 2001 = $4e^{-5}$; Tattersall *et al*, 2003 = $3.5e^{-5}$) and is used for all of the following simulations.

The critical velocity for deposition (u_{*cd}) is set globally to 0.01 ms^{-1} and is similarly unchanged for all the other simulations. This value was chosen using the modelled shear velocity time-series at Reydon (Figure 5.33). Near the beginning of the flood phase of the neap tide, there is a period of deceleration in the flow slightly below a shear stress of 0.01 ms^{-1}. This results in a long settling period of approximately 200 minutes, which is required to achieve the observed low suspended sediment concentrations. Below this critical velocity, deposition occurs according to Krone's formula (Equation 1.12) with a constant settling velocity (w_s) of 1.1 mms^{-1}. This value is derived from the maximum depth mean particle size and corresponding estimated density (Section 5.4.3).

The seaward boundary is parameterised with a constant suspended sediment concentration. Transmissometer derived suspended sediment data for Southwold Ferry (close to the mouth) from 1994 indicates spring flood tide concentrations of between 70-80 mgl^{-1} (unpublished CERU data). The spring tide model is therefore parameterised at 70 mgl^{-1}. The neap tide simulation is parameterised at a slightly lower concentration of 60 mgl^{-1}. These values are also in agreement with the median flood tide background concentrations calculated from long-term flux measurements by French *et al* (2004).

The sediment transport model was run at a 1 minute timestep, which was achieved by performing 5 interpolated sub-iterations of the hydrodynamic results file. The method of parameterising turbulence was found to have little effect on the model performance and was therefore modelled simply by using constant longitudinal and transverse dispersion coefficients both equal to 0.01. In addition, a minimum depth of 0.1 m was applied below which no erosion or deposition was calculated, which prevented problems associated with high values of shear velocity in shallow water. These run settings were found to provide a stable model output and were used for all the following simulations. Each model took ~5-7 hours to run on a Sun Blade 2000 workstation.

The modelled concentrations for the neap tide (Figure 5.37A) show some correspondence in amplitude with the observations. However, the model underestimates the amount of resuspension during both the flood and the ebb and the phasing of the flood peak in concentration is delayed.

For the spring tide, the modelled suspended sediment concentrations also show poor agreement with the observed data in terms of amplitude (Figure 5.38A). The ebb concentrations are too low and the flood concentrations are much too high. The error in the flood tide concentrations could be reduced by applying a constant tidal boundary input concentration of approximately 20 mgl^{-1}. However, this is much too low in comparison to observations. This discrepancy is caused by the simulation of substantial erosion from the main channel down-estuary from Reydon, which results in high flood concentrations and produces unrealistic bed level changes near Blackshore Quay.

It is concluded from this model that, for the spring tide simulation, the use of a single global value of u_{*ce} in the subtidal zone results in too much erosion towards the mouth of the estuary, and too little further up-stream. Conversely, the neap tide simulation shows reduced erosion both upstream and downstream of Reydon, resulting in low concentrations on both the flood and ebb. This finding suggests that the resistance of the bed in the subtidal channel (i.e. u_{*ce}) should be varied spatially as found by Tattersall *et al* (2003) in their model of the Tamar estuary. It also appears that the resistance of the bed may vary between the spring and neap tides.

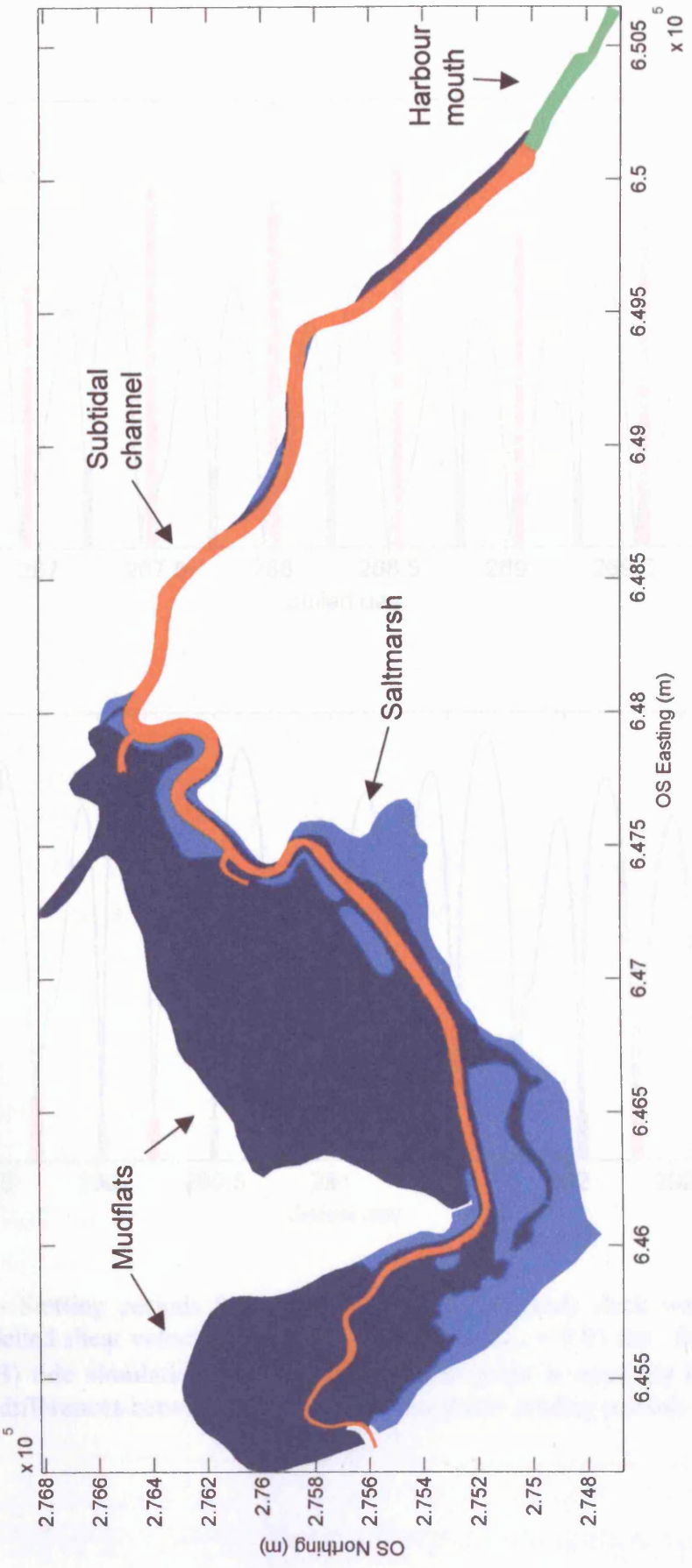

Figure 5.32 – Basic model sedimentary zones defined for the SUBIEF-2D bed model.

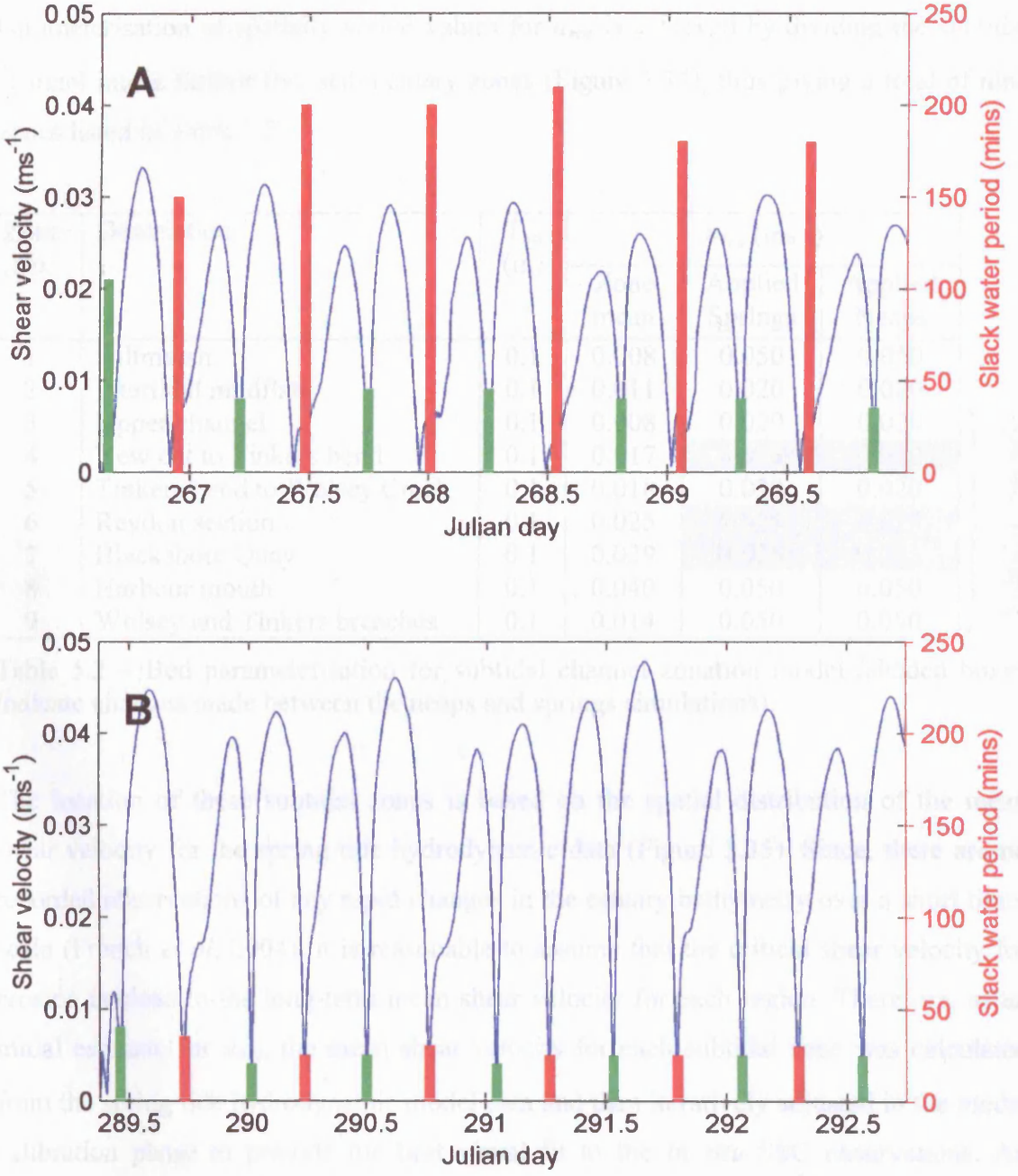

Figure 5.33 – Settling periods for high (green) and low (red) slack water, calculated from the modelled shear velocities at Reydon assuming $u_{*cd} = 0.01$ ms^{-1} for the neap (A) and spring (B) tide simulations. Note that the same scale is used for both graphs to highlight the differences between the spring and neap tide settling periods.

5.5.2 Model 2 – Subtidal zonation of critical shear stress for erosion

Parameterisation of spatially varied values for u_{*ce} is achieved by dividing the subtidal channel into a further five sedimentary zones (Figure 5.34), thus giving a total of nine zones listed in Table 5.2.

Zone No.	Description	T_{ini} (m)	u_{*ce} (ms^{-1})		
			Zone mean	Applied Springs	Applied Neaps
1	Saltmarsh	0.1	0.008	0.050	0.050
2	Intertidal mudflats	0.1	0.011	0.020	0.020
3	Upper channel	0.1	0.008	0.020	0.020
4	New cut to Tinkers bend	0.1	0.017	0.015	0.020
5	Tinkers bend to Wolsey Creek	0.1	0.018	0.020	0.020
6	Reydon section	0.1	0.025	0.025	0.015
7	Blackshore Quay	0.1	0.029	0.035	0.025
8	Harbour mouth	0.1	0.040	0.050	0.050
9	Wolsey and Tinkers breaches	0.1	0.014	0.050	0.050

Subtidal channel

Table 5.2 – Bed parameterisation for subtidal channel zonation model (shaded boxes indicate changes made between the neaps and springs simulations).

The location of these subtidal zones is based on the spatial distribution of the mean shear velocity for the spring tide hydrodynamic data (Figure 5.35). Since, there are no recorded observations of any rapid changes in the estuary bathymetry over a short time-scale (French *et al*, 2004), it is reasonable to assume that the critical shear velocity for erosion is close to the long-term mean shear velocity for each region. Therefore, as an initial estimate for u_{*ce}, the mean shear velocity for each subtidal zone was calculated from the spring tide hydrodynamic model data and then iteratively adjusted in the model calibration phase to provide the best visual fit to the *in situ* SSC observations. An exception to this is within the seawall breach zones, which are assigned a relatively high critical shear velocity value of 0.05 ms^{-1} in order to prevent any significant erosion. This is justified by the fact that armouring of the bed has occurred in these regions over a long period of time due to high shear stresses (French *et al*, 2004).

Values for u_{*ce} on the intertidal regions are not found to correspond with the mean shear velocity (Table 5.2) but are more comparable to the maximum shear. As in the basic model (Section 5.5.1), the saltmarsh is set to a value of 0.05 ms^{-1} (to account for stabilisation of the bed by vegetation) and the mudflats are kept at a value of 0.02 ms^{-1}.

This high value for the mudflats (in relation to the mean value) is possibly because of the effects of consolidation and drying of the mud. Wave action is also likely to increase the shear stress on the mudflats. The upper channel (zone 3) is considered physically comparable to the mudflats (zone 2) since it is largely unbounded by seawalls and is very shallow. It is therefore assigned the same value of u_{*ce}.

In order to provide a best fit with the *in situ* SSC data, the parameterisation of u_{*ce} is found to differ significantly between the neap and the spring tide in the middle portions of the main channel (indicated as shaded boxes in Table 5.2). During the spring tide there is a linear decrease in u_{*ce} from the mouth to the New Cut, suggesting that there is more erodable deposit landward. However, during the neap tide, the values for u_{*ce} are higher at the New Cut and lower at the Reydon section. This suggests that there is greater consolidation of sediment in the upper estuary and greater quantities of looser deposit further down the estuary in the main channel.

In this model, the erosion is controlled primarily by the u_{*ce} parameter, rather than by availability of sediment (as was the case in Model 1). Therefore, the bed thickness is initialised to 0.1 m across the entire domain, including the harbour mouth region. The settling velocity (w_s) is kept at a constant value of 1.1 mms^{-1}. Initial concentrations (C_{ini}) are again set globally to 75 mgl^{-1} and 50 mgl^{-1} for the spring and neap tides respectively.

As expected, the spring tide simulation results (Figure 5.38B) show reduced erosion towards the mouth of the estuary and greater erosion towards the New Cut due to the spatially varied values of u_{*ce}. Similarly, the neap tide model shows increased erosion at Reydon and further landwards (Figure 5.37B). Consequently, the sediment concentration maxima on are in better agreement with observations for both simulations.

Two main discrepancies between the modelled and observed concentrations are still apparent. First, the model fails to reproduce the resuspension event at the turn of the tide from low water springs. Second, the modelled concentrations are not fully in phase with the observations, which is again most apparent during the spring flood tide.

One possible cause for the phasing errors may be that the sediment concentrations were obtained from a non-fixed position while the boat was drifting. However, this is unlikely to be the main cause of the phase difference since the measurements were obtained along the central axis of the channel, and the observed phase difference is too large to be accounted for by a 50 m difference in measurement location. A more plausible explanation is that a 2D depth-averaged model has been used in which the vertical profile of suspended concentrations is assumed homogenous. In reality, the concentrations vary with depth. The Blyth water sample observations suggest that the concentration profiles do not consistently conform to a simplified profile such as defined by the Rouse formula (Equation 1.16). In fact, at times the concentrations are seen to *decrease* with depth, such as during the spring flood tide (Figure 5.7) when it appears that sediment is introduced into the top of the water column due to resuspension from the intertidal channel margins as they become flooded. This clearly has implications for the transport of sediment. If a 4 m water column is assumed to contain a uniformly mixed suspension of particles with a settling velocity of approximately 1 mms^{-1} and a period of settling (i.e. during which $u_* < u_{*cd}$) of 20 minutes is prescribed (Figure 5.33), only the particles in the bottom 1.2 m of the water column will reach the bed. If the concentration profile is now assumed to increase towards the bed according to the Rouse equation, the depth-averaged concentration will decrease more rapidly due to settling in comparison to the homogenously mixed case. This may explain the slightly delayed phase in modelled concentrations during the neap tide slack water periods and the spring tide low water. Conversely, in the case of lower concentrations towards the bed, the rate of deposition will be reduced, which possibly explains the phase difference between the observed and simulated concentrations for the late flood phase of the spring tide. It is probable that a 3D model is required in order to simulate the concentrations more realistically.

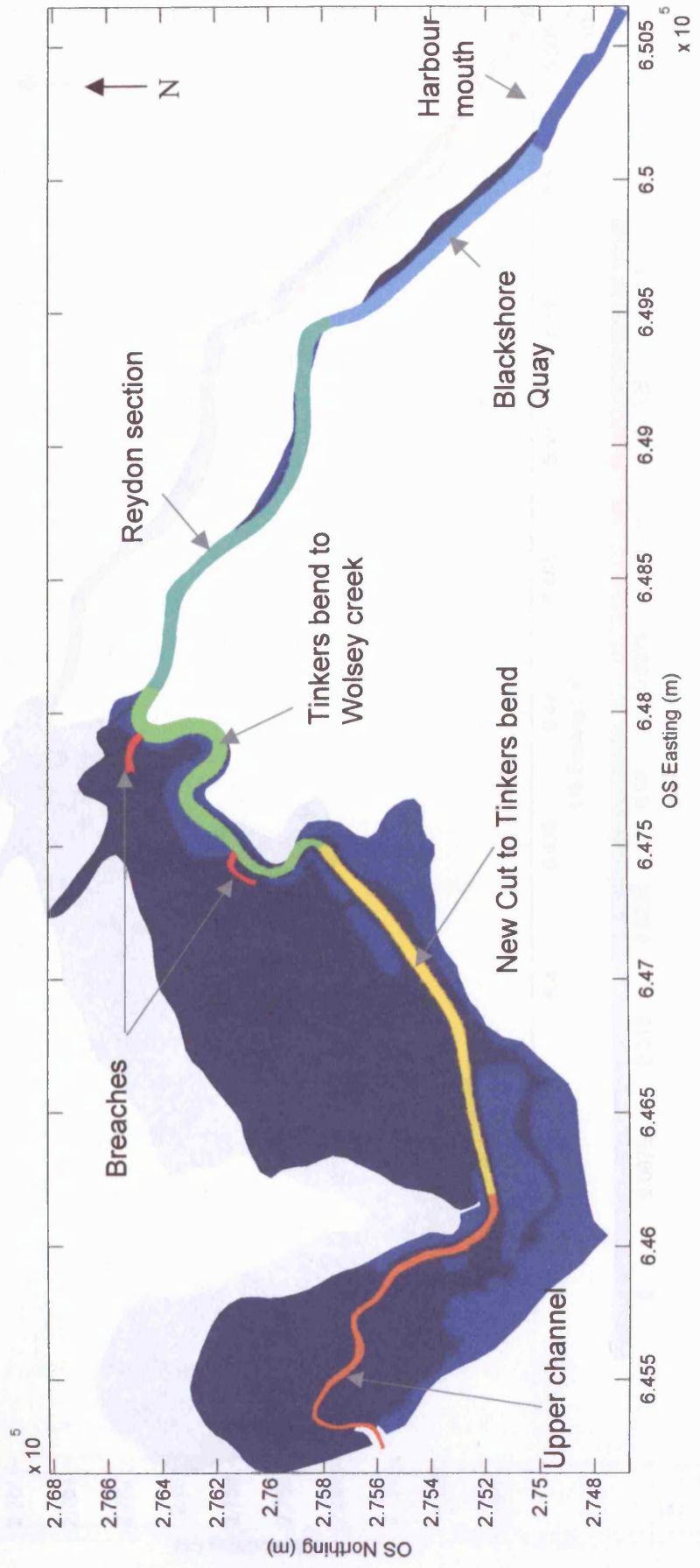

Figure 5.34 - Additional zonation of u_{*ce} in the subtidal zone (models 2 to 4).

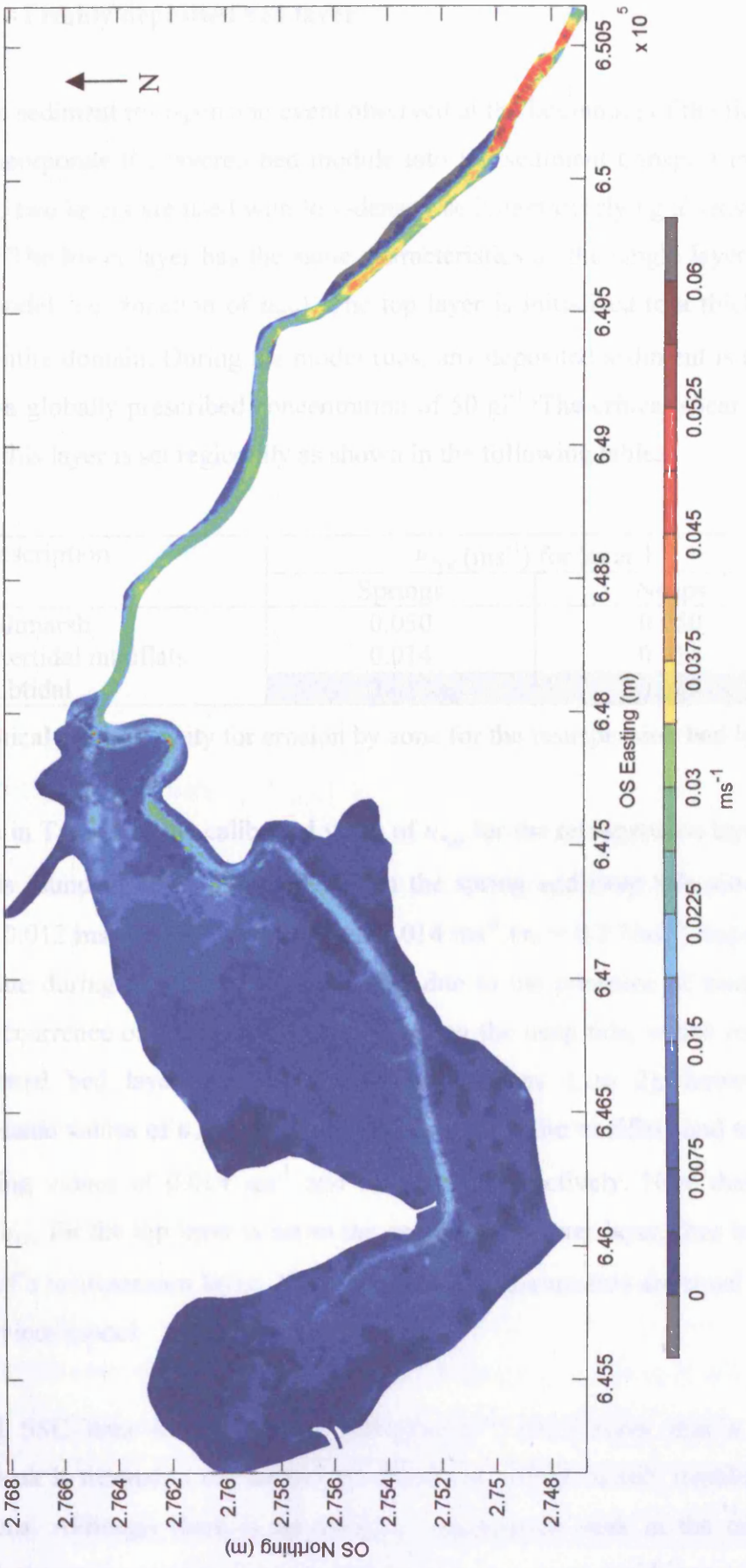

Figure 5.35 - Mean shear velocity for the spring tide hydrodynamic data

5.5.3 Model 3 – Freshly deposited bed layer

To simulate the sediment resuspension event observed at the beginning of the flood, it is necessary to incorporate the layered bed module into the sediment transport model. In this simulation, two layers are used with low-density sediment overlying a denser, more resistant layer. The lower layer has the same characteristics as the single layer used in the previous model (i.e. zonation of u_{*ce}). The top layer is initialised to a thickness of zero over the entire domain. During the model runs, any deposited sediment is added to this layer with a globally prescribed concentration of 50 gl^{-1}. The critical shear velocity for erosion for this layer is set regionally as shown in the following table.

Zone number	Description	u_{*ce} (ms^{-1}) for layer 1	
		Springs	Neaps
1	Saltmarsh	0.050	0.050
2	Intertidal mudflats	0.014	0.014
3 to 9	Subtidal	0.012	0.014

Table 5.3 – Critical shear velocity for erosion by zone for the resuspension bed layer.

As can be seen in Table 5.3, the calibrated value of u_{*ce} for the resuspension layer in the subtidal zone is found to differ slightly between the spring and neap tide simulations with values of 0.012 ms^{-1} (τ_b = 0.15 Nm^{-2}) and 0.014 ms^{-1} (τ_b = 0.2 Nm^{-2}) respectively. The higher value during the neap tide is possibly due to the presence of smaller floc sizes and the occurrence of a longer slack water during the neap tide, which result in a more consolidated bed layer. The intertidal zones (zones 1 to 2), however, are prescribed the same values of u_{*ce} for both simulations, with the mudflats and saltmarsh regions receiving values of 0.014 ms^{-1} and 0.05 ms^{-1} respectively. Note that on the saltmarsh, the u_{*ce} for the top layer is set to the same as the lower layer, thus inhibiting the formation of a resuspension layer. All the other model parameters are equal to those used in the previous model.

The simulated SSC data for the spring tide (Figure 5.38C) show that a distinct resuspension peak is formed at the start of the flood tide, which closely matches the *in situ* observations. Although there is no obvious resuspension peak in the neap data (Figure 5.37C), the resuspension of the top layer results in a more rapid increase n SSC at the start of the flood, which also improves the visual agreement with the *in situ*

observations. A slight phase difference is noted in the timing of this resuspension for the spring tide, but this could be attributed to the use of a 2D depth averaged model, which assumes a homogenously mixed water column as mentioned previously. This is unlikely to be true during the accelerating phase at the beginning of the tide, which will induce a strong gradient in concentration as sediment is eroded from the bed. This is substantiated by the observed variability with depth in the water bottle sample concentrations at times of resuspension (Figure 5.6B and Figure 5.7B)

5.5.4 Model 4 – Variable settling velocity

The variable settling velocity model (Section 5.4.3) is now applied to the existing sediment transport model. A problem arises because the calibration for particle size varies significantly between the flood and ebb phases of the tide (Section 5.3.4). A simple method has been devised which partially solves this problem in the situation of the Blyth estuary, by utilising two sediment types with the separate flocculation model calibrations calculated in Section 5.3.4. The first sediment type is applied at the mouth boundary and is prescribed the *marine sourced* sediment calibration. The second sediment type constitutes the initial bed sediment within the estuary and is prescribed the *estuarine sourced* sediment calibration. A link between the two sediment types is provided by converting the marine sourced sediment into estuarine bed sediment on deposition. In this way, the effects of intertidal consolidation of the sediment are also partially modelled. This is supported by laboratory evidence that eroded aggregates are larger than those observed during settling, which suggests that inter-aggregate bonds are formed on the bed surface (Dearnaley *et al*, 2002).

The settling velocity is then calculated in three stages. First, the particle size calibration coefficient (ζ) is calculated for each mesh node from Equation 5.8, using the total suspended sediment concentration and turbulence parameter (G). Second, the separate size calibrations are applied using Equation 5.9 to obtain the median particle size for each sediment type. Third, the settling velocities are calculated for each sediment type at each mesh node using the density adjusted Stokes' power law (Equation 5.12).

It is likely that the smallest median floc size is limited to the size of the tightly bonded micro-flocs rather than the size of the primary particles (~5 μm). Therefore, for modelling purposes, a minimum median particle size limit of 20 μm is applied in order to prevent underestimation of the settling velocity during very low flows and concentrations. This minimum value is similar to the findings of CE French *et al* (2000), who used a Malvern laser diffraction particle sizer to measure samples of mud from the Bulcamp mudflats, with values of between 10-16 μm. In this experiment, the samples were subjected to ultrasonic treatment to induce floc beak-up. These values are therefore likely to represent the absolute minimum diameter of the *in situ* flocs.

The modelled particle size data are shown in Figure 5.36 for the spring and neap tide simulations. Since the settling velocity is closely proportional to d^1, the equivalent calculated values are indicated on the second y-axis. For both the spring and the neap tide simulations, the particle size is plotted using both a single calibration and the differentiated calibration between estuarine and marine sourced sediment. For the spring flood tide, the use of two separate calibrations improves the modelled sizes considerably in comparison with observations (Figure 5.36B). In particular, note the large difference in calculated settling velocity between high and low water calibrations, with values of ~0.6 and ~1.1 respectively. This difference is increased as a result of using the two separate particle size calibrations. The modelling of the neap tide particle size (Figure 5.36A) is marginally less satisfactory, although it shows good similarity in the phase and maximum amplitude. Especially note the simulation of a reduction in particle size during the long slack low water period as a result of very low suspended concentrations (due to the settling of larger flocs). The reason for the slightly poorer agreement is possibly due to the higher percentage of low density organic material (Figure 5.21), the lower total concentrations (and hence a reduced total particle count), and the broad, multimodal size range throughout the tidal cycle (Figure 5.16), which will all introduce statistical errors in the calculation of a mass-weighted median diameter.

For both the neap (Figure 5.37D) and spring (Figure 5.38D) tide simulations, the use of a variable settling velocity results in improved agreement between modelled and observed concentrations. No adjustment was made to the estimated maximum settling velocity, which suggests that the use of an approximate model of floc density (as described in Section 5.3.3) is suitable.

Improvements in the modelled concentrations as a result of using variable settling velocities are particularly noticeable around slack low water, which has a longer period for which the shear velocity is below the critical shear velocity for deposition during both the spring and neap tides (Figure 5.33). During these longer slack water periods, more time is available for settling. Since the larger flocs represent the majority of the settling flux, there is a simultaneous reduction in suspended concentration and sorting of the sediment towards the smaller sizes. Hence, a fixed value for settling velocity is not sufficient. This is most apparent during the neap tide when the slow acceleration of the flood tide leads to a slack low water period in excess of 200 minutes, compared to a slack high water period of less than 40 minutes. Resuspension of material from further upstream is also reduced due to the lower shear stresses and increased consolidation of the top layer of sediment. Consequently, concentrations are relatively low at the end of the neap ebb tide and, hence, no flocculation peak is observed in the measurements at low water. During the shorter slack high water period, however, concentrations remain higher. Therefore a flocculation peak is observed, which is also shown in the model. During the spring tide, the slack water periods are shorter than during the neap tide and there is greater similarity between the high and low water with periods of ~20 and ~30 minutes respectively. Suspended concentrations therefore remain relatively high during both slack water periods, resulting in more pronounced flocculation peaks. High concentrations at the end of the spring tide ebb result in the formation of the largest observed floc sizes (and hence highest settling velocities) at Reydon. In this way, the settling velocity model improves the sediment transport model by providing a feedback mechanism that prevents the concentrations from: (1) becoming too low during the long slack low water period during the neap tide, and; (2) rapidly reduces the concentration at the end of the spring tide ebb when suspended concentrations are high (as a result of advection of large quantities of material from upstream).

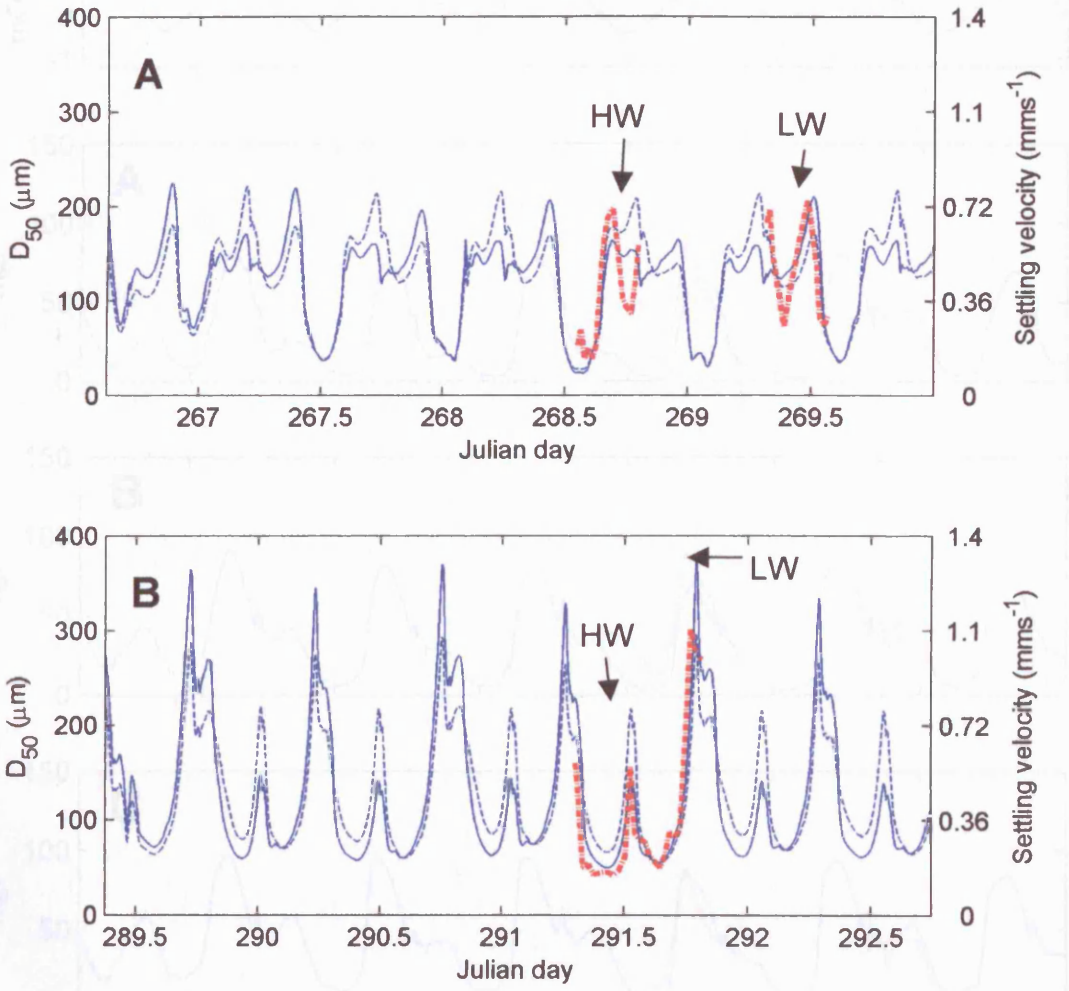

Figure 5.36 – Modelled and observed (bold line) particle size for neap (A) and spring (B) tides. Each graph shows the calibration using one (dashed line) and two (solid line) sediment types. The equivalent settling velocity is marked on the second y-axis. Note the improvement in the modelled particle size for the spring flood tide when using two sediment types. The neap tide is not significantly improved in this way, possibly due to the greater mixing of the marine and estuarine water masses and higher proportions of organic material.

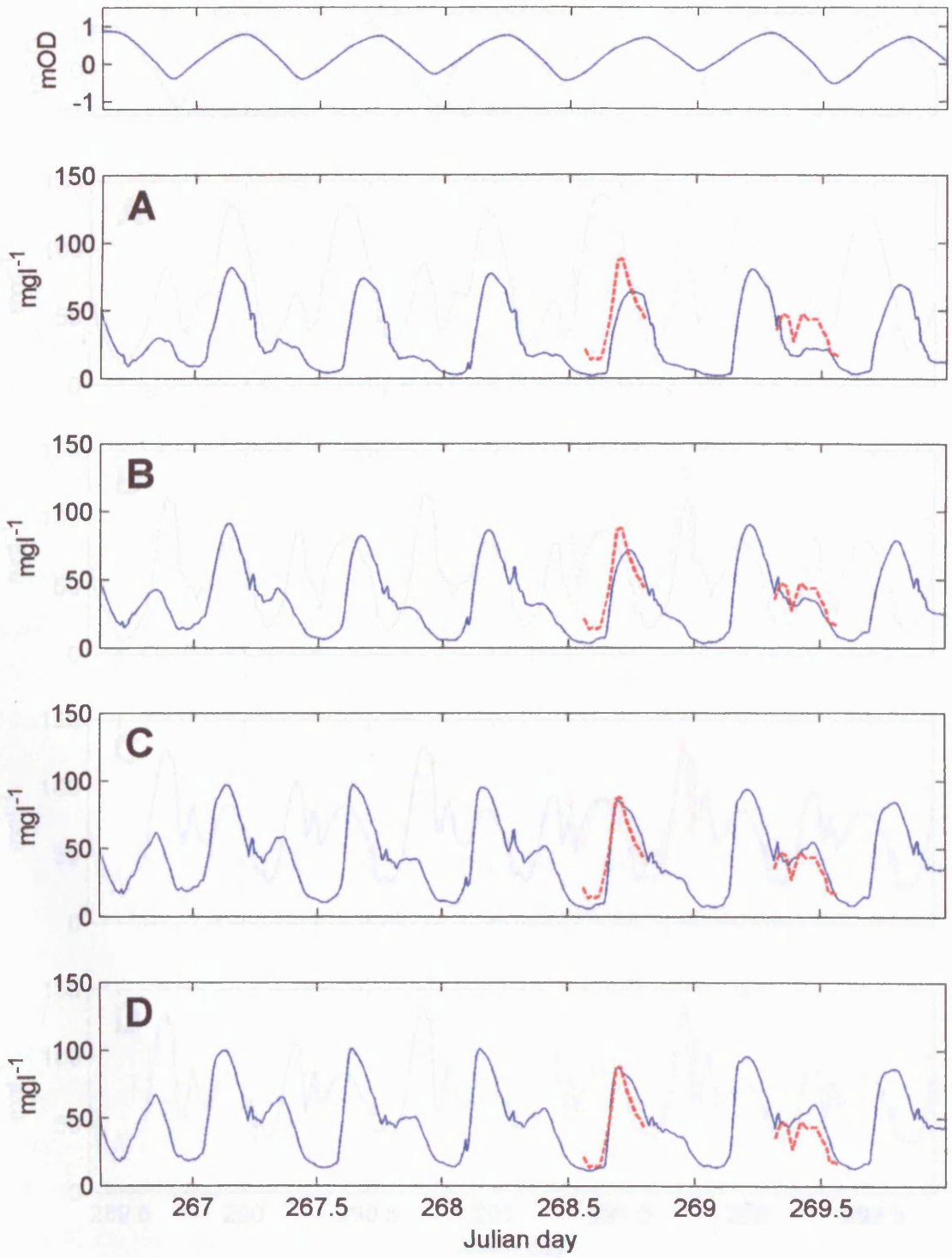

Figure 5.37 – Neap tide modelled (solid line) and observed (dashed line) suspended sediment concentration. Showing basic parameterisation (A) followed by sequential addition of spatially varied u_{*ce} (B), a resuspension bed layer (C), and a variable settling velocity model (D). The modelled water level at Reydon is plotted at the top.

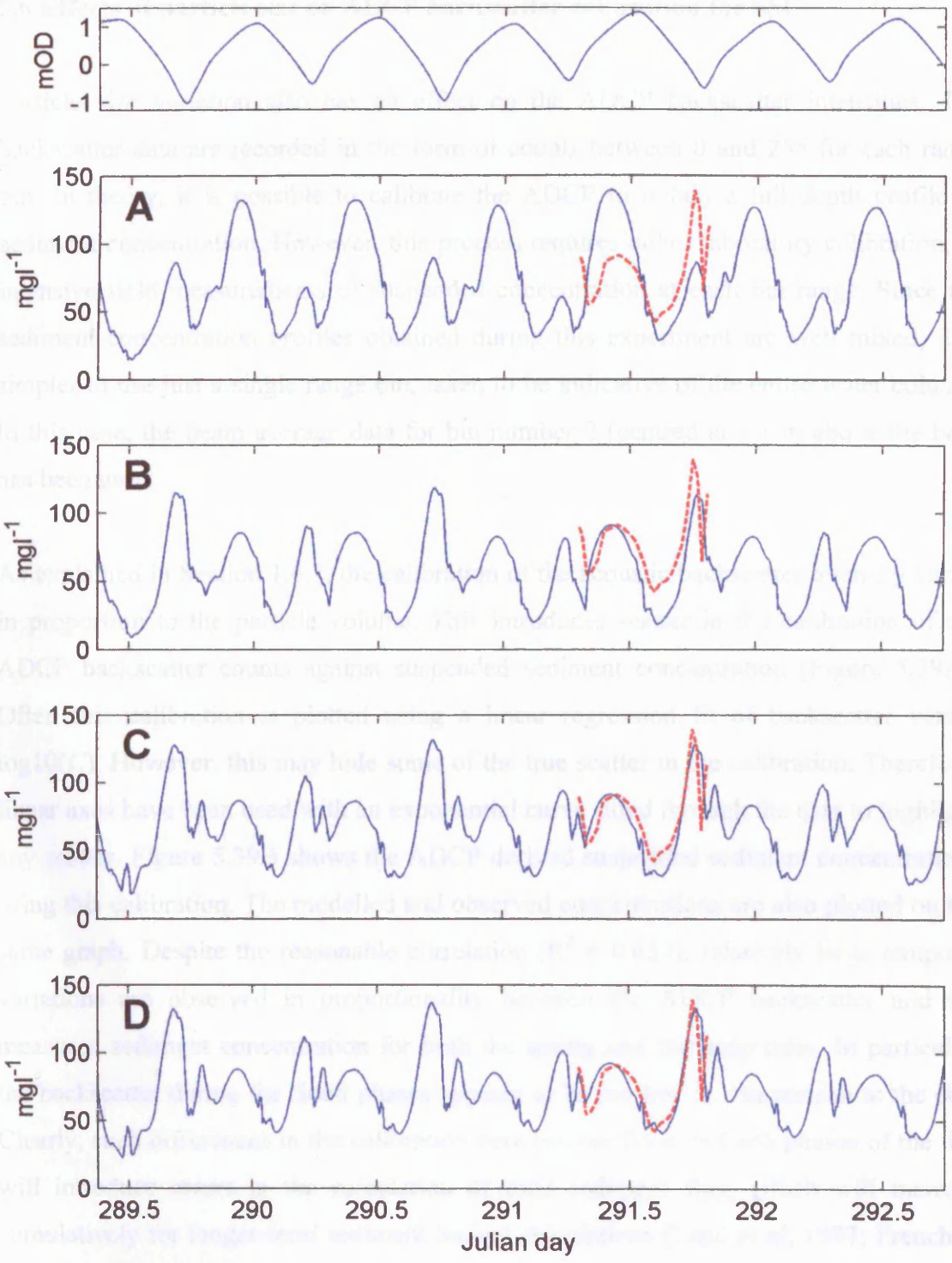

Figure 5.38 – Spring tide modelled (solid line) and observed (dashed line) suspended sediment concentration. Showing basic parameterisation (A) followed by sequential addition of spatially varied u_{*ce} (B), a resuspension bed layer (C), and a variable settling velocity model (D). The modelled water level at Reydon is plotted at the top.

5.6 Effects of particle size on ADCP backscatter calibration for SSC

Particle size variation also has an effect on the ADCP backscatter intensities. The backscatter data are recorded in the form of counts between 0 and 255 for each range bin. In theory, it is possible to calibrate the ADCP to obtain a full depth profile of sediment concentration. However, this process requires either laboratory calibration, or intensive field measurements of suspended concentration at each bin range. Since the sediment concentration profiles obtained during this experiment are well mixed, it is simpler to use just a single range bin, taken to be indicative of the entire water column. In this case, the beam average data for bin number 2 (centred at 1.1 m above the bed) has been used.

As explained in Section 1.4.2, the calibration of the acoustic backscatter intensity varies in proportion to the particle volume. This introduces scatter in the calibration of the ADCP backscatter counts against suspended sediment concentration (Figure 5.39A). Often this calibration is plotted using a linear regression fit of backscatter versus log10(C). However, this may hide some of the true scatter in the calibration. Therefore, linear axes have been used with an exponential curve fitted through the data to highlight any scatter. Figure 5.39B shows the ADCP derived suspended sediment concentrations using this calibration. The modelled and observed concentrations are also plotted on the same graph. Despite the reasonable correlation ($R^2 = 0.657$), relatively large temporal variations are observed in proportionality between the ADCP backscatter and the measured sediment concentration for both the spring and the neap tides. In particular, the backscatter during the flood phases appears to be too low in comparison to the ebb. Clearly, such differences in the calibration between the flood and ebb phases of the tide will introduce errors in the calculation of total sediment flux, which will increase cumulatively for longer-term sediment budget calculations (Lane *et al*, 1997; French *et al*, 2004).

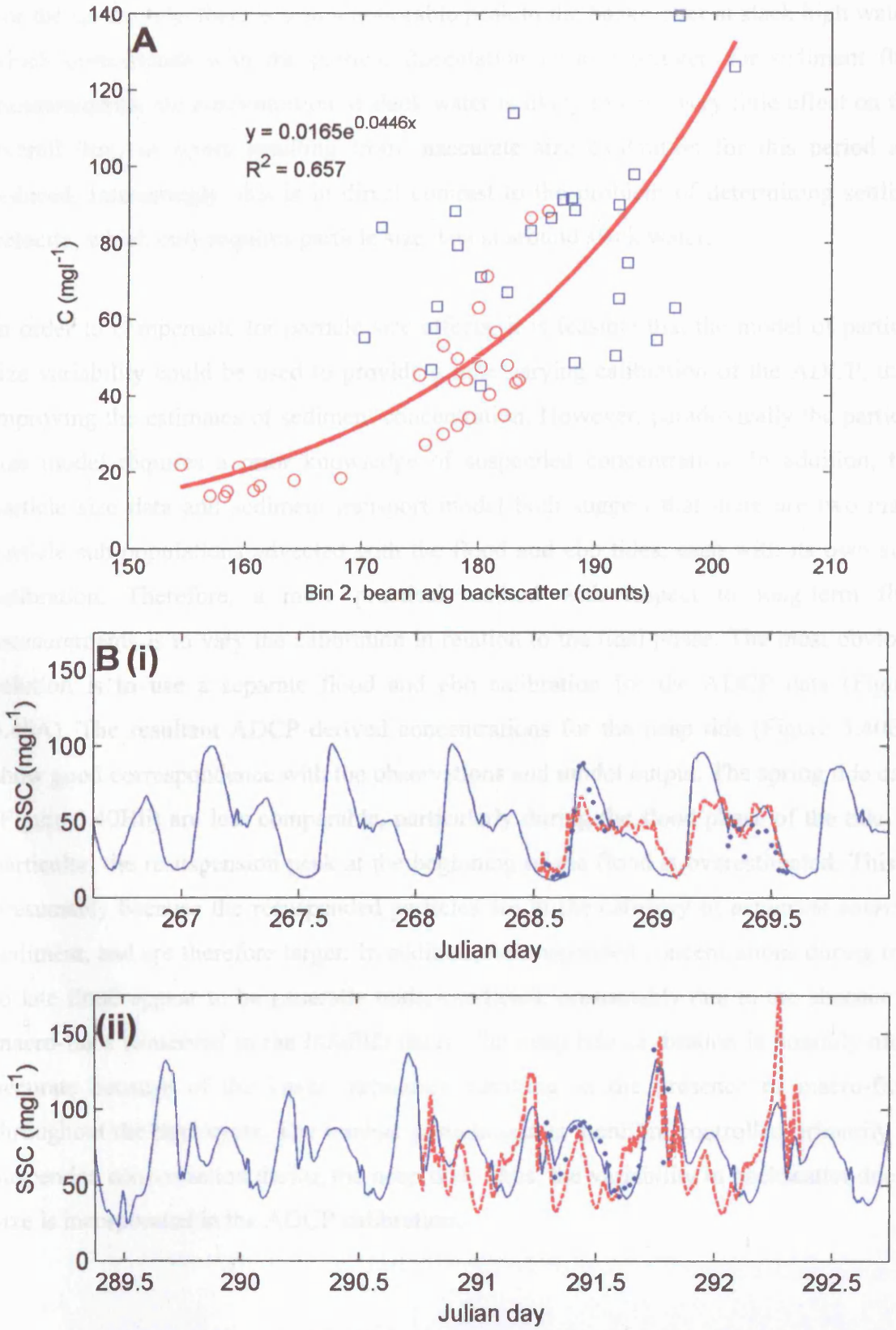

Figure 5.39 – (A) Single ADCP calibration for suspended sediment concentration using beam average backscatter for bin 2. (B) Modelled (solid line) and ADCP derived suspended concentrations (dashed line) for neap (i) and spring (ii) tides. Water bottle sample data are also plotted (•).

For the spring tide, there is also a noticeable peak in the backscatter at slack high water, which corresponds with the particle flocculation peak. However, for sediment flux measurements, the concentration at slack water is likely to have very little effect on the overall flux, so errors resulting from inaccurate size calibration for this period are reduced. Interestingly, this is in direct contrast to the problem of determining settling velocity, which only requires particle size data at around slack water.

In order to compensate for particle size effects, it is feasible that the model of particle size variability could be used to provide a time-varying calibration of the ADCP, thus improving the estimates of sediment concentration. However, paradoxically the particle size model requires a prior knowledge of suspended concentration. In addition, the particle size data and sediment transport model both suggest that there are two main particle sub-populations advected with the flood and ebb tides, each with its own size calibration. Therefore, a more practical method with respect to long-term flux measurements is to vary the calibration in relation to the tidal phase. The most obvious solution is to use a separate flood and ebb calibration for the ADCP data (Figure 5.40A). The resultant ADCP derived concentrations for the neap tide (Figure 5.40Bi) show good correspondence with the observations and model output. The spring tide data (Figure 5.40Bii) are less comparable, particularly during the flood phase of the tide. In particular, the resuspension peak at the beginning of the flood is overestimated. This is presumably because the resuspended particles are in the category of *estuarine sourced* sediment, and are therefore larger. In addition, the suspended concentrations during mid to late flood appear to be generally under-predicted, presumably due to the absence of macro-flocs (observed in the InSiPID data). The neap tide calibration is possibly more accurate because of the lower turbulence resulting in the presence of macro-flocs throughout the tidal cycle. The median particle size is therefore controlled primarily by suspended concentration during the neap tide. Thus, the variability in backscatter due to size is incorporated in the ADCP calibration.

Using a separate calibration for the flood and ebb phases of the tide provides a slight improvement in the correlation with field observations, especially in the neap tide calibration. However, this method fails to apply the calibrations in accordance with the different sediment types just after slack low water (i.e. before the marine sediment has been advected from the mouth to the point of measurement at Reydon). This problem is discussed further in the following Chapter.

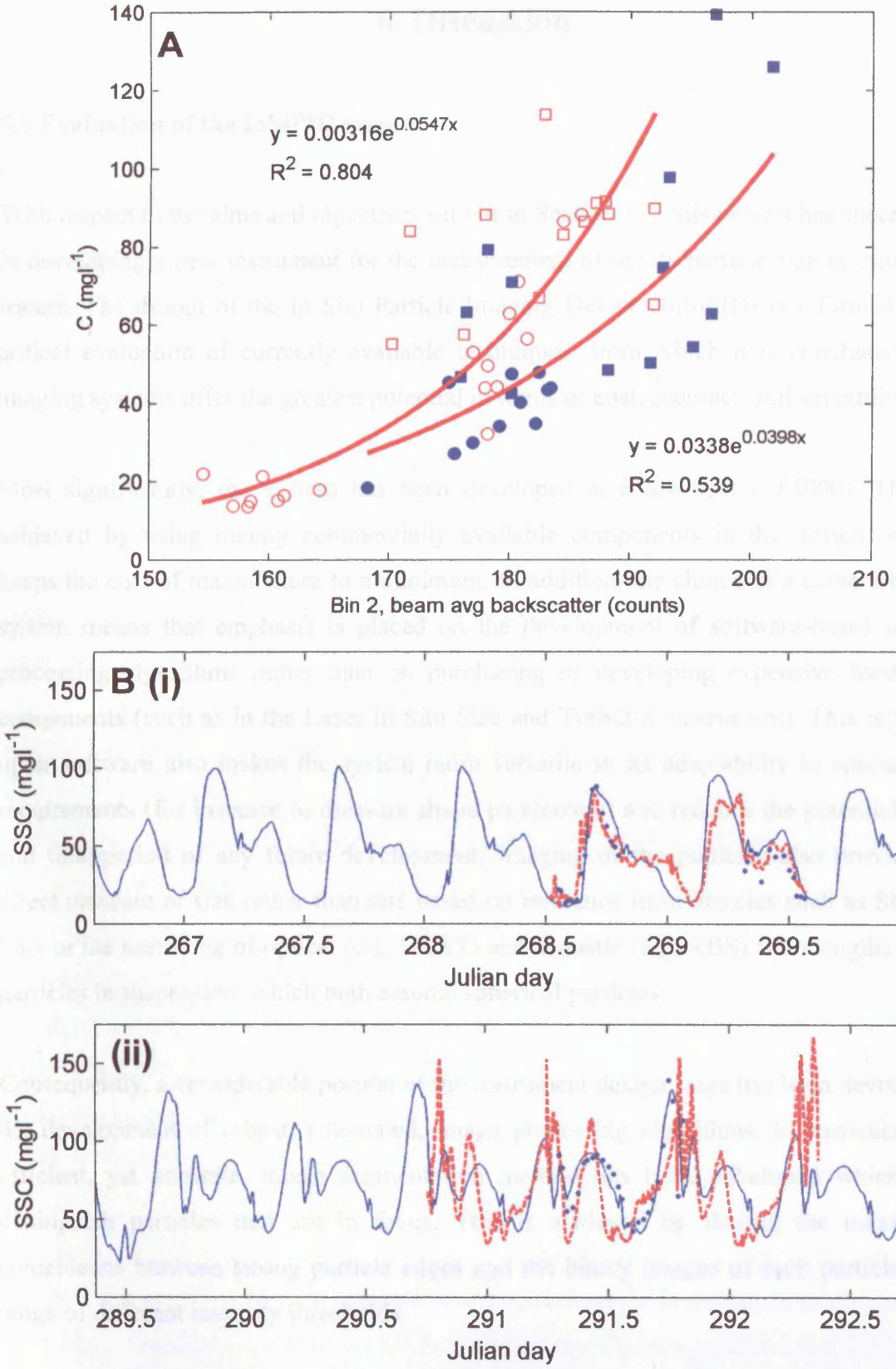

Figure 5.40 - (A) Separate flood and ebb ADCP calibration for suspended sediment concentration using beam average backscatter for bin 2. (B) Modelled (solid line) and ADCP derived suspended concentrations (dashed line) for neap (i) and spring (ii) tides. Water bottle sample data are also plotted (•).

6. Discussion

6.1 Evaluation of the InSiPID system

With respect to the aims and objectives set out in Section 1.5, this project has succeeded in developing a new instrument for the measurement of *in situ* particle size in estuarine waters. The design of the In Situ Particle Imaging Device (InSiPID) is informed by a critical evaluation of currently available techniques, from which it is concluded that imaging systems offer the greatest potential in terms of cost, accuracy and versatility.

Most significantly, the system has been developed at a low-cost (<£5000). This is achieved by using mainly commercially available components in the design, which keeps the cost of manufacture to a minimum. In addition, the choice of a camera-based system means that emphasis is placed on the development of software-based image processing algorithms rather than on purchasing or developing expensive hardware components (such as in the Laser In Situ Size and Turbidity instrument). This reliance upon software also makes the system more versatile in its adaptability to specialised requirements (for instance to measure shape parameters) and reduces the potential cost and time-period of any future development. Imaging of the particles also provides a direct measure of size rather than one based on inference from theories such as Stokes' Law or the scattering of optical (e.g. LISST) and acoustic (e.g. ABS) wavelengths from particles in suspension, which both assume spherical particles.

Consequently, a considerable portion of the instrument design stage has been devoted to the development of robust, automated, image processing algorithms. In particular, an efficient, yet accurate, image segmentation method has been developed which can distinguish particles that are in focus. This is achieved by finding the maximum coincidence between strong particle edges and the binary images of each particle at a range of different intensity thresholds.

Laboratory testing shows that the system provides accurate and precise data over a wide particle size range of ~4-3000 μm. The broad size range is achieved by using two cameras at different magnifications. Direct digitisation of the images, a rapid sample rate (up to 10 images s^{-1}) and automated particle size analysis allow a large number of

particles to be counted (~10,000 for each measurement). This increases the precision of the system. Testing of the system against known size standards shows that the system performs well in terms of accuracy, giving relative errors in median size of 11% and 4% for the high and low magnification systems respectively. Assuming a constant error with size, this equates to an accuracy of approximately ±0.4% at full-scale for both components of the camera system.

The system is also portable, of rugged construction and easy to use. The compact design is battery operated, with low power consumption. This has enabled *in situ* size measurements to be obtained from a small boat throughout a full tidal cycle in the Blyth estuary. The use of microsecond flash units provides blur-free images of particles in flow speeds in excess of 1 ms^{-1} (the maximum recorded flow during testing was 1.4 ms^{-1}). Currently the system has a 6 GB hard disk, enabling up to 40,000 images to be captured in a single deployment. This has proved to be sufficient for deployment over a complete tidal cycle at a sampling interval of approximately 20 minutes.

Results from the Blyth estuary case study indicate that the new instrument is a valuable tool for the characterisation of particle size variability in estuaries. In particular, the particle size data provided by the InSiPID exhibit a bimodal distribution of micro-flocs and macro-flocs, with a break at approximately 125 μm as observed by Eisma (1986). Most other methods of *in situ* particle sizing would not be able to fully resolve this bimodality because they either determine a mean size (e.g. ABS, model inversion) or do not have a broad measurable size range (e.g. laser diffraction (LISST) or single lens camera systems). The ability to measure the full size range has been shown to be crucial for distinguishing sediment sub-populations advected at different stages of the tidal cycle.

As well as the high accuracy and broad size range of the measurements, the ease with which the system can be used means that it is also capable of providing measurements with a high temporal resolution. This is necessary for obtaining data on the short-lived flocculation process. The ability for the system to obtain such measurements is highlighted by the time series for particle size over spring tide (Figure 5.14), which clearly shows the flocculation peaks at slack water.

6.2 Evaluation of improvements to sediment transport model parameterisation

6.2.1 Overview

During the development of the sediment transport model of the Blyth estuary, it was necessary to parameterise the spatial and temporal variability in the both the erosional and depositional properties of the sediment, by providing the following two sub-models:

- settling velocity model
- two layer bed model

The *in situ* particle size data obtained from the InSiPID have aided in the parameterisation of both of these sub-models in two ways.

First, the high accuracy and temporal resolution of the particle size measurements shows that the floc size varies significantly throughout the tidal cycle. This has led to the development of a semi-empirical flocculation model for the Blyth estuary, based on a measure of turbulence intensity and suspended sediment concentration. The flocculation model accurately replicates the observed particle size variability between consecutive high and low waters as well as between the spring and neap tidal cycles at the Reydon measurement site. Most significantly, during the spring tide, the median floc size is almost twice as large at slack low water than slack high water. During the neap tide, the floc size decreases significantly at slack low water due to the long period below the critical shear velocity for deposition, but remains relatively high during slack high water due to the rapid turn-around of the tide. The differences in floc size at each slack water are attributed to: (1) differences in the duration of the slack water period between the spring and neap tidal phases as well as between high and low slack water; (2) large differences in suspended sediment concentration at around slack water due to the advection of suspended sediment from up- or down-estuary (possibly as a result of differences in consolidation of the bed deposits). This strongly suggests that the use of a fixed value of settling velocity in the Blyth sediment transport model cannot accurately simulate the observed suspended concentrations (particularly for longer simulations spanning several tidal cycles). Thus it is essential to parameterise time-varying settling velocities in the sediment transport model. Settling velocity data are therefore derived

from the modelled particle size by means of a density adjusted Stokes' Law relationship and applied to the sediment transport model.

Second, the particle size data also indicate the presence of two separate sediment types, each with its own flocculation model calibration. This is highlighted by the absence of macro-flocs on the flood phase of the spring tide, which significantly affects the calibration of the particle size model. Consequently, the settling velocity during the spring high water is reduced further. The two sediment types are included in the model by applying one sediment type at the mouth boundary (classified as *marine sourced* sediment) and applying the second sediment type to the bed model (classified as *estuarine sourced* sediment). In addition, there appears to be a transition between the two particle sub-populations during slack high water when the fine sediment advected from the mouth settles to the bed and is resuspended as larger estuarine sourced flocs. Consequently, the two sediment types also affect the parameterisation of the bed model. This is applied numerically to the sediment transport model by converting the marine sourced sediment to estuarine sourced sediment immediately on deposition.

6.2.2 Reassessing the use of floc size to derive settling velocity

The settling velocity model described in this thesis uses an uncommon approach for cohesive sediments whereby the particle size is first modelled in relation to the suspended concentration and turbulent conditions. From these modelled sizes, settling velocity data are derived using Stokes' Law and an empirically derived model of floc density from compiled data.

In the case of cohesive sediments, the two main arguments against using this type of approach, are as follows:

- the overall accuracy of the settling velocity model relies upon an accurate model of the particle density variability with floc size (Manning & Dyer, 1999).
- the added complexity and computational overheads needed for calculating floc size are unnecessary in terms of improvements to model performance (Spearman & Roberts, 2002).

Manning & Dyer (1999) claim that *in situ* settling velocity data from the field site are necessary to include the effects of localised floc density variability in the model. They therefore advocate the use of instrumentation to determine the *in situ* settling velocity, from which an empirical model can be formulated (such as Equation 1.23). As discussed in Chapter 3, settling velocity measurements were originally obtained using field pipette withdrawal settling tubes (which measure the mass of sediment settling over time) from which it was first recognised that power law relationships could be derived between settling velocity and suspended concentration (Owen, 1971). More recently, these have been replaced by more complex instrumentation systems such as the camera based INSSEV (Fennessy *et al*, 1994), described in Chapter 3, which can measure both the particle size and settling velocity, thus providing insights into variability in floc density.

However, such instruments all suffer from problems associated with removal of the particles from the turbulent estuarine environment. They also have a relatively poor sampling rate due to the need to wait for the particles to settle before making the next measurement. For example, the INSSEV device traps a sample of water by closing two doors either size of a horizontally aligned square section tube. A subsection of suspended particles are then allowed to settle through a settling column by opening another trapdoor in the bottom of the tube. The settling column also contains higher salinity water than the estuary in order to damp out any turbulence. Since it is known that flocculation is affected by both salinity and turbulence (as discussed in Section 1.3.1), the measurement cannot be regarded as being truly *in situ*; rather the laboratory is taken to the estuary. In addition, the measurements are generally obtained from a very small subsection of particle flocs (<1000), thus reducing the precision of the resulting settling velocity estimates.

As an alternative, Spearman & Roberts (2002) suggest that settling velocities derived from Rouse profile measurements (as discussed in Chapter 3) are perhaps a better means of determining the settling velocity. This method was used by Wijngaarden (1999) in preference to measurements obtained using the Video In Situ camera system, which were found to be biased due to turbulence within the instrument's settling column. Tattersall *et al* (2003) also derived a settling velocity model from Rouse profile measurements. However, it should be noted that this technique is only applicable to

steady state situations where the flow is not rapidly accelerating or decelerating. Since maximum changes in flow velocity are observed at around slack water (at which point settling is most important), the validity of using the Rouse technique for providing settling velocity data is questionable (although it may provide reasonable data during the mid flood and ebb tidal phases). Measurements of the suspended concentration, required for determining the Rouse profile, are also reliant upon either water samples (which are labour intensive) or instrumentation such as the transmissometer or ADCP (which are known to suffer from errors due to particle size variability).

Consequently, there is generally poor comparison between different techniques for measuring the *in situ* settling velocity and, hence, there are still no proven methods (Spearman & Roberts, 2002). Here, it must be emphasised that an empirical model can only be as good as the measured data. Therefore, the uncertainty in the accuracy of the settling velocity measurements leads to the logical conclusion that any derived model of settling velocity must be used with caution and may be misleading.

In contrast, the InSiPID system has demonstrated that it is possible to obtain highly accurate and precise *in situ* particle size measurements at a low cost. Hence, an accurate model of particle size variability is obtained, from which settling velocity data can be calculated using a density adjusted Stokes' Law. Uncertainty in the effective density of the flocs is compensated for during the sediment transport model calibration phase by fine-tuning of the maximum settling velocity for a defined maximum floc size, whilst keeping the density of the minimum size at a constant value. An important observation is that the effect of the floc density on the conversion from a volume weighted to mass weighted median diameter is negligible. Therefore, adjustment of the effective densities in this fashion (without recalculating the median diameter) is considered valid. In addition, the validity of the Stokes' Law formula (which only applies to particles settling in viscous flow regime) is verified against the particle Reynolds number, and it is shown to be appropriate for the majority of floc sizes observed in the Blyth estuary.

The second argument against using a settling velocity model based on floc size is presented by Spearman & Roberts (2002) who suggest that the added complexity and computational overheads required for calculating the particle size and density in sediment transport models is unnecessary and no more accurate in terms of the

improvements to the model output. However, this argument is based largely upon tests carried out with the physically based model of settling velocity formulated by Winterwerp (1998), which is an extension of previous physical model of fractal floc formation proposed by Kranenburg (1994). In principle, Winterwerp's model is similar to that presented in this thesis since it is based on a model of floc formation, proportional to turbulence and suspended concentration, combined with a power law relationship between particle size and effective density, which are used to calculate the settling velocity via Stokes' Law. However, Spearman & Roberts (2002) found that Winterwerp's 1DV Eulerian model is difficult to implement and had high computational overheads. In addition, the model performed less satisfactorily than a simple power law relationship (although this could be accounted for by errors in the *in situ* settling velocity measurements which were carried out using INSSEV). Two important differences to Winterwerp's approach make the model presented in this thesis both simpler to implement and lower on computational overheads.

First, a major difference is in formulation of the particle size model, which uses a more empirical approach than the more physically based model of Winterwerp. Winterwerp's method is presented in two forms. The full model is in the form of a dynamic equation that incorporates a *time of flocculation* (T_f) variable for parameterising the amount of time necessary for the floc size to reach equilibrium. In theory, T_f is proportional to the frequency of collisions between particles. Therefore, it is inversely proportional to both the level of turbulence and the suspended concentration. Consequently, below a certain threshold of turbulence (i.e. at levels low enough to prevent flocs from breaking up), the floc size is proportional to both turbulence and suspended concentration. However, T_f is difficult to calibrate and tends to infinity during very low current flow speeds (Spearman & Roberts, 2002). The simpler version of Winterwerp's model assumes that there is always ample time to achieve equilibrium flocculation (i.e. $T_f = 0$). Hence, the model does not provide a mechanism to allow the floc size to decrease at very low levels of turbulence. This is therefore an oversimplification of the problem and is likely to be unreliable, particularly during the neap tide simulations when concentrations and turbulence are low, resulting in high values of T_f.

The particle size model described in this thesis uses a more top-down method (similar to that of van Leussen (1994) in Equation 1.22) and also allows the definition of the

location of the flocculation peak at a particular turbulence and suspended concentration, thus making it easier to calibrate. This is made possible by obtaining *in situ* measurements of particle size using the InSiPID instrument, which can then be used to empirically calibrate the model. The model also simulates a movement of the flocculation peak towards higher values of turbulence as the suspended concentration is decreased. In principle, this is similar to using a time of flocculation because, at higher suspended concentrations, the flocculation peak is located at a low turbulent threshold (equivalent to a short time of flocculation), whereas at lower suspended concentrations, greater turbulence is required to obtain a maximum floc size (equivalent to a short time of flocculation). This observation may also be accounted for by the observed increase in the proportion of organic material at lower concentrations, which is likely to increase the median size of the particle population by the presence of either large organic low density fragments that do not break up, or sticky organic compounds that may help to bind the flocs.

Second, the conversion from particle size to settling velocity is simplified from that of Winterwerp (1998) who uses the particle fractal dimension to adjust the power law exponent in Stokes' Law. In the new approach, the density power law is explicitly calculated (from a composite graph of previous data) before applying to Stokes' Law in the sediment transport model. Consequently, no measurements (or estimation) of the *in situ* fractal dimension are required. As discussed in Section 5.3.4, the Blyth data suggest that the fractal dimension is difficult to measure without expensive camera equipment, especially in the case of images containing particles that are not in focus. As already mentioned, an obvious problem with using a simplified density model is that it may not represent the true *in situ* density variability. Hence, errors may be introduced in the calculation of settling velocities. This is partially overcome in the new approach by iterative adjustment of the slope of the density power law curve during the calibration phase of the sediment transport model (a stage that is omitted in Winterwerp's approach).

The settling velocity model therefore consists of a three-stage calibration (Figure 6.1). The first involves the empirical calibration of the flocculation model from the *in situ* particle size measurements (Figure 6.1A). As found in the Blyth model, this may need to be carried out for more than one population of particles. The second stage is the

composition of an empirically derived model of particle density from previous work by a number of different authors (Figure 6.1B). This provides an approximate model of particle density variability. The third stage involves fine-tuning of the particle density model within the sediment transport model by iterative adjustment of the effective density for the maximum observed floc size, thus changing the slope of the power law equation (Figure 6.1C). This final stage of calibration is frequently ignored in investigations aimed purely at deriving a model of settling velocity from field or laboratory observations. In the context of sediment transport modelling, it is preferable (if not essential) to have a means of iteratively adjusting the particle density model due to the inability to accurately measure this variable *in situ*. In effect, the calibration slope of the particle density model could be treated as a model calibration parameter in a similar fashion to bed friction or eddy viscosity in the hydrodynamic model.

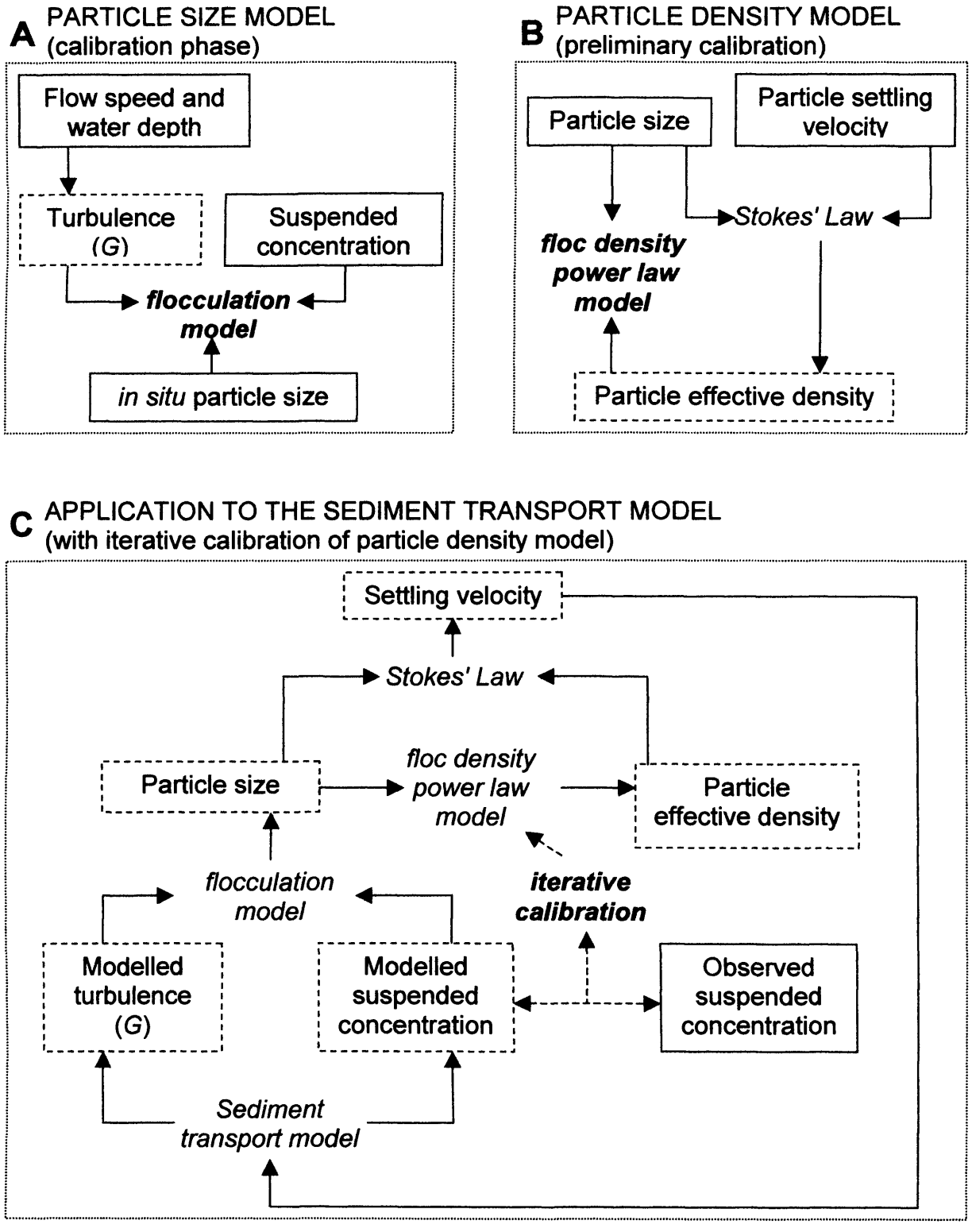

Figure 6.1 – Schematic diagram of the three calibration stages of the settling velocity model, showing (A) particle size model calibration, (B) preliminary calibration of the floc density power law relationship (using past data) and (C) application of the two models to provide settling velocity data to the sediment transport model, with iterative calibration of the particle density model if required. Note that the solid boxes represent observations, and the dashed boxes are data derived from model output.

Interestingly, the preliminary calibration of particle density variability (Figure 6.1B) performed in this project provided an almost linear relationship between particle size and settling velocity (Equation 5.12). In addition, no further fine adjustment of the effective density curve is required for calculating suitable settling velocity data for the sediment transport model of Blyth estuary. This supports the assumption that the fractal dimension of estuarine particles is ~2 (Kranenburg, 1994; Winterwerp, 1998). Hence, for modelling purposes, it may be possible to ignore the power exponent in the density adjusted Stokes' Law (Equation 5.11). Although further testing of this method is required in other estuaries, in the case of the Blyth it provides a simple and effective way of converting *in situ* particle size data to settling velocities.

The described approach to modelling of settling velocity also provides useful information for parameterisation of the different sediment types. Interestingly, previous work suggests that the poor correlation between modelled and observed settling velocities is mainly due to the advection of different particle populations from outside the measurement region at various stages of the tidal cycle in addition to the different characteristics of eroded sediment (van der Ham & Winterwerp, 2001; Spearman & Roberts, 2002). This is by no means a recent observation. Officer (1981), in a review of the state of knowledge of sediment transport in estuaries at that time, postulated that "substantial gains could be made in our understanding of suspended sediments by studying more fully both the vertical and longitudinal distribution and transport effects throughout a tidal cycle and the bottom source conditions and determining factors related thereto."

In relation to this, the Blyth data show that, by focusing attention on the particle size, some distinctions can be made between the advected and eroded particle sub-populations. The resuspended bed sediment exhibits a coarser median floc size, and a steeper calibration gradient in the flocculation model, whereas the sediment sourced at the mouth is considerably finer and less flocculative. The greater ease of measuring floc size in comparison to settling velocity means that reliable measurements of the full particle size range can be obtained at a high sample rate, thus providing further insights into the variability in particle characteristics. For the Blyth case study, this helps determine the existence of the two sediment sources, which are then parameterised in the sediment transport model with more confidence.

In summary, the approach used to derive settling velocities in this thesis is a compromise between accuracy, robustness and simplicity. It is shown to provide reasonable settling velocity data for the sediment transport model of the Blyth estuary and with low computational overheads. It is also designed for parameterising sediment transport models in general, rather than solely for this case study. In particular, the approach offers the following benefits:

- Ease and accuracy of the *in situ* measurements
- Simplicity and robustness of the theoretical formulae
- Applicability to sediment transport modelling via iterative calibration
- Ability to characterise particle sub-populations

Until a cheaper and more reliable method of measuring the *in situ* settling velocity is available, it is perhaps more appropriate to obtain more accurate particle size measurements over the full size range, at a high temporal resolution. These data can then be converted to settling velocities by means of a simplified density model and provide a better quantitative data on particle sub-populations. Further evaluation of this approach in comparison to other settling velocity models for a variety of different case studies is needed to resolve this issue.

6.2.3 Bed layer modelling: reducing the problem

Although this thesis was not initially concerned with modelling of the bed deposits, it is found that one of the most important parameters affecting the suspended concentrations is the critical shear velocity for erosion (u_{*ce}). This is found to vary both vertically (according to bed layering as a result of consolidation) and horizontally (according to location within the estuary), thus necessitating the use of a layered bed in the sediment transport model.

The bed layer model described in Section 5.4.2 allows the parameterisation of any number of bed layers, each with a prescribed thickness (T_{init}), critical shear velocity for erosion (u_{*ce}), erosion rate constant (M) and sediment concentration (C_b). However, considering the Blyth model contains over 11,000 nodes, this provides an impossibly large combination of values for parameterising the model. The problem is therefore reduced in a number of ways.

First, the number of bed layers is limited to just two, which is sufficient to model the resuspension event at the beginning of the flood tide. This is simplified further since it is found that the thickness of the top layer can be initialised to zero at the start of the model run.

Second, using globally defined values across the entire model domain reduces the number of variables. The erosion rate (M) is set to a single constant value of 0.00004 m^2s^{-1}, which is supported by other investigations (Mulder & Udink, 1991; Cancino & Neves, 1999a,b; Roberts *et al*, 2000; van der Ham & Winterwerp, 2001; Tattersall *et al*, 2003). In addition, the sediment concentration (C_b) may be parameterised across the entire domain with an approximate value for each layer (unless simulating bed elevations in detail) since it affects only the physical volume of the bed material and has no affect on the erosional properties. The second bed layer is also initialised to a nominal thickness of 0.1 m across the entire domain, which is sufficient to provide a constant source of sediment throughout the model run. Consequently, the spatial variability in bed properties is controlled entirely by the spatial parameterisation of the critical shear velocity for erosion (u_{*ce}) for the two bed layers.

Third, the complexity of parameterisation is reduced further by defining a relatively small number of sedimentary zones within the model mesh in comparison the number of nodes. For the Blyth model, only nine zones are defined. Importantly, seven of the bed model zones are used to divide the main sub-tidal channel. This is because the model calibration suggests a gradual increase in values of u_{*ce} towards the mouth. Although based purely on speculative evidence from the model calibration, this finding is supported by Tattersall *et al* (2003) who parameterise a sediment transport model of the Tamar estuary with linearly increasing values of u_{*ce} from the head to the mouth.

The simplification of the bed model makes parameterisation both less complicated and less time-consuming. Importantly, just a single, low-density bed surface layer is required to replicate the resuspension peak at the beginning of the flood tide. This peak is most distinguishable during the spring tide when the top sediment layer is less consolidated, resulting in rapid resuspension of the entire layer before maximum flood flows are reached. This is parameterised in the model as a reduction in u_{*ce} for the top sediment bed layer in the main channel from 0.014 ms^{-1} during the neap tide to 0.012 ms^{-1} during the spring tide.

The model calibration also suggests temporal variability (between spring and neap tides) in the horizontal distribution of u_{*ce} for the lower sediment layer. This is shown in a plot of u_{*ce} for the second layer in the subtidal channel zones (Figure 6.2). In particular, during the spring tide, the model calibration suggests that a pool of poorly consolidated material exists near to the New Cut (zone 4), which is advected on the ebb tide, resulting in a suspended concentration peak at the end of the ebb at Reydon. However, during the neap tide, the sediment is more resistant in the New Cut region and a pool of sediment is located nearer to Reydon (zone 6), resulting in relatively high concentrations on the flood tide and lower concentrations at the end of the ebb tide. Again, this finding is similar to that of Tattersall *et al* (2003) for the Tamar estuary. Clarke & Elliott (1998) also found similar differences between spring and neap values for critical shear velocity for erosion in the Firth of Forth.

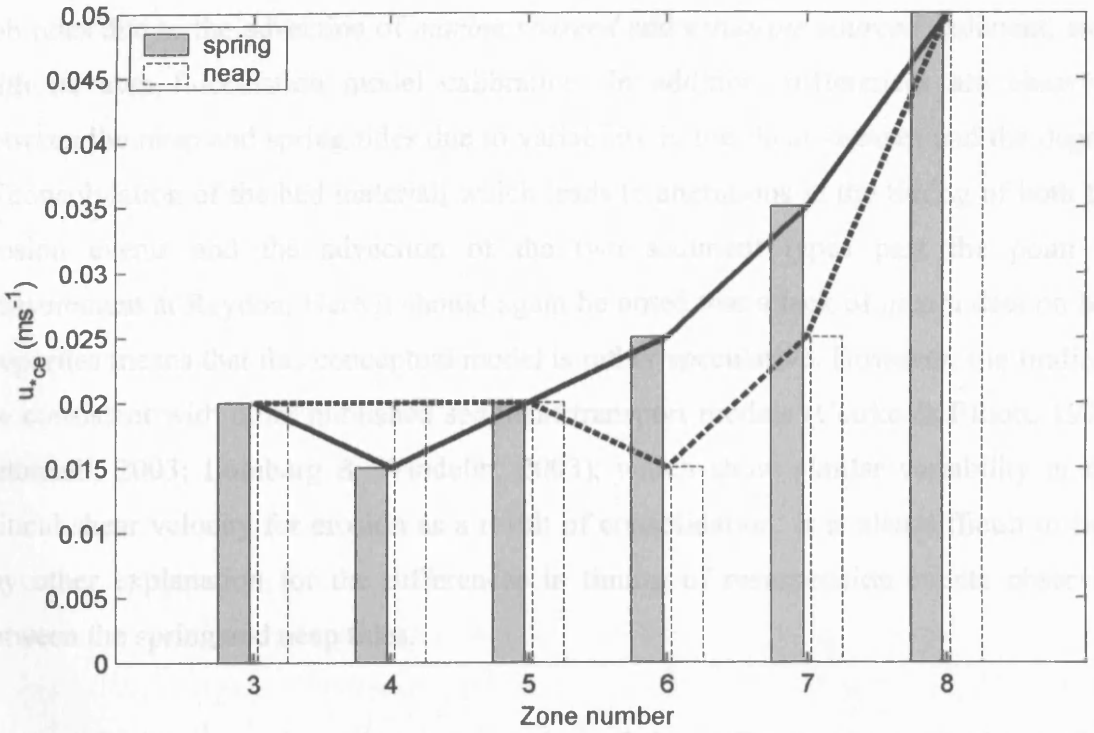

Figure 6.2 – Parameterisation of u_{*ce} for the neap (dashed line) and spring (solid line) tide simulations in the subtidal channel zones. (Zone numbering starts furthest from the estuary mouth as follows: 3 = upper channel, 4 = New cut to Tinkers Bend, 5 = Tinkers Bend to Wolsey Creek, 6 = Reydon section, 7 = Blackshore Quay, 8 = Harbour mouth). Note the shift in poorly consolidated sediment from zone 4 during the spring tide to zone 6 during the neap tide.

6.2.4 A conceptual model of sediment transport in the Blyth estuary

From the particle size data, ADCP backscatter intensities and model simulations, a conceptual model of sediment transport in the Blyth estuary can be formulated. Distinct differences are observed in the sediment transport processes between the flood and the ebb tides due to the advection of *marine sourced* and *estuarine sourced* sediment, each with its own flocculation model calibration. In addition, differences are observed between the neap and spring tides due to variability in the shear stresses and the degree of consolidation of the bed material, which leads to alterations in the timing of both the erosion events and the advection of the two sediment types past the point of measurement at Reydon. Here it should again be noted that a lack of *in situ* data on bed properties means that this conceptual model is rather speculative. However, the findings are consistent with other published sediment transport models (Clarke & Elliott, 1998; Tattersall, 2003; Lumborg & Windelin, 2003), which show similar variability in the critical shear velocity for erosion as a result of consolidation. It is also difficult to find any other explanation for the differences in timing of resuspension events observed between the spring and neap tides.

Figure 6.3 shows a schematic representation of the sediment transport observed at Reydon during the flood tide for both the neap and spring tides. During the neap tide (Figure 6.3A), the smaller tidal range means that the shear stresses are relatively low and, consequently, less sediment is eroded from the bed than during the spring tide. In addition, the slow acceleration of the flood tide (and hence greater residence time of the sediment in the bed) means that intertidal consolidation of the bed material occurs. This results in a positive feedback that reduces the quantity of eroded sediment further and delays the initiation of resuspension. Combined with the slower propagation of the tidal wave from the mouth, resuspension occurs at approximately the same time as the marine sourced sediment reaches the measurement point at Reydon. Hence, there is substantial mixing of the two sediment types throughout much of the neap flood tide. This is shown clearly in a plot the modelled concentration of each sediment type at Reydon (Figure 6.5A). This is a possible cause of the observed scatter in the neap tide particle size model (Figure 5.23) resulting in a less obvious distinction between the two particle size calibrations between flood and ebb.

During the spring flood tide (Figure 6.3B), there is a much greater separation between the two sediment types. This is due to the poorer consolidation of the top sediment layer and greater acceleration of the flow, which results in the complete erosion of the top layer before the marine sourced sediment reaches the measuring point at Reydon. In addition, there is a clear separation between the resuspension of this layer sediment and the underlying, more resistant deposit, which is again shown clearly in the modelled concentrations at Reydon (Figure 6.5B). The spring tide is therefore modelled well using a two-layer bed model. The neap tide, however, may be improved by increasing the number of layers and including a time dependent consolidation model.

The rapid resuspension of the top sediment layer means that, during most of the flood of the spring tide, the majority of the material in suspension is composed of marine sourced sediment. The marine sourced sediment is distinguished from the estuarine sediment by its smaller median size (due to the presence of fewer macro-flocs). The cause for this difference in size may be the high shear stresses towards the mouth of the estuary, which prevent flocculation of the marine sediment as it travels landward. In addition, this difference may be due to the lack of sticky organic compounds (Extracellular Polymeric Secretions; de Deckere *et al*, 2002; Tolhurst *et al*, 2002) in the marine sourced sediment, which aid in the binding of the estuarine sourced sediment (especially in the intertidal regions). Consequently, there is a reduction in the overall particle size during the spring flood tide, which both reduces the intensity of the ADCP backscatter (thus changing the calibration for suspended concentration) and decreases the settling velocity at high water.

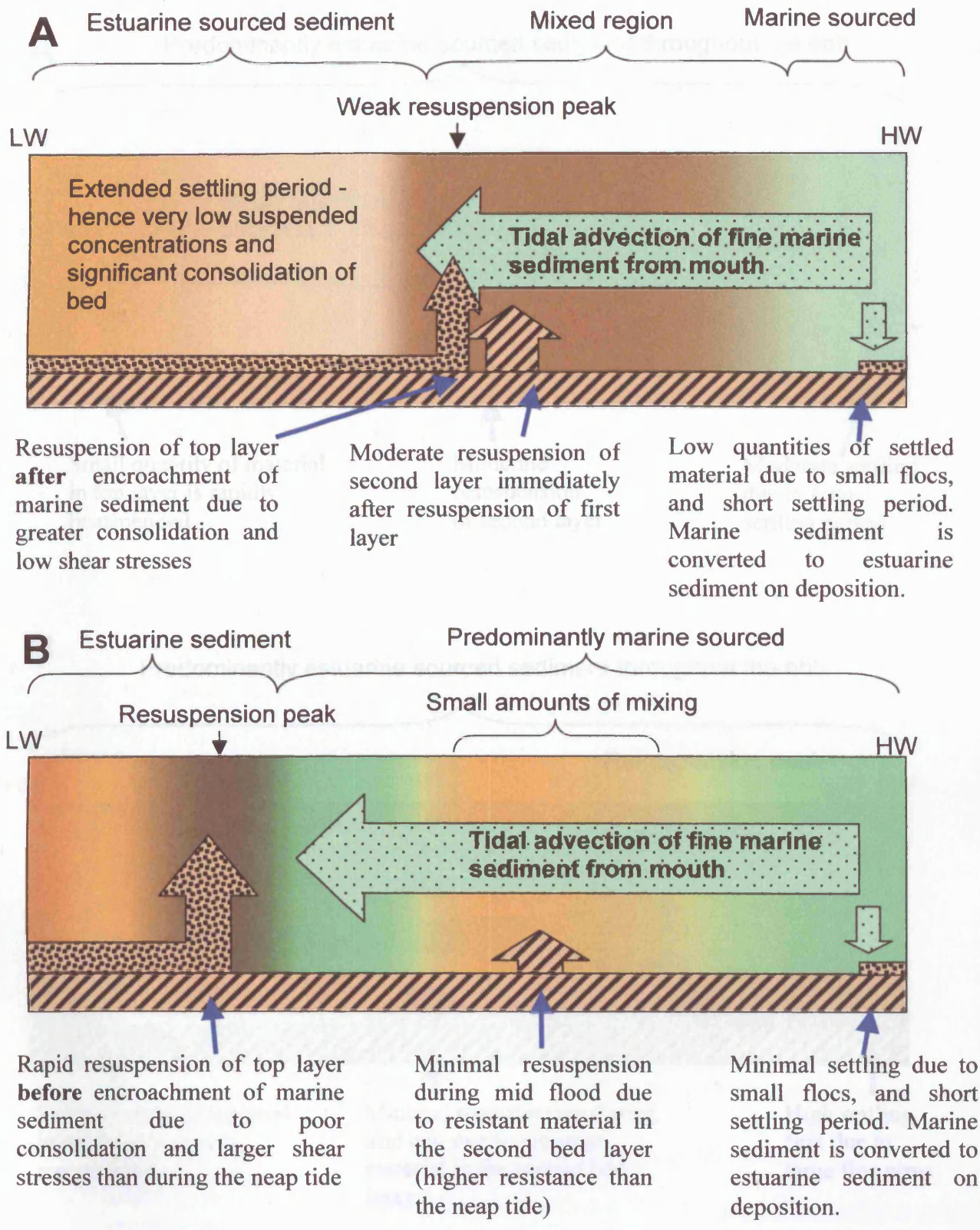

Figure 6.3 – Conceptual model of **flood** tide sediment transport observed at Reydon for (A) neap tide and (B) spring tide. In this model, the x-axis represents time from low water to high water. Note the conversion of marine sourced sediment to estuarine sourced sediment on deposition at slack high water.

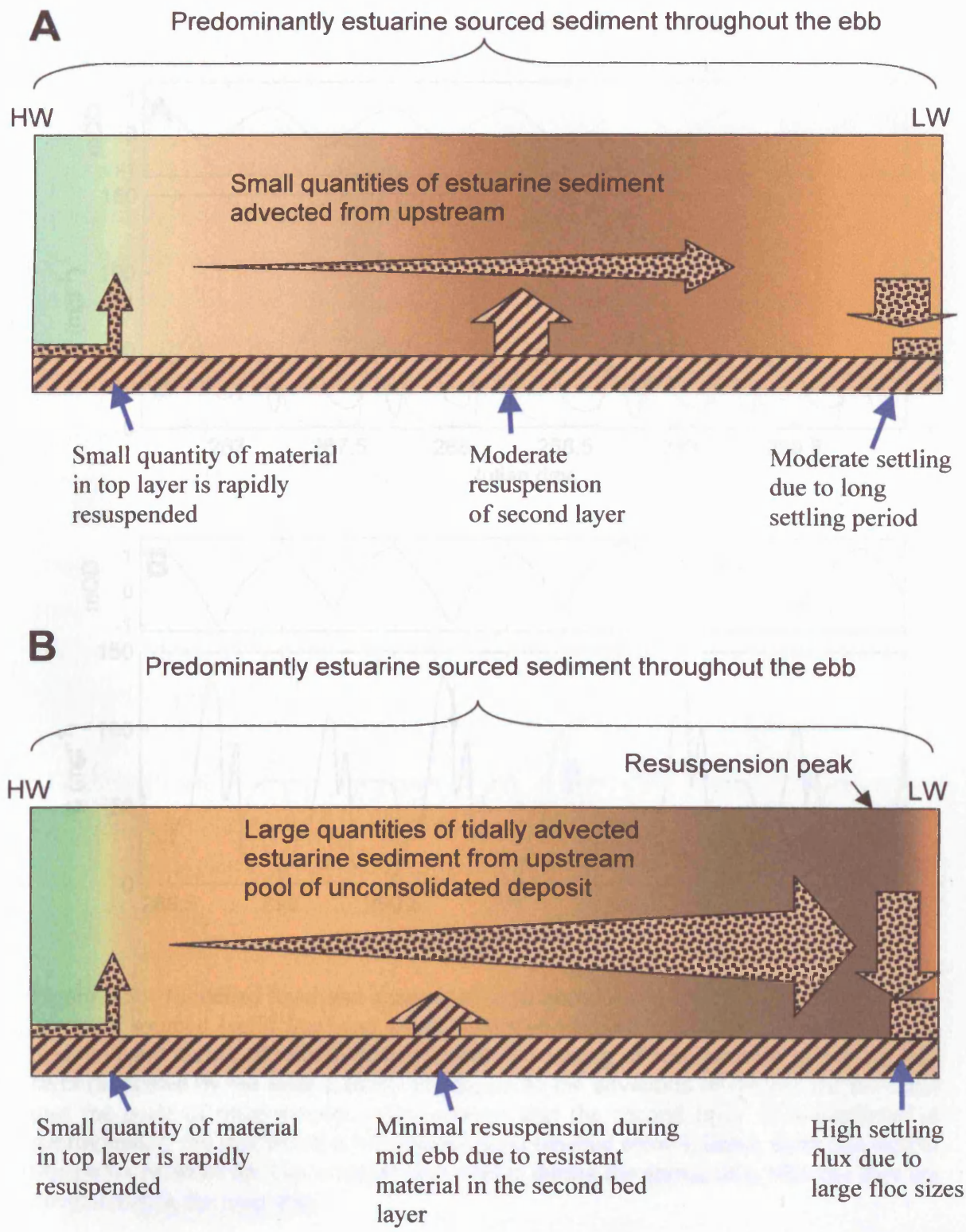

Figure 6.4 – Conceptual model of **ebb** tide sediment transport observed at Reydon for (A) neap tide and (B) spring tide. In this model, the x-axis represents time from high water to low water.

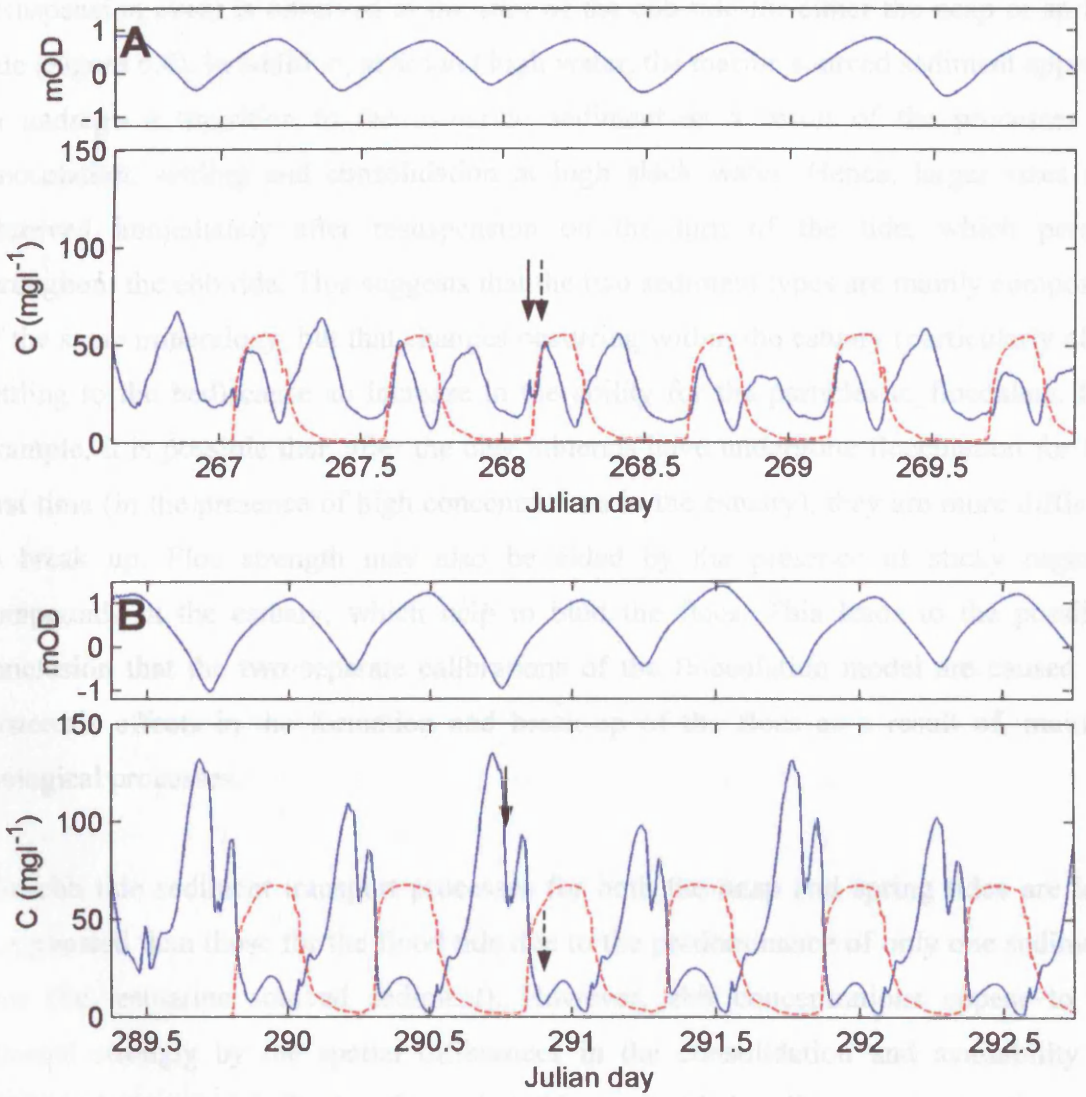

Figure 6.5 – Modelled level and suspended concentrations at Reydon (model 4) for the estuarine sourced (solid line) and marine sourced (dashed line) sediment types for the neap (A) and spring (B) tides. Note the different timing of resuspension of the top bed layer (indicated by the solid arrows) in relation to the advection of the marine sediment past the point of measurement. Also observe that the second layer is resuspended at approximately the mid flood in both simulations (dashed arrow), hence there is a visible separation between the two resuspension events during the spring tide, whereas they are merged during the neap tide.

During both the spring and neap tide, the high water slack periods are relatively short. Hence, the amount of time available for settling is limited. Therefore, no strong resuspension event is observed at the start of the ebb tide for either the neap or spring tide (Figure 6.4). In addition, at around high water, the marine sourced sediment appears to undergo a transition to the estuarine sediment as a result of the processes of flocculation, settling and consolidation at high slack water. Hence, larger sizes are observed immediately after resuspension on the turn of the tide, which persist throughout the ebb tide. This suggests that the two sediment types are mainly composed of the same mineralogy, but that changes occurring within the estuary (particularly after settling to the bed) cause an increase in the ability for the particles to flocculate. For example, it is possible that, after the clay minerals have undergone flocculation for the first time (in the presence of high concentrations in the estuary), they are more difficult to break up. Floc strength may also be aided by the presence of sticky organic compounds in the estuary, which help to bind the flocs. This leads to the possible conclusion that the two separate calibrations of the flocculation model are caused by hysteresis effects in the formation and break-up of the flocs as a result of, mainly, biological processes.

The ebb tide sediment transport processes for both the neap and spring tides are less complicated than those for the flood tide due to the predominance of only one sediment type (i.e. estuarine sourced sediment). However, ebb concentrations appear to be affected strongly by the spatial differences in the consolidation and availability of erodable bed material. During the spring tide, suspended sediment concentrations are influenced mainly by the advection of material from further up-estuary, towards the New Cut, where there is possibly a pool of poorly consolidated sediment. Therefore, the highest concentrations are observed at the end of the ebb. Consequently, the floc sizes at spring tide low water are very large, which results in a rapid settling velocity. Hence, the sediment quickly settles out of suspension to form the thick top bed layer, ready for resuspension at the start of the following flood.

It can be seen from this conceptual model that the flood tide concentrations are dominated by the quantity of sediment input at the mouth (particularly during the spring tide). This suggests that the net flux of sediment is largely controlled by the suspended concentrations of the North Sea, in proximity to the estuary mouth. Further modelling

and long-term estimates of sediment transport must therefore consider the time variability in suspended concentrations at the mouth. From this finding, it may also be postulated that storm induced sediment transport will have a large effect on the net sediment flux, both in and out of the estuary. For example, large swell waves near to the mouth of the estuary may raise the local suspended sediment concentrations, thus providing higher concentrations on the flood tide. Local storm events, however, are likely to induce waves over the mudflats, thus affecting the interior of the estuary and increasing the ebb tide suspended concentrations (French *et al*, 2004).

The conceptual model presented here is undoubtedly very simplified and therefore has a number of shortcomings. Most notably, the definition between marine and estuarine sediment is oversimplified since mixing between the two types will mean that neither are mutually exclusive. This is particularly the case during the beginning of the ebb, for both the spring and the neap tides, since not all the suspended sediment has time to settle out during the short high slack water. However, during the spring flood tide the distinction is much clearer due the narrow channel and resistant bed material between Reydon and the mouth of the estuary, which means that the suspended sediment is predominantly sourced from the sea.

A lack of *in situ* data on bed properties also means that the exact source of the sediment on the ebb tide is not known. This is particularly a problem on the mudflats where the small-scale hydrodynamics and sedimentary processes are not modelled by the Telemac2D model with a high degree of accuracy and cannot be validated here against *in situ* data. A better understanding of the sediment transport processes on the mudflats, coupled with *in situ* measurements of bed properties, may help to resolve this issue and support the theory (and provide a mechanism) for the formation of a pool of sediment near the New Cut.

6.2.5 The feasibility of using the sediment transport model output to provide a switch between ADCP calibrations

It is possible that the conceptual model of sediment transport in the Blyth estuary could be used to improve the calibration of the ADCP backscatter intensities to provide more accurate suspended sediment concentration data. By using the same data separation between estuarine and marine sourced sediment as defined for the particle size calibrations in Section 5.3.5, a new calibration is produced in Figure 6.6A. The estuarine sourced sediment calibration provides a reasonably good exponential fit (R^2 = 0.79). The marine sourced sediment calibration is less satisfactory (R^2 = 0.32), but this may well be due to the small number of data points.

With this approach, a complication arises in how to locate the correct point in time at which to switch between the two calibrations. To solve this issue, a method has been devised whereby the sediment transport model output is used to determine which calibration to use. In Figure 6.5 it can be seen that suspended concentration of marine sourced sediment increases almost instantaneously after it has been advected from the mouth. It then decreases rapidly at the turn of the tide due to settling, after which it is converted to estuarine sourced sediment in the model. Times for applying a separate calibration have therefore been derived from the model by assuming a switch from estuarine to marine sourced sediment when the concentration of marine sourced sediment exceeds a threshold of 20 mgl^{-1}. The calibration is then switched back at the start of the ebb tide (i.e. it is assumed that the particles undergo a transition after flocculation at high water).

Despite the relatively poor statistical correlation for the marine sourced sediment calibration, there is good visual comparison between the ADCP-derived concentrations and the suspended sediment model output (Figure 6.6B). In particular, the correspondence is improved for the spring flood tide compared with the previous methods of calibration (Figure 5.39 and Figure 5.40). It is also worth noting that the correspondence is reasonable for both the neap and spring tide, whereas the previous methods of calibration used in Section 5.6 each improved just one of the data sets.

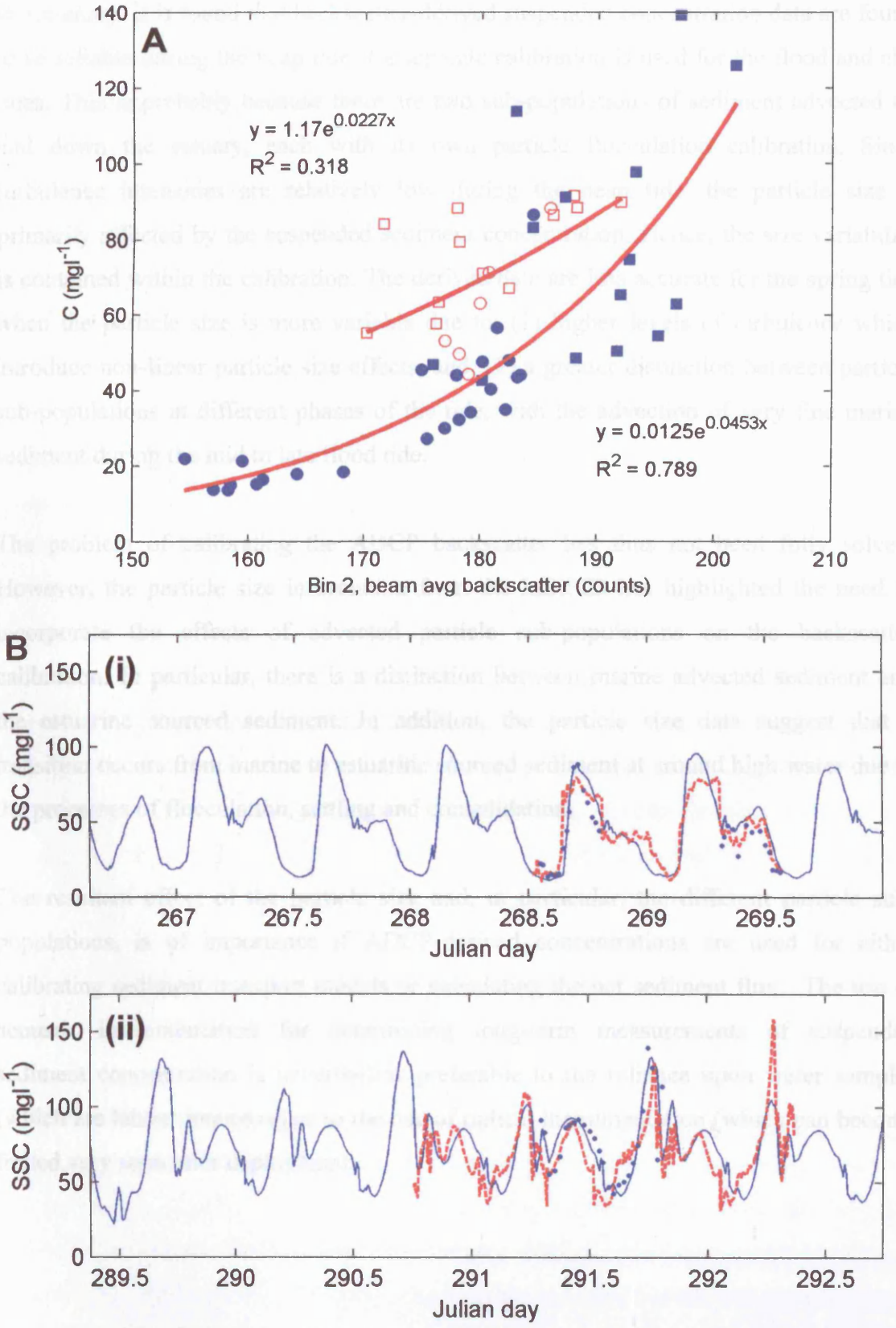

Figure 6.6 – (A) Separate estuarine and marine sourced sediment ADCP calibration for suspended sediment concentration using beam average backscatter for bin 2. (B) Modelled (solid line) and ADCP derived suspended concentrations (dashed line) for neap (i) and spring (ii) tides. Water bottle sample data are also plotted (•).

In summary, it is found that backscatter-derived suspended concentration data are found to be reliable during the neap tide if a separate calibration is used for the flood and ebb tides. This is probably because there are two sub-populations of sediment advected up and down the estuary, each with its own particle flocculation calibration. Since turbulence intensities are relatively low during the neap tide, the particle size is primarily affected by the suspended sediment concentration. Hence, the size variability is contained within the calibration. The derived data are less accurate for the spring tide when the particle size is more variable due to: (1) higher levels of turbulence which introduce non-linear particle size effects, and; (2) a greater distinction between particle sub-populations at different phases of the tide, with the advection of very fine marine sediment during the mid to late flood tide.

The problem of calibrating the ADCP backscatter has thus not been fully solved. However, the particle size information from the InSiPID has highlighted the need to incorporate the effects of advected particle sub-populations on the backscatter calibration. In particular, there is a distinction between marine advected sediment and the estuarine sourced sediment. In addition, the particle size data suggest that a transition occurs from marine to estuarine sourced sediment at around high water due to the processes of flocculation, settling and consolidation.

The resultant effect of the particle size and, in particular, the different particle sub-populations, is of importance if ADCP-derived concentrations are used for either calibrating sediment transport models or calculating the net sediment flux. The use of acoustic instrumentation for determining long-term measurements of suspended sediment concentration is nevertheless preferable to the reliance upon water samples (which are labour intensive) or to the use of optical instrumentation (which can become fouled very soon after deployment).

6.3 Future work

6.3.1 Possible improvements to the InSiPID design

With respect to any future commercial involvement, improvements to the design of the InSiPID could be made to both the software and hardware components. The main advantage of using an imaging based system means that many improvements are possible via development of the software. At present, the particle size analysis is carried out after image acquisition by a MATLAB program. This has been beneficial during the early stages of the system design due to the rapid development of the software algorithms, afforded by the interactive MATLAB environment. However, the computational inefficiency of MATLAB means that real time particle size information cannot yet be obtained from the system. Conversion of the image processing scripts to pre-compiled code would be an obvious step forward, possibly facilitating real time measurements. The image acquisition software is already written in compiled C code, thus the addition of image processing algorithms would be relatively straightforward. The ability to obtain direct measurements of particle size (and shape) information would also greatly decrease the amount of information storage space required for the measurements, thus allowing longer term monitoring of particle size. However, it should also be recognised that a record of each raw image is useful for checking for instances of fouling, or for further post-processing. In addition, the continued reduction in the price of large capacity hard disks provides the means for ample storage for thousands more images at a low cost. Currently (May 2004), the standard size of computer hard disks is ~40GB, which would hold over 250,000 images.

With increased data storage capacity and/or real time image processing, it could be envisaged that the InSiPID system could be used for longer term monitoring of particle size (and other particle characteristics). However, as with all optical systems, the main problem to overcome for long-term monitoring is fouling of the lens system by biota or detritus. Very few examples of anti-fouling devices are found in the literature, although Ridd & Larcombe (1994) describe an optical backscatter sensor with a mechanical wiper device. Even for short-term deployments, fouling may be an issue, and it is necessary for the images to be viewed on the screen during capture. It is therefore

difficult to envisage the full encapsulation of the system in the underwater housing without the need for an umbilical cable to a field computer.

The current accuracy of the calibration and validation of the InSiPID lens system has been limited due to the cost of commercially available microspheres, especially for the smaller size range. This has been partly overcome by using manually sized *Lycopodium* spores for the high magnification system. An improved calibration could be obtained if a sample of microspheres with a known particle size distribution that spans the ranges of the two cameras was used, thus providing a firmer basis for joining the two distributions. In addition, slight improvements in the calibration may be achieved by correcting for the lens distortion as part of the image processing stages.

The InSiPID hardware components could be improved further in a number of ways. First, recent advances in low-cost digital cameras may allow the system to be controlled from a laptop computer, rather than the more specialised Matrox framegrabber computer. This would significantly reduce the cost of the system for any potential customer. It would also reduce the complexity of the design and make the system more compatible in terms of integration with other field instruments.

Second, the underwater housing, which is currently made from brass and sealed with rubber gaskets, could instead be made from nylon or aluminium tubing with rubber o-ring seals to allow easier deployment and maintenance of the system. This would also increase the maximum depth rating for the system so that it could be used in larger estuaries and offshore environments.

Third, more powerful flash units could be used with automatic brightness control for taking measurements at higher suspended sediment concentrations. The maximum concentration at which size measurements can be obtained has not been fully tested, although no problems were encountered in the Blyth estuary where the maximum concentration was ~180 mgl^{-1}. However, it is likely that light attenuation would cause problems at suspended concentrations in excess of 400 to 500 mgl^{-1}.

Fourth, the InSiPID is currently not capable of measuring settling velocity. However, due to the versatility of the system it is feasible that the system could be modified to

determine the fall velocity of particles. This could be achieved using a stilling tank fitted between the camera and strobe housing of the low magnification system. The software could then be modified, perhaps using Particle Image Velocimetry (PIV) techniques (Utani & Ueno, 1991; Gui *et al*, 1997; Hart, 1998; Holland *et al*, 2001; Bradley *et al*, 2002; Creutin *et al*, 2003), to determine the settling velocity of the flocs, thus providing extra data for the calibration of the floc density model.

6.3.2 Possible improvements to the sediment transport model

The modelling of sediment transport in the Blyth estuary is still in its early stages and several emergent issues need to be addressed:

- A requirement for more extensive data sets for calibration and validation
- Parameterisation of other processes that influence sediment transport
- A move to a 3D model of sediment transport

Each of these points is discussed in more detail below.

Requirement for more extensive data sets for calibration and validation

The main requirement for improving the current sediment transport model is in the quantity and quality of data used for parameterisation of the boundary conditions. The Blyth case study has shown that possibly the most important and sensitive variable to parameterise in the sediment transport model is the critical shear velocity for erosion. Limited data are currently available for the parameterisation of this variable. Hence, a major aim of future work should be to obtain *in situ* measurements of the bed properties. Testing of extremely unconsolidated mud using *in situ* flumes is made complicated because the sediment is often too weak to take the weight of the instrument (Dearnaley *et al*, 2002). The availability of such instrumentation is also an issue. Instead, it is possible that further shear strength measurements could be obtained using shear vane data in intertidal regions. Shear strength measurements have been shown to be proportional to critical shear stress for erosion (Watts *et al*, 2003). This method

offers the additional capability of measuring the vertical profile of shear strength, which could help parameterise the layered bed model. Subtidal regions are more problematic, and perhaps more specialist equipment is required. For example, at present, no *in situ* measurement of the depth of tidally advected deposit (i.e. the bed model top layer) is available for the subtidal region of the Blyth estuary. The model suggests that most of the sediment advected with each tide is contained within the subtidal main channel. At present, there is little evidence to support this, apart from observations of a 'fluffy' layer at the top of short cores obtained in the New Cut using a Glew gravity corer (French *et al*, 2004). This could be verified relatively simply by using an underwater camera situated on, or close to, the bed with powerful illumination in order to determine an approximate depth of active sediment.

More extensive data sets of suspended sediment concentration are also required for the parameterisation, calibration and validation of the sediment transport model. In particular, concentration data are required at different locations within the estuary for improved validation of the model output. As mentioned in Section 6.2.4, concentrations in the coastal region adjacent to the mouth are likely to largely control the sediment flux during the flood tide. Thus, long term monitoring in this region is preferable, and it is desirable that future models be extended to include at least a portion of the coastal region.

Parameterisation of other processes that affect sediment transport

Further improvements in the sediment transport model may also be made by including other processes such as:

- Wind induced wave action
- Consolidation
- Biological mediation of sediment properties

The sediment transport model presented in this thesis does not take into account the effects of wind induced wave action. During both the field deployments described in the study, wind speeds were relatively low and, therefore, the effect of wind-induced waves

on the suspended concentrations was negligible. Maximum wind speeds measured by the weather station located at the northern end of the Bulcamp flats were <7 ms^{-1} during both the spring and neap tides sampled. It is likely that during stronger wind events, the resultant waves generated over the mudflats will cause greater resuspension than observed in this study. Examples of this are found in the Ems-Dollard estuary (Ridderinkhof *et al*, 2000) and the Rømø Dyb tidal area in Denmark (Lumborg & Windelin, 2003), where it has been observed that wind induced wave stress dramatically increases the concentrations over the mudflats. In the Blyth estuary, long-term meteorological observations show that the wind is predominantly from the Southwest (CE French *et al*, 2000). The East-West orientation of the estuary thus provides sufficient fetch for the generation of waves, particularly on the Bulcamp flats. Thus, wind forcing is likely to be an important factor during periods of strong wind (see also French *et al*, 2004).

A simple wave stress model, which could be applied in the future to the sediment transport model in order to test the effect of waves on the mudflats, is described by Roberts *et al* (2000). In this method, the shear stress induced by waves (τ_w) is calculated using the following formula.

$$\tau_w = \frac{1}{2}\rho f_w \frac{gH_s^2}{4h} \qquad (6.1)$$

where:

ρ = water density (kgm^{-3})
f_w = wave friction factor
g = acceleration due to gravity (ms^{-2})
H_s = significant wave height (m)
h = water depth (m)

In shallow water, the wave height is limited to half the water depth (Roberts *et al*, 2000). The wave friction factor (f_w) can only be accurately determined with *in situ* wave height and period data (Antunes Do Carmo *et al*, 2003). Therefore, a key area of future research should be to determine this value *in situ*. Assuming a value of 0.003 (which is towards the lower limit of estimated values in the literature), the wave stress can be

calculated from Equation 6.1 for each mesh node and converted to shear velocity using $u_* = \sqrt{\tau_b/\rho}$ (Figure 6.7). This is then added to the shear velocity induced by the currents (calculated from the hydrodynamic model output) to determine the erosional or depositional sediment flux. As shown in Figure 6.7, despite the low friction factor, the shear velocity induced by a 0.3 m wave in 1 m of water is high enough to initiate erosion of on the mudflats (assuming a critical shear velocity of erosion of 0.02 ms^{-1}).

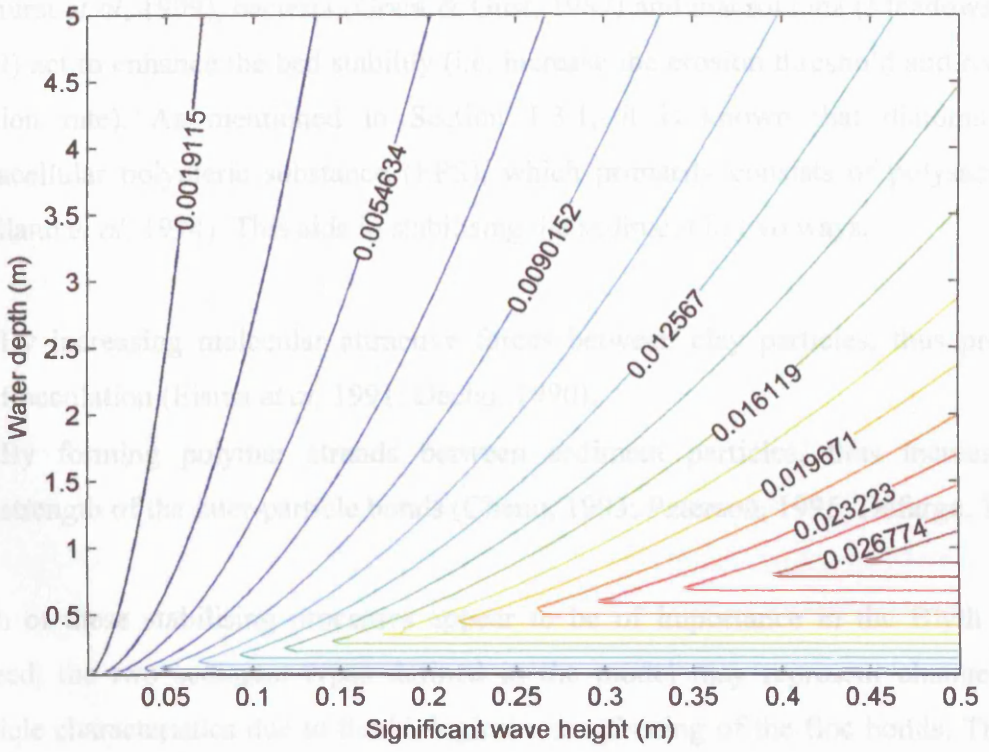

Figure 6.7 – Shear velocity induced at the bed by wind induced waves, calculated using Equation 5.11 ($f_w = 0.003$). Wave heights are limited to half the water depth.

For longer term modelling, the development of a sediment transport model spanning an entire spring to neap tidal cycle would require a time-variable consolidation model. This would be relatively simple to include in the present layered bed model by introducing a time limit, after which sediment in the top layer is moved to a lower, more consolidated layer. However, calibration of this type of model requires a more detailed investigation of the spatial and temporal variability in shear strength.

The bed model (and possibly the flocculation model) could also be extended to include biological effects. The contribution of biota to intertidal sediment dynamics is well-documented (Paterson, 1994, 1997; Tolhurst *et al*, 2002). Different organisms may act either to stabilise or destabilise the bed material. Bioturbation by meio- and macro-benthos results in destabilisation of the sediment due to an increase in in the water content or changes to the micro-topography (Davis, 1993; de Deckere *et al,* 2001) and indirectly by grazing on organisms that stabilise the sediment (Gerdol & Hughes, 1994; de Deckere *et al*, 2000, 2002). Intertidal organisms such as diatoms (Paterson, 1989; Tolhurst *et al*, 1999), bacteria (Grant & Gust, 1987) and macrofauna (Meadows & Tait, 1989) act to enhance the bed stability (i.e. increase the erosion threshold and reduce the erosion rate). As mentioned in Section 1.3.1, it is known that diatoms secrete extracellular polymeric substance (EPS), which primarily consists of polysaccharides (Holland *et al,* 1974). This aids in stabilising the sediment in two ways:

- By increasing molecular attractive forces between clay particles, thus promoting flocculation (Eisma *et al,* 1991; Decho, 1990).
- By forming polymer strands between sediment particles, thus increasing the strength of the inter-particle bonds (Chenu, 1993; Paterson, 1995; Défarge, 1997).

Both of these stabilising processes appear to be of importance in the Blyth estuary. Indeed, the two sediment types defined in the model may represent changes in the particle characteristics due to the biological strengthening of the floc bonds. Therefore, it is possible that the estuarine sourced sediment contains higher quantities of EPS, thus making it more flocculative. In fact, the method of changing the marine sourced sediment into estuarine sediment on deposition appears partially to account for these effects. This requires further investigation. In particular, measurements of the quantity of EPS in the marine and estuarine sourced sediment could provide evidence for this process.

Move to a 3D model of sediment transport

The model in this project has been restricted to a depth-averaged 2D formulation primarily because of the large computational overheads required for modelling the

expansive mudflat regions. As discussed in the Chaper 1, the transport of cohesive sediment is complicated due to the processes of flocculation, consolidation and the possible formation of fluid mud. Consequently, the vertical profile of suspended concentration cannot be modelled very accurately using a simple profile such as described by the Rouse equation. Therefore, improvements may be made by moving to a 3D model. However, vertical layering of the suspended concentration over the mudflats is likely to have a negligible effect on the sediment flux due to the shallow water depths and low flow speeds. In addition, the present model shows that most of the sediment is transported within the main channel. Therefore, it is envisaged that the 2D model output could be used to provide flow and concentration boundary conditions for the 3D model at the breaches and the channel cut-off points. The removal of the mudflat regions from the 3D model would greatly reduce the number of elements in the model mesh, thereby reducing model run-time considerably. The coupling of two models in this way is therefore considered a reasonable compromise between computational overheads and model accuracy.

The use of a 3D model could reduce the phase difference between modelled and observed suspended concentrations by simulating any vertical variability in the main channel. Phase errors are particularly noticeable during the spring flood tide. This is possibly caused by the erosion of sediment from the shallower regions on the channel margins, thus increasing the concentration in the surface waters. The combination of an inverse concentration profile and large water depth is likely to lead to a reduction in total mass of sediment reaching the bed at high water, thus causing the phase differences between the observed and modelled concentrations. This requires further examination.

The settling velocity model described in this thesis is well-suited for use in a 3D model. This is because a 3D model requires a knowledge of the settling velocity throughout the whole tidal cycle in order to calculate the shape of the vertical suspended concentration profile, whereas 2D models only need to know the settling rate during slack water. In the current model, depth variability has not been simulated and, therefore, the depth averaged turbulence dissipation parameter (G) is used (Equation 5.3). For 3D applications, the particle size model could simply be modified to use the depth dependent version of the equation, written as:

$$G = \left(\frac{u_*^3}{\kappa \cdot \nu \cdot z} \right)^{0.5} \qquad (6.2)$$

where:

u_* = shear velocity (ms^{-1})

κ = von Karman constant (0.41)

ν = kinematic viscosity ofwater (10^{-6})

z = height above the bed (m)

In this form, the particle size model could be applied at each height in the water column. Vertical modelling of settling velocity may also allow the parameterisation of hindered settling, fluid mud formation and associated buoyancy effects on the flow, as discussed in Chapter 1. However, since concentrations are generally less than 200 mgl^{-1} in the Blyth, these processes are likely to be of little importance. It is interesting to note, however, that the spring tide hydrodynamic model does not drain completely to observed levels. It is possible that more efficient draining of the real estuary may be caused by a reduction in the apparent bed roughness due to the higher suspended concentrations at the end of the ebb tide, thus introducing buoyancy effects on the flow. The 3D version of SUBIEF (called SEDI3D) allows this feedback process to be incorporated into the model by performing the sediment transport calculations at the same time as the hydrodynamic model (Le Normant, 1998). Unfortunately, this also increases the run time for each model, making it less feasible for applications with a large mesh (such as the Blyth).

With respect to further 2D modelling, it may be possible to simplify the settling velocity model further. Probably the most commonly used method of parameterising settling velocity in 2D models is simply to calculate it using a power law, proportional to suspended sediment concentration. The validity of this approach can be tested by plotting the suspended concentration data against the particle size calibration coefficient (Figure 6.8A). Since it is assumed that settling only occurs below a critical value of shear velocity (u_{*cd}), most of the particle size information is in fact redundant (the useful data are plotted as solid markers). In addition, because this value of u_{*cd} is relatively low (<0.01) the effects of turbulence are negligible and, therefore, the particle size

calibration coefficient can be modelled directly in proportion to the suspended concentration using a power law fit ($R^2 = 0.97$). Therefore, it is possible that the settling velocity could be parameterised solely in proportion to suspended concentration, as shown in Figure 6.8B. By substituting the power law regression curve from Figure 6.8 into the density adjusted Stokes' Law (Equation 5.12), the settling velocity (in mms^{-1}) can then be redefined as:

$$w_s = 0.0282C^{0.7794} \tag{6.3}$$

where:

C = suspended sediment concentration (mgl^{-1})

This approach is only suitable for two dimensional models that do not consider the shape of the vertical concentration profile. It should also be noted that this model does not take into account the differences between the two sediment types advected between flood and ebb. Such differences may be missed if using such a simple model due to the small number of data points (as observed in Figure 6.8B).

Consequently, it is concluded that measurement of the *in situ* particle size, using instrumentation such as the InSiPID, is of great benefit for sediment transport modelling due to the capacity to understand and model changes in sediment properties caused by the advection of particle sub-populations from different regions. Further investigations are needed in which accurate measurements of particle size are obtained in order to parameterise temporal changes in floc characteristics.

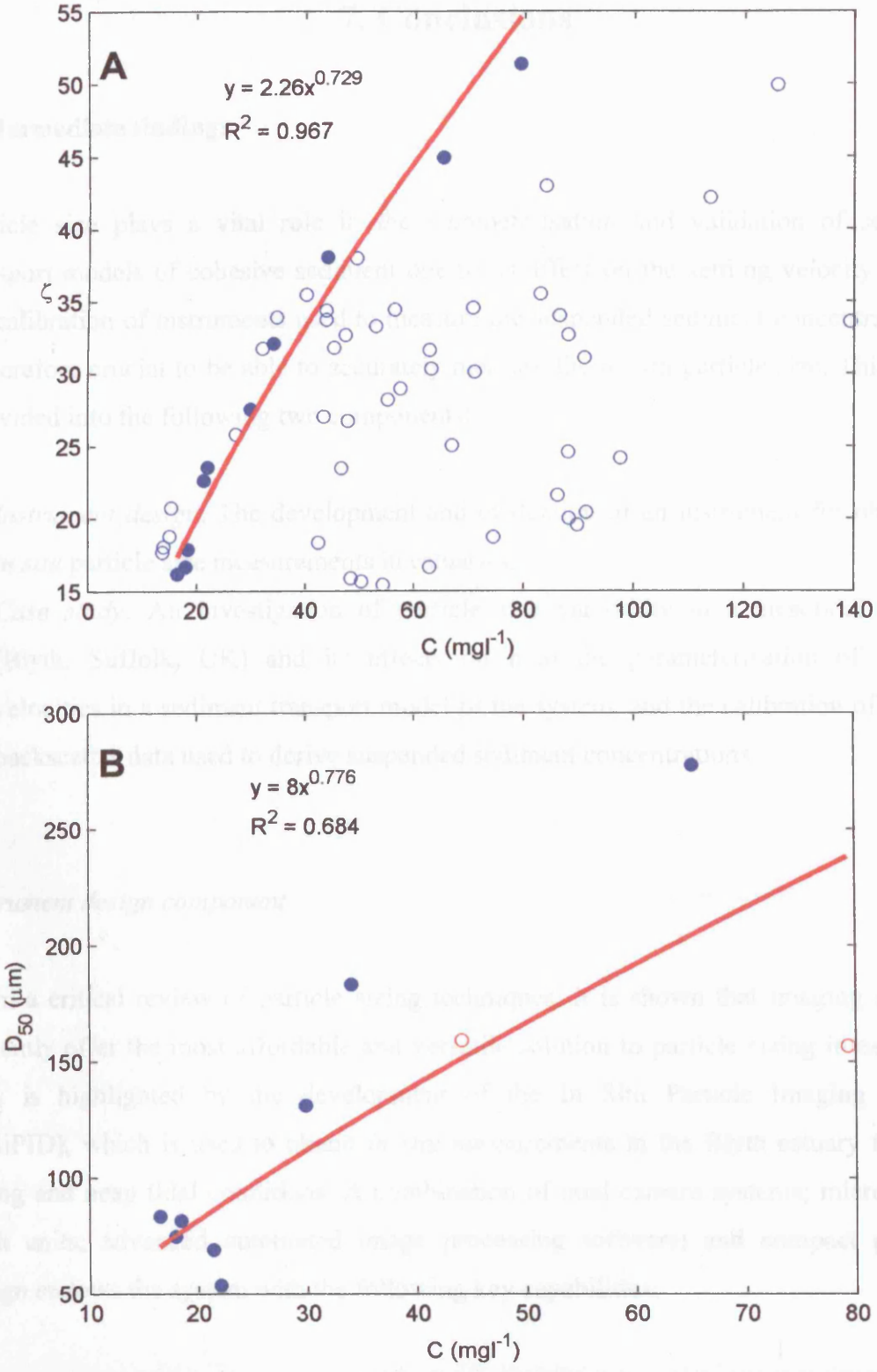

Figure 6.8 – (A) Suspended sediment concentration versus particle size calibration coefficient (ζ) with a power law regression fitted to data below the critical shear velocity, u_{*cd} = 0.01 ms^{-1} represented by filled markers (B) Suspended sediment concentration versus D_{50} for data below u_{*cd} = 0.01 ms^{-1}, with a power law regression line fitted through the data. The unfilled markers in graph B define mid to late flood tide data, indicating the requirement for two separate calibrations.

7. Conclusions

7.1 Immediate findings

Particle size plays a vital role in the parameterisation and validation of sediment transport models of cohesive sediment due to its affect on the settling velocity and on the calibration of instruments used to measure the suspended sediment concentration. It is therefore crucial to be able to accurately measure the *in situ* particle size. This thesis is divided into the following two components:

(1) *Instrument design*: The development and evaluation of an instrument for obtaining *in situ* particle size measurements in estuaries.
(2) *Case study*: An investigation of particle size variability in a mesotidal estuary (Blyth, Suffolk, UK) and its effects on both the parameterisation of settling velocities in a sediment transport model of the system, and the calibration of ADCP backscatter data used to derive suspended sediment concentrations.

Instrument design component

From a critical review of particle sizing techniques, it is shown that imaging systems currently offer the most affordable and versatile solution to particle sizing in estuaries. This is highlighted by the development of the In Situ Particle Imaging Device (InSiPID), which is used to obtain *in situ* measurements in the Blyth estuary for both spring and neap tidal conditions. A combination of dual camera systems; microsecond flash units; advanced automated image processing software; and compact portable design endows the system with the following key capabilities:

- high measurement accuracy (±0.4% FS)
- high precision (~10,000 particles counted for each measurement)
- wide size range (4-3000 μm)
- high sample rate (10 images s^{-1})
- the ability to be deployed from a small boat

These are all achieved at a low cost (<£5000) due to the use of commercially available components. The software-based approach means that most of the system development time is dedicated to programming of image processing algorithms. In particular, a novel image segmentation method is developed based on the coincidence between the detected particle edge pixels and possible particles in the binary image formed at a range of intensity thresholds. This reliance on software means that future improvements may be effected at little extra cost by improving the algorithms.

Blyth estuary case study

Data obtained from the InSiPID are used to derive a semi-empirical model of particle size variability. Floc size is shown to be mainly dependent on the following variables:

- turbulence (represented by the dissipation parameter, G)
- suspended sediment concentration

The InSiPID size measurements also indicate the presence of two distinct particle sub-populations, one sourced from local resuspension within the estuary (*estuarine sourced*) and the other, less flocculated, population introduced at the mouth of the estuary (*marine sourced*). These affect the calibration of the flocculation model at different stages of the tidal cycle. It is hypothesised that the distinction between the two sediment types is caused by: (1) consolidation of the flocs in the bed due to the weight of overlying sediment, thus forming stronger flocs; (2) the presence of microscopic benthic organisms in the estuarine sediment which cause an increase in the cohesive properties of the flocs by secreting sticky organic compounds (Extracellular Polymeric Substance) and forming polysaccharide fibrous bonds between particles.

The flocculation model is used to improve the parameterisation of settling velocity in a sediment transport model of the Blyth estuary. Two tracers are applied to the model, representing the two mentioned sediment types. The initial bed deposits are comprised entirely of the estuarine sourced sediment. The marine sourced sediment is introduced at the seaward boundary during the model run. On settling to the bed, the marine sourced sediment is converted to estuarine sourced sediment. Settling velocity data are derived

from the modelled floc size for each tracer using Stokes' Law. Variability in the floc density with size is modelled using a simple power law relationship based on previous investigations by a number of authors. Incorporation of the settling velocity model improves the similarity between modelled and observed concentrations at Reydon in comparison to using a fixed value. This approach to modelling settling velocity is similar to that of Winterwerp (1998), but the following differences make the new method simpler to implement in a sediment transport model:

- the flocculation model, which is similar to that of van Leussen (1994), is more practical to implement through empirical calibration with particle size data from the InSiPID.
- calibration of the flocculation model is also aided by the ability to manually define the location of the flocculation peak, with respect to turbulence and suspended concentration (not included in van Leussen's model).
- the modelled flocculation maximum moves towards higher levels of turbulence at lower suspended concentrations to emulate an increase in the *time of flocculation* (as used in Winterwerp's model).
- the floc density model is simplified by using an average floc density power law equation, which can be iteratively adjusted during the calibration of the sediment transport model (not included in Winterwerp's model).

It is argued that direct measurements of settling velocity from currently available instruments are compromised because:

- removal of the particles from the turbulent estuarine environment results in aggregation or break up of the fragile flocs.
- the presence of small scale convectional flow in settling tubes may influence the settling velocity of individual particles (even resulting in apparently negative velocities).
- observations are limited to a very small subsection of particles (and usually in the larger sizes).
- the mechanical nature of such designs means that they are large, are liable to failure, have high power requirements and are expensive.

Consequently, settling velocity measurements are both expensive and unreliable. In addition, distinctions between different sediment populations may be missed due to the poor precision and size range of the measurements. The InSiPID instrument, however, provides accurate *in situ* measurements of the full size range (4-3000 μm) at a high sample rate (~20 minute sample interval) and at a low cost (<£5000). By concentrating on *in situ* measurements of particle size rather than on settling velocity, a greater number of particles can be counted (>10,000), thus increasing the precision of the measurements and providing a firmer basis for modelling. It is therefore argued that the use of a semi-empirical model of settling velocity derived from particle size data is perhaps preferential to using a direct empirical model derived from settling velocity data due to the greater reliability of the *in situ* measurements.

The performance of the sediment transport model is also strongly influenced by the parameterisation of critical shear velocity for erosion (u_{*ce}). This is parameterised zonally using a two-layer bed model, with a less resistant top layer overlying a more consolidated lower layer. Differences are observed in both the vertical and horizontal distribution of the critical shear velocity for erosion between spring and neap tides. In particular, the value for u_{*ce} for the top layer increases in the subtidal regions during the neap tide, possibly as a result of consolidation of the bed material. In addition, there is speculative evidence (based solely on model calibration) for the movement of a pool of poorly consolidated sediment within the main tidal channel from up-estuary during the spring tide to a position further downstream (near to Reydon) during the neap tide.

The combined analysis of *in situ* particle size and SSC data show that particle size variability has a significant affect on the ADCP backscatter calibration for suspended concentration. Although flocculation of the particles is most significant at around slack water, the variability in the backscatter calibration during these periods is unlikely to significantly affect calculations of the net sediment flux. However, the presence of small marine sourced particles during the flood tide leads to an underestimation of the sediment input into the estuary if a single backscatter calibration is used for the entire tidal cycle. Improved agreement with observations is obtained by using separate calibrations for flood and ebb. This is further improved using a novel method whereby a switch in the ADCP calibration is timed to occur at the transition between marine sourced sediment (input at the mouth on the flood tide) and resuspended estuarine bed

sediment. The switch between the calibrations is provided by the relative concentrations of each tracer in the sediment transport model output. This method appears to improve the comparison between ADCP derived concentrations and observations from water bottle samples, but further data are needed to verify this.

7.2 Further work

Possible improvements to the InSiPID system are as follows:

- rewriting the image processing algorithms in pre-compiled code to provide real time measurements of particle size and shape.
- moving to a fully digital laptop-based system with larger data storage.
- improving the lens optics and calibration methods to provide better size measurements and perhaps enable fractal dimension measurements (which are currently not possible due to poor image resolution and defocusing).
- designing an improved underwater housing and illumination system to allow measurements in deeper and more turbid estuaries.
- adapting the system to provide measurements of settling velocity.

Further work is also required in monitoring and modelling of estuarine sediment transport processes, such as:

- acquiring more extensive ADCP and InSiPID data in order to improve the calibration of acoustic backscatter for suspended sediment concentration and to better validate the flocculation model
- obtaining more extensive measurements of the bed properties (in particular u_{*ce}) for better parameterisation in the sediment transport model.
- explaining the differences in the particle sub-populations, perhaps by measuring the quantities of EPS in both the bed deposits and the suspended sediment.
- moving to a 3D model of sediment transport to account for vertical structuring of the suspended concentrations and particle size, and include buoyancy effects.

Acknowledgements

This project was funded by the EPSRC in partnership with Sira Ltd. (Kent) and the University College London (Geography Department). I would particularly like to thank my current supervisor Dr Jon French (Coastal & Estuarine Research Unit, UCL) for his on-going support, thoughts and boat driving skills. Thanks also to my previous supervisor Dr Neil Stewart (Sira Ltd.) for aiming me in the right direction. A special thanks also goes to Dr Dan Robinson and David Gasca Tucker for their tireless efforts and humour when out in the field; Dr Helene Burningham for the helpful discussions over coffee; Janet Hope and Ian Patmore for their help in the laboratory; and Neil for his help in the Sira workshop. Finally, I would like to thank Outi for her love and support through the final stages.

References

ADDISON, P.S. (1997) *Fractals and Chaos: an Illustrated Course.* Institute of Physics Publishing, Philadelphia, 250 pp.

AGRAWAL, Y.C. & H.C. POTTSMITH (1994) Laser diffraction particle sizing in STRESS. *Continental Shelf Research,* **14,** 1101-21.

AGRAWAL, Y.C. & H.C. POTTSMITH (2000) Instruments for particle size and settling velocity observations in sediment transport. *Marine Geology,* **168,** 89-114.

AL ANI, S., K.R. DYER & D.A. HUNTLEY (1991) Measurement of the influence of salinity on floc density and strength. Geo-Marine Letters, **11,** 154–8.

ALAM, MD. F. & K.J. THOMSON (2001) Current constraints and future possibilities for Bangladesh fisheries. *Food Policy,* **26,** 297-313.

ALLDREDGE, A.L. & C. GOTSCHALK (1988) In situ settling behaviour of marine snow. *Limnological Oceanography,* **33,** 339–51.

AMOS, C.L., J. GRANT, DABORN, G.R. & K. BLACK (1992) Sea Carousel – a benthic, annular flume. *Estuarine and Coastal Shelf Science,* **34,** 557-77.

ANTUNES DO CARMO, J.S., A. TEMPERVILLE & F.J. SEABRA-SANTOS (2003) Bottom friction and time-dependent shear stress for wave-current interaction. *Journal of Hydraulic Research,* **41,** 27-37.

ARCEMENT, G.J. JR. & V.R. SCHNEIDER (1989) Guide for selecting Manning's roughness coefficients for natural channels and flood plains. *United States Geological Survey. Water-Supply Paper 2339.*

ARCHAMBAULT, M-C., J. GRANT & A. HATCHER (2001) The small volume particle microsampler (SVPM): a new approach to particle size distribution and composition. *Deep-Sea Research I,* **48,** 2331-46.

ARGAMAN, Y. & W.J. KAUFMAN (1970) Turbulence and flocculation. *Journal of Sanitary Engineering,* ASCE, **96,** 223-41.

ARIATHURAI, R. & R.B. KRONE (1976) Finite element model for cohesive sediment transport. *Journal of the Hydraulics Division,* ASCE, **102**(HY3), 323-38.

ARRIAGA, L., M. MONTAÑO & J. VÁSCONEZ (1999) Integrated management perspectives of the Bahía de Caráquez zone and Chone River estuary, Ecuador. *Ocean & Coastal Management,* **42,** 229-41.

ASHJIAN, C.J., C.S. DAVIS, S.M. GALLAGER & P. ALATALO (2001) Distribution of plankton, particles, and hydrographic features across Georges Bank described using the Video Plankton Recorder. *Deep-Sea Research II,* **48,** 245-82.

ASPER, V.L. (1987) Measuring the flux and sinking speed of marine snow aggregates. *Deep Sea Research,* **34,** 1-17.

BAKER, E.T. & J.W. LAVELLE (1984) The Effect of Particle Size on the Light Attenuation Coefficient of Natural Suspensions. *Journal of Geophysical Research,* **89,** 8197-203.

BALE, A.J. & A.W. MORRIS (1987) In-situ measurement of particle size in estuarine waters. *Estuarine, Coastal & Shelf Science,* **24,** 253-63.

BALE, A.J., R.J. UNCLES, J. WIDDOWS, M.D. BRINSLEY & C.D. BARRETT (2002) Direct observation of the formation and break-up of aggregates in an annular flume using laser reflectance particle sizing. In: J.C. Winterwerp & C. Kranenburg (Eds.) *Fine Sediment Dynamics In The Marine Environment,* proceedings of the 6th International Conference on Nearshore and Estuarine Cohesive Sediment Transport Processes (INTERCOH 2000), Delft. Elsevier Science, London. 189-201.

BARROS, A.P. (1996) An evaluation of model parameterizations of sediment pathways: A case study for the Tejo estuary, *Continental Shelf Research,* **16,** 1725-49.

BARTH, G.H. (1984) *Modern Methods of Particle Size Analysis.* (Chemical Analysis, vol.73), John Wiley & Sons, Chichester.

BARTZ, R., J.R.V. ZANEVELD, I.N. MCCAVE, F.R. HESS & A.R.M. NOWELL (1985) ROST and BEAST - Devices for in situ measurement of particle settling velocity. *Marine Geology*, **66**, 381-95.

BATES, P.D., M.G. ANDERSON, D.A. PRICE, R.J. HARDY & C.N. SMITH (1996) Analysis and development of hydraulic models for floodplain flows. In: Anderson, D.E. Walling, P.D. Bates (Eds.) *Floodplain Processes*, Wiley, Chichester, 215-54.

BEARDALL, C.H., R.C. DRYDEN & T.J. HOLZER (1991) *The Suffolk Estuaries*. Segment: Suffolk.

BELLOUTI, M., M.M. ALVES, J.M. NOVAIS & M. MOTA (1997) Flocs vs granules: differentiation by fractal dimension. *Water Research,* **31**, 1227-31.

BENFIELD, M.C., C.S. DAVIS, P.H. WIEBE, S.M. GALLAGER, R.G. LOUGH & N.J. COPLEY (1996) Video Plankton Recorder estimates of copepod, pteropod and larvacean distributions from a stratified region of Georges Bank with comparative measurements from a MOCNESS sampler. *Deep-Sea Research II,* **43**, 1925-45.

BENFIELD, M.C., P.H. WIEBE, T.K. STANTON, C.S. DAVIS, S.M. GALLAGER & C.H. GREENE (1998) Estimating the spatial distribution of zooplankton biomass by combining Video Plankton Recorder and single-frequency acoustic data. *Deep-Sea Research II,* **45**, 1175-99.

BERGERON, E., A.D. BOWE, W.J. HERSEY, W.N. LANGE & J.R. STRICKLER (1988) Reaching the ultimate goal: observing live zooplankton in situ. *EOS*, **69**, 1087.

BEUSELINCK, L., G. GOVERS, J. POESEN, G. DEGRAER & L. FROYEN (1998) Grain-size analysis by laser diffractometry: comparison with the sieve-pipette method. *Catena,* **32**, 193-208.

BHAGAT, R.P. (1996) Settling test and size determination - loading effect in settling of unflocculated particles and their size distribution. *Scandinavian Journal of Metallurgy*, **25**(2), 48-50.

BLACK, K. & A. CRAMP (1995) A device to examine the in situ response of intertidal cohesive sediment deposits to fluid shear. *Continental Shelf Science,* **15**, 1945-54.

BRADLEY, A.A., A. KRUGER, E.A. MESELHE, & M.V.I. MUSTE (2002) Flow measurement in streams using video imagery, *Water Resources Research,* **38**, 1315.

BREW, D.S., B.M. FUNNELL & A. KREISER (1992) Sedimentary environments and Holocene evolution of the lower Blyth estuary, Suffolk (England), and a comparison with other East Anglian coastal sequences. *Proceedings of the Geological Association,* **103**, 57-74.

BRINK, A.D. & N.E. PENDOCK (1996) Minimum cross-entropy threshold selection, *Pattern Recognition,* **29**, 179-88.

BROOKS, A.N. & T.J.R. HUGHES (1982) Streamline Upwind/Petrov Galerkin formulations for convection dominated flows with particular emphasis on the incompressible Navier-Stokes equations. *Computer Methods in Applied Mechanics and Engineering,* **32**, 199-259.

BUNT, J.A.C, P. LARCOMBE & C.F. JAGO (1999) Quantifying the response of optical backscatter devices and transmissometers to variations in suspended particulate matter. *Continental Shelf Research,* **19**, 1199-220.

BURT, N., PARKER, R. & WATTS, J. (1997) Cohesive sediments : 4th Nearshore and Estuarine Cohesive Sediment Transport Conference, Wiley, Chichester, 458 p.

CALLAWAY, R.J., A.M. TEETER, D.W. BROWNE & G.R. DITSWORTH (1976) Preliminary analysis of the dispersion of sewage sludge discharged from vessels to New York Bight waters, *American Society of Limnology & Oceanography Special Symposium,* **2**, 240-8.

CAMERON, W.M. & D.W. PRITCHARD (1963) Estuaries. In: *The Sea,* **2**, ed. M.N. Hill, 306-24. John Wiley and Sons, New York.

CANCINO, L. & R. NEVES (1994) 3D-numerical modelling of cohesive suspended sediment in the Western Scheldt estuary (The Netherlands). *Netherlands Journal of Aquatic Ecology*, **28**, 337-45.

CANCINO, L. & R. NEVES (1999a) Hydrodynamic and sediment suspension modelling in estuarine systems, Part I: Description of numerical models. *Journal of Marine Systems,* **22**, 105-16.

CANCINO, L. & R. NEVES (1999b) Hydrodynamic and sediment suspension modelling in estuarine systems, Part II: Application to the Western Scheldt and Gironde estuaries . *Journal of Marine Systems,* **22**, 117-31.

CARDER, K.L. (1979) Holographic microvelocimeter for use in studying ocean particle dynamics. *Optical Engineering,* **18**, 524-5.

CARDER, K.L., R.G. STEWART & P.R. BETZER (1982) In situ holographic measurements of the sizes and settling rates of oceanic particles. *Journal of Geophysical Research,* **87**, 5681-5.

CARLOTTO, M.J. (1997) Histogram analysis using a scale-space approach, *IEEE Transcripts on Pattern Analysis and Machine Intelligence,* **9**, 121-9.

CHADWICK, A. & J. MORFETT (1998) *Hydraulics in civil and environmental engineering. (3rd edition),* E & FN Spon, London.

CHALMERS, N. & P. PARKER (1986) *The OU Project Guide; Fieldwork and Statistics for Ecological Projects,* Field Studies Council Occasional Publication No. 9, Dorchester, 108pp.

CHEN, CHENG-LUNG (1991) Unified theory on power laws for flow resistance. *Journal of Hydraulic Engineering,* **117**, 371-89.

CHEN, S. & D. EISMA (1995) Fractal geometry of in situ flocs in the estuarine and coastal environments. *Netherlands Journal of Sea Research*, **32**, 173 –82.

CHEN, S., D. EISMA & J. KALF (1994) In situ distribution of suspended matter during the tidal cycle in the Elbe estuary. *Netherlands Journal of Sea Research*, **32**, 37-48.

CHENG, H.D., Y.H. CHEN & Y. SUN (1999) A novel fuzzy entropy approach to image enhancement and thresholding, *Signal Processing,* **75**, 277-301.

CHENG, S.C. & W.H. TSAI (1993) A neural network approach of the moment-preserving technique and its application to thresholding, *IEEE Transactions on Computers,* **42**, 501-7.

CHENU, C. (1993) Clay- or sand-polysaccharide associations as models for the interface between micro-organisms and soil: water related properties and microstructure, *Geoderma*, **56**, 143-56.

CHOW, VEN TE (1959) *Open Channel Hydraulics*, McGraw-Hill, Tokyo.

CIFFROY, C., C. MOULIN & J. GAILHARD (2000) A model simulating the transport of dissolved and particulate copper in the Seine river. *Ecological Modelling,* **127**, 99-117.

CLARKE, S. & A.J. ELLIOTT (1998) Modelling suspended sediment concentrations in the Firth of Forth. *Estuarine Coastal and Shelf Science*, **47**, 235-50.

CLIFFORD, N.J., K.S. RICHARDS, R.A. BROWN & S.N. LANE (1995) Laboratory and field assessment of an infrared turbidity probe and its response to particle size and variation in suspended sediment concentration. *Hydrological Sciences Journal*, **40**, 771-91.

CORNELISSE, J.M. (1996) The field pipette withdrawal tube (FIPIWITU). *Journal of Sea Research,* **36**, 37-9.

CRAWFORD, A.M. & A.E. HAY (1993) Determining suspended sand size and concentration from multifrequency acoustic backscatter. *Journal of the Acoustical Society of America,* **94**(6), 3312-24.

CREUTIN, J.D., M. MUSTE, A.A. BRADLEY, S.C. KIM & A. KRUGER (2003) River gauging using PIV techniques: a proof of concept experiment on the Iowa River, *Journal of Hydrology*, **277**, 182-94.

DALRYMPLE, R.W., ZAITLIN, B.A., BOYD, R. (1992) A conceptual model of estuarine sedimentation. *Journal Sedimentary Petrology*, **62**, 1130-46.

DARBYSHIRE, E.J. & J.R. WEST (1993) Turbulence and cohesive sediment transport in the Parrett estuary. In: Clifford, N.J., J.R. French & J. Hardisty (Eds.) *Turbulence: Perspectives and sediment transport.* Wiley, London.

DAVIES, J.L. (1964) A morphogenetic approach to world shorelines. *Zeitschrift fur Geomorphologie* **8**, 127-42.

DAVIS, C.S., S.M. GALLAGER, M. MARRA & W.K. STEWART (1996) Rapid visualisation of plankton abundance and taxonomic composition using the Video Plankton Recorder. *Deep-Sea Research II,* **43**, 1947-70.

DAVIS, C.S., S.M. GALLAGER, M.S. BERMAN, J.R. HAURY & J.R. STRICKLER (1992) The Video Plankton Recorder (VPR): design and initial results. *Archiv fèur Hydrobiologie Beiheft, Ergebnisse der Limnologie,* **36**, 67-81.

DAVIS, W.R. (1993) The role of bioturbation in sediment resuspension and its interaction with physical shearing, *Journal of experimental Marine Biology and Ecology,* **171**, 187-200.

DE DECKERE, E.M.G.T., B.A. KORNMAN, N. STAATS, G.R. TERMAAT, B. DE WINDER, L.J. STAL & C.H.R. HEIP (2002) The seasonal dynamics of benthic (micro) organisms ans extracellular carbohydrates in an intertidal mudflat and their effect on the concentration of suspended sediment. In: J.C. Winterwerp & C. Kranenburg (Eds.) *Fine Sediment Dynamics In The Marine Environment*, proceedings of the 6th International Conference on Nearshore and Estuarine Cohesive Sediment Transport Processes (INTERCOH 2000), Delft. Elsevier Science, London. 429-39.

DE DECKERE, E.M.G.T., J. VAN DE KOPPEL & C.H.R HEIP (2000) The influence of *Corophium volutator* abundance on resuspension, *Hydrobiologica*, **426**, 37-42.

DE DECKERE, E.M.G.T., T.J. TOLHURST & J.F.C. DE BROUWER (2001) Destabilisation of muddy intertidal sediments by benthos, *Estuarine, Coastal & Shelf Science,* **53**, 665-9.

DE JONGE, V.N. (2000) Importance of temporal and spatial scales in applying biological and physical process knowledge in coastal management, an example for the Ems estuary. *Continental Shelf Research,* **20**, 1655-86.

DE VRIEND, H.J., M. CAPOBIANCO, T. CHESHER, H.E. DE SWART, B. LATTEUX & M.J.F. STIVE (1993) Approaches to long-term modelling of coastal morphology: a review. *Coastal Engineering*, **21**, 225-69.

DE VRIES, M., G.J. KLASSEN & N. STRIKSMA (1989) On the use of moveable bed models for river bed problems: state of art. *Symposium of River Sedimentation,* Beijing, China.

DEARNALEY, M.P., W. ROBERTS, S. JONES, K.C. LEURER, D.G. LINTERN, L.M. MERCKELBACH, G.C. SILLS, E.A. TOORMAN & J.C. WINTERWERP (2002) Measurement and modelling of the properties of cohesive sediment deposits. In: J.C. Winterwerp & C. Kranenburg (Eds.) *Fine Sediment Dynamics In The Marine Environment*, proceedings of the 6th International Conference on Nearshore and Estuarine Cohesive Sediment Transport Processes (INTERCOH 2000), Delft. Elsevier Science, London. 57-74.

DECHO, A.W. (1990) Microbial exopolymer secretions in ocean environments: Their role(s) in food webs and marine processes, *Ocean and Marine Biology Annual Review,* **28**, 73-153.

DÉFARGE, C. (1997) Cryoscanning electron microscopy and high resolution scanning electron microscopy of organic matter and organomineral associations in modern microbial sediments, *Geomat. Pet. Sed.*, **324**, 553-61.

DELO, E.A. (1988) Estuarine muds manual. *Hydraulics Research*,Wallingford. Report No. SR164, 23–6.

DENNIS, J.M., J.R. SPEARMAN & M.P. DEARNALEY (2000) The development of a regime model for prediction of the long-term effects of civil engineering activities on estuaries, *Physics & Chemistry of the Earth, Part B - Hydrology Oceans and Atmosphere,* **25**, 45-50.

DIDDEN, N. (1987) Performance evaluation of a shipboard 115 kHz acoustic Doppler current profiler. *Continental Shelf Research*, **7**, 1231-1243.

DRAKE, D.E., R.L. KOLPACK & P.J. FISCHER (1972) Sediment transport on the Santa Barbara-Oxnard shelf, Santa Barbara Channel, California. In: Swift, D.J.P., D.B Duane, O.H. Pilkey (Eds.) *Shelf Sediment Transport.* Dowden, Hutchinson and Ross, Stroudsberg, 307-31.

DROPPO, I.G., G.G. LEPPARD, D.T. FLANNIGAN & S.N. LISS (1997) The freshwater floc: a functional relationship of water and organic and inorganic floc constituents affecting suspended sediment properties. *Water, Air and Soil Pollution*, **99**, 43-54.

DWORSKI, J.G. & D.R. JACKSON (1994) Spatial and temporal variation of acoustic backscatter in the stress experiment. *Continental Shelf Research,* **14**, 1221 *et seq.*

DYER, K.R. & A.J. MANNING (1999) Observation of the size, settling velocity and effective density of flocs, and their fractal dimensions. *Journal of Sea Research,* **41**, 87-95.

DYER, K.R. & E.M. EVANS (1989) Dynamics of turbidity maximum in a homogenous tidal channel. *Journal of Coastal Research*, Special issue No. 5, 23-30.

DYER, K.R. (1980) Velocity profiles over a rippled bed and the threshold of movement of sand. *Estuarine and Coastal Marine Science,* **10**, 184-99.

DYER, K.R. (1986) *Coastal and Estuarine Sediment Dynamics.* Wiley-Interscience Publication, 342 pp.

DYER, K.R. (1989) Sediment processes in estuaries: future research requirements. *Journal of Geophysical Research,* **94** , 14327–39.

DYER, K.R. (1997) *Estuaries: a physical introduction,* 2nd Ed., John Wiley & Sons, Chichester, 195 pp.

DYER, K.R., A.J. BALE, M.C. CHRISTIE, N. FEATES, S. JONES & A.J. MANNING (2002) The turbidity maximum in a mesotidal estuary, the Tamar estuary, UK: II. The floc properties. In: J.C. Winterwerp & C. Kranenburg (Eds.) *Fine Sediment Dynamics In The Marine Environment*, proceedings of the 6th International Conference on Nearshore and Estuarine Cohesive Sediment Transport Processes (INTERCOH 2000), Delft. Elsevier Science, London. 219-50.

DYER, K.R., J. CORNELISSE, M.P. DEARNALEY, M.J. FENNESSY, S.E. JONES, J. KAPPENBERG, I.N. MCCAVE, M. PEJRUP, W. PULS, W. VAN LEUSSEN & K. WOLFSTEIN (1996) A comparison of in situ techniques for estuarine floc settling velocity measurements. *Journal of Sea Research,* **36**, 15-29.

EDGERTON, H., P. ORNTER & W. MCELROY (1981) In situ plankton camera. *Oceans*, Sept 1981 edition, 558-60.

EDWARDS, S.D., P.J.S. JONES, D.E. NOWELL (1997) Participation in coastal zone management initiatives: a review and analysis of examples from the UK. *Ocean & Coastal Management,* **36**, 143-65.

EDZWALD, J.K., J.B. UPCHURCH & C.R. O'MELIA (1975) Coagulation in estuaries. *Environmental Science & Technology,* **8**, 58-63.

EISMA, D. & A. LI (1993) Changes in suspended-matter floc size during the tidal cycle in the Dollard estuary *Netherlands Journal of Sea Research*, **31**, 107-17.

EISMA, D. (1991) Particle Size of Suspended Matter in Estuaries. *Geo-Marine Letters*, **11**, 147-53.

EISMA, D., A.J. BALE, M.P. DEARNALEY, M.J. FENNESSEY, W. VAN LEUSSEN, M.-A. MALDINEY, A. PFEIFFER & J.T. WELLS (1996) Intercomparison of *in situ* suspended matter (floc) size measurements. *Journal of Sea Research*, **36**, 3-14.

EISMA, D., P. BERNARD, G.C. CADEE, V. ITTEKKOT, J. KALF, R. LAANE, J.M. MARTIN, W.G. MOOK, A. VAN PUT, T. SHUHMACHER (1991) Suspended matter particle size in some west European estuaries. *Nethetherlands Journal of Sea Research,* **28**, 193-220.

EISMA, D., T. SCHUHMACHER , H. BOEKEL, J. VAN HEERWAARDEN, H. FRANKEN, M. LAAN, A. VAARS, F. EIJGENRAAM & J. KALF (1990) A camera and image-analysis system for in situ observation of flocs in natural waters. *Netherlands Journal of Sea Research*, **27**, 43-56.

EISMA, D.J. (1986) Flocculation and de-flocculation of suspended matter in estuaries. *Netherlands Journals of Sea Research*, **20**, 183-99.

EISMA, D.J., J. KALF & M. VEENHIUS (1980) The formation of small particles and aggregates in the Rhine estuary. *Netherlands Journal of Sea Research*, **14**, 172-91.

ELDER, J.W. (1959) The dispersion of marked fluid in turbulent shear flow. *Journal of Fluid Mechanics*, **5**, 544-60.

EMPHASYS CONSORTIUM (2000a) A Guide to Prediction of Morphological Change within Estuarine Systems, *HR Wallingford Report*, TR114.

EMPHASYS CONSORTIUM (2000b) Recommendations for Phase 2 of the Estuaries Research Programme, *HR Wallingford Report*, TR113.

EMPHASYS CONSORTIUM (2000c) Modelling Estuary Morphology and Process, *HR Wallingford Report*, TR111.

FAIRBRIDGE, R.W. (1980) The estuary: its definition and geodynamic cycle. In: *Chemistry and biogeochemistry of estuaries.* Ed. E. Olausson & I. Cato, Wiley, New York, 1-35.

FALCONER, R.A. & B. LIN (1997) Three-dimensional modelling of water quality in the Humber estuary. *Water Research,* **31**, 1092-102.

FALCONER, R.A. & Y. CHEN (1996) Modelling sediment transport and water quality processes on tidal floodplains. In: Anderson, D.E. Walling, P.D. Bates (Eds.) *Floodplain Processes*, Wiley, Chichester, 361-98.

FENNESSY, M.J. & K.R. DYER (1996) Floc population characteristics measured with INSSEV during the Elbe estuary intercalibration experiment. *Journal of Sea Research*, **36**, 55-62.

FENNESSY, M.J., K.R. DYER & D.A. HUNTLEY (1994) INSSEV - An instrument to measure the size and settling velocity of flocs in-situ. *Marine Geology*, **117**, 107-17.

FERRIER, G. & J.M. ANDERSON (1997) A multi-disciplinary study of frontal systems in the Tay estuary, Scotland. *Estuarine and Coastal Shelf Science*, **45**, 317-36

FINLAYSON, B.L. (1985) Calibration of a recording turbidity meter. *Catena*, **12**, 141-7.

FISCHER, H.B. (1973) Longitudinal dispersion and turbulent mixing in open channel flow. *Annual Review of Fluid Mechanics,* **8**, 107-33.

FISHER, F.H. & V.P. SIMMONS (1977) Sound absorption in seawater. *Journal of the Acoustical Society of America,* **62**, 588-64.

FOSTER, E. & J. WATSON (1997) Holography for underwater inspection and measurement: an overview of current work. *Optics and Laser Technology*, **29**, 17-23.

FRENCH, C.E., J.R. FRENCH, N.J. CLIFFORD & C.J. WATSON (2000) Sedimentation-erosion dynamics of abandoned reclamations: the role of waves and tides. *Continental Shelf Research,* **20**, 1711-33.

FRENCH, J.R. & H. BURNINGHAM (2003) Tidal marsh sedimentation versus sea-level rise: a southeast England estuarine perspective. *Proceedings, Coastal Sediments '03*, Clearwater, Florida, 1-14.

FRENCH, J.R. & N.J. CLIFFORD (2000) Hydrodynamic modelling as a basis for explaining estuarine environmental dynamics: some computational and methodological issues. *Hydrological processes.* **14**, 2089-108.

FRENCH, J.R. (2001) *Hydrodynamic modelling of the Blyth estuary: Impacts of sea-level rise.* Coastal & Estuarine Research Unit, University College London, Report for the Environment Agency, Anglian Region, 113pp.

FRENCH, J.R., D. REEVE & M. OWEN (2002) Estuaries Research Programme: Phase 2 Research Plan. *DEFRA/Environment Agency Flood & Coastal Defence R&D programme.* Report FD2115, April

FRENCH, J.R., N.J. CLIFFORD & T. SPENCER (1993) High frequency flow and suspended sediment measurements in a tidal wetland channel. In: Clifford, N.J., J.R. French & J. Hardisty (Eds.) *Turbulence: Perspectives on Flow and Sediment transport.* Wiley.

FRENCH, J.R., T. BENSON & H. BURNINGHAM (2004) Morphodynamics and sediment flux in the Blyth estuary, Suffolk, UK: conceptual modelling and high resolution monitoring. In: DM Fitzgerald & J Knight (eds.) *Morphodynamics and sedimentary evolution of estuaries.* Kluwer (in press).

FUGATE, D.C. & C.T. FRIEDRICHS (2002) Determining concentration and fall velocity of estuarine particle populations using ADV, OBS and LISST. *Continental Shelf Research,* uncorrected proof.

GALLAGER, S.M., C.S. DAVIS, A.W. EPSTEIN, A. SOLOW & R.C. BEARDSLEY (1996) High-resolution observations of plankton spatial distributions correlated with hydrography in the Great South Channel, Georges Bank. *Deep-Sea Research II,* **43**, 1627-63.

GARTNER, J.W., R.T. CHENG, P-F. WANG, & K. RICHTER (2001) Laboratory and field evaluations of the LISST-100 instrument for suspended particle size determinations. *Marine Geology*, **175**, 199-219.

GERDOL, V. & R.G. HUGHES (1994) Effect of *Corophium volutator* on the abundance of benthic diatoms, bacteria and sediment stability in two estuaries in southeastern England. *Marine Ecology Progress Series,* **114**, 109–115.

GIBBS, R.J. & L. KONWAR (1983) Sampling of mineral flocs using Niskin bottles. *Environmental Science & Technology,* **17**, 374-5.

GIBBS, R.J. (1982) Floc stability during Coulter-counter size analysis. *Journal of Sedimentary Petrology,* **52**, 657-9.

GIBBS, R.J. (1985) Estuarine flocs: their size, settling velocity and density. *Journal of Geophysical Research,* **90**, 3249-51.

GIBBS, R.J., L. KONWAR & A. TERCHUNIAN (1983) Size of flocs suspended in Delaware Bay. *Canadian Journal of Fisheries & Aquatic Science*, **40**, 102-4.

GIPPEL, C.J. (1989) The use of turbidimeters in suspended sediment research. *Hydrobiologia,* **176**, 465-80.

GOLSTEIN, S. (1938) *Modern developments in fluid dynamics*, **1**, Oxford University Press, Oxford.

GONZALEZ, R. C. & R.E. WOODS (2002). *Digital Image Processing*, 2nd ed., Prentice Hall, Upper Saddle River, NJ.

GORSKY, G., C. ALDORF, M. KAGE, M. PICHERAL, Y. GARCIA & J. FAVOLE (1992) Vertical distribution of suspended aggregates determined by a new underwater video profiler. *Annales de l'Institut oceanographique,* Paris, **68**, 275-80.

GRANT, J & G. GUST (1987) Prediction of coastal sediment stability from photopigment content and mats of purplesulphur bacteria, *Nature,* **330**, 244-6.

GREEN, M.O. & K.P. BLACK (1999) Suspended-sediment reference concentration under waves: field observations and critical analysis of two predictive models. *Coastal Engineering,* **38**, 115-41.

GREGORY, J. (1997) The density of particle aggregates. *Water Science & Technology* **36**(4), 1-13.

GRIFFITHS, W.D., D. MARK, I.A. MARSHALL & A.L. NICHOLS (1998) Aerosol Particle Size Analysis - Good Calibration Practices. *The Royal Society of Chemistry*, Cambridge.

GUAN, W.B., E. WOLANSKI & L.X. DONG (1998) Cohesive sediment transport in the Jiaojiang River estuary, China. *Estuarine Coastal and Shelf Science*, **46**, 861-71.

GUI, L., R. LINDKEN & W. MERZKIRCH (1997) Phase-separated PIV measurements of the flow around systems of bubbles rising in water, *ASME Fluids Engineering Division Summer Meeting*, FEDSM'97, June 22-26.

GUST, G. & V. MÜLLER (1997) Interfacial dynamics and entrainment functions of currently used erosion devices. In: Burt, N. Parker, R., Watts, J. (Eds.) *Cohesive Sediments*. Wiley, New York, 149-74.

HANES, D.M., C.E. VINCENT, D.A. HUNTLEY & T.L. CLARKE (1988) Acoustic Measurements of suspended sand concentration in the C2S2 experiment at Stanhope-Lane, Prince-Edward-Island, *Marine Geology*, **81**, 185-96.

HARIHARAN, P. (1996) *Optical holography: Principles, techniques and applications*. 2nd Ed. Cambridge Studies in Modern Optics, Cambridge University Press, 424 pp.

HART, D.P. (1998) High-speed PIV analysis using compressed image correlation. *Journal of Fluids Engineering-Transactions of the ASME*, **120**, 463–470.

HAWLEY, N. (1982) Settling velocity distribution of natural aggregates. *Journal of Geophysical Research*, **87**(C12), 9489-98.

HAY, A.E. & J. SHENG (1992) Vertical profiles of suspended sand concentration and size from multifrequency acoustic backscatter. *Journal of Geophysical Research*, **97**(C10), 15661-77.

HAY, A.E. (1983) On the remote acoustic detection of suspended sediment at long wavelengths. *Journal of Geophysical Research.*, **88**, 7525-42.

HAYES, M.O. (1975) Morphology of sand accumulation in estuaries: an introduction to the symposium. In: Cronin, L.E. (Ed.), *Estuarine Research*, Vol. II. Academic Press, New York, 3-22.

HEALY, T.R. & R.M. KIRK (1992) Coasts. In: J.M. Soons & M.J. Selby (eds.) *Landforms of New Zealand*, Auckland, Longman Paul, 161-83.

HEFFLER, D., J.P.M. SYVITSKI & K.W. ASPREY (1991) The floc camera. In: Syvitski, J.P.M. (Ed.) *Theory, Methods and Applications of Particle Size Analysis*, Cambridge University Press, New York, 209-21.

HEFFLINGER, L.O., G.L. STEWART & C.R. BOOTH (1978) Holographic motion pictures of microscopic plankton. *Applied Optics*, **17**, 951-4.

HERTZ, L. & R. SCHAFER (1993) Measurement of edge coincidence in image thresholdings, *Journal of Visual Communications & Image Representation*, **4**, 149-56.

HERVOUET, J.M. & L. VAN HAREN (1996) Recent advances in numerical methods for fluid flows. In: Anderson, D.E. Walling, P.D. Bates (Eds.) *Floodplain Processes*, Wiley, Chichester, 183-214.

HERVOUET, J-M. (1986) CARAC, finite element convection module, for the method of characteristics. EDF report HE41/86.21.

HESS, F.R. & K.W. BEDFORD (1985) Acoustic backscatter system (ABSS) - The instrument and some preliminary-results, *Marine Geology*, **66**, 357-79.

HOBSON, P.R., E.P. KRANTZ, R.S. LAMPITT, A. ROGERSON & J. WATSON (1997) A preliminary study of te distribution of plankton using hologrammetry. *Optics and Laser Technology*, **29**, 25-33.

HODKINSON, J.R. (1963) Light Scattering & Extinction by Irregular Particles Larger than the Wavelength. In: *ICES Electromagnetic Scattering*, ed. M. Kerker, Pergamon Press, Oxford, 87-99.

HOLDAWAY, G.P., P.D. THORNE, D. FLATT, S.E. JONES & D. PRANDLE (1999) Comparison between ADCP and transmissometer measurements of suspended sediment concentration. *Continental Shelf Research,* **19**, 421-41.

HOLLAND, A.F., R.G. ZINGMARK & J.M. DEAN (1974) Quantitative evidence concerning the stabilization of sediments by marine benthic diatoms, *Marine Biology*, **27**, 191-6.

HOLLAND, K.T., J.A. PULEO & T. KOONEY (2001) Quantification of swash flows using video-based particle image velocimetry. *Coastal Engineering*, **44**, 65-77.

HONJO, S., K.W. DOHERTY, Y.C. AGRAWAL & V.L. ASPER (1984) Direct optical assessment of large amorphous aggregates (marine snow) in the deep ocean. *Deep Sea Research*, **31**, 67-76.

HOUWING, E-J. & L.C. VAN RIJN (1998) In Situ Erosion Flume (ISEF): determination of bed-shear stress and erosion of a kaolinite bed. *Journal of Sea Research,* 39, 243-53.

HUANG, L.K. & M.J.J. WANG (1995) Image thresholding by minimizing the measures of fuzziness, *Pattern Recognition,* **28**, 41-51.

HUGHES, S.A. (1993) *Physical models and laboratory techniques in coastal engineering*, Advanced Series on Ocean Engineering – Volume 7, World Scientific Publishing Co., Pte. Ltd., Singapore.

JACKSON, W.H. (1964) An investigation into silt in suspension in the River Humber. *Dock and Harbour Auth.,* **45**, p. 526.

JÄHNE, B. (2002) *Digital image processing*, 5th Ed. Springer, Berlin. 585pp.

JANIN, J.M., E. DAVID & T. DENOT (1997) TELEMAC-3D User Manual. *Electricité de France, Département Laboratoire National d'Hydraulique.*

JANIN, J.M., F. LEPEINTRE & P. PECHON (1992) TELEMAC-3D: a finite element code to solve 3D free surface flow problems. *Proceedings of Computer Modelling of Seas and Coastal Regions.* Southampton, UK.

JENKINS, G. (1993) Estimating eddy kinematic viscosity in compound channels. In: Wang, S. (Ed) *Advances in Hydro-Science and Engineering* 1(B), 1277-82.

JENNINGS, D.S., M.D. THOMAS & W. GARDNERS (1922) A new method of mechanical analysis of soils. *Soil Science,* **14**, 485-99.

JIA, J.J., W.J. LU & Y.D. QIAN (2000) Physical modeling of localized scour for the Yangtze Estuary Waterway Improvement Project, Phase I. *China Ocean Engineering*, **14**, 473-84.

JOHNSON, B.D. & P.J. WANGERSKY (1985) A recording backward scattering meter and camera system for examination of the distribution and morphology of macro-aggregates. *Deep Sea Research*, **32**, 1143-50.

JOHNSON, C.P., X.Y. LI & B.E. LOGAN (1996) Settling velocities of fractal aggregates. *Environmental science & technology*, **30**, 1911-18.

JONES, D. & M.S. WILLS (1956) The attenuation coefficients of light in sea and estuarine waters in relation to the concentration of suspended solid matter, *J. Marine Biology Association U.K.,* **35**, 431-44.

JONES, S.E. & C.F. JAGO (1996) Determination of settling velocity in the Elbe estuary using QUISSET tubes. *Journal of Sea Research*, **36**, 63-7.

KAPUR, J.N., P.K. SAHOO & A.K.C. WONG (1985) A new method for gray-level picture thresholding using the entropy of the histogram, *Graphical Models & Image Processing,* **29**, 273-85.

KATZ, J., P.L. DONAGHAY, J. ZHANG, S. KING & K. RUSSELL (1999) Submersible holocamera for detection of particle characteristics and motions in the ocean. *Deep-Sea Research I,* **46**, 1455-81.

KATZ, J., T.J. O'HERN & A.J. ACOSTA (1984) An underwater holographic camera system for detection of microparticulates. *Proceedings of the ASME Cavitation and Multiphase Flow Forum,* New Orleans.

KAYE, G.W.C. & T.H. LABY (1986) *Tables of physical and chemical constants*, Longman, UK, 477 pp.

KENCH, P.S. & R.F. MCLEAN (1996) Hydraulic characteristics of bioclastic deposits: new possibilities for environmental interpretation using settling velocity fractions. *Sedimentology,* **43**, 561-70.

KILS, U. (1992) The ecoScope and dynIMAGE: microscale tools for in situ studies of predator prey interactions. *Archiv fèur Hydrobiologie Beiheft, Ergebnisse der Limnologie,* **36**, 83-96.

KINEKE, G.C., R.W. STERNBERG & R. JOHNSON (1989) A new instrument for measuring settling velocities in situ. *Marine Geology.* **90**, 149-58.

KIRKBY, M.J., P.S. NADEN, T.P. BURT & D.P. BUTCHER (1992) *Computer simulaton in physical geography,* 2nd Ed. Wiley, Chichester. 154-73.

KITTLER, J. & J. ILLINGWORTH (1986) Minimum error thresholding, *Pattern Recognition,* **19**, 41-7.

KNOWLES, S.C. & J.T. WELLS (1996) Suspended aggregate analysis using ISAAC, Else river, 9-10 June 1993. *Journal of Sea Research,* **36**, 69-75.

KNOX, C. (1966) Holographic microscopy as a technique for recording dynamic microscopic subjects. *Science,* **153**, 989-90.

KOMAR, PAUL D. & C.E. REIMERS (1978) Grain shape effects on settling rates. *Journal of Geology,* **86**, 193-209.

KRANCK, K. & T. MILLIGAN (1980) Macroflocs: production of marine snow in the laboratory, *Marine Ecology Progress Series,* **3**, 19-24.

KRANCK, K., E. PETTICREW, T.G. MILLIGAN & I. DROPPO (1993) In situ particle size distributions resulting from flocculation of suspended sediment. In: Mehta, A.J. (Ed.), *Nearshore and Cohesive Sediment Transport.* Coastal and Estuarine Studies Series 42, Springer-Verlag, New York, 60-75.

KRANENBURG, C. (1994) The fractal structure of cohesive sediment aggregates. *Estuarine and Coastal Shelf Science,* **39**, 451–60.

KRONE, R.B. (1978) Aggregation of suspended particles in estuaries. In: *Estuarine Transport Processes* (Kjerfve, B., ed.). University of South Carolina Press, Columbia, 177-90.

KRONE, R.V. (1962) Flume studies of the transport of sediment in estuarial shoaling processes. *Hydraulic Engineering and Sanitary Engineering Research Laboratory,* University of California, Berkeley, 1-110.

KUSUDA, T. & T. FUTAWATARI (1992) Simulation of suspended sediment transport in a tidal river. *Water Sciience & Technology,* **26**, 1421-30.

LAGVANKAR, A.L. & R.S. GEMMELL (1968) A size-density relationship for flocs. *Journal of the American Water Works Association,* **60**, 1040-6.

LAND, J.M. & R.N. BRAY (1998). Acoustic Measurement of Suspended Solids for Monitoring of Dredging and Dredged Material Disposal. In: *Proceedings of the 15th World Dredging Congress 1998*, Las Vegas. Western Dredging Association.

LANE, A., D. PRANDLE, A.J. HARRISON, P.D. JONES & C.J. JARVIS (1997) Measuring fluxes in tidal estuaries: Sensitivity to instrumentation and associated data analyses. *Estuarine Coastal & Shelf Science,* **45**, 433-51.

LAW, D.J., A.J. BALE & S.E. JONES (1997) Adaptation of focused beam reflectance measurement to in-situ particle sizing in estuaries and coastal waters. *Marine Geology,* **140**, 47-59.

LAWRENCE, R. (1990) *Southwold River: Georgian life in the Blyth valley.* Southwold, Moxon, 150pp.

LE NORMANT, C. (1998) *Description of SEDI3D, the sediment library of TELEMAC-3D release 2.2.* Electricité de France, Département Laboratoire National d'Hydraulique, Report HE-42/98/032/A

LE NORMANT, C. (2000) Three-dimensional modelling of cohesive sediment transport in the Loire estuary. *Hydrological Processes,* **14**, 2231-43.

LE ROUX, J.P. (1998) Entrainment threshold of natural grains in liquids determined empirically from dimensionless settling velocities and other measures of grain size. *Sedimentary Geology,* **119**, 17-23.

LEUNG, C.K. & F.K. LAM (1996) Performance analysis of a class of iterative image thresholding algorithms, *Pattern Recognition,* **29**(9), 1523-30.

LI, C.H. & C.K. LEE (1993) Minimum cross-entropy thresholding, *Pattern Recognition,* **26**, 617-25.

LI, C.H. & P.K.S. TAM (1998) An iterative algorithm for minimum cross-entropy thresholding, *Pattern Recognition Letters,* **19**, 771-6.

LI, D. & J. GANCZARCZYK (1989) Fractal geometry of particle aggregates generated in water and wastewater treatment processes. *Environmental Science & Technology,* **23**, 1385-9.

LI, Z.H., K.D. NGUYEN, J.C. BRUN-COTTAN & J.M. MARTIN (1994) Numerical simulation of the turbidity maximum transport in the Gironde estuary (France). *Oceanologica Acta,* **17**, 479-500

LIBICKI, C., K.W. BEDFORD & J.F. LYNCH (1989) The interpretation and evaluation of a 3-MHz acoustic backscatter device for measuring benthic boundary-layer sediment dynamics. *Journal of the Acoustical Society of America,* **85**, 1501-11.

LICK, W., H. HUANG & R. JESPEN (1993) Flocculation of fine-grained sediments due to differential settling. *Journal of Geophysical Research,* **98**, 10279-88.

LIN, B. & R.A. FALCONER (1996) Numerical modelling of three-dimensional suspended sediment for estuarine and coastal waters. *Journal of Hydraulic Research,* **34**, 435-56.

LINDSAY, P., P.W. BALLS & J.R. WEST (1996) Influence of tidal range and river discharge on suspended particulate matter fluxes in the Forth estuary (Scotland), *Estuarine Coastal & Shelf Science.* **42**, 63-82.

LIU, W-C., M-H. HSU & A.Y. KUO (2002) Modelling of hydrodynamics and cohesive sediment trasnport in Tanshui River estuarine system, Taiwan. *Marine Pollution Bulletin,* in press.

LOIZEAU, J-L., D. ARBOUILLE, S. SANTIAGO & J-P. VERNET (1994) Evaluation of a wide range laser diffraction grain size analyser for use with sediments. *Sedimentology,* **41**, 353-61.

LUECK, R.G. & Y. LU (1997) The logarithmic layer in a tidal channel. *Continental Shelf Research,* **17**, 1785-801.

LUMBORG, U. & A. WINDELIN (2003) Hydrography and cohesive sediment modelling: application to the Rømø Dyb tidal area. *Journal of Marine Systems*, **38**, 287-303.

LYNCH, J.F. & Y.C. AGRAWAL (1991) A model-dependent method for inverting vertical profiles of scattering to obtain particle size spectra in boundary layers. *Marine Geology,* **99**, 387-401.

LYNCH, J.F. (1985) Theoretical-analysis of ABSS data for HEBBLE. *Marine Geology.* **66**, 277-89.

LYNCH, J.F. (1987) Deep water sediment concentration profiling in HEBBLE using a one megahertz acoustic backscatter system. *In: Nicholas C.Kraus (Ed.), Coastal Sediments '87,* I. American Society of Civil Engineers, 250-9.

LYNCH, J.F., J.D. IRISH, C.R. SHERWOOD & Y.C. AGRAWAL (1994) Determining suspended sediment particle size information from acoustical and optical backscatter systems. *Continental Shelf Research,* **14**, 1139-65.

LYNCH, J.F., T.F. GROSS, B.H. BRUMLEY & R.A. FILYO (1991) Sediment concentration profiling in HEBBLE using a 1-MHz acoustic backscatter system. *Marine Geology*, **99**, 361-85.

MAA, J.P-Y., L.D. WRIGHT, C-H. LEE & T.W. SHANNON (1993) VIMS Sea Carousel: a field instrument for studying sediment transport. *Marine Geology,* **115**, 271-87.

MALDINEY, M.A. & J.M. MOUCHEL (1995) In situ observation of suspended solid aggregates in rivers. *Hydrobiologia*, **300/301**, 365-73.

MANNING, A.J. & K.R. DYER (1999) A laboratory examination of floc characteristics with regard to turbulent shearing. *Marine Geology,* **160**, 147-70.

MANNING, A.J. & K.R. DYER (2002) A comparison of floc properties observed during neap and spring tidal conditions. In: J.C. Winterwerp & C. Kranenburg (Eds.) *Fine Sediment Dynamics In The Marine Environment*, proceedings of the 6th International Conference on Nearshore and Estuarine Cohesive Sediment Transport Processes (INTERCOH 2000), Delft. Elsevier Science, London. 233-49.

MCCARTHY, J.C., T.E. PYLE & G.M. GRIFFIN (1974) Light transmissivity, suspended sediments, and the legal definition of turbidity. *Estuarine Coastal & Marine Science,* **2**, 291-9.

MCCAVE, I.N. & J. JARVIS (1973) Use of the Model T Coulter Counter in size analysis of fine to coarse sand. *Sedimentology*, **20**, 305-15.

MCCAVE, I.N. (1975) Vertical flux of particles in the ocean. *Deep-Sea Research*, **22**, 491–502.

MCCAVE, I.N. (1983) Particulate size spectra, behavior, and origin of nepheloid layers over the Nova Scotian continental rise. *Journal of Geophysical Research-Oceans and atmospheres,* **88**, 7647-66.

MCCAVE, I.N. (1984) Size spectra and aggregation of suspended particles in the deep ocean. *Deep-Sea Research,* **31**, 329-52.

MEADOWS, P.S. & J. TAIT (1989) Modification of sediment permeability and shear strength by two burrowing invertebrates. *Marine Biology*, **101**, 75-82.

MEAKIN, P. (1991) Fractal aggregates in geophysics. *Reviews of Geophysics.* **29**, 317-354.

MEDWIN, H. & C.S. CLAY (1998) *Fundamentals of acoustical oceanography*, Academic Press, New York, 712 pp.

MEHTA, A.J. (1986) *Estuarine cohesive sediment dynamics : proceedings of a workshop on cohesive sediment dynamics with special reference to physical processes in estuaries.* Springer-Verlag, New York.

MIKKELSEN, O.A. & M. PEJRUP (2000) In situ particle size spectra and density of particle aggregates in a dredging plume. *Marine Geology,* **170**, 443-59.

MIKKELSEN, O.A. (2002) Examples of spatial and temporal variations of some fine-grained suspended particle characteristics in two Danish coastal water bodies. *Oceanologica Acta,* **25**, 39-49.

MILLIGAN, T.G. (1996) In situ particle (floc) size measurements with the Benthos 373 plankton silhouette camera. *Journal of Sea Research*, **36**, 93-100.

MOODY, J.A., B. BUTMAN & M.H. BOTHNER (1987) Near-bottom suspended matter concentration on the Continental Shelf during storms: estimates based on in situ observations of light transmission and a particle size dependent transmissometer calibration. *Continental Shelf Research*, Vol. 7, No. 6, pp. 609-628.

MOTYKA, J.M. & A.H. BRAMPTON (1993) *Coastal Management: Mapping of littoral cells.* Report SR 328, HR Wallingford, UK.

MOULIN, C. & E. BEN SLAMA (1998) The two-dimensional transport module SUBIEF. Applications to sediment transport and water quality processes. *Hydrological Processes,* **12**, 1183-95.

MULDER, H.P.J. & C. UDINK (1991) Modelling of cohesive sediment transport. A case study: the western Scheldt estuary. In: Edge, B.L. (Ed.), *Proceedings of the 22nd International Conference on Coastal Engineering.* American Society of Civil Engineers, New York, 3012-23.

MURRAY, P.B., I.N. MCCAVE, T.R.E. OWEN, M. MASON & M.O. GREEN (1996) A robust in situ settling velocity box for coastal seas. *Journal of Sea Research.* **36**, 101-7.

NORRBIN, M.F., C.S. DAVIS & S.M. GALLAGER (1996) Differences in fine-scale structure and composition of zooplankton between mixed and stratified regions of Georges Bank. *Deep-Sea Research II,* **43**, 1905-24.

O'BRIEN, M.P. (1969) Equilibrium flow areas of inlets on sandy coasts. *Journal of Waterways, Harbours & Coastal Engineering,* ASCE, **95**(WW1), 43-52.

O'CONNOR, B.A. & J.A. NICHOLSON (1988) Mud transport modelling. In: Dronkers, J. & W. van Leussen (Eds.) *Physical Processes in Estuaries*, Springer-Verlag, 532-44.

O'CONNOR, B.A. (1971) Mathematical model for sediment distribution. *Proceedings of the 14th IAHR conference,* Paper D23, Paris, France.

O'GORMAN, L. (1994) Binarization and multithresholding of document images using connectivity, *Graphical Models & Image Processing,* **56**, 494-506.

O'HERN, T.J., L. D'AGOSTINO & A.J. ACOSTA (1988) Comparison of holographic and Coulter Counter measurements of cavitation nuclei in the ocean. *Journal of Fluids Engineering,* **110**, 200-7.

O'MELIA, C.R. (1980) Aquasols: the behaviour of small particles in aquatic systems. *Environmental Science and Technology*, **14**, 1052-60.

ODD, N.V.M. & M.W. OWEN (1972) *A two-layer model of mud transport in the Thames estuary.* In: Proceedings of the Institution of Civil Engineers, London, 195-202.

OFFICER, C.B. (1981) Physical dynamics of estuarine suspended sediments. *Marine Geology*, **40**, 1-14.

OLIVO, J.C. (1994) Automatic threshold selection using the wavelet transform, *Graphical Models & Image Processing,* **56**, 205-18.

OTSU, N. (1979) A Threshold Selection Method from Gray-Level Histograms, *IEEE Transactions on Systems, Man and Cybernetics*, **9**(1), 62-6.

OWEN, M.W. (1971) The effect of turbulence on the settling velocities of silt flocs. *Proceedings of the 14th Congress of the International Association for Hydraulic Research,* Paris, **D-4**, 27-32.

OWEN, M.W. (1976) Determination of the settling velocities of cohesive muds. *HR Wallingford. Rep. IT161.*

PAFFENHOFER, G.A., T.B. STEWART, M.J. YOUNGBLUTH & T.G. BAILEY (1991) High-resolution vertical profiles of pelagic tunicates. *Journal of Plankton Research,* **13**, 971-81.

PAL, N.R. (1996) On minimum cross-entropy thresholding, *Pattern Recognition,* **29**(4), 575-80.

PAL, S.K. & A. ROSENFELD (1988) Image enhancement and thresholding by optimization of fuzzy compactness, *Pattern Recognition Letters*, **7**, 77-86.

PARKER, R. (1978) *Men of Dunwich*, London, Collins, 272pp.

PARTHENIADES, E. (1965) Erosion and deposition of cohesive soils, *Journal of the Hydrology Division*, ASCE, **91**(HY1), 105-39.

PATERSON, D.M. (1989) Short term changes in the erodibility of intertidal cohesive sediments related to the migratory behaviour of epipelic diatoms. *Limnology and Oceanography,* **34**, 223-34.

PATERSON, D.M. (1994) Microbial mediation of sediment structure and behaviour, In: L.J. Stal & P. Gaumthe (eds.) *Microbial Mats,* NATO ASI series, **635**, Springer-Verlag.

PATERSON, D.M. (1995) The biogenic structure of early sediment fabric visualised by low-temperature scanning electron microscopy. *Journal of the Geological Society,* **152**, 131-40.

PATERSON, D.M. (1997) Biological mediation of sediment erodability: ecology and physical dynamics. In: In: Burt, N. Parker, R., Watts, J. (Eds.) *Cohesive Sediments.* Wiley, New York.

PEJRUP, M. (1988) Flocculated suspended sediment in a micro-tidal environment, *Sedimentary Geology,* **57**, 249-56.

PELTIER, E. C. LE NORMANT, C. TEISSON, A. MALCHEREK, M. MARKOFSKY, W. ZIELKE, J. CORNELISSE, P. MOLINARO, S. CORTI & G. GRECO (1996) *Three dimensional numerical modelling of cohesive sediment transport processes in estuarine environments,* Final report to the EC Contract MAS2-CT92-0013, Departement Laboratoire National d'Hydraulique, EDF-DER, Paris.

PETHICK, J.S. (1996) The geomorphology of mudflats. In: *Estuarine Shores: evolution environments and human alterations.* K.F. Nordstrom & C.T. Roman (Eds.). John Wiley & Sons Ltd, Chichester, 185-211.

PETHICK, J.S. (2001) Coastal management and sea-level rise. *Catena,* **42**, 307-22.

PFEIFFER, A. (1996) In situ measurements of flocculated suspended matter with a video multi sensor array. *Journal of Sea Research,* **36**, 115-8.

PIKAZ, A. & A. AVERBUCH (1996) Digital image thresholding based on topological stable state, *Pattern Recognition,* **29**, 829-43.

PINKEL, R. (1983) Doppler sonar observations of internal waves: wave field structure off California. *Journal of Physical Oceanography,* **13**, 804-15.

POSFORD DUVIVIER (1999) Suffolk estuarine strategies. Phase II – Report A: Blyth estuary. Peterborough, Environment Agency, Anglian Region.

PRITCHARD, D.W. (1952). Salinity distribution and circulation in the Chesapeake Bay estuarine system. *Journal Marine Research,* **11**, 106-23.

PULS, W. & H. KÜHL (1996) Settling velocity determination using the BIGDAN settling tube and the Owen settling tube. *Journal of Sea Research,* 36, 119-25.

PULS, W., W. KUHL & K. HEYMANN (1988) Settling velocity of mud flocs: results of field measurements in the Elbe and Weser estuaries. In: Dronkers, J. & W. van Leussen (Eds.) *Physical Processes in Estuaries.* Springer-Verlag, Berlin, 404-24.

PUN, T. (1981) Entropic thresholding: A new approach, *Computer Graphics an Image Processing,* **16**, 210-39.

RASTOGI, A-K. & W. RODI (1978) Predictions of heat and mass transfer in open channels. *Journal of the Hydraulics Division, ASCE,* **104**(HY3), 397-420.

RAUDKIVI, A.J. (1990) The roughness height under waves – reply. *Journal of Hydraulic Research,* **28**, 647-649.

RD INSTRUMENTS (1998) Workhorse technical manual. P/N 957-6000-00, Change 2, January.

RD INSTRUMENTS (1999) TRANSECT User's manual. P/N 951-6092-00, Change 1, June.

REED, C.W., A.W. NIEDORODA & D.J.P. SWIFT (1999) Modeling sediment entrainment and transport processes limited by bed armoring, *Marine Geology,* **154**, 143-54.

REICHEL, G. & H.P. NACHTNEBEL (1994) Suspended sediment monitoring in a fluvial environment - Advantages and limitations of applying an acoustic-doppler-current-profiler. *Water Research,* **28**, 751-761.

RICHARDS, K.S., S. BROOKS, N. CLIFFORD, T. HARRIS, S. LANE (1997) Theory, measurement and testing in 'real' geomorphology and physical geography. In: *Process & Form in Geomorphology,* D.R. Stoddart (ed.), Routledge, London, 265-92.

RICHARDS, S.D., A.D. HEATHERSHAW & P.D. THORNE (1996) The effect of suspended particulate matter on sound attenuation in seawater. *Journal of the Acoustical Society of America,* **100**, 1447-50.

RIDDERINKHOF, H., R. VAN DER HAM & W. VAN DER LEE (2000) Temporal variations in concentration and transport of suspended sediments in a channel-flat system in the Ems-Dollard estuary. *Continental Shell Research,* **20**, 1479-93.

RIDLER, T.W. & S. CALVARD (1978) Picture thresholding using an iterative selection method, *IEEE Transactions on Systems, Man & Cybernetics,* **8**, 630-2.

ROBERTS, W., P. LE HIR & R.J.S. WHITEHOUSE (2000) Investigation using simple mathematical models of the effect of tidal currents and waves on the profile shape of intertidal mudflats. *Continental Shelf Research,* **20**, 1079-97.

ROSE, C.P. & P.D. THORNE (2001) Measurements of suspended sediment transport parameters in a tidal estuary. *Continental Shelf Research,* **21**, 1551-75.

ROSENFELD, A. & P. DE LA TORRE (1983) Histogram concavity analysis as an aid in threshold selection, *IEEE Transactions on Sytems, Man & Cybernetics,* **13**, 231-5.

ROSENFELD, A. (1984) The fuzzy geometry of image subsets, *Pattern Recognition Letters,* **2**, 311-7.

ROSS, M.A. & A.J. MEHTA (1989) On the mechanics of lutoclines and fluid mud. *Journal of Coastal Research,* **5**, 51-62.

ROUSE, H. (1937) Modern conception of the mechanics of fluid turbulence. *Transactions of the American Society of Civil Engineers,* **102**, 463-543.

ROY, P.S., R.J. WILLIAMS, A.R. JONES, I. YASSINI, P.J. GIBBS, B. COATES, R.J. WEST, P.R. SCANES, J.P. HUDSON & S. NICOLA (2001) Structure and function of South-east Australian estuaries. *Estuarine, Coastal & Shelf Science,* **53**, 351-84.

SAHOO, P, C. WILKINS & J. YEAGER (1997) Threshold selection using Renyi's entropy, *Pattern Recognition,* **30**, 71-84.

SCHAUER, U. (1987) Determination of the bottom boundary layer parameters at two shallow sea sites using the profile method. *Continental Shelf Research,* **7**, 1211-30.

SCHUBEL, J.R. & E.W. SCHIEMER (1972) A device for collecting in-situ samples of suspended sediment for microscopic analysis. *Journal of Marine Reseach,* **30**, 269-73.

SCHUBEL, J.R. (1969) Size distributions of the suspended particles of the Chesapeake Bay turbidity maximum. *Netherlands Journal of Sea Research,* **4**, 283-309.

SCHÜNEMANN, M. & H. KÜHL (1991) *A device for erosion-measurements on naturally formed, muddy sediments: the EROMES-system.* GKSS-Forschungszentrum Geesthacht GmbH, Report GKSS 91/E/18, 28 pp.

SEZAN, M.I. (1985) A peak detection algorithm and its application to histogram-based image data reduction, *Graphical Models & Image Processing,* **29**, 47-59.

SHANBAG, A.G. (1994) Utilization of information measure as a means of image thresholding, *Computer Vision Graphics & Image Processing,* **56**, 414-9.

SHELDON, R.W. (1968) Sedimentation in the Estuary of the River Crouch, Essex, England. *Limnology and Oceanography,* **13**, 72-83.

SHENG, J. & A.E. HAY (1988) An examination of the spherical scatterer approximation in aqueous suspensions of sand. *Journal of the Acoustical Society of America,* **83**, 598-610.

SHEWCHUCK, J.R. (1996) *Triangle: Engineering a 2D Quality Mesh Generator and Delaunay Triangulator.* First Workshop on Applied Computational Geometry (Philadelphia, Pennsylvania), pages 124-133, ACM, May 1996. http://www-2.cs.cmu.edu/~quake/tripaper/triangle0.html

SHI, C., S.M. HUTCHINSON, L. YU & S. XU (2001) Towards a sustainable coast: an integrated coastal zone management framework for Shanghai, People's Republic of China. *Ocean & Coastal Management,* **44**, 411-27.

SIMPER, R. (1994) *Rivers Alde, Ore and Blyth*, Lavenham, Creekside publishing, 84pp.
SIMPSON, M.R. & R.N. OLTMANN (1990) An acoustic Doppler discharge measurement system. *Proceedings of the 1990 National Conference on Hydraulic Engineering*, **2**, 903-8.
SLINGER, J.H. & C.M. BREEN (1995) Integrated research into estuarine management. *Water Science and Technology*, **32**(5-6), 79-86.
SMERDON, A.M., J.M. REES & C.E. VINCENT (1998) *An acoustic backscatter instrument to measure near-bed sediment processes*, Aquatec Electronics Ltd., Web publication.
SMITH, T.J. & R. KIRBY (1989) Generation, stabilisation and dissipation of layered fine sediment suspensions. *Journal of Coastal Research*, **5**, 63-73.
SMS USER MANUAL (2003) *Surface Water Modeling System*, version 8.1. Brigham Young University, Environmental Modeling Research Laboratory, December 15. http://www.bossintl.com
SOULSBY, R.L. & K.R. DYER (1981) The form of the near-bed velocity profile in a tidally accelerating flow. *Journal of geophysical research*, **86**, 8067-74.
SOULSBY, R.L., J.V. SMALLMAN, I.H. TOWNEND, M. OWEN & M. POSTLE (1997) Estuaries: the case for research into morphology and processes, *HR Wallingford Report* SR 478.
SPEARMAN, J.R. & W. ROBERTS (2002) Comparison of flocculation models for applied sediment transport modelling, In: J.C. Winterwerp & C. Kranenburg (Eds.) *Fine Sediment Dynamics In The Marine Environment*, proceedings of the 6th International Conference on Nearshore and Estuarine Cohesive Sediment Transport Processes (INTERCOH 2000), Delft. Elsevier Science, London. 277-93.
SPINRAD, R.W. & J.R.V. ZANEVELD (1982) An analysis of the optical features of the near-bottom and bottom nepheloid layers in the area of the Scotian Rise. *Journal of Geophysical Research*, **87**, 9553-61.
STERNBERG, R.W., A. OGSTON & R. JOHNSTON (1996) A video system for in-situ measurement of size and settling velocity of suspended particulates. *Journal of Sea Research*, **36**, 127-130.
STERNBERG, R.W., D.A. CACCHIONE, D.E. DRAKE & K. KRANCK (1986) Suspended sediment transport in an estuarine tidal channel within San Francisco Bay, California. *Marine Geology*, **71**, 237-58.
STERNBERG, R.W., I. BERHANE & A.S. OGSTON (1999) Measurement of size and settling velocity of suspended aggregates on the northern California continental shelf. *Marine Geology*, **154**, 43-53.
STEWART, G.L., J.R. BEERS & C. KNOX (1973) Application of holographic techniques to the study of marine plankton in the field and the laboratory. *Developments in Laser Technology – II*, In: *Proceedings of the Society of the Photo-Optics Instrumentation Engineering*, San Diego, **41**, 183.
STOKES, G.G. (1851) On the effect of the internal friction of liquids on the motion of pendulums. *Cambridge Philosophy Society Proceedings*, **9**, 8-106.
STOLZENBACH, K.D. & M. ELIMELICH (1994) The effect of density on collisions between sinking particles: implications for particle aggregation in the ocean. *Journal of Deep Sea Research I*, **41**, 469-83.
SWALES, A., T. HUME, J. HAWKEN, R. LIEFTING & M. CULLINGFORD (2001) Shifting sands: using image analysis and laser technology to study coastal sand dispersal. *Water & Atmosphere Online*, **9**(1).
SWIFT, D.J.P., J.R. SCHUBEL & R.W. SHELDON (1972) Size analysis of fine-grained suspended sediments. a review. *Journal of Sedimentary Petrology*, **42**, 122-34.

SWITHENBANK, J., D. BEER, D.S. TAYLOR, D. ABBOT & G.C. MCCREATH (1977) A laser diagnostic technique for the measurement of droplet and particle size distribution. In: Zinn, B.J. (Ed.) *Experimental Diagnostics in Gas Phase Combustion Systems, Progress in Aeronautics & Astronautics,* **53**, 421-47.

SYVITSKI, J. P. M., K.W. APREY & K.W.G. LEBLANC (1995) In-situ characterisitcs of particles settling within a deep-water estuary. *Deep Sea Research II,* **42**, 223-56.

TAMBO, N. & Y. WATANABE (1979) Physical aspects of flocculation I. The floc density function and aluminium floc. *Water Research,* **13**, 409-19.

TATTERSALL, G.R., A.J. ELLIOTT & N.M. LYNN (2003) Sediment concentrations in the Tamar estuary. *Estuarine Coastal & Shelf Science,* **57**, 679-88.

TEISSON, C. & D. FRITSCH (1988) New advances in numerical modelling of suspended sediment transport in the Loire Estuary. *IAHR symposium on mathematical modelling of sediment transport in the coastal zone.* Copenhagen. 30th May-1st June.

TEISSON, C. (1997) A review of cohesive sediment transport models. In: Cohesive Sediments (N. Burt, R. Parker, J. Watts, eds.), John Wiley & Sons, Chichester, 367-81.

THOMSEN, L., S. JÄHMLICH, G. GRAF, M. FIEDRICHS, S. WANNER & B. SPRINGER (1996) An instrument for aggregate studies in the benthic boundary layer. *Marine Geology,* **135**, 153-7.

THORN, C.E. (1981) At Kent-State Applied geomorphology, *Geotimes,* **26**, 22-3.

THORNE, P.D. & D.M. HANES (2002) A review of acoustic measurement of small-scale sediment processes. *Continental Shelf Research,* **22**, 603-32.

THORNE, P.D. & P.J. HARDCASTLE (1997) Acoustic measurements of suspended sediments in turbulent currents and comparison with in-situ samples. *Journal of the Acoustical Society of America,* **101**(5), 2603-14.

THORNE, P.D. & S.C. CAMPBELL (1992) Backscattering by a suspension of spheres. *Journal of the Acoustical Society of America,* **92**, 978-86.

THORNE, P.D., C.E. VINCENT, P.J. HARDCASTLE, S. REHMAN & N. PEARSON (1991) Measuring suspended sediment concentrations using acoustic backscatter devices, *Marine Geology,* **98**, 7-16.

THORNE, P.D., P.J. HARDCASTLE & R.L. SOULSBY (1993) Analysis of acoustic measurements of suspended sediments. *Journal of Geophysical Research-Oceans,* **98**, 899-910.

TITUS, J.G., R.A. PARK, S.P. LEATHERMAN, J.R. WEGGEL, M.S. GREENE, P.W. MAUSEL, S. BROWN, C. GAUNT, M. TREHAM & G. YOHE (1991) Greenhouse effect and sea-level rise: the cost of holding back the sea. *Coastal Management,* **19**, 171-210.

TOLHURST, T.J., G. GUST & D.M. PATERSON (2002) The influence of an extracellular polymeric substance (EPS) on cohesive sediment stability. In: J.C. Winterwerp & C. Kranenburg (Eds.) *Fine Sediment Dynamics In The Marine Environment,* proceedings of the 6th International Conference on Nearshore and Estuarine Cohesive Sediment Transport Processes (INTERCOH 2000), Delft. Elsevier Science, London. 409-25.

TOLHURST, T.J., K.S. BLACK, S.A. SHAYLER, S. MATHER, I. BLACK, K. BAKER, & D.M. PATERSON (1999) Measuring the in situ erosion shear stress of intertidal sediments with the Cohesive Strength Meter (CSM), *Estuarine Coastal & Shelf Science,* **49**, 281-94.

TOLHURST, T.J., R. RIETHMÜLLER & D.M. PATERSON (2000) In situ versus laboratory analysis of sediment stability from intertidal mudflats. *Continental Shelf Research,* **20**, 1317-34.

TORIU, T., H. IWASE & T. GOTOH (1990) A method for threshold selection using minimum filtering, *Systems & Computers in Japan,* **21**, 16-23.

TRAYKOVSKI, P., R.J. LATTER & J.D. IRISH (1999) A laboratory evaluation of the laser in situ scattering and transmissometry instrument using natural sediments. *Marine Geology,* **159**, 355-67.

TRUSSEL, H.J. (1979) Comments on picture thresholding using iterative selection method, *IEEE Transactions on Systems, Man & Cybernetics,* **9**, 311.

TSAI, C-H. & W. LICK (1986) A portable device for measuring sediment resuspension. *J. Great Lake Res.,* **12**, 314-21.

TSAI, C-H. (1996) An assessment of a time-of-transition laser sizer in measuring suspended particles in the ocean. *Marine Geology,* **134**, 95-112.

TSAI, W.H. (1985) Moment-preserving thresholding: A new approach, *Graphical Models & Image Processing,* **19**, 377-93.

U.S. ARMY CORPS OF ENGINEERS (1998) *Coastal Engineering Manual, Part III, Chapter 1, Coastal Sediment Properties,* report EC 1110-2-292.

UNCLES, R.J. & J.A. STEPHENS (2000) Observations of currents, salinity, turbidity and intertidal mudflat characteristics and properties in the Tavy Estuary, UK. *Continental Shelf Research,* **20**, 1531-49.

UTAMI, T. & T. UENO (1991) Experimental study on the compound meandering channel flow using flow visualisation and picture processing. *Journal of Hydro-science and Hydraulic Engineering,* **9**, 1-10.

VAN DER HAM, R. & J.C. WINTERWERP (2001) Turbulent exchange of fine sediments in a tidal channel in the Ems/Dollard estuary. Part II: Analysis with a 1DV numerical model. *Continental Shelf Research,* **21**, 1629-47.

VAN DER HULST, H.C. (1989) *Light Scattering by Small Particles.* Dover Publications, New York, 63-224.

VAN DER LEE, W.T.B. (2000) Temporal variation in floc size and settling velocity in the Dollard estuary. *Continental Shelf Research,* **20**, 1495-511.

VAN LEUSSEN, W. & J.M. CORNELISSE (1993) The determination of the sizes and settling velocities of estuarine flocs by an underwater video system. *Netherlands Journal of Sea Research,* **31**, 231-41.

VAN LEUSSEN, W. (1994) *Estuarine macroflocs and their role in fine-grained transport,* PhD thesis, Universiteit Utrecht, Netherlands, 488 pp.

VAN LEUSSEN, W. (1996), The RWS field settling tube. *Journal of Sea Research,* **36**, 83-6.

VAN RIJN, L.C. & L.E.A. NIENHUIS (1985) In situ determination of the fall velocity of suspended sediment. *Proceedings of the 21st Congress IAHR, Melbourne, Australia,* **4**, 144-8.

VAN RIJN, L.C., H.V. ROSSUM & P. TERMES (1990) Field verification of 2D and 3D suspended-sediment models. *Journal of Hydraulic Engineering,* **166**, 1270-88.

VARADAN, V.V., Y. MA & V.K. VARADAN (1985) Theoretical-analysis of the acoustic response of suspended sediment for HEBBLE. *Marine Geology,* **66**, 267-76.

VIOLEAU, D., S. BOURBAN, C. CHEVIET, M. MARKOFSKY, O. PETERSON, W. ROBERTS, J. SPEARMAN, E. TOORMAN, H.J. VESTED & H. WEILBEER (2002) Numerical simulation of cohesive transport: intercomparison of several numerical models. In: J.C. Winterwerp & C. Kranenburg (Eds.) *Fine Sediment Dynamics In The Marine Environment,* proceedings of the 6th International Conference on Nearshore and Estuarine Cohesive Sediment Transport Processes (INTERCOH 2000), Delft. Elsevier Science, London. 75-90.

WALLING, D.E. (1977) Assessing the Accuracy of Suspended Sediment Rating Curves for a Small Basin. *Water Resources Research,* **13**, 531-8.

WATTS, C.W., T.J. TOLHURST, K.S. BLACK & A.P. WHITMORE (2003) In situ measurements of the intertidal shear stress and geotechnical shear strength of the intertidal sediments of the experimental managed realignment scheme at Tollesbury, Essex, UK. *Estuarine, Coastal and Shelf Science,* **58**, 611-20.

WELLS, J.T. & A.L. SHANKS (1987) Observations and geologic significance of marine snow in a shallow-water, partially enclosed marine embayment. *Journal of Geophysical Research*, **92**(C2), 13185-90.

WELLS, J.T. & S-Y. KIM (1991) The Relationship between beam transmission and concentration of suspended particulate material in the Neuse river estuary, North Carolina. *Estuaries*, **14**, 395-403.

WELLS, P.G. & G.R. DABORNE (1997) *The Rio de la Plata: An environmental overview. An EcoPlata Project Background Report.* ISBN 0-7703-0467-2, Dalhousie University, Halifax, Nova Scotia. 248 pp.

WENNER, E.L. & M. GEIST (2001) The National Estuarine Research Reserves program to monitor and preserve estuarine waters. *Coastal Management*, **29**, 1-17.

WHITEHOUSE, R.J.S., R.L. SOULSBY, W. ROBERTS & H.J. MITCHENER (2000) *Dynamics of estuarine muds, A manual for practical applications*, Thomas Telford Publications.

WIBERG, P.L., D.E. DRAKE & D.A. CACCHIONE (1994) Sediment resuspension and bed armoring during high bottom stress events on the northern California inner continental shelf: measurements and predictions. *Continental Shelf Research*, **14**, 1191-219.

WIJNGAARDEN, M.V. (1999) A two-dimensional model for suspended sediment transport in the southern branch of the Rhine-Meuse estuary, the Netherlands. *Earth Surface Processes and Landforms*, **24**, 1173-88.

WILLIAMSON, H.S. & M.C. OCKENDEN (1996) ISIS: an instrument for measuring erosion shear stress in situ. *Estuarine Coastal Shelf Science*, **42**, 1-18.

WILSON, C.A.M.E, P.D. BATES & J-M. HERVOUET (2002) Comparison of turbulence models for stage-discharge rating curve prediction in reach-scale compound channel flows using two-dimensional finite element methods. *Journal of Hydrology,* **257**, 42-8.

WINTERWERP, J.C. (1998) A simple model for turbulence induced flocculation of cohesive sediment. J. Hydraulic Res., IAHR. *Journal of Hydraulic Engineering,* **36**, 309-36.

WINTERWERP, J.C. (2002) On the flocculation and settling velocity of estuarine mud. *Continental Shelf Research,* **22**, 1339-60.

WINTERWERP, J.C., A.J. BALE, M.C. CHRISTIE, K.R. DYER, S. JONES, D.G. LINTERN, A.J. MANNING & W. ROBERTS (2002) Flocculation and settling velocity of fine sediment. In: J.C. Winterwerp & C. Kranenburg (Eds.) *Fine Sediment Dynamics In The Marine Environment*, proceedings of the 6th International Conference on Nearshore and Estuarine Cohesive Sediment Transport Processes (INTERCOH 2000), Delft. Elsevier Science, London. 25-39.

WITHER, A.W., J. LAND, C.C. JARVIS & P.D. JONES (1998) *A new technique for Contaminant flux measurement in estuaries*. Conference on estuarine research and management in developed and developing countries. Organised by Centre for Estuarine Research and Management (RSA) & Estuarine and Coastal Sciences Association (UK). University of Port Elizabeth. July.

WOLANSKI, E., B. KING & D. GALLOWAY (1995) Dynamics of the turbidity maximum in the Fly River estuary, Papua-New-Guinea. *Estuarine Coastal & Shelf Science,* **40**, 321-37.

WOLFSTEIN, K.W. (1996) Fractionation and measurements of settling velocities of suspended matter using an Owen Tube. *Journal of Sea Research*, **36**, 147-52.

WOLLAST, R. (1986) The Scheldt estuary. In Salomon, W., B.L. Bayne, E.K. Duursma & U. Forstner (Eds.) *Pollution of the North Sea. An Assessment.* Springer-Verlag, 183-93.

WOOD, I.R. & T. LIANG (1990) Dispersion in an open channel with a step in the cross-section. *Journal of Hydraulic Research,* IAHR, **27**, 587-601.

WRIGHT, A. & P. NORTON (2000) Inter-comparison between one, two and three-dimensional numerical models. In: EMPHASYS Consortium (2000) Modelling Estuary Morphology and Process, *HR Wallingford Report*, TR111.

YANNI, M.K. & E. HORNE (1994) A new approach to dynamic thresholding, *9th European Conference on Signal Processing,* **1**, 34-44.

YEN, J.C., F.J. CHANG & S.CHANG (1995) A new criterion for automatic multilevel thresholding, *IEEE Transactions on Image Processing,* **4**, 370-8.

YOUNG, R.A. (1976) Seaflume: a device for in-situ studies of threshold erosion velocity and erosional behaviour of undisturbed marine muds. *Marine Geology,* **23**, 11-8.

YOUNG, R.A., J.T. MERRILL, T.L. CLARKE & J.R. PRONI (1982) Acoustic profiling of suspended sediments in the marine bottom boundary layer. *Geophysical Research Letters,* **9**, 175-178.

ZANEVELD, J.R.V., R.W. SPINRAD & R. BARTZ (1982) An optical settling tube for determination of particle-size distributions. *Marine Geology,* **49**, 357-76.

ZEDEL, L., G.B. CRAWFORD & L. GORDON (1996) On the determination of wind direction using an upward looking acoustic Doppler current profiler. *Journal of Geophysical Research,* **101**, 12163-76.